

# **Solution Processed Hole Extraction Interfaces for Polymer Solar Cells**

Abdullah S Alsulami

Department of Physics and Astronomy

University of Sheffield



The  
University  
Of  
Sheffield.

Thesis submitted for the degree of

Doctor of Philosophy

August 2016





## Acknowledgements

---

I would not have been able to undertake a PhD were it not for the help of my parents, my wife and my brothers and sisters. Thank you for all your love and support and for having faith in me to pursue this degree. I would like also thank both of my supervisors: Dr. Alastair Buckley, whose guidance, character and support got me through these four years, who was always there to pick me up and keep me going when things were down and ideas were reaching dead ends; Professor. David Lidzey, who always had the time to offer help and guidance, gave advice on any aspect of the project and offer critical analysis.

A huge thank you goes to Jonathan Griffin, Andrew Pearson and Darren Watters who have helped me cope with any stress I faced, were always there to discuss problems, and gave me inspiration to keep going when things didn't always go according to plan.

Thank you to Andrew Brook for starting me off in the lab and providing me with my initial training.

I would also like to thank everyone in EPMM group past and present for all of their scientific and non-scientific discussions. Special thanks go to James Kingsley, Edward Bovill and Nick Scarratt for all their help and guidance in the Kroto Centre and other labs.

Last, but by no means least, thanks to the Saudi Cultural Bureau in London, UK, and King Abdulaziz City for Science and Technology (KACST) in Riyadh, Saudi Arabia, for the provision of a PhD scholarship.

# Publications

---

1. B. Mustafa, J. Griffin, A. S. Alsulami, D. G. Lidzey and A. R. Buckley, *Solution processed nickel oxide anodes for organic photovoltaic devices*, Applied Physics Letters **104** (2014), no. 6.
2. K. Adhitya, A. Alsulami, A. Buckley, R. C. Tozer and M. Grell, *Intensity-modulated spectroscopy on loaded organic photovoltaic cells*, Ieee Journal of Photovoltaics **5** (2015), no. 5, 1414-1421.
3. Alsulami, A.; Griffin, J.; Alqurashi, R.; Yi, H.; Iraqi, A.; Lidzey, D.; Buckley, A. *Thermally Stable Solution Processed Vanadium Oxide as a Hole Extraction Layer in Organic Solar Cells*. Materials **2016**, 9, 235.
4. R. Alqurashi; J. Griffin; A. Alsulami; A. Buckley, *Open-Circuit Voltage in Inverted Polycarbazole:Fullerene Bulk Heterojunction Solar Cells*, in IEEE Journal of Photovoltaics , vol.PP, no.99, pp.1-6
5. Alsulami, A.; Griffin, J.; Alqurashi, R.; Yi, H.; Iraqi, A.; Lidzey, D.; Buckley, A. *The operational stability of polymer solar cells incorporating a vanadium oxide hole-extraction layer deposited from Vanadium(V) oxytriisopropoxide precursor*, (Manuscript in preparation).

## Conferences

---

- UK Semiconductors 2013; on July 3<sup>rd</sup>-4<sup>th</sup> 2013 – Sheffield
- International Conference on Hybrid and Organic Photovoltaics; from 11<sup>st</sup> to 14<sup>th</sup> May 2014 - Lausanne, Switzerland; Poster, *High performance of organic solar cells with solution-processed vanadium pentoxide hole extraction layer*
- UK Semiconductors 2014; on July 9<sup>rd</sup>-10<sup>th</sup> 2014 – Sheffield; Oral presentation, *High performance of organic solar cells with solution-processed vanadium pentoxide hole extraction layer*
- International Conference on Hybrid and Organic Photovoltaics; from 10<sup>th</sup> to 13<sup>th</sup> May 2015 - Rome, Italy; Poster, *Lifetime analysis and degradation study of OPVs utilising a solution processed V<sub>2</sub>O<sub>x</sub> interlayer*
- UK Semiconductors 2015; on July 1<sup>st</sup>-2<sup>nd</sup> 2015 – Sheffield; Oral presentation, *Lifetime analysis and degradation study of OPVs utilising a solution processed V<sub>2</sub>O<sub>x</sub> interlayer*

# Abstract

---

Organic semiconductors often make poor ohmic contacts with electrodes due to the deep energy levels forming an energetic barrier at the interfaces between the organic layer and the electrode contact. The mismatch in energy levels at the interface was overcome by inserting PEDOT:PSS material as an anode interlayer for achieving good ohmic contact and selecting single types of charge carriers at the polymer-electrode interface. Despite the significant development that was observed in the OPVs performance, the residual moisture and the acidic nature of PEDOT:PSS can cause degradation of the organic films and therefore affect long term stability. Metal oxides were later suggested as alternative interlayers to the PEDOT:PSS which exhibited high performance and long lifetimes. However, many of the metal oxide studies reported in literature used vacuum deposition methods, such as thermal evaporation and sputter deposition, which are not necessarily desirable for large-scale production.

This thesis shows that it is possible to deposit Vanadium oxide ( $V_2O_x$ ) from solution in ambient conditions requiring no post-deposition treatment and achieving comparable efficiency to the most widely used interlayer materials. Using a combination of spectroscopic techniques and device characterisation, it is shown that solution-processed  $V_2O_x$  can be used to replace evaporated metal oxides in optoelectronic devices which are fabricated at high temperatures. The work also goes on to show that it is possible to solution-process nickel oxide from a nickel acetylacetonate precursor and obtain a power conversion efficiency  $> 5\%$ . Finally, the lifetime study of OPV devices utilising various anode interlayer materials shows that the stability of optimised  $V_2O_x$  devices can be comparable with other interlayer materials.

# Contents

---

## Chapter 1 Introduction

1.1	Solar Energy.....	1
1.2	Organic Solar Cells .....	3
1.3	Thesis Summary.....	6
1.4	References.....	9

## Chapter 2 Background

2.1	Introduction.....	15
2.2	Organic Semiconductors .....	15
2.2.1	Chemical Structure .....	16
2.2.2	Electronic Structure .....	18
2.2.3	Optical Transitions in Conjugated Polymers.....	20
2.3	Basic Working Principles of BHJs .....	24
2.3.1	Light Absorption .....	26
2.3.2	Exciton Generation.....	27
2.3.3	Exciton Diffusion .....	27
2.3.4	Exciton Dissociation.....	28
2.3.5	Charge Transport .....	29
2.3.6	Charge Extraction .....	30
2.4	Characterisation of Power Conversion Efficiency.....	31
2.5	The Interfacial Energy Level Alignment in OPV .....	35
2.6	Roles of Interfacial Layers.....	39
2.6.1	Electrical Effects .....	40
2.6.2	Optical Effects .....	41
2.6.3	Morphology .....	45
2.6.4	Improving OPV Stability.....	47



# Contents

---

2.7	Utilising Metal Oxides at the Anode Buffer Layer.....	48
2.7.1	Molybdenum Oxide ( $\text{MoO}_3$ ) .....	48
2.7.2	Nickel Oxide ( $\text{NiO}$ ) .....	51
2.7.3	Tungsten Oxide ( $\text{WO}_3$ ) .....	53
2.7.4	Vanadium Oxide ( $\text{V}_2\text{O}_5$ ) .....	55
2.8	References.....	58

## Chapter 3 Experimental Techniques and Methods

3.1	Introduction .....	84
3.2	Experimental Techniques.....	84
3.2.1	Ultraviolet Photoelectron Spectroscopy .....	84
3.2.2	X-ray Photoelectron Spectroscopy .....	89
3.2.3	Atomic Force Microscopy .....	92
3.2.4	Spectrofluorometer .....	93
3.2.5	Spectroscopic Ellipsometry .....	95
3.2.6	Electrical Characterisation of Devices .....	97
3.2.7	Laser Beam Induced Current Mapping (LBIC) .....	98
3.2.8	The Lifetime Tester .....	100
3.2.9	Thermal Evaporator .....	101
3.2.10	Solution Deposition Technique .....	102
3.3	OPV Device Fabrication .....	106
3.3.1	Materials and Solution Preparation .....	106
3.3.2	Thin Films Preparation .....	109
3.3.3	Device Fabrication .....	110
3.4	References .....	113

# Contents

---

## Chapter 4 Optical and Electronic Structure Characterisation of Materials

4.1 Introduction .....	117
4.2 Metal Oxides .....	118
4.2.1 Vanadium Oxide.....	118
4.2.2 Molybdenum Oxide.....	124
4.3 Organic Semiconductors .....	127
4.3.1 PCDTBT.....	127
4.3.2 PFDT2BT_8 .....	129
4.4 Conclusion.....	130
4.5 References .....	132

## Chapter 5 Vanadium Oxide OPV Devices

5.1 Introduction .....	139
5.2 Influence of ITO Surface Cleaning Method on OPV Performance .....	141
5.3 Optimisation of the Thickness of the s-V <sub>2</sub> O <sub>x</sub> Anode Buffer Layer for Organic Photovoltaic Devices .....	142
5.4 Hydrolysis .....	144
5.5 Influence of Surface Roughness on OPV Device Performance .....	146
5.6 Impact of Atmosphere Gases in s-V <sub>2</sub> O <sub>x</sub> Morphology .....	149
5.7 Spray Coating vs Spin Coating .....	150
5.8 Comparison of s-V <sub>2</sub> O <sub>x</sub> Films with Commonly Utilised Hole- extracting Materials.....	152
5.9 Inverted OPVs with a s-V <sub>2</sub> O <sub>x</sub> Thin Layer .....	157
5.9.1 Optimising TiO <sub>x</sub> as an Electron Extracting Layer with e-MoO <sub>3</sub> .....	157
5.9.2 Inverted OPV Device with a s-V <sub>2</sub> O <sub>x</sub> Layer on the Top.....	159
5.10 Thermally Stable s-V <sub>2</sub> O <sub>x</sub> as a Hole Extraction Layer in OPV .....	160
5.11 Conclusion.....	170

# Contents

---

5.12 References .....	167
-----------------------	-----

## **Chapter 6 Solution-Processed Nickel Oxide Devices**

6.1 Introduction .....	179
6.2 Optimisation of NiO Devices by Thermal Annealing.....	180
6.3 O <sub>2</sub> -plasma treatment.....	185
6.4 Conclusion.....	190
6.5 References .....	192

## **Chapter 7 Lifetime Study of V<sub>2</sub>O<sub>x</sub> Devices**

7.1 Introduction .....	194
7.2 Degradation and Stability of OPVs.....	195
7.2.1 Anode Interfacial Layer for Stable PSCs .....	197
7.3 Stability Study of V <sub>2</sub> O <sub>x</sub> Devices .....	201
7.3.1 Lifetime Measurement.....	201
7.3.2 Stability of s-V <sub>2</sub> O <sub>x</sub> vs MoO <sub>3</sub> and PEDOT:PSS .....	202
7.3.3 Thickness Impact.....	208
7.3.4 Thermal Annealing .....	211
7.4 Conclusion.....	221
7.5 References .....	223

## **Chapter 8 Conclusion and Further Work**

8.1 Conclusions of Work Undertaken .....	233
8.2 Suggestions for Further Work.....	235
8.3 References .....	238

## List of Figures

---

<b>List of Figures</b>	<b>page</b>
1.1. Average annual global solar power potential .....	2
2.1. (a) PCDTBT copolymer with a carbazole donor that is connected via thiophenes to a benzothiadiazole acceptor unit. (b) and (c) The chemical structures in the bottom represent thiophene rings in P3HT that can be connected either regioregular (b) or regiorandom (c) .....	17
2.2. Energy level diagram illustrating absorption, fluorescence and intersystem crossing process of a molecule. Dashed lines correspond to vibrational energy levels within each state, whilst the vertical arrows illustrate an electronic transition. The figure is adapted from reference. ....	21
2.3. Absorption (solid line) and fluorescence (dashed line) spectra of perylene dissolved in toluene. The sample was excited at 490 nm and the absorption data were collected using a spectral bandwidth of 1.0 nm. The two peaks at 531 and 540 nm correspond to the principle transition between the lowest vibrational levels of the ground and first excited state. Low intensity peaks represent transitions between modes of higher vibrational energy. Data provided by the PhotochemCAD libraryThe chemical structure is shown in the bottom .....	22
2.4. Morphology model of the donor and acceptor active layer in a BHJ device (left) and general device structure (right).....	25
2.5. Schematic representation shows energy levels and the operating mechanism of a bulk heterojunction device. (1) A photon is absorbed forming an exciton. (2) The generated exciton diffuses to the interface of the donor/acceptor. (3) Separation of the exciton into free charges. (4)	

## List of Figures

---

Transport charge carriers to the electrode interface. (5) Free charges are extracted into electrodes. ....	25
<b>2.6.</b> Current-density voltage characteristics of a solar cell under illumination. ....	32
<b>2.7.</b> Equivalent circuit of an OPV device where $J$ is the photocurrent, $R_{SH}$ is the shunt resistance, $R_S$ is the series resistance and $V$ is the applied voltage. ....	34
<b>2.8.</b> (a) plotting dipole interface at an organic layer as a function of the metal work function. The data is adapted from ref. [40] for interfaces between tris(8-hydroxyquinoline) aluminium (Alq) and varied work function metals. (b) and (c) show schematic illustration of vacuum level alignment and Fermi level alignment for metal-organic interface. $\Phi$ is the work function and $\Delta$ is the interface dipole. ....	37
<b>2.9.</b> Structures of OPV devices with various interfacial layers and their corresponding electric field intensity within the P3HT:PCBM thin film. ....	42
<b>2.10.</b> Illustration of metal oxide nanorods as charge collectors. ....	46
<b>3.1.</b> Schematic of a photoelectron spectrometer with an electrostatic electron energy analyser used for XPS and UPS investigation. ....	86
<b>3.2.</b> (a) An example of an UPS spectra, (b) the low energy cut-off (c) the Fermi level of a metal (d) valence band or HOMO onset for a semiconductor. ....	88
<b>3.3.</b> (a) an XPS spectrum with a Shirley background and (b) the spectrum after removal of background with fitted peaks. ....	91
<b>3.4.</b> Simplified schematic of the principal components in an AFM. The cantilever was connected to a piezoelectric component to enable smooth contact with the sample surface. ....	93

## List of Figures

---

<b>3.5.</b> Schematic of the optical components of the Horiba Fluoromax 4. The instrument is divided into two main components; the excitation part on the right with the beam defined in red and emission part defined in orange on the left. ....	94
<b>3.6.</b> Schematic of a spectroscopic ellipsometer with the two components; the light source on the right and the analyser on the left. ....	95
<b>3.7.</b> Newport 92251A-1000 Solar Simulator that generates an AM1.5 output radiation (left). The aperture mask used for OPV characterization (right).....	98
<b>3.8.</b> Laser Beam Induced Current Mapping (LBIC) Setup.....	99
<b>3.9.</b> (a) Image of an ATLAS suntest CPS+ model. (b) The circuit board containing temperature and photodiodes sensors that was used for measuring up to 8 devices.....	100
<b>3.10.</b> Cathode evaporation mask for deposition of desired material over a determined area of the substrate. ....	102
<b>3.11.</b> Thicknesses of vanadium (V) oxide vs. spin speeds for different concentrations of solution.....	104
<b>3.12.</b> Schematics of the ultrasonic spray coating setup, a hot plate is used during deposition process in order to control solvent evaporation rate.....	104
<b>3.13.</b> ITO coated substrate as six pixel design. (b) shows the OPV device structure for normal architecture. ....	112
<b>4.1.</b> (a) Optical transmission spectra of the $V_2O_x$ films with different thicknesses; (○) 5 nm, (△) 10 nm, (▽) 20 nm, for solution-processed vanadium oxide and (□) 10 nm for vacuum evaporated film. The absorption coefficient $(\alpha h\nu)^2$ as a function of the photon energy for 20 nm of $V_2O_x$ films. ....	119

## List of Figures

---

- 4.2.** XPS spectra of  $V_2O_x$  thin films deposited by (a) spin-coating method and (b) vacuum thermal evaporation. The energy difference between the O1s and  $V2p_{3/2}$  peaks was used for measuring the oxidation state of vanadium oxide. .... 121
- 4.3.** (a) UPS measurements showing the secondary electron cut-off region and the expanded region near the Fermi level for  $V_2O_x$  films fabricated by solution ( $\circ$ ) and vacuum evaporated process ( $\square$ ) and (b) energy level alignment scheme at the ITO/ $V_2O_x$  interface showing dipole interface ( $\Delta$ ) of 0.5 eV and the work function ( $\Phi$ ) of s-  $V_2O_x$ . VL,  $E_F$  and VB are vacuum level, Fermi level and valence band, respectively. .... 123
- 4.4.** (a) Optical transmission spectra of vacuum deposited  $MoO_3$  thin film, (b) The absorption coefficient  $(\alpha h\nu)^2$  as a function of the photon energy for 20 nm of  $MoO_3$  films..... 125
- 4.5.** XPS spectra of vacuum evaporated  $MoO_3$  thin film, (a) the O1s peak with three different species are observed, (b) the Mo3d peaks involve two different Molybdenum species.  $Mo^{5+}$  oxidation state arises as a low-energy shoulder in the core levels of  $3d_{5/2}$  and  $3d_{3/2}$  to deposition condition. .... 125
- 4.6.** UPS spectrum of vacuum deposited  $MoO_3$  thin film showing the secondary electron cut off and the valence band region..... 126
- 4.7.** (a) Normalised absorption spectra, and (b) UPS spectra for PCDTBT thin film spun from chlorobenzene on ITO substrate. .... 128
- 4.8.** UV-Vis absorbance spectrum of PFDT2BT-8 thin film spun from  $CHCl_3$ . .... 129

## List of Figures

---

- 4.9.** The relevant energy levels of electrodes, HELs, and active layer materials used throughout the following experimental chapters either determined through spectroscopy of materials or from literature. ....131
- 5.1.** Current density-voltage (J-V) characteristics for PCDTBT:PC<sub>70</sub>BM devices with various thicknesses of s-V<sub>2</sub>O<sub>x</sub> films; (□) 5 nm, (○) 10 nm, (△) 15 nm, (▽) 20 nm and (◇) 25 nm.....143
- 5.2.** Comparison of PFDT2BT-8:PC<sub>70</sub>BM device performance with vanadium oxide spin coated from solution and stored in ambient conditions for different periods of time. ....145
- 5.3.** AFM height images with a size of 4 μm x 3 μm for (a) the bare Si surface and (b-d) s-V<sub>2</sub>O<sub>x</sub> thin films spin coated on a Si surface showing rms of 17, 4.8, 1.2 nm respectively. e-h are the phase images for the same samples. ....147
- 5.4.** The roughness (rms) of s-V<sub>2</sub>O<sub>x</sub> spin cast from concentrations (▽) 1 mg/ml, (△) 3 mg/ml, (○) 5 mg/ml and (□) 10 mg/ml at different spin speeds.....148
- 5.5.** AFM topography image of the s-V<sub>2</sub>O<sub>x</sub> layer deposited in the nitrogen glove box; (a) height image and (b) phase image.....150
- 5.6.** shows surface morphology of the solution-processed V<sub>2</sub>O<sub>x</sub> film deposited by (a) spin coating and (b) spray coating techniques. ....151
- 5.7.** (a) J-V characteristics of optimised devices with a PFDT2BT-8:PC<sub>70</sub>BM active layer for various hole extraction materials; PEDOT:PSS, solution processed vanadium oxide and vacuum deposited V<sub>2</sub>O<sub>x</sub> and MoO<sub>3</sub>. (b) Comparison of performance parameters of devices. ....154



## List of Figures

---

- 5.8.** (a) J-V characteristics of optimised devices with a PCDTBT:PC<sub>70</sub>BM active layer for various HEL materials; PEDOT:PSS, solution processed V<sub>2</sub>O<sub>x</sub> and MoO<sub>3</sub>, and vacuum deposited V<sub>2</sub>O<sub>x</sub> and MoO<sub>3</sub>. (b) Comparison of performance parameters of OPV devices..... 155
- 5.9.** Dependence of inverted OPV parameters upon light soaking with TiO<sub>x</sub> buffer layer as an electron extraction layer. The devices were fabricated with a PCDTBT:PC<sub>70</sub>BM active layer and vacuum deposited MoO<sub>3</sub> on the top. .... 157
- 5.10.** (a) the current density-voltage characteristics of PFDT2BT-8:PC<sub>70</sub>BM devices with (□) unannealed s-V<sub>2</sub>O<sub>x</sub> interlayer and annealed at 75°C for (○) 10 minutes, (△) 30 minutes, (▽) 60 minutes and (◇) 120 minutes. (b) The series resistance R<sub>s</sub> and shunt resistance R<sub>sh</sub> as a function of time. (c) and (d) Comparison of performance parameters of OPV devices. .... 161
- 5.11.** (a) The current density-voltage characteristics of PFDT2BT-8:PC<sub>70</sub>BM based solar cell with (□) unannealed s-V<sub>2</sub>O<sub>x</sub> thin film and annealed for 30 minutes at (○) 100°C, (△) 200°C, (▽) 300°C and (◇) 400°C. (b) The series resistance R<sub>s</sub> and shunt resistance R<sub>sh</sub> as a function of annealing temperature. (c) and (d) Comparison of performance parameters of OPV devices as a function of annealing temperature..... 162
- 5.12.** LBIC images show photocurrent map within the active area for PFDT2BT-8:PC<sub>70</sub>BM devices with (a) unannealed s-V<sub>2</sub>O<sub>x</sub>, (b) annealed at 200°C and (c) annealed at 400°C. The colour scale for the LBIC images was adjusted with high generated current indicated by red, and low current indicated by dark blue. .... 164
- 5.13.** Optical transmission spectra of the s-V<sub>2</sub>O<sub>x</sub> films with different Annealing temperature; (□) unannealed, (○) 100°C, (△) 200°C, (▽) 300°C and

## List of Figures

---

- 400°C (◇) . The insert shows the absorption coefficient  $(\alpha h\nu)^2$  as a function of the photon energy.....165
- 5.14.** AFM topography (2  $\mu\text{m}$  x 2  $\mu\text{m}$ ) of a 10 nm thick s-V<sub>2</sub>O<sub>x</sub> layer deposited on top of Si with native oxide; (a) as deposited, (b) Annealed at 200°C, (C) Annealed at 400°C. The average grain size 163 was 21.3 nm, 16.8 nm and 19.6 nm, respectively. ....166
- 5.15.** Photoelectron spectroscopy scans of s-V<sub>2</sub>O<sub>x</sub> thin film deposited on ITO in air. (a) XPS data for (i) unannealed film and those annealed at (ii) 200°C, (iii) 300°C and (iv) 400°C. (b) UPS scans for films with (□) no annealing, (○) 200°C, (△) 300°C and (▽) 400°C .....169
- 5.16.** Schematic energy level diagrams of the s-V<sub>2</sub>O<sub>x</sub> thin film deposited on ITO in air without annealing and those annealed at 200°C, 300°C and 400°C..... 170
- 6.1.** (a) The current density-voltage characteristics of PCDTBT:PC<sub>70</sub>BM based solar cell with (□) unannealed NiO thin film and annealed for 30 minutes at (○)100°C, (△) 200°C, (▽) 300°C, (◇) 400°C and (◀) 500°C . (b) The series resistance R<sub>s</sub> and shunt resistance R<sub>sh</sub> as a function of annealing temperature. (c) and (d) Dependence of OPV parameters upon annealing temperature.....181
- 6.2.** Photoelectron spectroscopy data of nickel acetylacetonate films deposited onto ITO for films as-deposited and with post deposition annealing between 250°C and 500°C. (a), (b) are UPS measurements (c) the Ni2p spectra, (d) O1s spectra.....183
- 6.3.** (a) The current density-voltage characteristics of OPV devices with thermally annealed NiO films at 400°C; (□) before O<sub>2</sub>-plasma treatment

## List of Figures

---

- and (○) after treatment. (b) and (c) comparison of performance parameters of OPV devices for films with oxygen plasma treatment for pressure of 0.5 mbar (filled shapes) and 1.5 mbar (open shapes) after annealing at 400°C.....186
- 6.4.** Photoelectron spectroscopy data of nickel acetylacetonate films after post-deposition annealing at 400°C with and without oxygen plasma treatment. (a), (b) are UPS measurements (c) O1s spectra, and (d) the Ni2p spectra.....189
- 6.5.** Schematic energy level diagrams of nickel acetylacetonate films deposited onto ITO for films as-deposited, with post deposition annealing at 400°C and oxygen plasma treatment after annealing.....190
- 7.1.** the temperature and light intensity values measured inside the lifetime test chamber. The temperature values are the mean of four temperature sensors while the light intensity values are the mean of eight silicon photodiodes. The average temperature is  $36.7^{\circ}\text{C} \pm 0.7$ .....202
- 7.2.** The normalised PCE,  $V_{oc}$ ,  $J_{sc}$  and FF of PEDOT:PSS, s- $V_2O_x$  and  $MoO_3$  devices extracted from the ATLAS Suntest CPS+ data as a function of irradiation time. Each value represents the mean of at least 10 pixels from 12 pixels and each pixel was measured every 15 minutes. The linear phase of PCE curves was used for calculating  $T_{80}$  and  $T_{50}$  lifetimes.....203
- 7.3.** Current density-voltage (J-V) characteristics for PEDOT:PSS,  $V_2O_x$  and  $MoO_3$  devices under the AM1.5G solar spectrum before (left) and after 500 hours of lifetime testing (right).....206
- 7.4.** Laser beam-induced current (LBIC) images for s- $V_2O_x$ -based devices before (left) and after 500 hours of lifetime testing (right). The colour scale in the figure shows the intensity of the generated current in which

## List of Figures

---

- the red colour indicates high current density while the dark blue indicates low current. ....208
- 7.5.** The normalised PCE,  $V_{oc}$ ,  $J_{sc}$  and FF of s- $V_2O_x$ -based devices extracted from the ATLAS Suntest CPS+ data as a function of irradiation time. The PFDT2BT-8:PC<sub>70</sub>BM devices were fabricated with 5 nm, 10 nm, 15 nm or 20 nm thickness of s- $V_2O_x$  films. Each value represents the mean of at least 10 pixels from 12 pixels and each pixel was measured every 15 minutes.....209
- 7.6.** Comparison of Photovoltaic parameters for PFDT2BT-8:PC<sub>70</sub>BM devices under the AM1.5G solar spectrum with various thicknesses of s- $V_2O_x$  thin layers. The open shapes represent pre-illumination characterisation and the filled shapes represent the post-illumination measurements. ....210
- 7.7.** (J-V) characteristics for s- $V_2O_x$ -based devices under the AM1.5G solar spectrum before (left) and after 150 hours of illumination (right). The s- $V_2O_x$  thin films with thickness of 5 nm were thermally annealed in air for durations ranging from 10 to 80 minutes before spin coating the PFDT2BT-8:PC<sub>70</sub>BM blend inside a nitrogen filled glovebox.....213
- 7.8.** Comparison of performance parameters for devices with 5 nm thickness of s- $V_2O_x$  thin layer that were annealed between 10 to 80 minutes in air. The open shapes represent pre-illumination characterisation and the filled shapes represent the post-illumination measurements.....214
- 7.9.** Current density-voltage (J-V) characteristics for s- $V_2O_x$ -based devices under the AM1.5G solar spectrum before (left) and after 150 hours of illumination (right). The s- $V_2O_x$  thin films with thicknesses of 5, 10, 15, 20 nm were thermally annealed at 150 °C under ambient conditions for

## List of Figures

---

30 minutes before spin coating the PFDT2BT-8:PC70BM blend inside a nitrogen filled glovebox.....	215
<b>7.10.</b> Comparison of performance parameters for devices with various thicknesses of s-V <sub>2</sub> O <sub>x</sub> thin layers that were annealed for 30 minutes in air. The open shapes represent pre-illumination characterisation and the filled shapes represent the post-illumination measurements. ....	216
<b>7.11.</b> Photoelectron Spectroscopy scans of unannealed solution processed vanadium oxide film and annealed film at 200°C in air where (a) is the C1s spectra and (b) O1s spectra. ....	217
<b>7.12.</b> The normalised photovoltaic parameters extracted from the ATLAS Suntest CPS+ data as a function of irradiation time for OPV devices utilising the different HEL materials. Each value represents the mean of at least 10 pixels from 12 pixels and each pixel was measured every 15 minutes. The linear phase of PCE curves was used for calculating T <sub>80</sub> lifetimes. ....	219

# Chapter 1

## Introduction

### 1.1 Solar Energy

In the 21st century energy is still the main driving force for economic growth, and humanitarian development. Indeed, the global demand for energy has increased significantly over the past five decades due to the rapid growth in population and economic development [1]. It is estimated that total global consumption of energy will rise by 31% between 2010 and 2040 [2]. Furthermore, there are many poor communities that live in non-electrified regions with limited access to energy. Over 1.3 billion people in the world suffer from a lack of access to modern energy services as the cost of energy continues to rise. Currently, the main source of global energy depends essentially on non-sustainable resources (i.e. fossil fuels) which are the main reason for some environmental problems such as global warming and climate change [3]. Recent studies have demonstrated that atmospheric emissions in the last decade increased 2.2% per year which was double the rate in the period between 1970 to 2000 [4]. As a result, clean and sustainable sources of energy are needed to reduce emissions of air pollutants as well as greenhouse gases.

Renewable energy sources such as solar, wind and geothermal can be exploited as alternatives to fossil fuels. The development and use of renewable energy sources will

provide a secure, long-term sustainable energy supply. Photovoltaic (PV) technology offers an inexhaustible and an omnipresent energy source by direct harvesting of energy from sunlight. Moreover, most developing nations are located in regions with high average annual solar reception making solar systems relatively affordable and applicable in those regions (see **Figure 1**) [5].

The initial developments of silicon-based solar cells achieved a power conversion efficiency (PCE) of up to 6% which then improved rapidly up to 10 % [6]. Subsequent efforts have been made to improve the performance of photovoltaic devices and reduce their cost. The physical properties of crystalline silicon (i.e. a narrow band gap of 1.1 eV and high mobility of free charges) have made it possible to achieve a PCE of 25 % [7]. Using gallium arsenide (GaAs) as an alternative to silicon semiconductors developed a PV efficiency exceeding 28% [7].

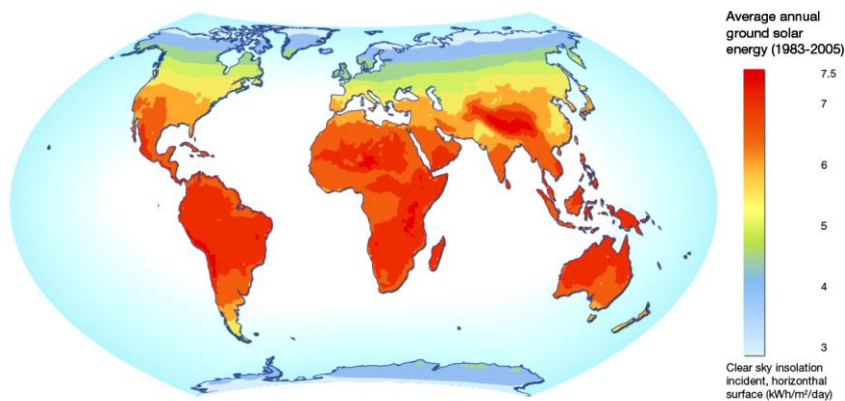


**Figure 1** Average annual global solar power potential [5]

So far, the high cost of crystalline silicon remains as one obstacle for expanding the use of solar cells. Researchers have studied numerous materials as alternatives to high-cost semiconductors. Fabrication methods of inorganic semiconducting thin films such as GaAs, CdTe and amorphous silicon were developed to decrease manufacturing cost and material consumption [8, 9]. Consequently, these materials have resulted in modest decreases in PV module prices. Nevertheless, the electricity produced from coal is still much cheaper than solar electricity. For this reason, organic polymers have been researched as substantially low-cost photovoltaic materials. Furthermore, organic photovoltaics (OPVs) exhibit several advantages, such as solution-processability, mechanical-flexibility and being light-weight. Organic semiconductors can be deposited by different methods such as gravure printing, inkjet printing and spray coating allowing them to be applicable in the manufacturing of plastic solar cells. Although OPVs are inefficient compared to inorganic solar cells, dramatic improvement has been observed in recent years (now reaching about 11.1% as reported by Heliatek for laboratory cells) [10].

### 1.2 Organic Solar Cells

The first OPV cell was first created in 1959 by sandwiching an anthracene single crystal between two electrodes [11]. The resulting device showed very low PCE and very low open circuit voltage  $V_{oc}$  (the maximum voltage a solar cell can produce) of 200 mV due to the inefficient exciton dissociation. Unlike inorganic solar cells that generate free electrons and holes, separating the strongly bound excitons into free charges in the single active layer is difficult, resulting in poor performance and an efficiency of less than 0.1 %.



In 1986, Tang introduced a two-layer OPV that comprised bilayer cells with a PCE of about 1% [12]. The improved efficiency was ascribed to the active layer that contained two different organic semiconductors: one worked as an electron donor (D) and the other as an electron acceptor (A), forming a D/A interface of a planar heterojunction (PHJ). As a result, the excitons generated in bilayer devices dissociate effectively at the interface better than single layer cells do. However, the efficiency of bilayer OPVs was still low due to the short diffusion length of the excitons (i.e., the average distance travelled by the exciton prior to recombination, which is typically  $< 10$  nm) [13]. Accordingly, the excitons' dissociation was limited to this length at each side of the interface while the remaining thickness increased the series resistance of the device.

In 1995, a change in the active layer morphology was suggested by blending an electron-donating polymer and an electron-accepting fullerene derivative to form a bulk heterojunction (BHJ) device [14, 15]. As a result, a significant increase in the organic device PCE (up to 3%) was achieved. The blended materials exhibited a nanostructure thin film where the interface could be distributed throughout the active layer. Early studies showed that the transfer of photoinduced electrons from a polymer donor to C60 derivatives within a BHJ device can be achieved in femtosecond scale, which is  $10^3$  times faster than the radiative and non-radiative decay of the photoexcitations. Thus, the BHJ device showed a quantum efficiency of charge separation that was close to unity [16].

Nevertheless, organic semiconductors often make poor ohmic contacts with electrodes due to the mismatch of energy levels [17, 18], the presence of interfacial dipoles [19, 20], and high densities of interfacial trap states [21]. Therefore, inserting an interlayer between the active layer and the electrode has been suggested for achieving good ohmic

contact and high built-in potential via shifting the vacuum level, bending energy levels, and pinning the Fermi level at the polymer-electrode interface. In addition, the interlayer film can work as a selective contact for single types of charge carriers and suppress some chemical reactions that might occur at the polymer-electrode interface. Among the different interlayer materials used in organic electronics, polyethylene dioxythiophene:polystyrenesulfonate (PEDOT:PSS) has exhibited a significant improvement in OPV performance.

Despite the positive aspects of aqueous PEDOT:PSS, the residual moisture (hygroscopic) and the acidic nature of PEDOT:PSS can cause degradation [22, 23] of the organic films and therefore reduce the device's stability. In the late 1990s, metal oxides (e.g., molybdenum oxide ( $\text{MoO}_3$ ), ruthenium(II) oxide  $\text{RuO}_x$  and vanadium oxide  $\text{V}_2\text{O}_5$ ) were suggested as alternative interlayers to the PEDOT:PSS between the anode and the organic material in organic light emitting diodes (OLEDs) [24]. Following this suggestion, numerous studies developed many forms of metal oxides for use in OPV and OLEDs as cathode and anode interlayers. For instance,  $\text{MoO}_3$ , nickel oxide (NiO) and  $\text{V}_2\text{O}_5$  have been used in OPVs as a hole extraction layer (HEL) with a work function of  $\geq 6.5$  eV [25]. This deep level energy allows a decrease in the extraction barrier at the interface between the active layer and electrode. Furthermore, metal oxides have other properties such as high optical transparency due to their large band gap, and good stability allowing them to be competitive with other aqueous conducting polymers [26].

Recent studies have demonstrated the role of the interfacial metal oxide layer in OPVs for efficient hole extraction, reducing the recombination of charge carriers and increasing the lifetime [27, 28]. Until recently, many of the metal oxide studies reported

in literature used vacuum deposition methods such as thermal evaporation and sputter deposition. These methods are not necessarily desirable for high-throughput and large-scale production.

Solution-processing of the metal oxide interfacial layers is therefore an important target to achieve in order to reduce the cost of the deposition of these layers. However, most of those aqueous metal oxides require post-deposition treatment such as thermal annealing and oxygen plasma treatment [29-33]. These two techniques, although not difficult to implement, are often time-consuming and can destroy the organic active layer. In addition, for technologies such as organic photovoltaics the incorporation of these post-deposition processing techniques in roll-to-roll processing is extremely impractical. Until recently, studies on solution-processed metal oxides as an anode interlayer with stable performance and without post-deposition treatment are still limited. Further understanding of the impact of different processing conditions on metal oxide interfaces and thus the energy alignment between layers is required.

### 1.3 Thesis Summary

**Chapter 2** provides the background theory, discussing the physical aspects of photocurrent generation in organic photovoltaics and the interactions that occur at the interfaces between the active layer and metal oxide interlayers.

**Chapter 3** describes the experimental methods for fabricating the organic photovoltaic devices; this includes solution preparation methods and deposition techniques used to form thin films and their post-deposition treatment. In addition, the methods for characterising the fabricated OPV devices and thin films of the materials used are presented.

**Chapter 4** presents the optical and electronic characterisation of metal oxides and organic polymers used in this thesis. Vanadium oxide thin films deposited by either thermal evaporation or by solution-processing had comparable characteristics with large work functions. A similar result was found for thermally-evaporated molybdenum oxide ( $\text{MoO}_x$ ). The Results of optical investigations showed wide band gaps allowing for maximising the intensity of light passing through to the organic bulk-heterojunction. In addition, the transparent region of the spectra covered most of the absorption band of the donor polymers used in this work.

**Chapter 5** discusses the performance of OPV devices utilising solution-processed  $\text{V}_2\text{O}_x$  as the HEL deposited from a Vanadium (V) Isopropoxide precursor and how different processing conditions affect the photovoltaic parameters of these devices. The optimised results are compared against OPV devices utilising widely-used HEL materials offering comparable performances to these materials. In addition, the performance of  $\text{V}_2\text{O}_x$  thin films annealed at high temperatures before spin coating the active layer is also included to highlight their thermal stability. The efficiency of these devices was reduced by 15% after annealing s- $\text{V}_2\text{O}_x$  layers at  $400^\circ\text{C}$  demonstrating its capability to replace evaporated metal oxides in optoelectronic devices which are fabricated at high temperatures.

**Chapter 6** shows that it is possible to achieve a high PCE of 5.2% with solution-processed nickel oxide as the HEL prepared from a nickel acetylacetonate precursor. This was carried out by the use of post-deposition thermal annealing followed by oxygen plasma treatment. Furthermore, it shows that annealing leads to the thermal decomposition of the acetylacetonate precursor causing an increase of the work function and a reduction in the Ni oxidation state. Post-annealing oxygen plasma treatment

further reduces the work function by oxidising the surface layer of the sample that facilitates charge extraction at the organic interface.

**Chapter 7** is the final experimental chapter and investigates the lifetime of an OPV device that utilises vanadium (V) oxytriisopropoxide as HEL. The results were compared to devices with HELs including PEDOT:PSS and thermally-evaporated MoO<sub>x</sub>. The lifetime tests of all OPV devices were carried out using an indoor laboratory testing system conforming to the ISOS-L-1 testing standards [34]. The OPV devices were placed in the lifetime tester for between 150 and 500 hours under constant illumination and the results were compared against the Newport solar simulator. Laser beam induced current mapping (LBIC) and photoelectron spectroscopy were used to characterise the defects formed in the OPV device. Furthermore, several experiments were carried out to show the impact of different processing conditions such as film thickness and thermal annealing of the anode interlayer on the stability of devices.

## 1.4 References

1. P. Moriarty and D. Honnery, *What is the global potential for renewable energy?*, *Renewable & Sustainable Energy Reviews* **16** (2012), no. 1, 244-252.
2. U. S. E. I. A. (EIA), "The international energy outlook 2014."
3. V. Ramanathan and Y. Feng, *Air pollution, greenhouse gases and climate change: Global and regional perspectives*, *Atmospheric Environment* **43** (2009), no. 1, 37-50.
4. M. Hosenuzzaman, N. A. Rahim, J. Selvaraj, M. Hasanuzzaman, A. B. M. A. Malek and A. Nahar, *Global prospects, progress, policies, and environmental impact of solar photovoltaic power generation*, *Renewable & Sustainable Energy Reviews* **41** (2015), 284-297.
5. "Grid-arendal centre. solar power potential map," March 2015, <http://www.grida.no/publications/et/ep5/page/1416.aspx>, 2011.
6. D. M. Chapin, C. S. Fuller and G. L. Pearson, *A new silicon p-n junction photocell for converting solar radiation into electrical power*, *Journal of Applied Physics* **25** (1954), no. 5, 676-677.
7. P. K. Nayak and D. Cahen, *Updated assessment of possibilities and limits for solar cells*, *Advanced Materials* **26** (2014), no. 10, 1622-1628.

8. M. A. Steiner, J. F. Geisz, I. Garcia, D. J. Friedman, A. Duda and S. R. Kurtz, *Optical enhancement of the open-circuit voltage in high quality gaas solar cells*, Journal of Applied Physics **113** (2013), no. 12, 11.
9. M. A. Green, K. Emery, Y. Hishikawa, W. Warta and E. D. Dunlop, *Solar cell efficiency tables (version 46)*, Progress in Photovoltaics **23** (2015), no. 7, 805-812.
10. N. Kaur, M. Singh, D. Pathak, T. Wagner and J. M. Nunzi, *Organic materials for photovoltaic applications: Review and mechanism*, Synthetic Metals **190** (2014), 20-26.
11. H. Kallmann and M. Pope, *Photovoltaic effect in organic crystals*, Journal of Chemical Physics **30** (1959), no. 2, 585-586.
12. C. W. Tang, *Two-layer organic photovoltaic cell*, Applied Physics Letters **48** (1986), no. 2, 183-185.
13. D. E. Markov, C. Tanase, P. W. M. Blom and J. Wildeman, *Simultaneous enhancement of charge transport and exciton diffusion in poly(p-phenylene vinylene) derivatives*, Physical Review B **72** (2005), no. 4, 045217.
14. G. Yu, J. Gao, J. C. Hummelen, F. Wudl and A. J. Heeger, *Polymer photovoltaic cells: Enhanced efficiencies via a network of internal donor-acceptor heterojunctions*, Science **270** (1995), no. 5243, 1789-1791.

15. J. J. M. Halls, C. A. Walsh, N. C. Greenham, E. A. Marseglia, R. H. Friend, S. C. Moratti and A. B. Holmes, *Efficient photodiodes from interpenetrating polymer networks*, *Nature* **376** (1995), no. 6540, 498-500.
16. N. S. Sariciftci, L. Smilowitz, A. J. Heeger and F. Wudl, *Photoinduced electron transfer from a conducting polymer to buckminsterfullerene*, *Science* **258** (1992), no. 5087, 1474-1476.
17. H. Ishii, K. Sugiyama, E. Ito and K. Seki, *Energy level alignment and interfacial electronic structures at organic metal and organic organic interfaces*, *Advanced Materials* **11** (1999), no. 8, 605-+.
18. K. Sugiyama, H. Ishii, Y. Ouchi and K. Seki, *Dependence of indium-tin-oxide work function on surface cleaning method as studied by ultraviolet and x-ray photoemission spectroscopies*, *Journal of Applied Physics* **87** (2000), no. 1, 295-298.
19. H. Ishii, K. Sugiyama, D. Yoshimura, E. Ito, Y. Ouchi and K. Seki, *Energy-level alignment at model interfaces of organic electroluminescent devices studied by uv photoemission: Trend in the deviation from the traditional way of estimating the interfacial electronic structures*, *Selected Topics in Quantum Electronics, IEEE Journal of* **4** (1998), no. 1, 24-33.
20. I. G. Hill, D. Milliron, J. Schwartz and A. Kahn, *Organic semiconductor interfaces: Electronic structure and transport properties*, *Applied Surface Science* **166** (2000), no. 1-4, 354-362.



21. M. A. Baldo and S. R. Forrest, *Interface-limited injection in amorphous organic semiconductors*, Physical Review B **64** (2001), no. 8, 085201.
22. W. C. Yang, Y. Yao and C. Q. Wu, *Mechanisms of device degradation in organic solar cells: Influence of charge injection at the metal/organic contacts*, Organic Electronics **14** (2013), no. 8, 1992-2000.
23. N. Grossiord, J. M. Kroon, R. Andriessen and P. W. M. Blom, *Degradation mechanisms in organic photovoltaic devices*, Organic Electronics **13** (2012), no. 3, 432-456.
24. S. Tokito, K. Noda and Y. Taga, *Metal oxides as a hole-injecting layer for an organic electroluminescent device*, Journal of Physics D-Applied Physics **29** (1996), no. 11, 2750-2753.
25. D. Y. Kim, J. Subbiah, G. Sarasqueta, F. So, H. Ding, Irfan and Y. Gao, *The effect of molybdenum oxide interlayer on organic photovoltaic cells*, Applied Physics Letters **95** (2009), no. 9, 093304-093303.
26. M. T. Greiner and Z.-H. Lu, *Thin-film metal oxides in organic semiconductor devices: Their electronic structures, work functions and interfaces*, Npg Asia Materials **5** (2013).
27. I. Litzov and C. J. Brabec, *Development of efficient and stable inverted bulk heterojunction (bhj) solar cells using different metal oxide interfaces*, Materials **6** (2013), no. 12, 5796-5820.

28. G. Li, R. Zhu and Y. Yang, *Polymer solar cells*, *Nature Photonics* **6** (2012), no. 3, 153-161.
29. V. Shrotriya, G. Li, Y. Yao, C. W. Chu and Y. Yang, *Transition metal oxides as the buffer layer for polymer photovoltaic cells*, *Applied Physics Letters* **88** (2006), no. 7.
30. R. Jose, V. Thavasi and S. Ramakrishna, *Metal oxides for dye-sensitized solar cells*, *Journal of the American Ceramic Society* **92** (2009), no. 2, 289-301.
31. S. Chen, J. R. Manders, S.-W. Tsang and F. So, *Metal oxides for interface engineering in polymer solar cells*, *Journal of Materials Chemistry* **22** (2012), no. 46, 24202-24212.
32. J. Meyer, S. Hamwi, M. Kroger, W. Kowalsky, T. Riedl and A. Kahn, *Transition metal oxides for organic electronics: Energetics, device physics and applications*, *Advanced Materials* **24** (2012), no. 40, 5408-5427.
33. B. Mustafa, J. Griffin, A. S. Alsulami, D. G. Lidzey and A. R. Buckley, *Solution processed nickel oxide anodes for organic photovoltaic devices*, *Applied Physics Letters* **104** (2014), no. 6.
34. M. O. Reese, S. A. Gevorgyan, M. Jorgensen, E. Bundgaard, S. R. Kurtz, D. S. Ginley, D. C. Olson, M. T. Lloyd, P. Moryillo, E. A. Katz, A. Elschner, O. Haillant, T. R. Currier, V. Shrotriya, M. Hermenau, M. Riede, K. R. Kirov, G. Trimmel, T. Rath, O. Inganäs, F. Zhang, M. Andersson, K. Tvingstedt, M. Lira-Cantu, D. Laird, C. McGuinness, S. Gowrisanker, M. Pannone, M. Xiao, J. Hauch,

R. Steim, D. M. DeLongchamp, R. Roesch, H. Hoppe, N. Espinosa, A. Urbina, G. Yaman-Uzunoglu, J.-B. Bonekamp, A. J. J. M. van Breemen, C. Girotto, E. Voroshazi and F. C. Krebs, *Consensus stability testing protocols for organic photovoltaic materials and devices*, *Solar Energy Materials and Solar Cells* **95** (2011), no. 5, 1253-1267.

# Chapter 2

## Background

### 2.1 Introduction

In this chapter the physical and chemical properties of conjugated polymers and metal oxides and their use in solar cells is discussed. Starting from a general overview of the chemical structure and optical properties of semiconducting polymers in section 2.2, a brief overview of the fundamental physical processes and basic working principles of a BHJ device is presented in section 2.3. Section 2.4 highlights the key factors that have a significant role in the determination of the efficiency of a solar cell. Section 2.5 considers how the interfacial energy level alignment impacts upon the performance of OPVs. Section 2.6 details the main roles of interfacial buffer layers included in the structure of organic solar cells. Finally, section 2.7 contains a brief review of experimental results from the literature for utilising metal oxides at the anode buffer layer.

### 2.2 Organic Semiconductors

Organic materials can be defined as components that contain essentially carbon and hydrogen atoms with some few heteroatoms such as oxygen, nitrogen and sulphur. These materials can offer some properties that are usually associated with

semiconductors such as partial electrical conductivity when alternating single-double or single-triple covalent bonds (conjugation) exist along a molecule or monomer. In addition, they can absorb and emit light in the visible spectral range. These properties have allowed the development of organic semiconductor devices such as organic photovoltaics (OPVs), organic light-emitting diodes (OLEDs), and organic field-effect-transistors (FETs). However, there are some considerable differences between organic and inorganic semiconductors. For example, traditional inorganic semiconductors have low band gaps such as 1.1 eV (Si) and 0.67 eV (Ge) in which free charges are generated by thermal excitation at room temperature. Furthermore, coulomb effects between electrons and holes are negligible due to the large dielectric constant (typically  $\sim 10$  as compared to 3 in organic semiconductors). To understand the origin of these differences between organic and inorganic semiconductors a brief overview of the chemical and electronic structure of organic semiconductors is given in the following sections. Since most of the organic materials used in this thesis were semiconducting polymers, the discussion will be limited to this type of organic semiconductors.

### 2.2.1 Chemical Structure

In the context of organic semiconductors, polymers are made up of at least 100 repeating single units (i.e. monomer units). Short chains which contain 20 repeat units or fewer are usually known as oligomers. If the repeat units are arranged identically they form a homopolymer but if different repeat units are connected this forms copolymers. For instance, poly[[9-(1-octylnonyl)-9H-carbazole-2,7-diyl]-2,5-thiophenediyl-2,1,3-benzothiadiazole-4,7-diyl-2,5-thiophenediyl] (PCDTBT) is a copolymer that consists of a carbazole donor connecting to a benzothiadiazole acceptor unit via thiophenes as shown in **Figure 2.1**.

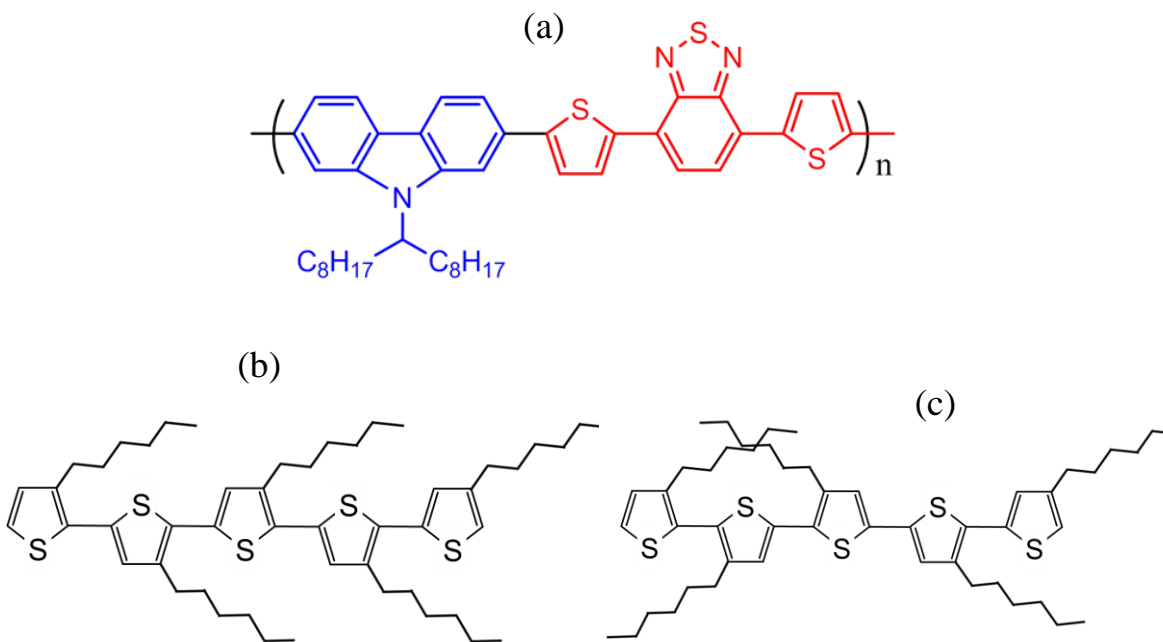


**Figure 2.1** (a) PCDTBT copolymer with a carbazole donor that is connected via thiophenes to a benzothiadiazole acceptor unit. (b) and (c) The chemical structures in the bottom represent thiophene rings in P3HT that can be connected either regioregular (b) or regiorandom (c) .

Connecting these monomer units together forms essentially the main polymer architecture which is referred to as the polymer backbone. Organic polymers can involve a number of side chain polymers that are attached to the backbone. The significance of these side chains is to make semiconducting polymers soluble in various organic solvents which provides the major advantage of solution processing semiconductors. Furthermore, they can control the distance between the polymer chains after deposition on a surface and also control the relative orientation of these chains to each other.

Thiophene rings in some types of semiconducting polymers can be attached together or with side chains in different ways [1]. They can form a regioregular (rr) structure when the side chains are oriented in the same direction “head-to-tail”. Other connections

involve irregular side chains directions which are referred to as a regiorandom (ra) structure (i.e. the backbone contains head-to-head, tail-to-tail or head-to-tail connections). The typical example is P3HT which contains a hexyl group which can be synthesised as a regioregular or regiorandom structure as shown in **Figure 2.1**.

### 2.2.2 Electronic Structure

In the polymer structures that have been presented in the previous section it can be noticed that there are alternating single and double bonds along the hydrocarbon chains. Such polymers are called conjugated polymers in which every carbon atom is bonded via  $sp_2$  hybrid orbitals (head-on overlap) forming a ( $\sigma$ ) bond (i.e. a strong net attractive interaction between the nuclei involved and then strong bond). Therefore, a large resonance integral with  $\sigma$  and a  $\sigma^*$  orbitals are pushed far apart forming large splitting between them. In contrast, the remaining  $p_z$  orbital in each carbon atom interacts by overlapping sideways to form what is called a ( $\pi$ ) bond. The  $\pi$ -orbital contributes only little to the attractive force between the nuclei (i.e weak bond) because the overlap electron density occurs further away from the internuclear axis and therefore it can delocalise across several neighbouring molecular units. This results in lower splitting between  $\pi$  and  $\pi^*$  orbitals than  $\sigma$  and  $\sigma^*$  which can then determine the electronic and optical properties (e.g. charge conductivity and light absorption) of semiconducting polymers as will be discussed later.

In order to understand the conductivity characteristics of the organic semiconducting, we need to look at the difference between conductors, semiconductors and insulators. In a conductor, there is no energy gap between the valence and conduction band edges and the conduction band can be partially occupied. At 0 K, the valence band is completely

filled and the conduction band is completely unfilled. Therefore, the Fermi level (i.e. the position where the probability of finding an electron is  $1/2$ ) of a conductor is positioned at the valence and conduction band edge overlap. For inorganic semiconductors, an energy gap ( $E_g$ ) exists between the edge of the valence and conduction bands. If this bandgap is too large (typically  $> 3.5$  eV), the material can be described as insulator.

In a similar situation to inorganic semiconductors, conjugated polymers have similar energy bands. Occupied  $\pi$ -bonding orbitals correspond to the Highest Occupied Molecular Orbital (HOMO) which is analogous to the valence band in inorganic semiconductors. The Lowest Unoccupied Molecular Orbital (LUMO) corresponds to the unoccupied  $\pi^*$ -antibonding orbital similar to the conduction band. Therefore, the energy bandgap ( $E_g$ ) in semiconducting polymers can be defined as the difference in energy between the HOMO and LUMO levels. In addition, the ionisation potential (IP) and the electron affinity (EA) of a molecule corresponds to the energy separations from the HOMO and LUMO levels to the vacuum level (VL) respectively. The vacuum level corresponds to the energy of an electron at rest just outside the solid. The work function is therefore the minimum energy required to remove an electron from a bound state to the VL.

Since atoms in inorganic semiconductors can be formed in a periodic lattice, free electrons therefore move in a wave-like mode. However, most organic semiconductors have disordered morphology and thus wave-like propagation of excited electrons is unlikely to occur. Instead, charge transport can be described as a random 'hopping' process either along a molecular chain or between chains towards sites lower in energy. Consequently, the mobility of charge carriers in organic semiconductors is much slower



and in orders of magnitude smaller than those in inorganic semiconductors. This will be discussed in more detail later in this chapter.

### 2.2.3 Optical Transitions in Conjugated Polymers

One of the key properties of many conjugated polymers is having a band gap that is similar to, or smaller than, the energy of visible photons. Therefore, if a photon has energy equal to, or higher than the energy gap, the photon is absorbed and thus an electron will be promoted to excited electronic levels. An energy level diagram based on the Frank-Condon principle is shown in **Figure 2.2** to understand the electronic transitions that occur in the excited molecule. Here, the  $S_0$  curve represents the ground state (i.e. HOMO level) and  $S_1$  singlet level represents the excited states (i.e. LUMO level). A variety of quantised vibrational levels exist within each state and are denoted with (n). The excited electron will be promoted into the  $S_{1,n}$  level leaving a hole residing in the  $S_{0,n}$  level. This transition occurs rapidly in comparison to nuclear motion and thus it is defined by a vertical arrow (according to the Frank-Cordon principle) as shown in the energy level diagram.

If the electron absorbs a photon with an energy greater than the energy gap, it will be promoted to a higher vibrational level and then undergo fast radiationless relaxation to its equilibrium configuration (i.e.  $n = 0$ ). The resulting electron-hole pair is referred to as an exciton which is neutral electrically. Exciton recombination may occur in a process called fluorescence in which a photon of equal or lower energy than that for absorption can be emitted. If the transition occurs at higher vibronic modes in the  $S_0$  or HOMO level, the emitted photon will have lower energy.

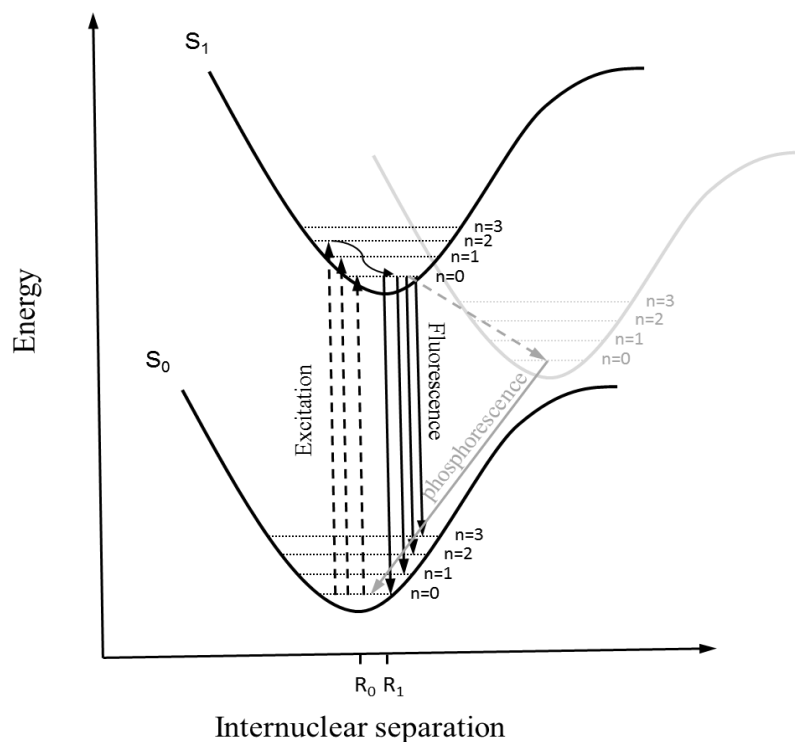


**Figure 2.2** Energy level diagram illustrating absorption, fluorescence and intersystem crossing process of a molecule. Horizontal dashed lines correspond to vibrational energy levels within each state, whilst the vertical arrows illustrate an electronic transition. The figure is adapted from reference [2].

To illustrate this process, the absorption and fluorescence spectra from perylene dissolved in toluene are shown in **Figure 2.3** [3]. It can be noticed that the absorbed and emitted photons do not have the same energy, even those that undergo similar transitions. In such these cases (red-shift), which are referred to as Stokes shift occur due to the internal relaxation process and impact of the used solvent [4].

The radiative decay can occur in different processes in which the electron relaxes from a lower energy excited state called triplet state instead of the excited single state as shown in **Figure 2.3**. In such these radiative decays are referred to as phosphorescence. To

understand how these radiative transitions occur, and what rules can govern them, it is helpful to briefly introduce a quantum mechanical description for the electron wavefunctions and the spin state changes of the exciton upon light absorption.

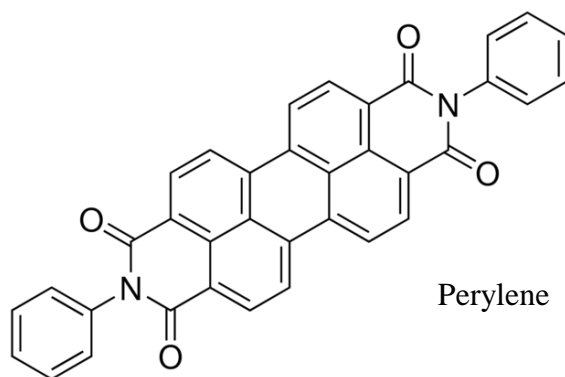
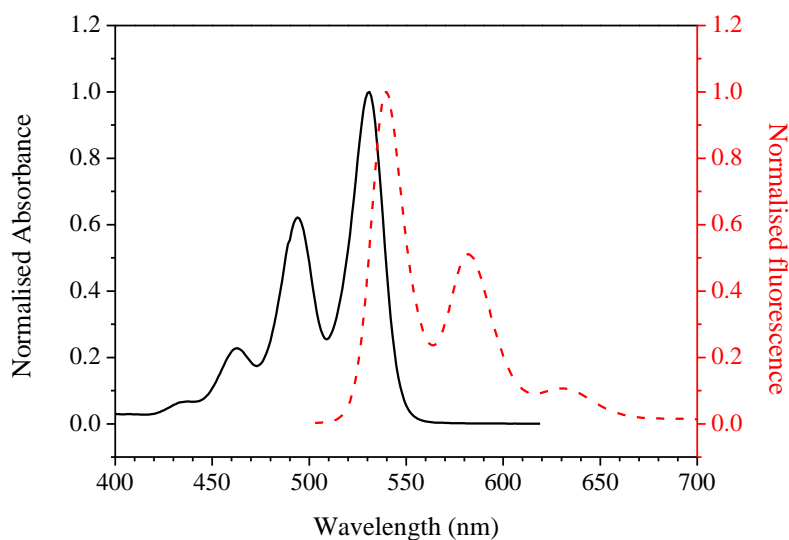


**Figure 2.3** Absorption (solid line) and fluorescence (dashed line) spectra of perylene dissolved in toluene. The sample was excited at 490 nm and the absorption data were collected using a spectral bandwidth of 1.0 nm. The two peaks at 531 and 540 nm correspond to the principle transition between the lowest vibrational levels of the ground and first excited state. Low intensity peaks represent transitions between modes of higher vibrational energy. Data provided by the PhotochemCAD library [3]. The chemical structure is shown in the bottom.

For simplicity, the system may be described as two coupled charge carriers with spin =  $1/2$  for each carrier (i.e. hole and electron). According to the Pauli exclusion principle, their spins can combine in four different ways to give a total spin angular momentum of  $S=0$  (a singlet state) or  $S=1$  (a triplet state). The excited singlet state has only one eigenvector and can be expressed by the following wavefunction:

$$\psi_{S_1} = \frac{1}{\sqrt{2}}(|\uparrow\downarrow\rangle - |\downarrow\uparrow\rangle) \quad (2.1)$$

Here, the two charge carriers occupy the same orbital with antisymmetric spins. The other three combinations include three eigenvectors (i.e. three configurations are possible) in which the spin part of the wavefunction may be symmetric forming a triplet state.

$$\psi_{T_0} = \frac{1}{\sqrt{2}}(|\uparrow\downarrow\rangle + |\downarrow\uparrow\rangle), |\uparrow\uparrow\rangle, |\downarrow\downarrow\rangle \quad (2.2)$$

The singlet ground state  $S_0$  is given by:

$$\psi_{S_0} = |\uparrow\downarrow\rangle \quad (2.3)$$

The electronic transition between states is possible when the overall wavefunction is antisymmetric to satisfy the Pauli exclusion principle. Consequently, the symmetry of the spin part in the wavefunction must be opposite to the spatial part. In addition, while the ground and triplet states are symmetric under particle interchange (i.e. orbital angular momentum  $L=0$ ), the singlet state is antisymmetric (i.e.  $L = 1$ ). Since photons have orbital angular momentum  $L=1$ , it is important that the change in the ( $L$ ) is equal 1 for an optical transition to be allowed. Therefore, the absorption transition from the ground state to the singlet state is allowed because it fulfils the  $\Delta L$  rule. Fluorescence

emission is the inverse process. In contrast, transition between ground state to the triplet state is forbidden because it does not result in a change in the orbital angular momentum.

It is however possible for triplet transitions to occur due to spin-orbit coupling, an interaction between the particle's spin and its orbital angular momentum. As a result, transition from the ground state to the singlet state is possible providing the spin of the electron "flips". Populating the triplet state is most likely via intersystem crossing, i.e. ground state  $\rightarrow$  singlet  $\rightarrow$  triplet state. Relaxation to the ground state from the triplet state by emission of a photon is called phosphorescence as shown in a Jablonski diagram.

### 2.3 Basic Working Principles of BHJs

BHJ devices are usually fabricated on a supporting substrate such as plastic, glass or metal foil, which is often covered with a transparent conducting film (e.g. indium tin oxide ITO) that serves as an electrode. This layer is coated with an interlayer film which is referred to as the hole extraction layer (HEL). This is often either a conducting polymer (e.g. PEDOT:PSS) or a transparent metal oxide, such as  $\text{MoO}_3$ ,  $\text{V}_2\text{O}_5$ , and  $\text{NiO}$  for conventional devices or  $\text{ZnO}$  and  $\text{TiO}_x$  for inverted structures (in which the transparent cathode is on the bottom). Next, this conducting layer is coated with a blending donor-acceptor polymer as an active layer. Finally, a very thin buffer layer (often  $\text{Ca}$  or  $\text{LiF}$ ) is deposited (i.e. electron transport layer ETL) followed by a metal electrode (typically  $\text{Al}$  or  $\text{Ag}$ ). The schematic device structure for a donor/acceptor bulk heterojunction solar cell is illustrated in **Figure 2.4**. The following section discusses the

energy conversion process and working mechanism of BHJ devices for either normal or inverted architectures which is summarised in **Figure 2.5**.

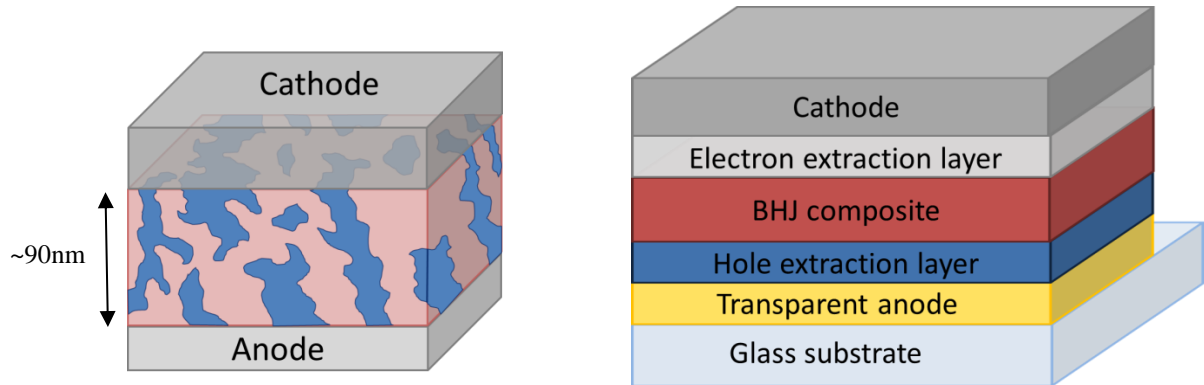


**Figure 2.4** Morphology model of the donor and acceptor active layer in a BHJ device (left) and general device structure (right).

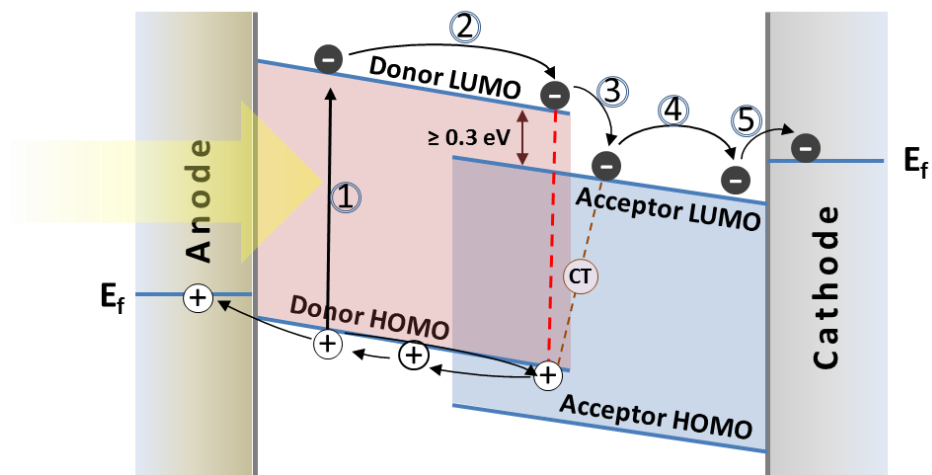


**Figure 2.5** Schematic representation shows energy levels and the operating mechanism of a bulk heterojunction device. (1) A photon is absorbed forming an exciton. (2) The generated exciton diffuses to the interface of the donor/acceptor. (3) Separation of the exciton into free charges. (4) Transport charge carriers to the electrode interface. (5) Free charges are extracted into Fermi level ( $E_f$ ) of electrodes.

### 2.3.1 Light Absorption

Conjugated polymers display high absorption coefficients (usually  $\geq 10^5 \text{ cm}^{-1}$ ) due to the large wavefunction overlap between the ground state and the lowest excited states. Therefore, a thin film with a thickness  $< 200$  nanometres can absorb nearly 100% of the incident light at the peak absorption region [5]. However, the simple semiconducting polymer (e.g. poly(3-hexylthiophene) P3HT) typically has a relatively large band gap compared to inorganic semiconductors, which causes a mismatch between the peak absorption region and the solar spectrum peaks. Therefore, only a small amount of the incident light can be absorbed in which photons with energies  $>E_g$  are absorbed but photons with energies  $<E_g$  cannot be absorbed. The relatively large bandgap of organic polymer is a significant reason why the PCE of OPVs is generally less than that of inorganic solar cells. For instance, P3HT thin film can absorb 95% of incident light over the absorption band (i.e., 450-600 nm). However, the absorbed light represents just 20% of the solar spectrum [6]. Increasing the polymer layer thickness to increase the total absorption ( $\eta_A$ ) is not a solution as thick polymer increases the series resistance due to the low charge carrier mobility in organic polymers. More sophisticated polymer design allows low band gap polymers (broad absorption band) to absorb up to 40% of the incident light. However, other properties such as  $V_{oc}$ , can be affected. Furthermore, other strategies for increasing the light absorption have been suggested, such as a) using less symmetrical fullerenes (e.g.,  $C_{70}$  and  $C_{71}$  derivatives) [7], b) inserting an antireflection layer or structuring the interfaces to minimise reflection losses, c) modifying the optical interference within the whole device structure in order to maximise the electromagnetic field inside the active layer [8, 9], and d) fabricating a tandem device by stacking two or more devices in series.[10].

### 2.3.2 Exciton Generation

If a photon with energy equal to or greater than the energy gap of a donor polymer is absorbed, an electron will be excited into the LUMO level, generating an electron-hole pair (exciton) in a singlet exciton state with opposite spin bound by their Coulomb attraction. In general,  $\pi$ -conjugated polymers have a singlet ground state denoted  $S_0$  and the lowest singlet excited state is  $S_1$  so one photon is usually allowed [5]. While the binding energy of the hole-electron pair in an inorganic semiconductor is quite weak at about  $\sim 25$  meV at room temperature (Mott–Wannier-type excitons) due to the large dielectric constants, free charges can be generated immediately after photoexcitation. In contrast, the relatively low dielectric constant of polymers, typically  $\sim 3$  as compared to 10 in inorganic semiconductors, leads to strongly bound (in the order of hundreds of meV) Frenkel-like localised excitons .

### 2.3.3 Exciton Diffusion

The strongly bound excitons need to diffuse to the donor-acceptor interface where they can dissociate. Due to the neutral nature of excitons, their diffusion is independent of the electric field, and their movement is typically described as a random ‘hopping’ process. The motion of singlet excitons generated by light absorption can be described by Förster resonance energy transfer (FRET) [11]. This mechanism results from a resonant coupling between neighbouring molecular dipoles that exhibit a short lifetime and then a short diffusion length of a few nm. In addition, the FRET process is inversely dependent on the donor-acceptor separation distance and the overlap between the donor emission and the acceptor absorption spectra, as well as the relative orientation of their dipole moments.



In addition, the hopping process in semiconducting polymers significantly depends on the exciton diffusion length (i.e. exciton lifetime) ranges between 1 and 20 nm [12]. Values of exciton diffusion length of spin-cast films of conjugated polymers are typically within the range of 5-10 nm [13, 14]. The short exciton diffusion length was overcome by introducing a bulk heterojunction (BHJ) layer to provide phase domains of the order of the diffusion length. On the other hand, very small domain sizes can cause limited percolation and therefore limit charges movement to the electrodes. Consequently, increasing the exciton diffusion length by improving the charge carrier mobility is still necessary to enhance the overall OPV performance.

### 2.3.4 Exciton Dissociation

In BHJ solar cells exciton dissociation takes place at the interface if the energy difference between the HOMO levels  $\Delta E$  is greater than the binding energy of the exciton ( $\Delta E \geq 0.3$  eV) [15]. Furthermore, the HOMO level of the donor should be at a higher energy relative to the acceptor HOMO for the hole transfer. However, making  $\Delta E$  too large can reduce the performance of the photovoltaic device as the maximum voltage decreases. Whilst the influence of electric fields on exciton dissociation is not fully understood, several studies have shown that a strong electric field is necessary for separation [16]. In addition, the large difference between the mobility of electrons and holes can enhance the dissociation process [17, 18]. However, although the mechanism of dissociation is still subject to debate, the overall charge dissociation process must be energetically favourable, (i.e. the change in the Gibbs free energy ( $\Delta G$ ) of separating the hole-electron pair into free charges must be negative).

Recently, it has been found that the presence of the hole on the HOMO level of the donor molecule and the electron on the LUMO level of an acceptor molecule can form a Coulombic attraction which is called charge-transfer state (CT) [19]. Therefore,  $\Delta G$  can be estimated as the energy difference of the constituents in their final and initial states, accounting for the Coulombic attraction ( $E_{\text{cou}}$ ) between the two charges in the charge-separated state [20].  $\Delta G$  for exciton dissociation can be expressed as

$$\Delta G = E^{\text{D}^+} + E^{\text{A}^-} - E^{\text{D}^*} - E^{\text{A}} + \Delta E_{\text{cou}} \quad (2.4)$$

where  $E^{\text{D}^*}$ ,  $E^{\text{D}^+}$ ,  $E^{\text{A}}$ , and  $E^{\text{A}^-}$  represent the total energies of the isolated donor in the equilibrium geometries of the lowest excited state and of the cationic state and the total energies of the isolated acceptor in the equilibrium geometries of the ground state and of the anionic state, respectively. Note that the entropy contributions are often not enough and the enthalpy change must be  $> 0.2$  eV. Furthermore, it has been found that  $\Delta G$  becomes increasingly negative when the dielectric constant is increased. Therefore, the bound polaron pair can either separate into free charge carriers or decay to its ground state. The probability of exciton separation into free charge carriers at a given electric field  $E$  and temperature  $T$  can be calculated using Onsager's theory [21].

### 2.3.5 Charge Transport

After the exciton separation, holes remain in the donor phase, whereas electrons are transported to the acceptor phase. Subsequently, the free charge carriers will be transported to the electrodes of a device through a hopping mechanism rather than through band-like transport due to the disordered nature of organic materials and the low coupling energies between molecules [6, 22]. Consequently, a photocurrent is

produced that exhibits a current density ( $J$ ) consisting of a drift and a diffusion component [12]. These two components can be represented in the following equation:

$$\vec{J} = q\mu_i\rho_i\vec{E} + qD_i\vec{\nabla}\rho_i \quad (2.5)$$

where  $q$  is the elementary charge,  $\mu$  is the charge carrier mobility,  $\rho$  is the charge density,  $E$  is the electric field,  $D$  is the diffusion constant, and  $i$  indicates negative (n) or positive (p) charge carriers. The photocurrent in the planar bilayer is governed by the diffusion current in which  $V_{oc}$  values are larger than the difference in the work function of the anode and cathode. In contrast, the net diffusion current in BHJ devices is small, and the drift current is dominant.

An interesting value that can be used for testing the quality of PV devices is called the internal quantum efficiency (IQE), which is defined as the ratio of the number of collected electrons at an electrode to the number of absorbed photons. Several studies have revealed that the IQE value in BHJ devices is close to 100%, implying that all absorbed photons lead to free charge carriers that can be collected at the electrodes [23].

### 2.3.6 Charge Extraction

Once the free charges reach the organic-electrode interface, they must be transported efficiently from the bulk of the semiconducting film to electrodes with minimum loss. Previous studies have suggested that the charge transport from the active layer (LUMO level for electrons and HOMO level for holes) to the Fermi level of the electrode occurs by either the hopping process [24] or tunnelling extraction for large energy barriers at the interface [25]. However, the charge extraction in OPV devices is more complicated due to the chemical and morphological nature of the organic-electrode interface.

Therefore, the energy levels at the interface can be affected by several factors, such as interfacial dipoles [26], band bending [27], and chemical reaction [28] and thus influence the extraction process.

Indeed, inserting an interlayer between the active layer and the metal cathode or the active layer and the ITO substrate has considerably improved the extraction efficiency of free charges that are generated from the active layer [29]. The hole extraction layer can control the energy level alignment and the effective work function at the interface, and thus minimise the charge extraction barrier in organic devices [30]. Furthermore, interlayers between the active layer and the cathode can significantly enhance extraction of electrons and block leaking of holes to the cathode [31]. More details about the key factors that determine the efficiency of an OPV device will be discussed in the following section.

### 2.4 Characterisation of Power Conversion Efficiency

The overall efficiency of the photocurrent generated in any type of solar cells, i.e. power conversion efficiency (PCE), can be determined by plotting the photocurrent response of the device as a function of applied voltage which is called current-density voltage (J–V) characterisation as shown in **Figure 2.6**. Under illumination conditions, when the applied voltage is larger than the open circuit voltage ( $V_{oc}$ ), the device is biased in a forward direction (the opposite direction to the built-in field) while for voltages smaller than  $V_{oc}$  it is in a reverse bias condition (i.e. in the direction of built-in field). The short circuit current density ( $J_{sc}$ ) corresponds to the measured current at zero applied voltage with unit of  $\text{mA cm}^{-2}$ .

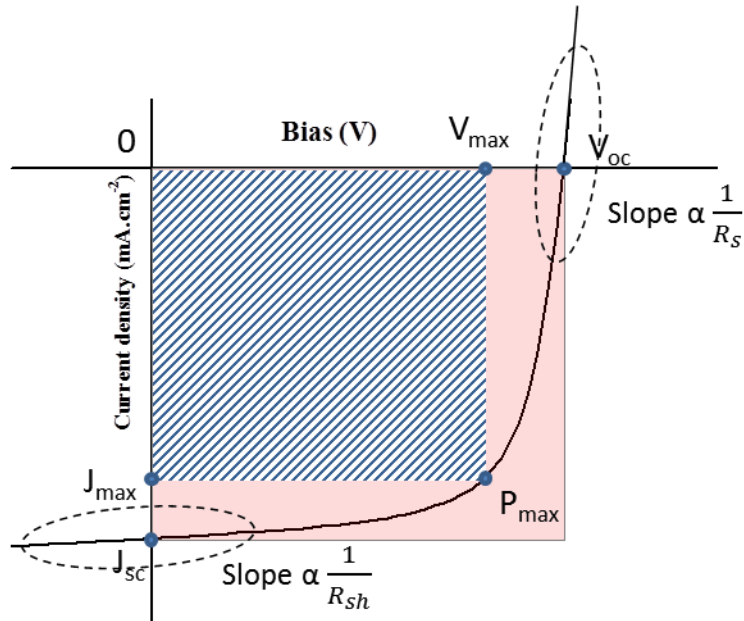


**Figure 2.6** Current-density voltage characteristics of a solar cell under illumination.

The open circuit voltage ( $V_{oc}$ ) corresponds to the voltage measured under open circuit conditions which represents the largest voltage attainable from the solar cell. Therefore, the maximum power ( $P_{max}$ ) produced by a PV cell can be determined at the point in the (J-V) curve where the power per unit area is maximum (i.e.  $J_{sc}$  and  $V_{oc}$  are the largest). In addition, the ratio of  $P_{max}$  to the product of  $J_{sc}$  and  $V_{oc}$  is called fill factor (FF) which is as close to unity as possible. The maximum value of FF can be described by the following expression:

$$FF = \frac{J_m V_m}{J_{sc} V_{oc}} \quad (2.6)$$

J–V characteristic with a high FF shows a convex shape while the low FF displays a linear or concave shape. Moreover, two factors can control the fill factor value: the series resistance ( $R_s$ ) and shunt resistance ( $R_{sh}$ ) of the solar cell.  $R_s$  represents the resistance of the whole device structure (i.e. active layer, buffer layers, electrodes, and

the contact resistance between them).  $R_{sh}$  can be affected by the performance of the thin layers and their interfaces in which  $R_{sh}$  decreases as a result of the charge recombination and trapping of the charge carriers. The maximum limit of values for  $R_{sh}$  and  $R_s$  can be calculated from the gradient of  $JV$  curves at open and short circuit; with  $R_{sh}$  primarily affecting the shape of the curve at short circuit, and  $R_s$  primarily affecting the shape of the curve at open circuit. The effect of both  $R_s$  and  $R_{sh}$  on the performance of an organic photovoltaic device can be expressed as an equivalent circuit, as shown in **Figure 2.7**. PCE can be calculated from the following relationship

$$PCE = \frac{\text{Power out}}{\text{Power in}} = \frac{J_{sc} V_{oc} FF}{P_{light}} \quad (2.7)$$

where  $P_{light}$  represents the incident light power.

There is another method to express OPV efficiency called external quantum efficiency ( $\eta_{EQE}$ ). It represents the ratio of the number of photogenerated charges collected from an OPV device to the number of incident photons and is expressed as

$$\eta_{EQE} = \frac{J_{sc}(\lambda)hc}{e P(\lambda)\lambda} \quad (2.8)$$

where  $P(\lambda)$  is the incident optical power as a function of wavelength,  $h$  is Plank's constant,  $c$  is speed of light, and  $e$  is the elementary electron charge. Furthermore,  $\eta_{EQE}$  can be expressed based on the exciton dissociation mechanism in the photoactive layer as presented previously in **2.3 Basic Working Principles of BHJs**. Consequently,  $\eta_{EQE}$  can be represented by the product of five efficiencies: absorption efficiency ( $\eta_A$ ), exciton diffusion efficiency ( $\eta_{ED}$ ), exciton dissociation efficiency ( $\eta_{Dis}$ ), free charge transport efficiency ( $\eta_{CT}$ ) and charge collection efficiency ( $\eta_{CC}$ ) as follows [32]

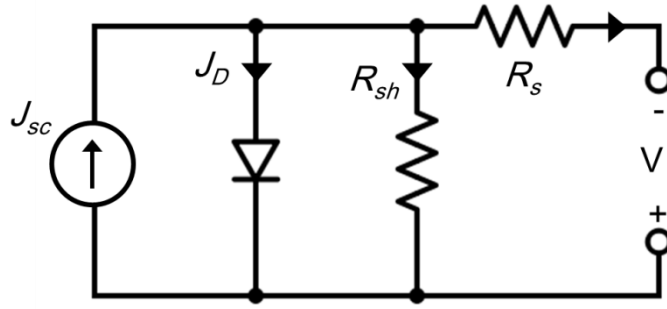


**Figure 2.7** Equivalent circuit of an OPV device where  $J$  is the photocurrent,  $R_{SH}$  is the shunt resistance,  $R_S$  is the series resistance and  $V$  is the applied voltage.

$$\eta_{EQE} = \eta_A \eta_{ED} \eta_{Dis} \eta_{CT} \eta_{CC} \quad (2.9)$$

The parameters  $\eta_A$ ,  $\eta_{ED}$ ,  $\eta_{Dis}$ ,  $\eta_{CT}$ ,  $\eta_{CC}$  correspond to steps 1 to 5 in **Figure 2.5**, respectively. If we assume that  $\eta_{EQE}$  equals unity and the semiconducting polymer absorbs all photons in the specific region of the spectrum in which one electron is generated from absorption one photon,  $J_{sc}$  can be estimated as [12]:

$$J_{sc} = \frac{e}{hc} \int_{\lambda_1}^{\lambda_2} P_{light} \lambda d\lambda \quad (2.10)$$

Calculating the maximum value of  $V_{oc}$  is perhaps more difficult. Until recently, several studies suggested that  $V_{oc}$  does not relate to the work function of the electrode materials and the maximum  $V_{oc}$  may exceed the difference between the cathode and anode work functions. There is evidence to suggest that  $V_{oc}$  correlates with the energy difference between the HOMO and the LUMO levels of the donor and acceptor polymers respectively [33, 34]. Therefore, a simple relationship can be deduced as follows:

$$V_{oc} = \frac{1}{e} \times (D_{HOMO} - A_{LUMO}) - 0.3 \quad (2.11)$$

where  $e$  is the elementary charge. Another useful equation that was commonly used is

$$V_{oc} = \frac{kT}{q} \ln \left( \frac{J_{sc}}{J_0} + 1 \right) \quad (2.12)$$

where  $k$  is the Boltzmann constant,  $T$  is the absolute room temperature and  $J_0$  is the dark saturation current [35]. Up to now, the most popular methods for increasing the  $V_{oc}$  of OPVs are modification of the energy levels of semiconducting polymers. However, it has been found that reducing the electronic coupling between the donor and the acceptor polymers will reduce  $J_0$  and thus increase  $V_{oc}$  [36].

### 2.5 The Interfacial Energy Level Alignment in OPV

The significance of interfaces for the performance of OPVs cannot be overstated, because they determine charge extraction and charge flow in the devices. One of the critical issues is the electronic and structural properties of interfaces between the buffer interlayer and polymer films in the devices. An understanding of the interfacial electronic structure and how energy levels are aligned at the interfaces is significant for designing better buffer layers and thus improving charge extraction efficiency for OPVs. To understand the effect of interfaces on OPV performance we will briefly discuss some basic concepts of interface energetics.

When two materials are separated, their vacuum levels are aligned. However, when the materials are brought into contact forming an interface, charge carriers can be injected. The earliest model proposed that the vacuum level at the interface should be simply aligned [37]. Later studies suggested the formation of an interface dipole between two materials to satisfy the thermal equilibrium at the interface. In this model Fermi level alignment can occur where the Fermi levels of the two materials are equalised with the formation of the interfacial dipole [30, 38].



It is worth mentioning here that the work function of the metal can have a considerable effect on the magnitude of the interface dipole. If the work function is small, the vacuum level of the organic material shifts upwards (i.e. setting up an upward dipole barrier at the interface between the two materials, and the Fermi level of the metal approaches the electron affinity of the organic material). For large work functions the vacuum level shifts to the opposite direction and the Fermi level of the metal comes close to the HOMO level of the organic semiconductor. If the work function of the metal is between these values, Fermi level alignment is not satisfied and the interface will remain vacuum level aligned [39]. **Figure 2.8** shows the value of the interface dipole at metal-semiconductor interfaces as a function of the metal work function. The figure is adapted from reference [40].

The interface dipole model has provided better understanding of the metal-inorganic material interface. However, the interface nature between metal and organic materials depends significantly on the strength of the interaction between them. Many surface analytical studies have investigated how the interface dipole is formed by using several techniques such as ultra violet photoemission spectroscopy (UPS), X-ray photoelectron spectroscopy (XPS) and inverse photoemission spectroscopy (IPES). Their results have suggested several mechanisms such as charge transfer across the interface, chemical reactions and formation of the interface state [41]. Therefore, various models have been developed to describe the different types of interfaces such as Integer Charge-Transfer (ICT) model and Induced Density of States (IDS) model [39, 42-44]. It is noteworthy that application of these models on different types of organic-metal or metal-organic interfaces is still under debate. Therefore, the following discussion will be limited to the

ICT model which is the most commonly used in polymer devices while the IDS model is more suitable for interfaces formed by vapour deposition of  $\pi$ -conjugated molecules.

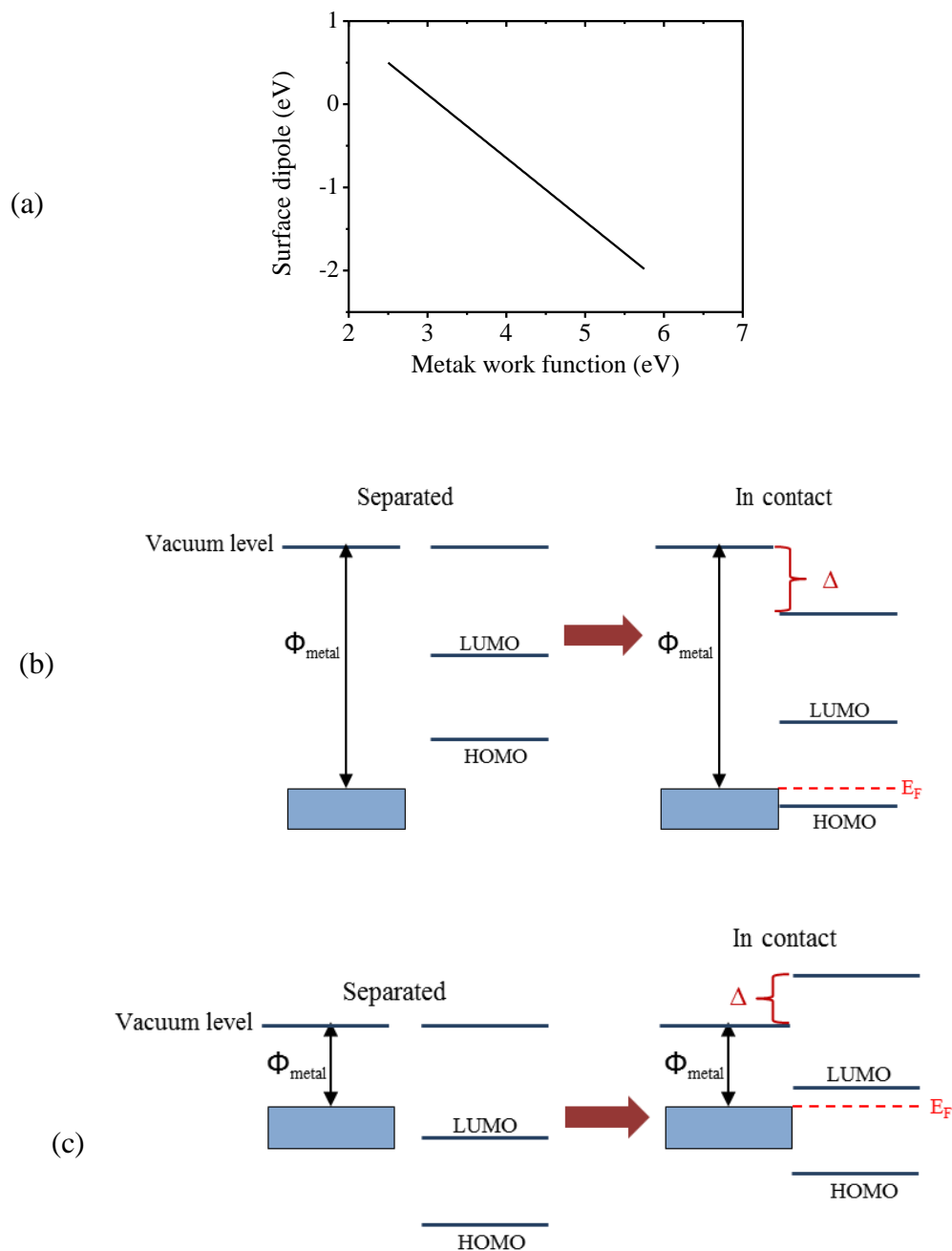


**Figure 2.8** (a) plotting dipole interface at an organic layer as a function of the metal work function. The data is adapted from ref. [40] for interfaces between tris(8-hydroxyquinoline) aluminium (Alq) and varied work function metals. (b) and (c) show schematic illustration of vacuum level alignment and Fermi level alignment for metal-organic interface.  $\Phi$  is the work function and  $\Delta$  is the interface dipole.

The integer charge transfer model provides a good description for most interfaces in OPV and particularly for those which are fabricated by solution-processing methods under ambient conditions. This theory implies Fermi-level pinning at the interface between the organic semiconductor and the electrode [39, 45, 46]. Furthermore, electron transfer between thin films can occur via tunneling such that an integer amount of charge can be transferred into well-defined charged states. This model defines the energy of a positive (or negative) integer charge-transfer state,  $E_{ICT+}$  (or  $E_{ICT-}$ ), as the energy needed to extract (or inject) one electron from (or to) the molecule generating a fully relaxed state. Therefore, three mechanisms at the electrode-organic interface can be defined by this model: a) when the  $E_{ICT-}$  of the organic semiconductor is higher than the electrode work function, electrons will flow from the electrode to the polymer semiconductor and the Fermi level will eventually be pinned to the  $E_{ICT-}$ ; (b) if the electrode work function is in between the two integer charge-transfer states, no Fermi level pinning will take place at the interface; (c) when the  $E_{ICT+}$  is lower than the electrode work function, holes will transfer from the electrode to the semiconductor polymer and the Fermi level will eventually be pinned to the  $E_{ICT+}$ . This model has been verified experimentally by a considerable amount of studies [47-50]. Nevertheless, due to the dependence of the composition of semiconducting polymers on the processing conditions, several parameters can influence the use of the ICT model to describe the interface mechanism between the electrodes and the polymer film. In addition, the presence of surface hydrocarbons can modify the work function and the oxidation state of metal electrode through the push-back effect. The electrode deposition through the thermal evaporation method can also induce undesired chemical reactions or lead to diffusion of metal films into the organic film. Despite the wide range of studies published on this topic, understanding of the energy level alignment at interfaces is still

uncertain, and a comprehensive and quantitative predictive model for OPV device performance has not been developed.

### 2.6 Roles of Interfacial Layers

The poor energy-level alignment (i.e. presence of barriers for charge extraction) can result in poor performing OPV. Therefore, inserting suitable interlayers between the electrodes and the active layer is a significant method to align energy levels at interfaces and to fabricate a well-performing solar cell. Furthermore, the appropriate choice of interlayer material can in fact enhance significantly both the performance of OPVs and their stability. Buffer layer engineering is another important aspect that has been suggested to play significant role in minimising deviation from ideal conditions. The development of interfacial materials has shown a wide range of different effects on OPV properties. The main effects can be summarised as follows:

- 1) Minimisation of the energy barrier at interfaces;
- 2) Enhancement of the electrode selectivity for one type of charge carrier;
- 3) Determination of the relative polarity of the devices;
- 4) Decrease in the chemical reactions and diffusion between the semiconducting polymer and electrode;
- 5) Decrease in the degradation processes at interface between the active layer and electrode and thus improvement of the overall OPV stability.
- 6) Modifying the optical interference within the whole device structure in order to maximise the electromagnetic field inside the active layer.

Consequently, the use of buffer layers has significantly developed the electrical and optical properties of OPVs. These effects will be discussed in some detail in the following sections.

### 2.6.1 Electrical Effects

Efficient collection of free charges at the electrodes is one of the key points that considerably influence the electrical performance of OPV devices. The most common electrode anode used in OPVs is indium tin oxide (ITO) which has a work function of around 4.7 eV. The relative low work function is usually in between the HOMO and the LUMO of the active layer of an OPV leading to poor selectivity for charges. Moreover, in BHJ devices the electrodes are in contact with both donor and acceptor materials resulting in increased exciton quenching and charge recombination at the interface. For that reason, inserting a functional interlayer between the active layer and the electrode with suitable work function will result in collecting just a single type of charge carriers. However, some interfacial materials that have appropriate energy levels can increase the contact resistance and thus increase the overall series resistance of the device. In this case, charge recombination at the interfaces governs the  $V_{OC}$  of the OPV device. Therefore, using high-resistivity interlayers are limited to just very thin films to avoid the leakage current and charge recombination. Indeed, the suitable selection of the buffer layer materials combined with the optimisation of the experimental conditions can reduce the series resistance of the device. In addition, using the buffer layers has enhanced fabrication of inverted architecture devices with the same bottom transparent electrode (usually ITO). Therefore, buffer layers allow for fine tuning of the energy-level alignment at interfaces and thus high selectivity with defined polarity. In a previous study, different types of metal anodes with increasing work functions from 4.3

eV to 5.3 eV were used in the fabrication of OPV devices [51]. It was found that the high work function metal can form Ohmic contact and the  $V_{oc}$  of the inverted cells reduced with the decrease of the work function. By inserting a PEDOT:PSS interlayer, OPV devices showed high  $V_{oc}$  independent of the used metal anode. A similar study was carried out for the extraction of electrons from the LUMO of the acceptor to different metal cathodes. The results showed that although there was formation of non-Ohmic metal-organic contact for high work function metals, the presence of an energy barrier at the interface does not increase the contact resistance and thus does not stop extraction of free charges from the active layer. Furthermore, buffer layers with large bandgap can enhance the exciton separation efficiency by confining excitons in the active layer and they also can show a further exciton dissociation interface [52, 53].

### 2.6.2 Optical Effects

Another significant strategy to develop the performance of OPVs can be achieved by maximising the absorption efficiency of the polymer thin film. Interfacial engineering therefore becomes a critical aspect of OPV fabrication by using light-trapping strategies as such buffer layers which can control the interference effects in the active layer. The incident light upon an OPV device passes through multiple thin films with different optical properties, such as a glass substrate, transparent electrode and active layer. Therefore, the light waves experience several reflections at each interface before reaching the back electrode. In addition, when the light reaches the electrode, it is reflected back through all the layers, resulting in optical interference (constructive and destructive). Therefore, the optical field energy dissipated by multiple stacked thin films contains three major components: an optical field propagating in parallel with incident light, a field spreading in the opposite direction to incident light, and the third one is due

to interferences between the incident and reflected waves [54, 55]. Depending on the refractive indices of these films and their thicknesses, distribution of the light intensity becomes non-uniform inside the OPV device. Typically, the light intensity should be as high as possible so that the active layer can absorb ample light. **Figure 2.9** shows the result of a simulated example for impact of the electrical field distribution on the active layer of the P3HT:PCBM model system and how electrode reflectivity, thickness of the optical spacers and tuning the refractive index can improve light absorption [56].

It has been shown in many experimental studies that some hole-blocking metal oxides, such as  $\text{TiO}_x$  and  $\text{ZnO}$ , can be used as optical spacers in conventionally structured OPVs to adjust the spatial distribution of the light intensity [57-59]. Moreover, numerous studies have revealed that electron-blocking metal oxides can act as optical spacers to enhance the electrical field distribution inside the photoactive layer. A recent study by Gupta et al. examined the role of  $\text{MoO}_3$  thickness to maximise the electrical field intensity in the active layer and thus improve the performance of a P3HT:PCBM device [55].

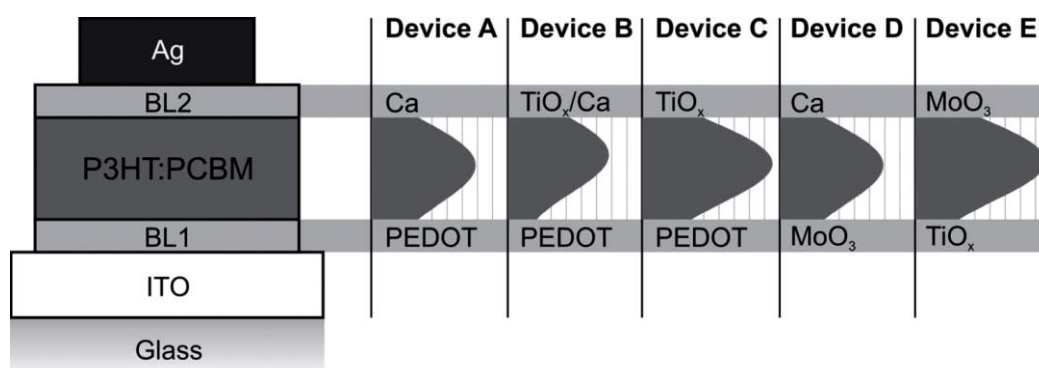


**Figure 2.9** Structures of OPV devices with various interfacial layers and their corresponding electric field intensity within the P3HT:PCBM thin film [56].

It was found that among various thicknesses of MoO<sub>3</sub> (2.5, 5, 10, and 15 nm), the 10-nm thickness exhibited the field maxima at the centre of the active layer. Consequently, the OPV with a 10-nm MoO<sub>3</sub> showed the highest  $J_{sc}$  and PCE, 8.55 mA cm<sup>-2</sup> and 3.18% respectively. In a similar study, it was observed that the maximum intensity tends to shift to the centre of the active layer when MoO<sub>3</sub> thickness increases from 2.5 to 25 nm, showing the highest PCE at 15 nm for small molecules inverted OPV [60].

Transition metal oxides, such as MoO<sub>3</sub>, WO<sub>3</sub>, and V<sub>2</sub>O<sub>5</sub>, have drawn much attention as anode interlayers due to high optical transparencies in the visible region for photon transmission. Wide band gap ( $E_g$ ) transition metal oxides are excellent choices for OPVs, because they allow incident light to reach the active layer. According to several studies [61, 62], the minimum performance requirement for a metal oxide can be defined as a transmittance of at least 85% of light in the visible range. Therefore, the metal oxides should have an  $E_g$  of at least 3.1 eV to exhibit high optical transparency. More significantly, their electronic energy levels, and thereby their  $E_g$ , can be tuned by varying the deposition parameters or their stoichiometry [63]. For instance, the optical band gap of evaporated WO<sub>3</sub> thin films has been determined over the range 3.20-3.40 eV, and was found that annealing films in air results in reduce the band gap by 0.5 eV. In another study, Greiner et al. observed a metallic valence band structure when MoO<sub>3</sub> was strongly reduced from Mo<sup>5+</sup> to Mo<sup>4+</sup> states. In contrast, this metal-like electrical property of strongly reduced MoO<sub>3</sub> resulted in absorption losses [64]. Vasilopoulou et al. demonstrated that substoichiometric MoO<sub>x</sub> films have a smaller band gap than fully oxidised films [65]. Moreover, control of MoO<sub>x</sub> stoichiometry by hydrogen reduction can convert the wide band gap of MoO<sub>3</sub> into a nearly zero band gap, at which point the device no longer shows semiconductor behaviour but rather the behaviours of a metallic



oxide. The variation in  $E_g$  of metal oxides can be also attributed to how exactly the location of the band edge is defined and where the maximum slope of absorption extrapolates to zero [66]. **Table 2.1** shows the measured band gap energies in literature for various metal oxides prepared by different deposition methods.

**Table 2.1** The reported band gap of various metal oxides in which "e-" and "s-" denote the thermal evaporation process and solution process, respectively.

Metal oxide	Band gap (eV)				
e-MoO <sub>3</sub>	3.1 [65]	3-3.3 [63]	3 [67]	3-3.2 [68]	3 [69]
s-MoO <sub>3</sub>	3, 3.3 [70]				
e-WO <sub>3</sub>	3.5 [69]	3.35 [71]	3.38 [72]	3.15 [73]	3.3 [74]
s-WO <sub>3</sub>	3.45 [75]	2.6 [76]			
e-NiO	3.3 [77]	3.4 [78]	3.5-4 [79]		
s-NiO	3.1, 3.6 [80]	3.6 [81]	3.8 [82]		
e-V <sub>2</sub> O <sub>5</sub>	2.8 [83]	2.8, 3.6 [84]	2.5 [85]		
s-V <sub>2</sub> O <sub>5</sub>	3.6 [84]	2.7, 3.2 [70]	3.2 [86]	2.3 [87, 88]	

### 2.6.3 Morphology

The microstructure of the active layer is a critical issue that affects significantly the photogenerating mechanism (i.e. light absorption, exciton generation, exciton dissociation, charge transport and charge collection) in OPVs. Phase-separated domains of a polymer blend with a size of around 10 nm are an ideal morphology for organic solar cells. In addition, the vertical composition and nanoscale phase separation are critical issues in the free charge transport and collection mechanism in BHJ devices. Therefore, development of alternative strategies to control the structure of the active layer remains a challenge to improving OPV performance. Tuning the surface chemistry and surface energy is a powerful method to control phase separation inside the photoactive film for both vertical and lateral separation. A self-assembled monolayer-based interfacial technique can be potentially used to control the film formation process and the orientation of the polymer backbone. Previous studies examined the impact of substrate surface energy ( $\gamma$ ) on the vertical composition of P3HT:PCBM thin film [89-91]. When the blend solution was deposited on PEDOT:PSS layer ( $\gamma = 45 \text{ mN m}^{-2}$ ), P3HT ( $\gamma = 26.9 \text{ mN m}^{-2}$ ) was enhanced at the top of the blend film but some PCBM particles ( $\gamma = 37.8 \text{ mN m}^{-2}$ ) was observed at the buried interface on PEDOT:PSS.

Furthermore, the structure of thin-film metal oxides is another essential issue that significantly influences the performance of OPVs. The surface topography must be as smooth as possible to ensure good contact with the subsequent layer. For instance, the roughness of various thicknesses of solution-processed NiO thin films has been investigated by atomic force microscopy (AFM) [81]. It was found that the root mean square (rms) roughness of a 5 nm NiO thick is about 6.1 nm, which is similar to that of the bare ITO. By increasing the thickness of the NiO layer, the surface became

smoother, and the rms roughness reduced to 2.1 nm. As a result, the photovoltaic characteristics of OPV with 20-nm thick NiO layers displayed a series resistance ( $R_s$ ) and a PCE of  $27 \Omega\text{cm}^2$  and 1.7%, respectively, compared to a  $R_s$  of  $94 \Omega\text{cm}^2$  and a PCE of 0.25% for devices with 5-nm thick NiO layers. In another study, the thin film of crystal  $\text{V}_2\text{O}_5$  nanoparticles was investigated as a hole-extraction interlayer in OPV [92]. The nanocrystal film showed better conductivity and a smoother surface than amorphous  $\text{V}_2\text{O}_5$  film. In addition, the OPV device with the nanocrystal buffer displays a smaller  $R_s$  than the device buffered by an amorphous layer. Although the PCE efficiency of the nanocrystal  $\text{V}_2\text{O}_5$  device is slightly smaller than the device with the amorphous layer, it showed a good performance at a thickness of 200 nm. An amorphous structure can have a maximum thickness of only 30 nm.

A promising morphology is an array of vertically oriented nanorods extending from the metal oxide surface to the active layer, as this can provide continuous pathways for charge transport from the active layer to the electrodes, as shown in **Figure 2.10** [93, 94]. However, most studies demonstrate that the internal space between metal oxide nanorods is still too wide (~100 nm). Developers will need to fill the space with polymer to decrease the internal space between nanorods. Practically, the current density of the OPV device with this approach is predicted to be improved significantly compared to conventional surface [95, 96].

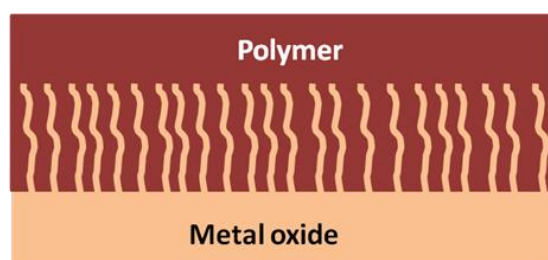


**Figure 2.10** Illustration of metal oxide nanorods as charge collectors.

### 2.6.4 Improving OPV Stability

Stability is another significant issue that should be developed to make OPV a commercially available technology. As the organic polymers suffer from chemical degradation, particularly under illumination, a number of degradation mechanisms of OPV have been recognised including chemical and physical degradation of the active layer, interlayer materials and electrodes [97-99]. Although OPV devices are encapsulated to minimise the degradation processes by reducing diffusion of atmospheric gases into the device, developing more stable solar cells is still important to be compatible with the roll-to-roll technique.

Consequently, fabrication of highly stable buffer layers can protect the active layer and minimise undesired chemical and physical reactions between electrodes and the photoactive layer. PEDOT:PSS is the most commonly used interlayer material as hole extraction interfacial layer showing high efficiency OPV devices and good electrical properties. On the other hand, the residual moisture and the acidic nature of PEDOT:PSS can cause degradation of the electrode and organic films and therefore reduce the device operational lifetime [31, 100-102]. In addition PEDOT:PSS is highly hygroscopic allowing for the wicking of moisture into devices, this results in several different degradation mechanisms that can occur including delamination of weakly adhered layers within the device, and chemical reactions both within the bulk and at interfaces within devices that can lead to the introduction of trap states [100]. These studies suggested that PEDOT:PSS is unlikely to be an effective interlayer for stable OPV devices. To overcome some of these issues thin metal oxides such as  $\text{TiO}_x$ ,  $\text{ZnO}$ ,  $\text{MoO}_3$ ,  $\text{NiO}$  and  $\text{V}_2\text{O}_5$  have been used, these materials showing both good charge

selectivity and high performances that are similar to or better than OPVs with a conventional interfacial PEDOT:PSS layer [103-106].

## 2.7 Utilising Metal Oxides at the Anode Buffer Layer

Transparent metal oxides such as MoO<sub>3</sub>, NiO, and V<sub>2</sub>O<sub>5</sub> have been widely used as interfacial hole extraction layers between the positive electrode and the active layer in OPVs. Thin metal oxides in OPVs exhibit a performance that is similar to or better than OPVs with an interfacial PEDOT:PSS layer. To highlight the significant developments that have resulted from applying thin metal oxides, a brief literature review will be presented below.

### 2.7.1 Molybdenum Oxide (MoO<sub>3</sub>)

In the early studies, MoO<sub>3</sub> thin film was employed as a hole injection material in OLEDs where the hole injecting layer has a deep HOMO level. MoO<sub>3</sub> can be deposited mainly through vacuum deposition due to its low melting temperature (795 °C) and thus its thickness can be controlled at a nanometer scale. Investigation of MoO<sub>3</sub> with ultraviolet and inverse photoemission spectroscopy (UPS) and (IPES), respectively, has revealed a good ohmic contact with many semiconducting polymers [107].

In recent years, there has been an increasing amount of literature on using MoO<sub>3</sub> thin layers in OPVs. Shrotriya et al. evaporated a 5-nm thick MoO<sub>3</sub> layer as the anode interlayer in a P3HT:PCBM device with a conventional structure, and this device exhibited a PCE of 3.3%, which was higher than the OPVs with a PEDOT:PSS layer [103]. Shortly afterwards, another study reported that the vacuum deposition of a 10-nm thick MoO<sub>3</sub> interfacial layer in both solution-processed polymers and vacuum-deposited

small-molecule photovoltaic devices exhibited interesting improvement in the PCE compared to devices with a PEDOT:PSS buffer layer. In addition, using a MoO<sub>3</sub> interfacial layer resulted in a significant increase of the fill factor and a reduction in the series resistance [107]. Recently, inverted devices have been made by evaporating MoO<sub>3</sub> and silver sequentially onto the active layer to serve as a top p-contact instead of serving as a conventional bottom MoO<sub>3</sub> interlayer. An inverted P3HT:PCBM device with a PCE of up to 5% has been produced. The efficiency of devices with P3HT:PCBM has been consistently higher than the efficiency of conventional devices using PEDOT:PSS as the bottom electrode film [108, 109].

Deposition of MoO<sub>3</sub> by solution processing such as spin casting and spray coating is more desirable due to its low cost and short processing time. The thin layer of MoO<sub>3</sub> deposited from a solution should have a low surface roughness as well as a high work function. Liu et al. made the first attempt at using MoO<sub>3</sub> solution processing (s-MoO<sub>x</sub>) in OPVs [110]. They prepared the MoO<sub>3</sub> solution by dissolving a precursor that contained ammonium molybdate into a mixture of deionised water and hydrochloric acid. After the spin coating process, the film was annealed at 160 °C in nitrogen. The produced OPV showed a PCE of 3.1% which is similar to the PCE of the PEDOT:PSS devices that are made under the same conditions. **Table 2.2** summarises the literature review of the photovoltaic parameters of OPV devices fabricated with MoO<sub>3</sub> thin films.

**Table 2.2** The reported OPVs made with a MoO<sub>3</sub> layer as the anode interlayer in which "e-" and "s-" denote the thermal evaporation process and solution process, respectively

Anode interlayer	Electron-donor polymer	Cathode interlayer	Jsc (mA cm <sup>-2</sup> )	Voc (V)	FF	PCE (%)	Ref
e-MoO <sub>3</sub>	PCDTBT	Sol-gel ZnO	10.4	0.88	69	6.3	[111]
	PCDTBT	s-TiO <sub>x</sub>	11.9	0.91	66	7.2	[112]
	P3HT	ZnO NP	12.6	0.63	62	4.9	[109]
	PDTS-TPD	ZnO NP	11.3	0.89	67	6.7	[113]
	PDTG-TPD	Sol-gel ZnO	14	0.86	67	8.1	[114]
	PDTS-TPD	ZnO NP	13.1	0.9	66	7.8	[115]
	PTB7	ZnO	13.54	0.71	67	6.48	[69]
	P3HT	Cs <sub>2</sub> CO <sub>3</sub>	10.03	0.62	63	3.94	[116]
	PCDTBT	MoO <sub>3</sub> -Al	10.7	0.89	66	6.28	[117]
	PCDTBT	TiO <sub>x</sub>	10.2	0.85	56	4.9	[118]
	PCDTBT	Ca	8.6	0.89	60	4.55	[119]
s-MoO <sub>3</sub>	P3HT	Ca	9.29	0.55	67	3.5	[120]
	PBDTTT-C-T	TiO <sub>2</sub>	16.7	0.77	61	7.94	[121]
	P3HT	LiF	8.9	5.6	68	3.4	[122]
	P3HT	Ca	8.88	0.6	63	3.56	[123]
	P3HT	LiF	8.22	0.73	60	3.6	[124]
	P3HT	(TOPD)	12.75	0.58	54.2	4	[125]
	P3HT	-	9.5	0.59	68	3.8	[126]
	P3HT	Ca	9.4	0.62	67	4	[70]
	PBDTTT-C-T	Ca	16.4	0.76	0.62	7.75	[70]
	P3HT:IC <sub>70</sub> BA	Ca	11.1	0.84	70.5	6.57	[127]
	P3HT	Ca	8.7	0.58	69	3.5	[128]
	PCDTBT	Ca	9.1	0.88	52	4.1	[129]

### 2.7.2 Nickel Oxide (NiO)

In the last few years, NiO thin film has received significantly more attention than previously, because it is transparent and can behave as a p-type semiconductor with a large band gap energy in the 3.5-4.0 eV range. NiO is p-type-like metal oxide as a result of two positively charged holes that accompany each Ni<sup>2+</sup> vacancy in the lattice for charge neutrality [130, 131]. Irwin et al. are the first researchers to use the NiO interlayer in polymer solar cells [66]. They deposited the NiO thin film via pulsed laser deposition (PLD), which significantly enhanced the performance of the polymer photovoltaic. Their fabricated P3HT:PCBM devices exhibited PCE as high as 5.2% and a fill factor of up to 69% compared with the PEDOT:PSS devices. Moreover, NiO devices showed good stability for 8 weeks of continuous operation.

Later, a number of studies reported good performance of organic photovoltaic devices with different methods of NiO deposition, such as sputtering [132, 133], PLD [134], and O<sub>2</sub> plasma treatment of evaporated NiO films [135]. Despite this range of choices, manufacturers still prefer solution-processed metal oxides for fabricating OPVs for commercial purposes. Therefore, several studies have examined deposition NiO in a wide variety of solution processing, such as the “sol-gel” technique [136-138], peptised nickel hydroxide for fabrication films as anode interlayer [139], and a dispersion of fine NiO powder into solvents for deposition on the top of the active layer in inverted solar cells [140]. Steirer et al. made the first organic solar cell with solution-processed NiO and used the sol-gel process for producing nickel ink from nickel formate [136]. They formed the NiO thin layers with the spincoating process followed by heat treatment (250–300 °C) in air. Subsequently, the NiO films were treated by O<sub>2</sub> plasma to increase the work function, which resulted in devices with a PCE that was



similar to those made with PEDOT:PSS. In another study, Steirer et al. produced PCDTBT:PC<sub>70</sub>BM BHJ solar cells with solution-processed NiO, which resulted in a PCE of 6.7%, which is considerably higher than PEDOT:PSS devices [138]. This high efficiency was ascribed to the high work function of NiO due to the O<sub>2</sub> plasma treatment. Furthermore, the devices made with the NiO thin films showed higher stability than those fabricated with PEDOT:PSS. The device characteristics of OPVs containing NiO thin films as reported in literature are summarised in **Table 2.3**.

**Table 2.3** Different processing methods of NiO have been applied for producing OPV devices. "e-" and "s-" denote the thermal evaporation process and solution process, respectively

Anode interlayer	Heating Temp. °C	electron- donor polymer	Cathode interlayer	J <sub>sc</sub> (mA cm <sup>-2</sup> )	V <sub>oc</sub> (V)	FF	PCE (%)	Ref
s-NiO	275	pDTG-TPD	LiF	13.9	0.82	68.4	7.8	[82]
	-	P3HT	ZnO	10	0.58	51	3	[140]
	280	P3HT	LiF	8.7	0.6	66	3.5	[139]
	350	P3HT	LiF	8.7	0.57	56.5	2.83	[141]
	300	P3HT	Ca	9.7	0.58	67	3.7	[80]
	350	P3HT	LiF	7.7	0.57	51	2.2	[81]
	250	P3HT	Ca	8.6	0.58	0.71	3.6	[136]
	500	P3HT	LiF	6.1	0.53	52	2	[142]
	300	PCDTBT	Ca	11.5	0.88	65	6.7	[138]
	-	PCDTBT	Ca	11.4	0.90	62.5	6.4	[143]
Sputtered-NiO	-	P3HT	-	10.5	0.56	55	3.26	[144]
Sputtered-NiO	-	P3HT	-	10.6	0.52	59	3.3	[132]
RFM sputtered-NiO	-	P3HT	Ca	10.5	0.58	-	3.84	[145]
PLD-NiO	-	P3HT	LiF	8.8	0.59	55	5.96	[66]
PLD-NiO	-	P3HT	Ca	9.8	0.57	58	3.2	[146]
e-NiO	-	P3HT	BCP/LiF	12	0.65	45	3.5	[135]

Despite the promising performance of the NiO interlayer material, fabrication NiO films with high temperature annealing may become an obstacle for its applications in large scale printing such as roll-to-roll processing. A better understanding of the chemical processes and electronic structure during the thermal annealing can help researchers to find a method to fabricate NiO films from solution at low temperature processing.

### 2.7.3 Tungsten Oxide (WO<sub>3</sub>)

Tungsten oxide is another transition metal oxide that has been used in OPVs due to its large work function. Furthermore, its electronic structure is similar to MoO<sub>3</sub>, because it strongly depends on a crystalline structure, stoichiometry and deposition conditions [106]. Recently, several studies have been published about using WO<sub>3</sub> thin-film as an interlayer between the active layer and the metal electrode in OPVs. Tao et al. used thermal-evaporated WO<sub>3</sub> as a top anode interlayer for inverted P3HT:PCBM devices. This solution displayed a high FF and a V<sub>oc</sub> of 0.6 V [147]. In a similar study, WO<sub>3</sub> thin film was inserted as the bottom anode interlayer with low surface roughness (r.m.s = 0.9 nm) in a conventional structure [148]. The device performance was similar to that of inverted devices, because its PCE and FF were 3.1% and 70, respectively. The e-WO<sub>3</sub> thin film also exhibited a large work function and small energy barrier at the interface with using deep HOMO energies, such as F8BT (5.9 eV).

Other research groups have investigated solution-processing WO<sub>3</sub> thin films as an anode interlayer for OPVs. Choi et al. investigated a conventional structure of P3HT:PCBM cells with a solution-processed WO<sub>3</sub> interlayer made from a tungsten ethoxide [W(OC<sub>2</sub>H<sub>5</sub>)<sub>6</sub>] solution. The WO<sub>3</sub> buffer layer showed a larger work function than PEDOT:PSS. The buffer layer also offered a PCE of 3.4%, which was similar to the

devices made with a PEDOT:PSS interlayer. In a recent study, a P3HT:PCBM device with a PCE of 6.4% has been created by using solution-processed WO<sub>3</sub> as an interlayer anode. This efficiency is far superior to that of the devices with PEDOT:PSS as the anode buffer layer, which offer a PCE of 3.8% [76]. In addition, the WO<sub>3</sub> layer made of tungsten(VI) isopropoxide as a precursor showed high hole mobility and high light transmittance. However, the thermal annealing of WO<sub>3</sub> thin films can be an obstacle to using some organic polymers in OPVs, and can be worthless economically due to consuming more energy during fabrication. Using solution-processed metal oxide without post-deposition processing is highly desirable for commercial purposes.

**Table 2.4** summarises the literature review of the photovoltaic properties of OPV devices fabricated with WO<sub>3</sub> thin films.

**Table 2.4** Various organic devices have been fabricated with WO<sub>3</sub> film as a hole extraction layer in which "e-" and "s-" denote the thermal evaporation process and solution process, respectively

Anode interlayer	Annealing Temp. °C	electron- donor polymer	Cathode interlayer	Jsc (mA cm <sup>-2</sup> )	Voc (V)	FF	PCE (%)	Ref
e-WO <sub>3</sub>	-	PTB7	ZnO	0.72	14.3	64.2	6.7	[69]
	-	PCDTBT	TiO <sub>x</sub>	10.3	89	58	5.3	[149]
	-	P3HT	ZnO-Al	13.5	0.54	65	4.8	[150]
	-	P3HT	-	7.8	0.62	55	2.6	[151]
	-	P3HT	TiO <sub>2</sub>	7.2	0.6	60	2.6	[147]
s-WO <sub>3</sub>	300	P3HT	-	8.3	0.49	50	2	[75]
	-	Si-PCPDTBT	Al doped ZnO	10.5	0.52	59	3.3	[152]
	-	P3HT	-	8.6	0.62	63	3.4	[153]
	150	P3HT	Ca	10.8	0.84	70	6.36	[76]
	-	P3HT	-	8.5	0.59	65	3.2	[154]
	80	P3HT	Al doped ZnO	12.8	0.62	60	4.8	[154]

### 2.7.4 Vanadium Oxide ( $V_2O_5$ )

Vanadium oxide is another n-type semiconducting oxide that has been recently used as the anode interlayer. When researchers investigated its electronic structure with UPS and IPES, they found a band gap of 2.8 eV, which partially covers the absorption band of PC<sub>71</sub>BM. The first researcher to use  $V_2O_5$  as a buffer layer in OPV cells was Shrotriya (2006) [103]. Shrotriya fabricated a P3HT:PCBM cell with thermally evaporated  $V_2O_5$  as an anode interlayer, and this cell exhibited a PCE of 3.1%, which is very similar to the PCE of devices with a PEDOT:PSS interlayer. Wang et al. investigated the impact of  $V_2O_5$  morphology on the performance of OPVs [92], and they found that a nanocrystal  $V_2O_5$  thick layer (200 nm) can work effectively as a hole-extraction layer in OPV devices. In contrast, an amorphous  $V_2O_5$  structure can have a maximum thickness of only 30 nm. In a more recent study, OPV based on a P3HT polymer with a solution-processed  $VO_x$  interlayer anode was examined for two different fullerene derivatives (IC<sub>70</sub>BA and PC<sub>70</sub>BM) as acceptors [155]. The PV devices demonstrated a better performance than those made with PEDOT:PSS for both acceptor polymers. Moreover, the PCE of s- $VO_x$ -based OPV devices fabricated with P3HT:IC70BA as active layer showed efficiency of 6.35% and a FF of 70 %.

Compared to the studies that have examined  $MoO_3$ , fewer studies have been done on OPVs with a  $V_2O_5$  interlayer. To gain a better understanding of the charge extraction mechanism at interface of the  $V_2O_5$  polymer or electrode- $V_2O_5$ , further studies of the interface electronic structures are required. Moreover, most solution-processed vanadium oxide required post-deposition treatment such as thermal annealing and oxygen plasma treatment. In this work I show that it is possible to deposit  $V_2O_x$  from a vanadium oxytriisopropoxide precursor requiring no plasma treatment or post

deposition annealing. Films of solution processed  $V_2O_x$  have been incorporated into PFDT2BT-8:PC<sub>70</sub>BM OPV devices achieving a power conversion efficiency of 6.5%, comparable to PEDOT:PSS (6.5%) and vacuum deposited MoO<sub>3</sub> (6.3%). **Table 2.5** shows the OPV devices characteristics employing  $V_2O_5$  interlayer as described within the literature.

**Table 2.5** The reported OPVs made with a  $V_2O_5$  layer as an anode interlayer. "e-" and "s-" denote the thermal evaporation process and solution process, respectively

Anode interlayer	Annealing Temp. °C	electron-donor polymer	Cathode interlayer	Jsc (mA cm <sup>-2</sup> )	Voc (V)	FF	PCE (%)	Ref
S-VO <sub>x</sub>	-	OPV3	Ca	12.4	0.72	69	6.15	[156]
	-	OPV3	ZnO	12.2	0.72	70	6.1	[156]
	-	P3HT	Ca	9.7	0.63	64	3.9	[70]
	-	PBDTTT-C-T	Ca	16.5	0.76	61	7.6	[70]
	-	Si-PCPDTBT	Ca	11.6	0.61	64	4.5	[92]
	-	P3HT	TiO <sub>x</sub>	9.5	0.52	60	3	[84]
	140	P3HT	BCP	8.1	0.59	65	3.3	[86]
	80	P3HT	TiO <sub>x</sub>	8.1	0.56	53	2.4	[88]
	-	P3HT	-	9.5	0.53	58	2.9	[157]
	150	P3HT	Ca	10.6	0.85	70	6.35	[155]
	210	PTB7	PFN	15.8	0.73	66.8	7.7	[158]
	-	PCDTBT	Ca	9.4	0.85	65	5.2	[159]
e-VO <sub>x</sub>	-	P3HT	TiO <sub>x</sub>	10.7	0.53	51	2.9	[84]
	-	P3HT	Ca	8.8	0.59	59	3.1	[103]
	-	P3HT	ZnO	10.6	0.57	5.6	3.9	[160]

## 2.8 References

1. R. Mauer, M. Kastler and F. Laquai, *The impact of polymer regioregularity on charge transport and efficiency of P3HT:PCBM photovoltaic devices*, *Advanced Functional Materials* **20** (2010), no. 13, 2085-2092.
2. A. Kohler and H. Baessler, *Electronic processes in organic semiconductors : An introduction*, Wiley-VCH, Weinheim, Germany, 2015.
3. J. M. Dixon, M. Taniguchi and J. S. Lindsey, *Photochemcad 2: A refined program with accompanying spectral databases for photochemical calculations*, *Photochemistry and Photobiology* **81** (2005), no. 1, 212-213.
4. P. Atkins and J. D. Paula, *Physical chemistry*, Oxford University Press Oxford, 2010.
5. B. Kippelen and J.-L. Bredas, *Organic photovoltaics*, *Energy & Environmental Science* **2** (2009), no. 3, 251-261.
6. K. M. Coakley and M. D. McGehee, *Conjugated polymer photovoltaic cells*, *Chemistry of Materials* **16** (2004), no. 23, 4533-4542.
7. M. M. Wienk, J. M. Kroon, W. J. H. Verhees, J. Knol, J. C. Hummelen, P. A. van Hal and R. A. J. Janssen, *Efficient Methano 70 fullerene/MDMO-PPV bulk heterojunction photovoltaic cells*, *Angewandte Chemie-International Edition* **42** (2003), no. 29, 3371-3375.

8. A. J. Moule and K. Meerholz, *Minimizing optical losses in bulk heterojunction polymer solar cells*, Applied Physics B-Lasers and Optics **86** (2007), no. 4, 721-727.
9. A. Meyer and H. Ade, *The effect of angle of incidence on the optical field distribution within thin film organic solar cells*, Journal of Applied Physics **106** (2009), no. 11, 113101-113105.
10. J. Y. Kim, K. Lee, N. E. Coates, D. Moses, T.-Q. Nguyen, M. Dante and A. J. Heeger, *Efficient tandem polymer solar cells fabricated by all-solution processing*, Science **317** (2007), no. 5835, 222-225.
11. J. L. Bredas, J. E. Norton, J. Cornil and V. Coropceanu, *Molecular understanding of organic solar cells: The challenges*, Accounts of Chemical Research **42** (2009), no. 11, 1691-1699.
12. P. G. Nicholson and F. A. Castro, *Organic photovoltaics: Principles and techniques for nanometre scale characterization*, Nanotechnology **21** (2010), no. 49.
13. P. E. Shaw, A. Ruseckas and I. D. W. Samuel, *Exciton diffusion measurements in poly(3-hexylthiophene)*, Advanced Materials **20** (2008), no. 18, 3516-+.
14. S. R. Scully and M. D. McGehee, *Effects of optical interference and energy transfer on exciton diffusion length measurements in organic semiconductors*, Journal of Applied Physics **100** (2006), no. 3.



15. M. C. Scharber, D. Wuhlbacher, M. Koppe, P. Denk, C. Waldauf, A. J. Heeger and C. L. Brabec, *Design rules for donors in bulk-heterojunction solar cells - towards 10 % energy-conversion efficiency*, *Advanced Materials* **18** (2006), no. 6, 789-+.
16. R. Kersting, U. Lemmer, M. Deussen, H. J. Bakker, R. F. Mahrt, H. Kurz, V. I. Arkhipov, H. Bässler and E. O. Göbel, *Ultrafast field-induced dissociation of excitons in conjugated polymers*, *Physical Review Letters* **73** (1994), no. 10, 1440-1443.
17. T. Offermans, S. C. J. Meskers and R. A. J. Janssen, *Monte-carlo simulations of geminate electron-hole pair dissociation in a molecular heterojunction: A two-step dissociation mechanism*, *Chemical Physics* **308** (2005), no. 1-2, 125-133.
18. P. Peumans and S. R. Forrest, *Separation of geminate charge-pairs at donor-acceptor interfaces in disordered solids*, *Chemical Physics Letters* **398** (2004), no. 1-3, 27-31.
19. C. L. Braun, *Electric-field assisted dissociation of charge-transfer states as a mechanism of photocarrier production*, *Journal of Chemical Physics* **80** (1984), no. 9, 4157-4161.
20. V. Lemaire, M. Steel, D. Beljonne, J. L. Bredas and J. Cornil, *Photoinduced charge generation and recombination dynamics in model donor/acceptor pairs for organic solar cell applications: A full quantum-chemical treatment*, *Journal of the American Chemical Society* **127** (2005), no. 16, 6077-6086.

21. L. Onsager, *Initial recombination of ions*, Physical Review **54** (1938), no. 8, 554-557.
22. S. Günes, H. Neugebauer and N. S. Sariciftci, *Conjugated polymer-based organic solar cells*, Chemical Reviews **107** (2007), no. 4, 1324-1338.
23. S. H. Park, A. Roy, S. Beaupre, S. Cho, N. Coates, J. S. Moon, D. Moses, M. Leclerc, K. Lee and A. J. Heeger, *Bulk heterojunction solar cells with internal quantum efficiency approaching 100%*, Nature Photonics **3** (2009), no. 5, 297-U295.
24. S. S. M., *Physics of semiconducting devices* Wiley, New York, 1981.
25. I. D. Parker, *Carrier tunneling and device characteristics in polymer light-emitting diodes*, Journal of Applied Physics **75** (1994), no. 3, 1656-1666.
26. F. Nuesch, F. Rotzinger, L. Si-Ahmed and L. Zuppiroli, *Chemical potential shifts at organic device electrodes induced by grafted monolayers*, Chemical Physics Letters **288** (1998), no. 5-6, 861-867.
27. M. Kemerink, J. M. Kramer, H. H. P. Gommans and R. A. J. Janssen, *Temperature-dependent built-in potential in organic semiconductor devices*, Applied Physics Letters **88** (2006), no. 19.
28. T. W. Lee and O. O. Park, *The effect of different heat treatments on the luminescence efficiency of polymer light-emitting diodes*, Advanced Materials **12** (2000), no. 11, 801-804.

29. S. Tokito, K. Noda and Y. Taga, *Metal oxides as a hole-injecting layer for an organic electroluminescent device*, *Journal of Physics D-Applied Physics* **29** (1996), no. 11, 2750-2753.
30. H. Ishii, K. Sugiyama, E. Ito and K. Seki, *Energy level alignment and interfacial electronic structures at organic metal and organic organic interfaces*, *Advanced Materials* **11** (1999), no. 8, 605-+.
31. K. Lee, J. Y. Kim, S. H. Park, S. H. Kim, S. Cho and A. J. Heeger, *Air-stable polymer electronic devices*, *Advanced Materials* **19** (2007), no. 18, 2445-+.
32. G. Li, R. Zhu and Y. Yang, *Polymer solar cells*, *Nature Photonics* **6** (2012), no. 3, 153-161.
33. D. Cheyns, J. Poortmans, P. Heremans, C. Deibel, S. Verlaak, B. P. Rand and J. Genoe, *Analytical model for the open-circuit voltage and its associated resistance in organic planar heterojunction solar cells*, *Physical Review B* **77** (2008), no. 16.
34. A. Gadisa, M. Svensson, M. R. Andersson and O. Inganäs, *Correlation between oxidation potential and open-circuit voltage of composite solar cells based on blends of polythiophenes/fullerene derivative*, *Applied Physics Letters* **84** (2004), no. 9, 1609-1611.
35. K. Vandewal, K. Tvingstedt, A. Gadisa, O. Inganäs and J. V. Manca, *On the origin of the open-circuit voltage of polymer-fullerene solar cells*, *Nature Materials* **8** (2009), no. 11, 904-909.

36. M. D. Perez, C. Borek, S. R. Forrest and M. E. Thompson, *Molecular and morphological influences on the open circuit voltages of organic photovoltaic devices*, Journal of the American Chemical Society **131** (2009), no. 26, 9281-9286.
37. W. R. Salaneck, S. Stafstrom and J.-L. Bredas, *Conjugated polymer surfaces and interfaces*, Cambridge University Press, New York, 1996.
38. H. Ishii, K. Sugiyama, D. Yoshimura, E. Ito, Y. Ouchi and K. Seki, *Energy-level alignment at model interfaces of organic electroluminescent devices studied by UV photoemission: Trend in the deviation from the traditional way of estimating the interfacial electronic structures*, Selected Topics in Quantum Electronics, IEEE Journal of **4** (1998), no. 1, 24-33.
39. S. Braun, W. R. Salaneck and M. Fahlman, *Energy-level alignment at organic/metal and organic/organic interfaces*, Advanced Materials **21** (2009), no. 14-15, 1450-1472.
40. L. Yan, N. J. Watkins, S. Zorba, Y. L. Gao and C. W. Tang, *Thermodynamic equilibrium and metal-organic interface dipole*, Applied Physics Letters **81** (2002), no. 15, 2752-2754.
41. Y. Gao, *Surface analytical studies of interfaces in organic semiconductor devices*, Materials Science & Engineering R-Reports **68** (2010), no. 3, 39-87.
42. R. Steim, F. R. Kogler and C. J. Brabec, *Interface materials for organic solar cells*, Journal of Materials Chemistry **20** (2010), no. 13, 2499-2512.

43. C. D. Lindstrom and X. Y. Zhu, *Photoinduced electron transfer at molecule-metal interfaces*, Chemical Reviews **106** (2006), no. 10, 4281-4300.
44. X. Crispin, V. Geskin, A. Crispin, J. Cornil, R. Lazzaroni, W. R. Salaneck and J. L. Bredas, *Characterization of the interface dipole at organic/metal interfaces*, Journal of the American Chemical Society **124** (2002), no. 27, 8131-8141.
45. H.-L. Yip and A. K. Y. Jen, *Recent advances in solution-processed interfacial materials for efficient and stable polymer solar cells*, Energy & Environmental Science **5** (2012), no. 3, 5994-6011.
46. C. Tengstedt, W. Osikowicz, W. R. Salaneck, I. D. Parker, C. H. Hsu and M. Fahlman, *Fermi-level pinning at conjugated polymer interfaces*, Applied Physics Letters **88** (2006), no. 5.
47. D. Cakir, M. Bokdam, M. P. de Jong, M. Fahlman and G. Brocks, *Modeling charge transfer at organic donor-acceptor semiconductor interfaces*, Applied Physics Letters **100** (2012), no. 20, 4.
48. G. Brocks, D. Cakir, M. Bokdam, M. P. de Jong and M. Fahlman, *Charge equilibration and potential steps in organic semiconductor multilayers*, Organic Electronics **13** (2012), no. 10, 1793-1801.
49. M. Bokdam, D. Cakir and G. Brocks, *Fermi level pinning by integer charge transfer at electrode-organic semiconductor interfaces*, Applied Physics Letters **98** (2011), no. 11.

50. L. Lindell, D. Cakir, G. Brocks, M. Fahlman and S. Braun, *Role of intrinsic molecular dipole in energy level alignment at organic interfaces*, Applied Physics Letters **102** (2013), no. 22, 4.
51. S. K. Hau, K. M. O'Malley, Y.-J. Cheng, H.-L. Yip, H. Ma and A. K. Y. Jen, *Optimization of active layer and anode electrode for high-performance inverted bulk-heterojunction solar cells*, Ieee Journal of Selected Topics in Quantum Electronics **16** (2010), no. 6, 1665-1675.
52. P. Peumans and S. R. Forrest, *Very-high-efficiency double-heterostructure copper phthalocyanine/C<sub>60</sub> photovoltaic cells*, Applied Physics Letters **79** (2001), no. 1, 126-128.
53. S. K. Hau, H.-L. Yip, O. Acton, N. S. Baek, H. Ma and A. K. Y. Jen, *Interfacial modification to improve inverted polymer solar cells*, Journal of Materials Chemistry **18** (2008), no. 42, 5113-5119.
54. L. A. A. Pettersson, L. S. Roman and O. Inganäs, *Modeling photocurrent action spectra of photovoltaic devices based on organic thin films*, Journal of Applied Physics **86** (1999), no. 1, 487-496.
55. S. K. Gupta, A. Sharma, S. Banerjee, R. Gahlot, N. Aggarwal, Deepak and A. Garg, *Understanding the role of thickness and morphology of the constituent layers on the performance of inverted organic solar cells*, Solar Energy Materials and Solar Cells **116** (2013), no. 0, 135-143.

56. A. Hadipour, D. Cheyuns, P. Heremans and B. P. Rand, *Electrode considerations for the optical enhancement of organic bulk heterojunction solar cells*, *Advanced Energy Materials* **1** (2011), no. 5, 930-935.
57. J. Gilot, I. Barbu, M. M. Wienk and R. A. J. Janssen, *The use of ZnO as optical spacer in polymer solar cells: Theoretical and experimental study*, *Applied Physics Letters* **91** (2007), no. 11.
58. J. Y. Kim, S. H. Kim, H. H. Lee, K. Lee, W. L. Ma, X. Gong and A. J. Heeger, *New architecture for high-efficiency polymer photovoltaic cells using solution-based titanium oxide as an optical spacer*, *Advanced Materials* **18** (2006), no. 5, 572-+.
59. A. Roy, S. H. Park, S. Cowan, M. H. Tong, S. Cho, K. Lee and A. J. Heeger, *Titanium suboxide as an optical spacer in polymer solar cells*, *Applied Physics Letters* **95** (2009), no. 1.
60. Y. Zang, J. Huang, H. Li, J. Yu and Y. Jiang, *Effect of molybdenum oxide anode buffer layer on the performance of inverted small molecular organic solar cells*, *Energy Procedia* **12** (2011), no. 0, 513-518.
61. T. Minami, *Transparent conducting oxide semiconductors for transparent electrodes*, *Semiconductor Science and Technology* **20** (2005), no. 4, S35-S44.
62. J. Meyer, S. Hamwi, M. Kroger, W. Kowalsky, T. Riedl and A. Kahn, *Transition metal oxides for organic electronics: Energetics, device physics and applications*, *Advanced Materials* **24** (2012), no. 40, 5408-5427.

63. M. C. Gwinner, R. Di Pietro, Y. Vaynzof, K. J. Greenberg, P. K. H. Ho, R. H. Friend and H. Sirringhaus, *Doping of organic semiconductors using molybdenum trioxide: A quantitative time-dependent electrical and spectroscopic study*, *Advanced Functional Materials* **21** (2011), no. 8, 1432-1441.
64. M. T. Greiner, M. G. Helander, Z. B. Wang, W. M. Tang, J. Qiu and Z. H. Lu, *A metallic molybdenum suboxide buffer layer for organic electronic devices*, *Applied Physics Letters* **96** (2010), no. 21, 213302-213303.
65. M. Vasilopoulou, L. C. Palilis, D. G. Georgiadou, S. Kennou, I. Kostis, D. Davazoglou and P. Argitis, *Barrierless hole injection through sub-bandgap occupied states in organic light emitting diodes using substoichiometric MoO<sub>x</sub> anode interfacial layer*, *Applied Physics Letters* **100** (2012), no. 1, 013311-013314.
66. M. D. Irwin, B. Buchholz, A. W. Hains, R. P. H. Chang and T. J. Marks, *P-type semiconducting nickel oxide as an efficiency-enhancing anode interfacial layer in polymer bulk-heterojunction solar cells*, *Proceedings of the National Academy of Sciences of the United States of America* **105** (2008), no. 8, 2783-2787.
67. J. Meyer and A. Kahn, *Electronic structure of molybdenum-oxide films and associated charge injection mechanisms in organic devices*, *Journal of Photonics for Energy* **1** (2011).
68. M. Kröger, S. Hamwi, J. Meyer, T. Riedl, W. Kowalsky and A. Kahn, *P-type doping of organic wide band gap materials by transition metal oxides: A case-study on molybdenum trioxide*, *Organic Electronics: physics, materials, applications* **10** (2009), no. 5, 932-938.



69. R. Lampande, G. W. Kim, J. Boizot, Y. J. Kim, R. Pode and J. H. Kwon, *A highly efficient transition metal oxide layer for hole extraction and transport in inverted polymer bulk heterojunction solar cells*, *Journal of Materials Chemistry A* **1** (2013), no. 23, 6895-6900.
70. F. X. Xie, W. C. H. Choy, C. D. Wang, X. C. Li, S. Q. Zhang and J. H. Hou, *Low-temperature solution-processed hydrogen molybdenum and vanadium bronzes for an efficient hole-transport layer in organic electronics*, *Advanced Materials* **25** (2013), no. 14, 2051-2055.
71. L. Fang, S. J. Baik, J. W. Kim, S. J. Kang, J. W. Seo, J.-W. Jeon, Y. H. Kim and K. S. Lim, *Tunable work function of a  $wO_x$  buffer layer for enhanced photocarrier collection of pin-type amorphous silicon solar cells*, *Journal of Applied Physics* **109** (2011), no. 10, 104501-104504.
72. J. Meyer, M. Kroger, S. Hamwi, F. Gnam, T. Riedl, W. Kowalsky and A. Kahn, *Charge generation layers comprising transition metal-oxide/organic interfaces: Electronic structure and charge generation mechanism*, *Applied Physics Letters* **96** (2010), no. 19, 193302-193303.
73. M. Vasilopoulou, G. Papadimitropoulos, L. C. Palilis, D. G. Georgiadou, P. Argitis, S. Kennou, I. Kostis, N. Vourdas, N. A. Stathopoulos and D. Davazoglou, *High performance organic light emitting diodes using substoichiometric tungsten oxide as efficient hole injection layer*, *Organic Electronics* **13** (2012), no. 5, 796-806.
74. Y. H. Kim, S. Kwon, J. H. Lee, S. M. Park, Y. M. Lee and J. W. Kim, *Hole injection enhancement by a  $WO_3$  inter layer in inverted organic light-emitting diodes and*

- their interfacial electronic structures*, Journal of Physical Chemistry C **115** (2011), no. 14, 6599-6604.
75. J.-S. Lee, I.-H. Jang and N.-G. Park, *Effects of oxidation state and crystallinity of tungsten oxide interlayer on photovoltaic property in bulk hetero-junction solar cell*, Journal of Physical Chemistry C **116** (2012), no. 25, 13480-13487.
76. Z. a. Tan, L. Li, C. Cui, Y. Ding, Q. Xu, S. Li, D. Qian and Y. Li, *Solution-processed tungsten oxide as an effective anode buffer layer for high-performance polymer solar cells*, The Journal of Physical Chemistry C **116** (2012), no. 35, 18626-18632.
77. H. Yang, C. Gong, G. Hong Guai and C. Ming Li, *Organic solar cells employing electrodeposited nickel oxide nanostructures as the anode buffer layer*, Solar Energy Materials and Solar Cells **101** (2012), no. 0, 256-261.
78. K. Nakaoka, J. Ueyama and K. Ogura, *Semiconductor and electrochromic properties of electrochemically deposited nickel oxide films*, Journal of Electroanalytical Chemistry **571** (2004), no. 1, 93-99.
79. H. Sato, T. Minami, S. Takata and T. Yamada, *Transparent conducting p-type NiO thin-films prepared by magnetron sputtering*, Thin Solid Films **236** (1993), no. 1-2, 27-31.
80. E. L. Ratcliff, J. Meyer, K. X. Steirer, A. Garcia, J. J. Berry, D. S. Ginley, D. C. Olson, A. Kahn and N. R. Armstrong, *Evidence for near-surface NiOOH species in solution-processed NiO<sub>x</sub> selective interlayer materials: Impact on energetics and the*

*performance of polymer bulk heterojunction photovoltaics*, Chemistry of Materials **23** (2011), no. 22, 4988-5000.

81. K. H. Kim, C. Takahashi, T. Okubo, Y. Abe and M. Kawamura, *Influence of NiO anode buffer layer prepared by solution on performance of bulk-heterojunction solar cells*, Applied Surface Science **258** (2012), no. 20, 7809-7812.

82. J. R. Manders, S.-W. Tsang, M. J. Hartel, T.-H. Lai, S. Chen, C. M. Amb, J. R. Reynolds and F. So, *Solution-processed nickel oxide hole transport layers in high efficiency polymer photovoltaic cells*, Advanced Functional Materials **23** (2013), no. 23, 2993-3001.

83. J. Meyer, K. Zilberberg, T. Riedl and A. Kahn, *Electronic structure of vanadium pentoxide: An efficient hole injector for organic electronic materials*, Journal of Applied Physics **110** (2011), no. 3, 033710-033715.

84. K. Zilberberg, S. Trost, J. Meyer, A. Kahn, A. Behrendt, D. Luetzenkirchen-Hecht, R. Frahm and T. Riedl, *Inverted organic solar cells with sol-gel processed high work-function vanadium oxide hole-extraction layers*, Advanced Functional Materials **21** (2011), no. 24, 4776-4783.

85. I. Hancox, L. A. Rochford, D. Clare, P. Sullivan and T. S. Jones, *Utilizing n-type vanadium oxide films as hole-extracting layers for small molecule organic photovoltaics*, Applied Physics Letters **99** (2011), no. 1, 3.

86. I. Hancox, L. A. Rochford, D. Clare, M. Walker, J. J. Mudd, P. Sullivan, S. Schumann, C. F. McConville and T. S. Jones, *Optimization of a high work function*

- solution processed vanadium oxide hole-extracting layer for small molecule and polymer organic photovoltaic cells*, Journal of Physical Chemistry C **117** (2013), no. 1, 49-57.
87. J. S. Huang, C. Y. Chou, M. Y. Liu, K. H. Tsai, W. H. Lin and C. F. Lin, *Solution-processed vanadium oxide as an anode interlayer for inverted polymer solar cells hybridized with ZnO nanorods*, Organic Electronics **10** (2009), no. 6, 1060-1065.
88. J. Wu, Y. Zhang, P. Xu, W. Guo, L. Shen and S. Ruan, *Role of solution-processed V<sub>2</sub>O<sub>5</sub> in P3HT:PCBM based inverted polymer solar cells*, Synthetic Metals **170** (2013), no. 0, 7-10.
89. D. S. Germack, C. K. Chan, R. J. Kline, D. A. Fischer, D. J. Gundlach, M. F. Toney, L. J. Richter and D. M. DeLongchamp, *Interfacial segregation in polymer/fullerene blend films for photovoltaic devices*, Macromolecules **43** (2010), no. 8, 3828-3836.
90. D. S. Germack, C. K. Chan, B. H. Hamadani, L. J. Richter, D. A. Fischer, D. J. Gundlach and D. M. DeLongchamp, *Substrate-dependent interface composition and charge transport in films for organic photovoltaics*, Applied Physics Letters **94** (2009), no. 23.
91. A. F. Tillack, K. M. Noone, B. A. MacLeod, D. Nordlund, K. P. Nagle, J. A. Bradley, S. K. Hau, H.-L. Yip, A. K. Y. Jen, G. T. Seidler and D. S. Ginger, *Surface characterization of polythiophene:Fullerene blends on different electrodes using near edge X-ray absorption fine structure*, Acs Applied Materials & Interfaces **3** (2011), no. 3, 726-732.

92. H.-Q. Wang, N. Li, N. S. Guldal and C. J. Brabec, *Nanocrystal  $V_2O_5$  thin film as hole-extraction layer in normal architecture organic solar cells*, *Organic Electronics* **13** (2012), no. 12, 3014-3021.
93. T. Gershon, *Metal oxide applications in organic-based photovoltaics*, *Materials Science and Technology* **27** (2011), no. 9, 1357-1371.
94. D. C. Olson, J. Pirus, R. T. Collins, S. E. Shaheen and D. S. Ginley, *Hybrid photovoltaic devices of polymer and ZnO nanofiber composites*, *Thin Solid Films* **496** (2006), no. 1, 26-29.
95. P. Ravirajan, A. M. Peiro, M. K. Nazeeruddin, M. Graetzel, D. D. C. Bradley, J. R. Durrant and J. Nelson, *Hybrid polymer/zinc oxide photovoltaic devices with vertically oriented ZnO nanorods and an amphiphilic molecular interface layer*, *Journal of Physical Chemistry B* **110** (2006), no. 15, 7635-7639.
96. D. C. Olson, S. E. Shaheen, R. T. Collins and D. S. Ginley, *The effect of atmosphere and ZnO morphology on the performance of hybrid poly(3-hexylthiophene)/ZnO nanofiber photovoltaic devices*, *Journal of Physical Chemistry C* **111** (2007), no. 44, 16670-16678.
97. M. Jorgensen, K. Norrman, S. A. Gevorgyan, T. Tromholt, B. Andreasen and F. C. Krebs, *Stability of polymer solar cells*, *Advanced Materials* **24** (2012), no. 5, 580-612.
98. M. Jorgensen, K. Norrman and F. C. Krebs, *Stability/degradation of polymer solar cells*, *Solar Energy Materials and Solar Cells* **92** (2008), no. 7, 686-714.

99. S. Savagatrup, A. D. Printz, T. F. O'Connor, A. V. Zaretski, D. Rodriguez, E. J. Sawyer, K. M. Rajan, R. I. Acosta, S. E. Root and D. J. Lipomi, *Mechanical degradation and stability of organic solar cells: Molecular and microstructural determinants*, *Energy & Environmental Science* **8** (2015), no. 1, 55-80.
100. K. Norrman, M. V. Madsen, S. A. Gevorgyan and F. C. Krebs, *Degradation patterns in water and oxygen of an inverted polymer solar cell*, *Journal of the American Chemical Society* **132** (2010), no. 47, 16883-16892.
101. E. L. Ratcliff, B. Zacher and N. R. Armstrong, *Selective inter layers and contacts in organic photovoltaic cells*, *Journal of Physical Chemistry Letters* **2** (2011), no. 11, 1337-1350.
102. M. P. de Jong, L. J. van Ijzendoorn and M. J. A. de Voigt, *Stability of the interface between indium-tin-oxide and poly(3,4-ethylenedioxythiophene)/poly(styrenesulfonate) in polymer light-emitting diodes*, *Applied Physics Letters* **77** (2000), no. 14, 2255-2257.
103. V. Shrotriya, G. Li, Y. Yao, C. W. Chu and Y. Yang, *Transition metal oxides as the buffer layer for polymer photovoltaic cells*, *Applied Physics Letters* **88** (2006), no. 7.
104. J. H. Park, T. W. Lee, B. D. Chin, D. H. Wang and O. O. Park, *Roles of interlayers in efficient organic photovoltaic devices*, *Macromolecular Rapid Communications* **31** (2010), no. 24, 2095-2108.

105. R. Jose, V. Thavasi and S. Ramakrishna, *Metal oxides for dye-sensitized solar cells*, Journal of the American Ceramic Society **92** (2009), no. 2, 289-301.
106. S. Chen, J. R. Manders, S.-W. Tsang and F. So, *Metal oxides for interface engineering in polymer solar cells*, Journal of Materials Chemistry **22** (2012), no. 46, 24202-24212.
107. D. Y. Kim, J. Subbiah, G. Sarasqueta, F. So, H. Ding, Irfan and Y. Gao, *The effect of molybdenum oxide interlayer on organic photovoltaic cells*, Applied Physics Letters **95** (2009), no. 9, 093304-093303.
108. S. Chen, K. R. Choudhury, J. Subbiah, C. M. Amb, J. R. Reynolds and F. So, *Photo-carrier recombination in polymer solar cells based on P3HT and silole-based copolymer*, Advanced Energy Materials **1** (2011), no. 5, 963-969.
109. S. K. Hau, H.-L. Yip, H. Ma and A. K. Y. Jen, *High performance ambient processed inverted polymer solar cells through interfacial modification with a fullerene self-assembled monolayer*, Applied Physics Letters **93** (2008), no. 23.
110. F. Liu, S. Shao, X. Guo, Y. Zhao and Z. Xie, *Efficient polymer photovoltaic cells using solution-processed MoO<sub>3</sub> as anode buffer layer*, Solar Energy Materials and Solar Cells **94** (2010), no. 5, 842-845.
111. Y. Sun, J. H. Seo, C. J. Takacs, J. Seifert and A. J. Heeger, *Inverted polymer solar cells integrated with a low-temperature-annealed sol-gel-derived ZnO film as an electron transport layer*, Advanced Materials **23** (2011), no. 14, 1679-+.

112. Y. Sun, C. J. Takacs, S. R. Cowan, J. H. Seo, X. Gong, A. Roy and A. J. Heeger, *Efficient, air-stable bulk heterojunction polymer solar cells using MoO<sub>x</sub> as the anode interfacial layer*, *Advanced Materials* **23** (2011), no. 19, 2226-+.
113. T. Y. Chu, S. W. Tsang, J. Y. Zhou, P. G. Verly, J. P. Lu, S. Beaupre, M. Leclerc and Y. Tao, *High-efficiency inverted solar cells based on a low bandgap polymer with excellent air stability*, *Solar Energy Materials and Solar Cells* **96** (2012), no. 1, 155-159.
114. C. E. Small, S. Chen, J. Subbiah, C. M. Amb, S. W. Tsang, T. H. Lai, J. R. Reynolds and F. So, *High-efficiency inverted dithienogermole-thienopyrrolodione-based polymer solar cells*, *Nature Photonics* **6** (2012), no. 2, 115-120.
115. S. Chen, C. E. Small, C. M. Amb, J. Subbiah, T.-h. Lai, S.-W. Tsang, J. R. Manders, J. R. Reynolds and F. So, *Inverted polymer solar cells with reduced interface recombination*, *Advanced Energy Materials* **2** (2012), no. 11, 1333-1337.
116. J. Wu, X. Y. Guo and Z. Y. Xie, *Effects of the molybdenum oxide/metal anode interfaces on inverted polymer solar cells*, *Chinese Physics Letters* **29** (2012), no. 9.
117. J. Liu, S. Y. Shao, G. Fang, B. Meng, Z. Y. Xie and L. X. Wang, *High-efficiency inverted polymer solar cells with transparent and work-function tunable MoO<sub>3</sub>-Al composite film as cathode buffer layer*, *Advanced Materials* **24** (2012), no. 20, 2774-2779.



118. K. Zilberberg, A. Behrendt, M. Kraft, U. Scherf and T. Riedl, *Ultrathin interlayers of a conjugated polyelectrolyte for low work-function cathodes in efficient inverted organic solar cells*, *Organic Electronics* **14** (2013), no. 3, 951-957.
119. C. Bracher, H. N. Yi, N. W. Scarratt, R. Masters, A. J. Pearson, C. Rodenburg, A. Iraqi and D. G. Lidzey, *The effect of residual palladium catalyst on the performance and stability of pcdtbt:Pc70bm organic solar cells*, *Organic Electronics* **27** (2015), 266-273.
120. S. R. Hammond, J. Meyer, N. E. Widjonarko, P. F. Ndione, A. K. Sigdel, A. Garcia, A. Miedaner, M. T. Lloyd, A. Kahn, D. S. Ginley, J. J. Berry and D. C. Olson, *Low-temperature, solution-processed molybdenum oxide hole-collection layer for organic photovoltaics*, *Journal of Materials Chemistry* **22** (2012), no. 7, 3249-3254.
121. X. Li, W. C. H. Choy, F. Xie, S. Zhang and J. Hou, *Room-temperature solution-processed molybdenum oxide as a hole transport layer with ag nanoparticles for highly efficient inverted organic solar cells*, *Journal of Materials Chemistry A* **1** (2013), no. 22, 6614-6621.
122. K. H. Wong, K. Ananthanarayanan, J. Luther and P. Balaya, *Origin of hole selectivity and the role of defects in low-temperature solution-processed molybdenum oxide interfacial layer for organic solar cells*, *The Journal of Physical Chemistry C* **116** (2012), no. 31, 16346-16351.

123. C. Yao, X. J. Xu, J. S. Wang, L. L. Shi and L. D. Li, *Low-temperature, solution-processed hole selective layers for polymer solar cells*, *Acs Applied Materials & Interfaces* **5** (2013), no. 3, 1100-1107.
124. M. F. Xu, L. S. Cui, X. Z. Zhu, C. H. Gao, X. B. Shi, Z. M. Jin, Z. K. Wang and L. S. Liao, *Aqueous solution-processed MoO<sub>3</sub> as an effective interfacial layer in polymer/fullerene based organic solar cells*, *Organic Electronics* **14** (2013), no. 2, 657-664.
125. F. Z. Wang, Q. Xu, Z. A. Tan, D. P. Qian, Y. Q. Ding, L. J. Li, S. S. Li and Y. F. Li, *Alcohol soluble titanium(iv) oxide bis(2,4-pentanedionate) as electron collection layer for efficient inverted polymer solar cells*, *Organic Electronics* **13** (2012), no. 11, 2429-2435.
126. J. J. Jasieniak, J. Seifert, J. Jo, T. Mates and A. J. Heeger, *A solution-processed MoO<sub>x</sub> anode interlayer for use within organic photovoltaic devices*, *Advanced Functional Materials* **22** (2012), no. 12, 2594-2605.
127. Z. A. Tan, D. P. Qian, W. Q. Zhang, L. J. Li, Y. Q. Ding, Q. Xu, F. Z. Wang and Y. F. Li, *Efficient and stable polymer solar cells with solution-processed molybdenum oxide interfacial layer*, *Journal of Materials Chemistry A* **1** (2013), no. 3, 657-664.
128. K. H. Wong, K. Ananthanarayanan, J. Luther and P. Balaya, *Origin of hole selectivity and the role of defects in low-temperature solution-processed molybdenum oxide interfacial layer for organic solar cells*, *Journal of Physical Chemistry C* **116** (2012), no. 31, 16346-16351.

129. J. Griffin, A. J. Pearson, N. W. Scarratt, T. Wang, D. G. Lidzey and A. R. Buckley, *Organic photovoltaic devices incorporating a molybdenum oxide hole-extraction layer deposited by spray-coating from an ammonium molybdate tetrahydrate precursor*, *Organic Electronics* **15** (2014), no. 3, 692-700.
130. S. Mrowec and Z. Grzesik, *Oxidation of nickel and transport properties of nickel oxide*, *Journal of Physics and Chemistry of Solids* **65** (2004), no. 10, 1651-1657.
131. D. Adler and J. Feinleib, *Electrical and optical properties of narrow-band materials*, *Physical Review B* **2** (1970), no. 8, 3112-3134.
132. R. Betancur, M. Maymó, X. Elias, L. T. Vuong and J. Martorell, *Sputtered NiO as electron blocking layer in P3HT:PCBM solar cells fabricated in ambient air*, *Solar Energy Materials and Solar Cells* **95** (2011), no. 2, 735-739.
133. J. K. a. H. W. a. M. H. a. S.-W. Chang, *Effect of hole transporting layers on the performance of PCPDTBT:PCBM organic solar cells*, *Journal of Physics D: Applied Physics* **45** (2012), no. 12, 125102.
134. M. D. Irwin, J. D. Servaites, D. B. Buchholz, B. J. Leever, J. Liu, J. D. Emery, M. Zhang, J. H. Song, M. F. Durstock, A. J. Freeman, M. J. Bedzyk, M. C. Hersam, R. P. H. Chang, M. A. Ratner and T. J. Marks, *Structural and electrical functionality of NiO interfacial films in bulk heterojunction organic solar cells*, *Chemistry of Materials* **23** (2011), no. 8, 2218-2226.

135. Z. Yi Wang, S.-H. Lee, D.-H. Kim, J.-H. Kim and J.-G. Park, *Effect of NiO<sub>x</sub> thin layer fabricated by oxygen-plasma treatment on polymer photovoltaic cell*, *Solar Energy Materials and Solar Cells* **94** (2010), no. 10, 1591-1596.
136. K. X. Steirer, J. P. Chesin, N. E. Widjonarko, J. J. Berry, A. Miedaner, D. S. Ginley and D. C. Olson, *Solution deposited NiO thin-films as hole transport layers in organic photovoltaics*, *Organic Electronics* **11** (2010), no. 8, 1414-1418.
137. E. L. Ratcliff, J. Meyer, K. X. Steirer, N. R. Armstrong, D. Olson and A. Kahn, *Energy level alignment in PCDTBT:PC<sub>70</sub>BM solar cells: Solution processed NiO<sub>x</sub> for improved hole collection and efficiency*, *Organic Electronics* **13** (2012), no. 5, 744-749.
138. K. X. Steirer, P. F. Ndione, N. E. Widjonarko, M. T. Lloyd, J. Meyer, E. L. Ratcliff, A. Kahn, N. R. Armstrong, C. J. Curtis, D. S. Ginley, J. J. Berry and D. C. Olson, *Enhanced efficiency in plastic solar cells via energy matched solution processed NiO<sub>x</sub> interlayers*, *Advanced Energy Materials* **1** (2011), no. 5, 813-820.
139. M. S. Ryu and J. Jang, *Effect of solution processed graphene oxide/nickel oxide bi-layer on cell performance of bulk-heterojunction organic photovoltaic*, *Solar Energy Materials and Solar Cells* **95** (2011), no. 10, 2893-2896.
140. D. C. Lim, Y. T. Kim, W. H. Shim, A. Y. Jang, J.-H. Lim, Y. Do Kim, Y. Jeong, Y. D. Kim and K. H. Lee, *Wet-chemically prepared NiO layers as hole transport layer in the inverted organic solar cell*, *Bulletin of the Korean Chemical Society* **32** (2011), no. 3, 1067-1070.

141. K. H. Wong, K. Ananthanarayanan, M. D. Heinemann, J. Luther and P. Balaya, *Enhanced photocurrent and stability of organic solar cells using solution-based NiO interfacial layer*, *Solar Energy* **86** (2012), no. 11, 3190-3195.
142. J. Jung, D. L. Kim, S. H. Oh and H. J. Kim, *Stability enhancement of organic solar cells with solution-processed nickel oxide thin films as hole transport layers*, *Solar Energy Materials and Solar Cells* **102** (2012), no. 0, 103-108.
143. F. Jiang, W. C. H. Choy, X. Li, D. Zhang and J. Cheng, *Post-treatment-free solution-processed non-stoichiometric NiO<sub>x</sub> nanoparticles for efficient hole-transport layers of organic optoelectronic devices*, *Advanced Materials* **27** (2015), no. 18, 2930-+.
144. N. Sun, G. Fang, P. Qin, Q. Zheng, M. Wang, X. Fan, F. Cheng, J. Wan, X. Zhao, J. Liu, D. L. Carroll and J. Ye, *Efficient flexible organic solar cells with room temperature sputtered and highly conductive NiO as hole-transporting layer*, *Journal of Physics D-Applied Physics* **43** (2010), no. 44.
145. N. E. Widjonarko, E. L. Ratcliff, C. L. Perkins, A. K. Sigdel, A. Zakutayev, P. F. Ndione, D. T. Gillaspie, D. S. Ginley, D. C. Olson and J. J. Berry, *Sputtered nickel oxide thin film for efficient hole transport layer in polymer–fullerene bulk-heterojunction organic solar cell*, *Thin Solid Films* **520** (2012), no. 10, 3813-3818.
146. J. J. Berry, N. E. Widjonarko, B. A. Bailey, A. K. Sigdel, D. S. Ginley and D. C. Olson, *Surface treatment of NiO hole transport layers for organic solar cells*, *Selected Topics in Quantum Electronics, IEEE Journal of* **16** (2010), no. 6, 1649-1655.

147. C. Tao, S. Ruan, G. Xie, X. Kong, L. Shen, F. Meng, C. Liu, X. Zhang, W. Dong and W. Chen, *Role of tungsten oxide in inverted polymer solar cells*, Applied Physics Letters **94** (2009), no. 4, 043311-043313.
148. S. Han, W. S. Shin, M. Seo, D. Gupta, S.-J. Moon and S. Yoo, *Improving performance of organic solar cells using amorphous tungsten oxides as an interfacial buffer layer on transparent anodes*, Organic Electronics **10** (2009), no. 5, 791-797.
149. D. Han, S. Lee, H. Kim, S. Jeong and S. Yoo, *Cathodic multilayer transparent electrodes for ITO-free inverted organic solar cells*, Organic Electronics **14** (2013), no. 6, 1477-1482.
150. S. Schumann, R. Da Campo, B. Illy, A. C. Cruickshank, M. A. McLachlan, M. P. Ryan, D. J. Riley, D. W. McComb and T. S. Jones, *Inverted organic photovoltaic devices with high efficiency and stability based on metal oxide charge extraction layers*, Journal of Materials Chemistry **21** (2011), no. 7, 2381-2386.
151. I. Oh, G. Kim, S. Han and S. Oh, *PEDOT:PSS-free organic photovoltaic cells using tungsten oxides as buffer layer on anodes*, Electronic Materials Letters **9** (2013), no. 4, 375-379.
152. N. Li, T. Stubhan, N. A. Luechinger, S. C. Halim, G. J. Matt, T. Ameri and C. J. Brabec, *Inverted structure organic photovoltaic devices employing a low temperature solution processed WO<sub>3</sub> anode buffer layer*, Organic Electronics **13** (2012), no. 11, 2479-2484.

153. H. Choi, B. Kim, M. J. Ko, D.-K. Lee, H. Kim, S. H. Kim and K. Kim, *Solution processed WO<sub>3</sub> layer for the replacement of PEDOT:PSS layer in organic photovoltaic cells*, *Organic Electronics* **13** (2012), no. 6, 959-968.
154. T. Stubhan, N. Li, N. A. Luechinger, S. C. Halim, G. J. Matt and C. J. Brabec, *High fill factor polymer solar cells incorporating a low temperature solution processed WO<sub>3</sub> hole extraction layer*, *Advanced Energy Materials* **2** (2012), no. 12, 1433-1438.
155. Z. A. Tan, W. Q. Zhang, C. H. Cui, Y. Q. Ding, D. P. Qian, Q. Xu, L. J. Li, S. S. Li and Y. F. Li, *Solution-processed vanadium oxide as a hole collection layer on an ITO electrode for high-performance polymer solar cells*, *Physical Chemistry Chemical Physics* **14** (2012), no. 42, 14589-14595.
156. Y.-M. Chang and J.-M. Ding, *High efficiency inverted polymer solar cells with the sol-gel derived vanadium oxide interlayer*, *Thin Solid Films* **520** (2012), no. 16, 5400-5404.
157. K. Zilberberg, S. Trost, H. Schmidt and T. Riedl, *Solution processed vanadium pentoxide as charge extraction layer for organic solar cells*, *Advanced Energy Materials* **1** (2011), no. 3, 377-381.
158. W. Z. Xu, Y. T. Liu, X. J. Huang, L. L. Jiang, Q. D. Li, X. Q. Hu, F. Huang, X. Gong and Y. Cao, *Solution-processed VO<sub>x</sub> prepared using a novel synthetic method as the hole extraction layer for polymer solar cells*, *Journal of Materials Chemistry C* **4** (2016), no. 10, 1953-1958.

159. E. Bovill, N. Scarratt, J. Griffin, H. Yi, A. Iraqi, A. R. Buckley, J. W. Kingsley and D. G. Lidzey, *The role of the hole-extraction layer in determining the operational stability of a polycarbazole: Fullerene bulk-heterojunction photovoltaic device*, Applied Physics Letters **106** (2015), no. 7.
160. K. Takanezawa, K. Tajima and K. Hashimoto, *Efficiency enhancement of polymer photovoltaic devices hybridized with ZnO nanorod arrays by the introduction of a vanadium oxide buffer layer*, Applied Physics Letters **93** (2008), no. 6, 063308-063303.



# Chapter 3

## Experimental Techniques and Methods

### 3.1 Introduction

In this chapter the procedures for OPV devices preparation and the various techniques employed throughout this work are discussed. In Section 3.2 the materials used in this thesis are described with more details regarding the solutions, thin films and device preparations. Due to the deposition thin films from solution is highly desirable for the commercialisation of organic PV technology; most of the thin layers in this work were prepared by solution processed methods. The different experimental techniques used are then discussed in section 3.3 to study the properties of the thin films (e.g. electrical and optical properties, chemical state, topography and film thickness) and probe OPV device performance.

### 3.2 Experimental Techniques

#### 3.2.1 Ultraviolet Photoelectron Spectroscopy

In photoelectron spectroscopy, the binding energy of occupied electronic states of materials can be measured with respect to the Fermi level ( $E_F$ ) of the instrument and the vacuum level. Therefore, any electron in the occupied states should absorb enough

energy to exceed its atom or molecule ionisation limit so that it can escape the binding forces of that atom or molecule. Thus, the ionisation energy can be defined as the minimum energy required for an electron to become liberated. When the molecules of a surface are illuminated by a photon with sufficient energy ( $h\nu$ ), an excited electron escapes the surface possessing a kinetic energy that is equal to the excess energy from photoionisation [1, 2]. The kinetic energy  $E_k$  of the emitted electron is given by the Einstein relation,

$$E_k = h\nu - E_b \quad (3.1)$$

where  $E_b$  is the binding energy of the electron before excitation. Therefore, the work function of a metal  $\Phi_m$  can be calculated from the maximum kinetic energy  $E_{max}$  of its electrons with the following relation [3, 4]:

$$\Phi_m = h\nu - E_{max} \quad (3.2)$$

In the majority of molecules, the first ionisation energies are usually high, exceeding 9 eV. Therefore, ultraviolet light of wavelengths of  $\leq 140$  nm is required to reach the first ionisation limit [1, 5]. A He gas discharge lamp is often used for generating photons with an energy of 21.22 eV (He I) or 40.8 eV (He II) depending on the ionisation state of the gas. This lamp is also preferred for its small line width of about 20 meV, because this width will produce higher resolution spectra of the valence levels. **Figure 3.1** shows the basic geometry of an ultraviolet photoelectron spectroscopy chamber. The ejected electrons pass a hemispherical or an electrostatic analyser by following a specific curved path into the exit slits under selected voltages on the analyser.

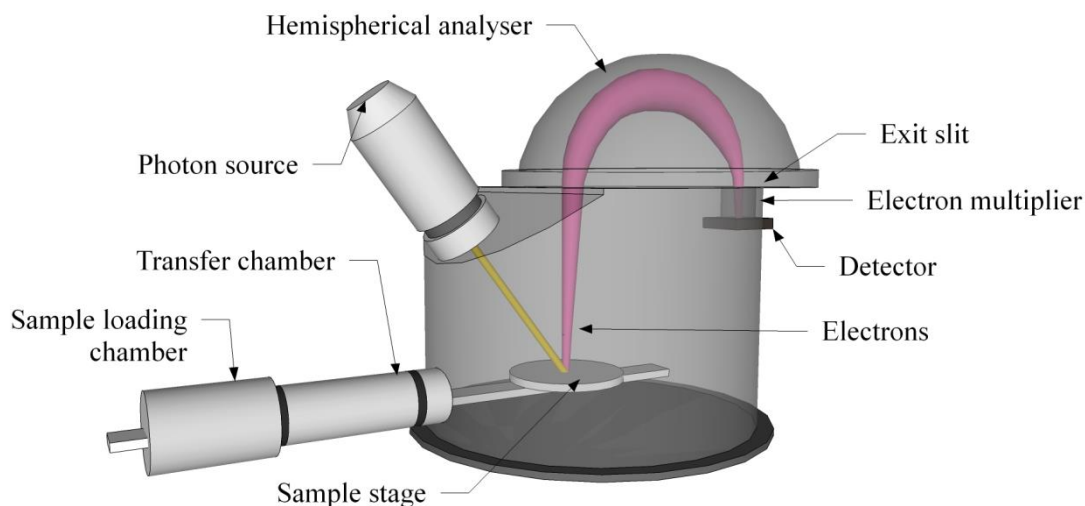


**Figure 3.1** Schematic of a photoelectron spectrometer with an electrostatic electron energy analyser used for XPS and UPS investigation.

The other electrons with higher or lower kinetic energies vanish by colliding with the wall at various trajectories depending on the strength of the electric field. The electric field applied on the analyser generates a magnetic field in which the emitted electrons that pass through the hemispherical analyser will experience the Lorentz force [2, 6]. The equation for the Lorentz and centripetal force acting upon an electron is given by the following equations, respectively:

$$\mathbf{F} = e\bar{v} \times \bar{\mathbf{B}} \quad (3.3)$$

$$F = \frac{m_e v^2}{r} \quad (3.4)$$

where  $r$  is the radius of the analyser,  $e$  is the elementary charge and  $B$  is the applied magnetic field. These equations allow us to determine the kinetic energy of an electron that passes through the hemispherical analyser from the applied magnetic field alone. An electron multiplier tube is used to amplify the signal and then the a detector

measures the electron current as a function of the voltage applied for obtaining the given spectrum of kinetic energy. To acquire precise measurements, the photoelectron spectrometer must be kept under a high vacuum [5, 7]. The investigated sample is usually a thin sample, because thicker films might accumulate a positive charge at the sample surface after the liberation of the negatively charged electrons. A typical binding energy spectrum for a material measured by UPS is displayed in **Figure 3.2(a)**.

Determination of the energy positions of the UPS features can be used to measure the work function of a material, the Fermi level, the valence band or HOMO position, and density of occupied states close to the Fermi level. These characteristics are significant for a better understanding of how charge carriers will behave at an interface. The low energy cut-off position of the secondary electron emission is used for calculating the work function. This position represents the highest binding energy of the measured secondary electrons. This point can be determined by linear fit the high binding energy portion of the spectrum to the energy axis as shown in **Figure 3.2(b)**. The physical interpretation behind this emission is due to the fact that emitted electrons undergo inelastic scattering before reaching the surface leading to further energy loss besides their bound orbital energy. Therefore, the work function of some material depends on the maximum amount of energy required for an electron to overcome both the binding energy from which it originates and the loss of energy. The work function ( $\Phi$ ) can be then calculated by the following equation:

$$\Phi = h\nu - E_{cut-off} \quad (3.5)$$

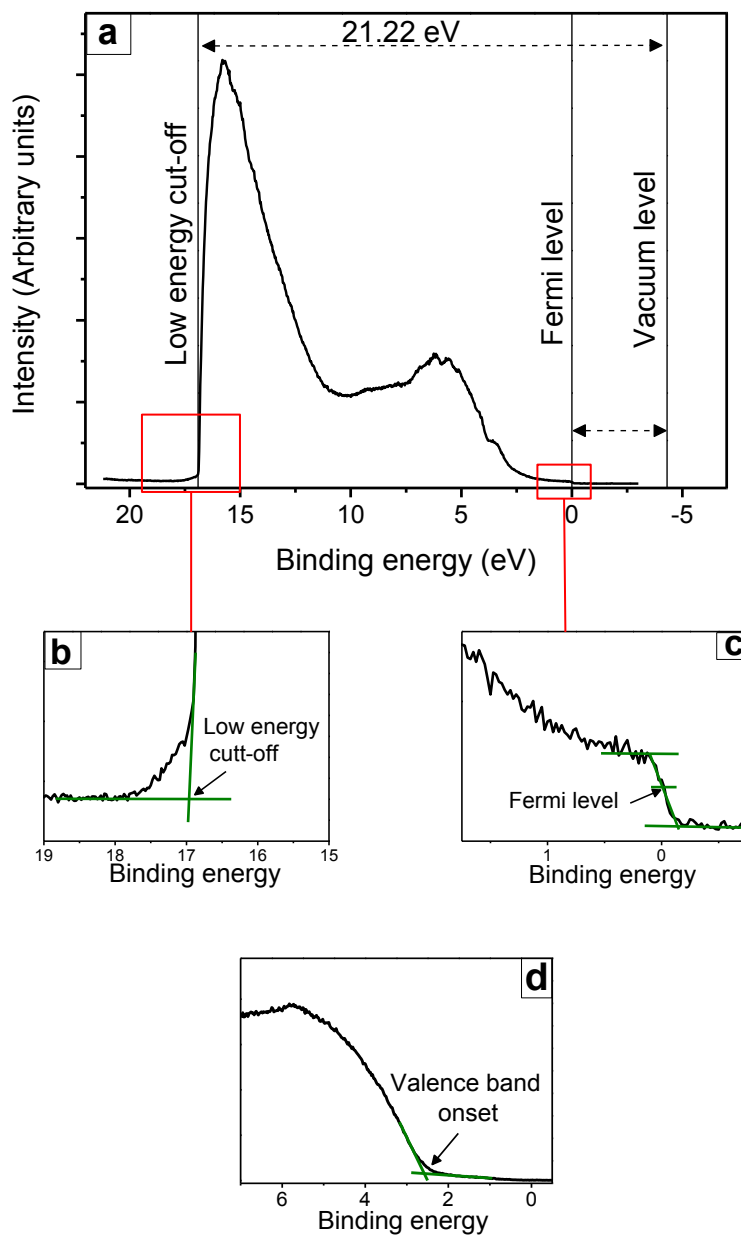


**Figure 3.2** (a) An example of an UPS spectra, (b) the low energy cut-off (c) the Fermi level of a metal (d) valence band or HOMO onset for a semiconductor.

The Fermi level (i.e. of sample and instrument) is used as a reference point and calibrated to zero binding energy for an accurate scale. The Fermi level position within a material can vary depending on the tested material. The high density of occupied states in metals extends to the Fermi level and thus determination of the Fermi level

position is fairly simple, see **Figure 3.2(c)**. If the surface is composed of semiconducting material, determination the Fermi level position is difficult due to the lack of density of states between the Fermi level and the valence band edge. The position of the valence level can be used for calculating ionization potential of the semiconductor. For organic semiconductors the ionization potential represents the lowest binding energy (i.e. HOMO level) and can be determined by linear extrapolating of the low binding energy edge to the energy axis, see **Figure 3.2(d)**. Valence band onset or HOMO features in UPS spectra originate due to primary electron emission as these electrons are emitted from the sample without any of scattering events occurring. UPS data reported in this thesis has been analysed using CasaXPS software package, data has then been exported to Origin graphing software to create plots and perform smoothing of the spectra.

### 3.2.2 X-ray Photoelectron Spectroscopy

XPS is a similar technique to UPS, because XPS likewise depends on photoelectron emission; however, it creates higher excitation energy. The most commonly used photon sources for XPS are the monochromatised  $K_{\alpha}$  radiation from bombarding aluminium or magnesium targets. These sources generate Al  $K_{\alpha}$  and Mg  $K_{\alpha}$  lines peaks at 1486.6 eV and 1254.6 eV, respectively [2, 8]. The relatively high photon energy of the XPS (i.e., X-ray) can excite the inner shell electrons with kinetic energy ( $E_k$ ). By knowing the work function of the sample, the binding energy of the excited electrons can be calculated to identify the chemical elements of the sample. Therefore, any change in the chemical structure of the specimen probed by XPS can result in a small shift in the binding energy of a core-level electron due to the redistribution of HOMO energy level charges. The minimum binding energy that can be observed by high

resolution scans is around 100 eV because lower binding energies cannot be detected due to the low intensity of emission. For instance, most samples can be contaminated by atmospheric gases (Carbon, Nitrogen and Oxygen elements). Therefore, binding energies of the 2s and 2p orbitals of these elements cannot be measured as these energies are in the low intensity region of the XPS spectra. The binding energy of these emissions (i.e. 284.2eV, 409.9eV and 543.1eV, respectively) can be only observed from 1s-orbitals [8, 9].

A typical XPS spectrum is a plot of intensity versus binding energy, which shows a set of peaks that are related to the concentration of the element in the examined region. Therefore, XPS provides both qualitative and quantitative analyses of the chemical composition in the studied sample. Because of its ability in surface chemical analysis, XPS is also known as ESCA (Electron Spectroscopy for Chemical Analysis) [10]. In order to determine the chemical state (e.g. the oxidation state in metal oxides) of an examined material, the spectral line must be broken down into several individual Gaussian peaks offset. This process requires a background correction to reduce the background spectra caused by the secondary electrons. The linear, Shirley and Tougaard backgrounds are the most commonly used background corrections. While Tougaard backgrounds are useful for estimating the background intensity over large regions, The Shirley background is a very powerful background for calculating the area for electrons with energies above and below the peak energy [11, 12, 13].

**Figure 3.3** (a) shows an example of  $V_2O_5$  XPS spectra before correction along with the background intensity. **Figure 3.3**(b) shows the spectra after correction by a Shirley background method with several peaks fitted corresponding to different chemical states that that the element is within. It has been observed that shifts in the binding energy can

occur due to changes within the oxidation state and the surrounding environment effects. This shift results from the change in the electromagnetic forces between the outer electrons and the core levels [8, 14]. Furthermore, calibration is sometimes needed to determine peak position in an XPS spectrum. C1s peak at 285 eV from carbon adsorbed on the sample surface is commonly used for calibrating an XPS spectrum.

The UPS and XPS measurements in this report were achieved with Kroto Ultra AXIS photoelectron spectroscopy. Al(K $\alpha$ ) radiation with an energy of 1486.6 eV was used for XPS as the excitation source with a line width of less than 1.0 eV to ensure good energy resolution. The energy stop and the pass energy were measured at 10 eV and 0.025 eV, respectively. The aperture size was adjusted at 110  $\mu$ m. The dwell time was 250 ms (dwell time is the duration of each analysis step; the higher the dwell time means the higher the number of detected electrons).

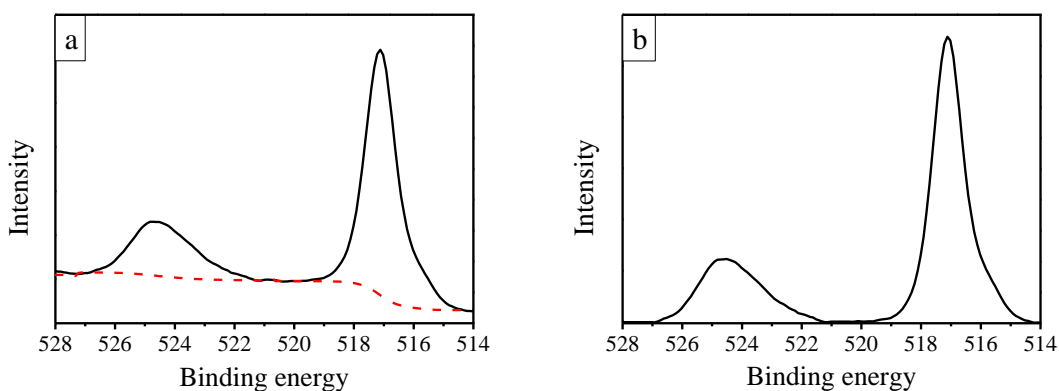


**Figure 3.3** (a) an XPS spectrum with a Shirley background and (b) the spectrum after removal of background with fitted peaks.



### 3.2.3 Atomic Force Microscopy

Atomic Force Microscopy (AFM) is a scanning probe microscopy technique capable of detailed surface topography with atomic resolution. The technique relies upon interactions between an atomically sharp tip and the surface where a cantilever with a sharp tip on one end is scanned across the surface of a sample. The magnitudes of cantilever forces are monitored as a function of the tip position on the specimen surface. AFM can operate by keeping the tip in direct contact with the sample surface throughout the measurement (i.e., contact mode) or by oscillating the cantilever between the tip and the sample due to the long-range attractive van der Waals interactions (i.e., tapping mode) [15]. In contact mode, the tip is deflected by short-range repulsive interactions between the sample and tip. These deflections are typically related to the height and measured with a beam deflection system. In tapping mode, the tip is oscillated at a constant height above the surface, typically 10-100 nm. The AFM studies in this work were conducted with the tapping mode to keep the samples from becoming contaminated and to prevent the tip from degrading the surface.

**Figure 3.4** shows a schematic of the basic arrangement of an AFM components. The cantilever is vibrated near the surface of a sample with distance of the order of nanometers and close to its resonant frequency. The scanner height along the sample surface is adjusted by a number of piezoelectric drivers. The changes in the distance between the tip and the surface are detected optically by using a focused laser beam that is reflected from the surface of the cantilever and measuring the position of the laser spot using a quadrant photodiode. An electronic feedback loop can be used to keep the oscillation amplitude constant. A map of the sample surface topography is generated by recording the relative height of the scanner at each position in the specimen.

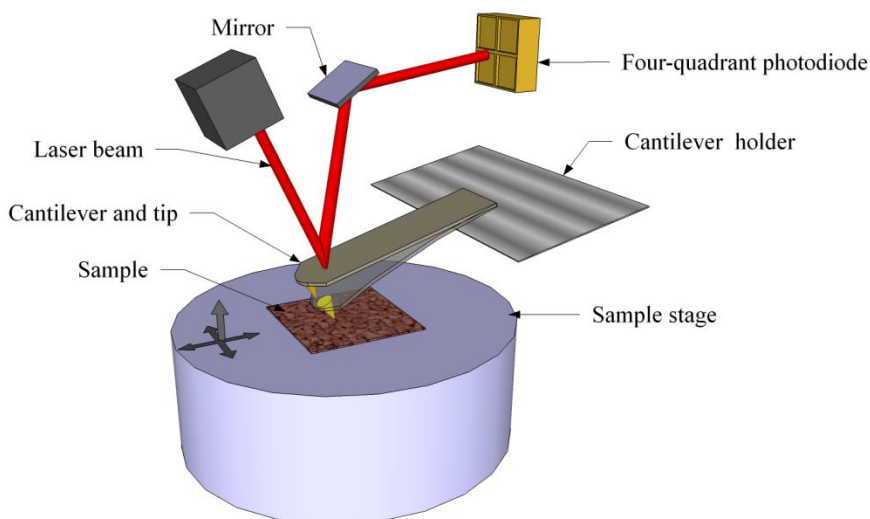


**Figure 3.4** Simplified schematic of the principal components in an AFM. The cantilever was connected to a piezoelectric component to enable smooth contact with the sample surface.

In addition, the phase imaging provides information about the surface properties, such as friction and adhesion, by measuring the phase shift of the oscillating cantilever relative to the driving signal [16, 17]. The image resolution is highly dependent on the sharpness of the tip, resolutions of  $0.1 \text{ \AA}$  in the x and y directions and  $0.01 \text{ \AA}$  perpendicular to the surface are possible with an atomically sharp tip.

A Veeco Instruments Dimension 3100 was used to perform the AFM. Aluminium coated silicon tips from Budget Sensors (Tap 300 Al-G) with a resonance frequency of 300 kHz and a spring constant of  $40 \text{ N m}^{-1}$  were used throughout. The obtained data were processed using the Gwyddion software package.

### 3.2.4 Spectrofluorometer

Absorption measurements were conducted under ambient conditions using a Horiba Fluoromax 4 spectrometer. A schematic of the Fluoromax 4 is displayed in **Figure 3.5**.

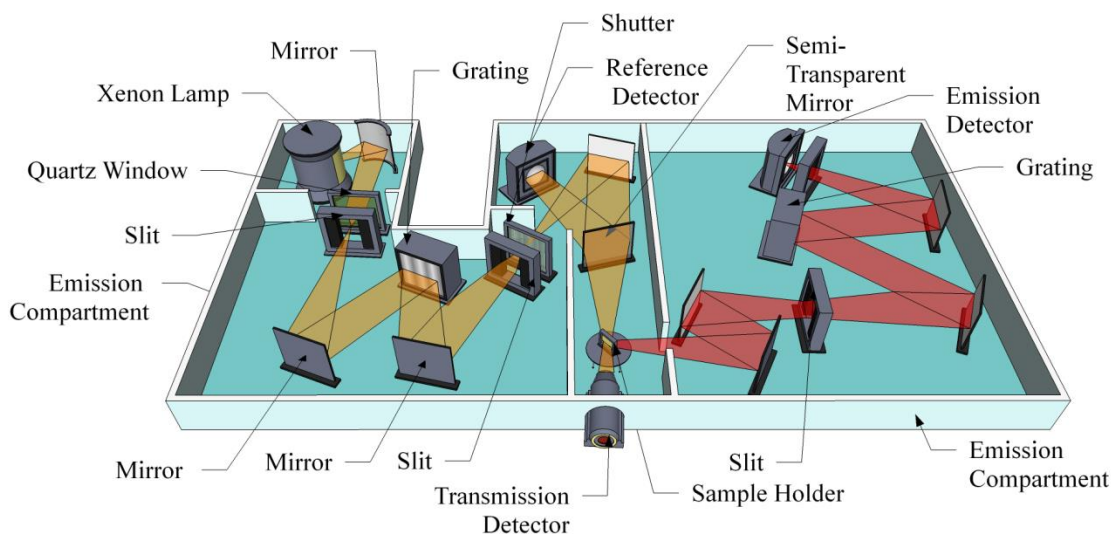


**Figure 3.5** Schematic of the optical components of the Horiba Fluoromax 4. The instrument is divided into two main components; the excitation part on the right with the beam defined in red and emission part defined in orange on the left.

A xenon arc lamp (200 to 950 nm) is focused onto the entrance slit of the excitation monochromator by an elliptical mirror. The slits determine the bandpass of the light and their width is adjustable by the computer in units of millimetres to provide high resolution and instant reproducibility. In the excitation monochromator the beam is diffracted by a blazed grating (1,200 grooves/mm) which fits through another slit. Before the excitation light reaches the sample, a silicon photodiode reference detector monitors the intensity as a function of time and wavelength. A silicon photodiode was placed upon a sample in the path of the sample light incident to measure the intensity of the transmitted light. Therefore, it is possible to calculate the transmittance of a sample and hence its absorbance. The absorbance  $A$  is given by the Beer-Lambert relationship,

$$A = -\log_{10} \left[ \frac{I(\lambda)}{I_0(\lambda)} \right] \quad (3.6)$$

where  $I(\lambda)$  is the intensity of light transmitted, and  $I_o(\lambda)$  is the intensity of light incident upon the sample. Both transmittance spectra were normalised against the power output recorded by the reference detector to account for any potential variations in light output between the separate measurements. Transmittance and absorbance of all the samples in this work were measured with the range 300-900 nm in increments of 2 nm and a slit size of 2 nm.

### 3.2.5 Spectroscopic Ellipsometry

Spectroscopic ellipsometry is an optical technique for investigating the optical properties (i.e. the refractive index ( $n$ ) and the extinction coefficient ( $k$ )) and thickness of thin films by measuring the change in polarisation and phase of a light beam reflected from a sample relative to the incident radiation [18, 19]. In this work, a J A Wollam M2000v instrument was used for measuring the thicknesses of investigated metal oxides and its schematic is displayed in **Figure 3.6**.

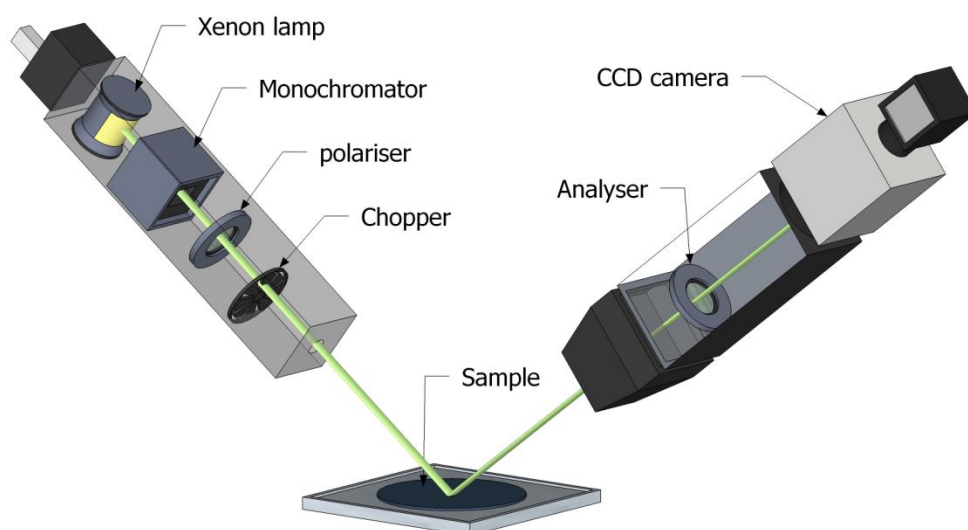


**Figure 3.6** Schematic of a spectroscopic ellipsometer with the two components; the light source on the right and the analyser on the left.

In this technique, a xenon lamp generates light with a broad wavelength (370-1000 nm) that passes through a monochromator, polariser, and then mechanical chopper, after which it falls onto the sample. The reflected light passes through another polarising filter, which is the analyser, and falls into a detector. The polarisation state of the reflected light can be discovered by characterising two components,  $r_s$  and  $r_p$ , which represent the amplitude of the light oscillating perpendicular and parallel to the plane of incidence, respectively. Therefore, the reflectance ratio  $\rho$  can be defined as the ratio of  $r_s$  to  $r_p$  as in the following equation [19, 20]:

$$\rho = \frac{r_s}{r_p} = \tan \Psi e^{i\Delta} \quad (3.7)$$

$\Psi$  and  $\Delta$  are the ratio of amplitudes and the change in phase, respectively, that can determine the thickness and complex refractive index of the sample. Ellipsometry cannot measure directly the thickness or optical properties of a material. Therefore a model is used to approximate the structure of the sample being measured. Properties such as the thickness of these layers and the complex refractive index can then be varied to determine values for  $\Delta$  and  $\Psi$ . These calculated values can then be compared against the values measured experimentally, in order to obtain the most accurate value. An iterative process of changing the values is used to obtain the minimum least-square error when matching the simulated data against the experimentally measured data.

Practically,  $\Psi$  and  $\Delta$  of the Si and SiO<sub>2</sub> layers of a substrate should be measured to be used as reference data before modelling the sample.

Film thicknesses were estimated using a Cauchy dispersion model as shown in the following relationship [21, 22]:

$$n = A + \frac{B}{\lambda^2} + \frac{C}{\lambda^4} \quad (3.8)$$

$n$  is the real part of the refractive index.  $A$ ,  $B$  and  $C$  are positive constants that are adjusted to match the refractive index for the material. However, this model does not take account of the absorbing region of a material. To expand this model to a wider region of the spectrum additional Lorentz oscillator component can be used to model the complex part of the refractive index which can be written in the following form [23, 24]

$$\tilde{\varepsilon}(E) = \varepsilon_{offset} + \frac{AE_c}{E_c - E^2 - iBE} \quad (3.9)$$

where  $E$  is the photon energy,  $A$  is the amplitude,  $B$  is the broadening of the oscillator peak,  $E_c$  is the energy of the peak and  $\varepsilon_{offset}$  represents the offset for the real part of the dielectric constant. The ellipsometry data in this work was collected and modelled by the CompleteVASE software package.

#### 3.2.6 Electrical Characterisation of Devices

The power conversion efficiency (PCE) of a PV device was determined by measuring photocurrent or current density as a function of applied bias. A test board was placed beneath a Newport 92251A-1000 Solar Simulator that generates light with an output of  $1000 \text{ W/m}^2$  and consistent with the standard solar spectra of AM1.5. An NREL calibrated silicon diode was used to calibrate the power output of the solar simulator. An OPV device was connected to a test board designed by Ossila Ltd as shown in **Figure 3.7**. The test board was connected to a Keithly 237 source measure unit by a BNC connection, controlled via a MATLAB program, to measure the current from the OPV as a function of applied bias. For accurate calculation OPV devices were measured

by using an aperture mask to determine an area of illumination as shown in **Figure 3.7**. Each pixel aperture in the mask is square-shaped and has an area of  $0.0256 \text{ cm}^2$  as quoted by the manufacturer.

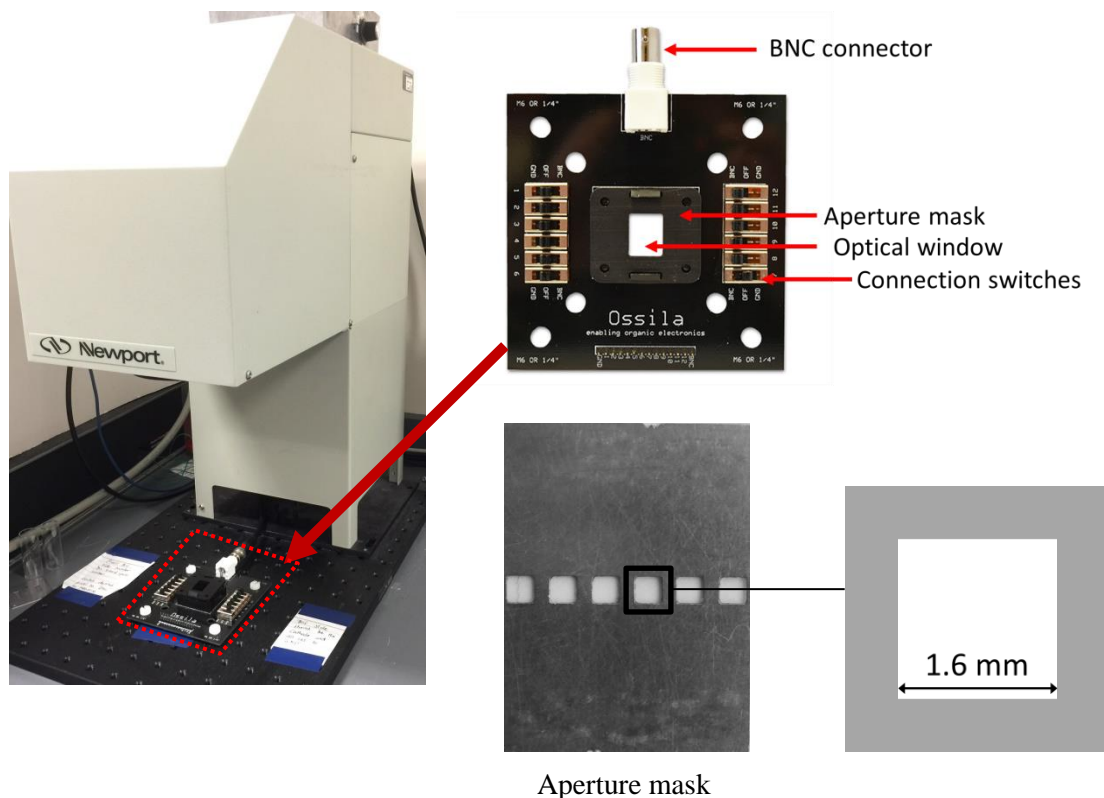


**Figure 3.7** Newport 92251A-1000 Solar Simulator that generates an AM1.5 output radiation (left). The aperture mask used for OPV characterization (right).

### 3.2.7 Laser Beam Induced Current Mapping (LBIC)

Laser Beam Induced Current Mapping (LBIC) is a spatially resolved method that provides information about the local efficiency distribution of an individual pixel in OPV devices. The generated images can be used to understand the processes responsible for poor efficiency and OPV degradation such as local defects, weak

interconnections and crystal grain boundaries [25]. **Figure 3.8** shows the basic principle of the LBIC operating where a point by point scanning is run across the surface of a specimen. The LBIC system in this work was developed by Mr. Nick Scarratt. In this setup, a laser beam with a wavelength of 405 nm and a power of 4 mW was focused by a 50X Mitutoyo infinity-corrected objective lens. The lens was mounted onto a z-axis translation stage to reduce spot size width to the minimum possible ( $< 5 \mu\text{m}$ ).

An OPV device was placed beneath the lens holder and was mounted onto x-y stage where the pixel position was controlled by the computer. The focused laser beam was scanned line by line across the surface. The incident beam at some point on the surface generated electrical current which was measured and normalised to the incident light intensity for producing a current map. A model SR830 lock-in amplifier was used to remove the generated noise signals. All the components were controlled by LabView computer program for collecting data.

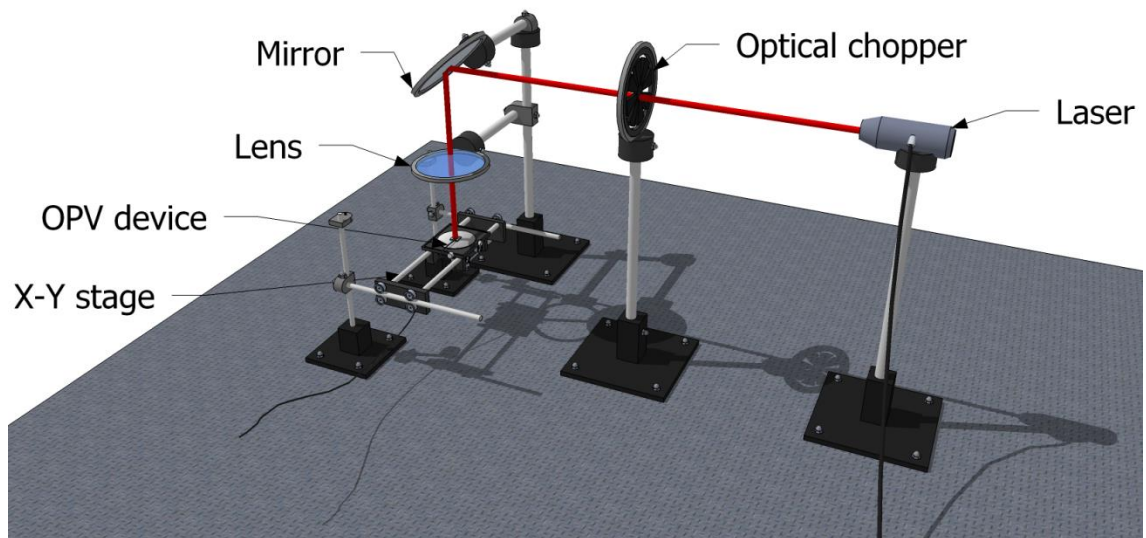


**Figure 3.8** Laser Beam Induced Current Mapping (LBIC) Setup.



### 3.2.8 The Lifetime Tester

The laboratory lifetime testing setup used in this work was an ATLAS suntest CPS+ model, see **Figure 3.9(a)**. CPS+ consists of a fully mirror-coated test chamber with exposure area inside the chamber of 560 cm<sup>2</sup>. A 1500 W air-cooled Xenon Lamp was used with fan-controlled temperature from 45-100 °C. The lamp was modified with quartz filters to match output radiation at the wavelength range 300-800 nm. The output spectrum was measured by a calibrated StellarNet Inc. Blue Wave USB spectrometer. Furthermore, by tuning the irradiance power from 350 Wm<sup>-2</sup> to 750 Wm<sup>-2</sup>, it was found that the power of 550 Wm<sup>-2</sup> shows 1 sun intensity (1000Wm<sup>-2</sup>).

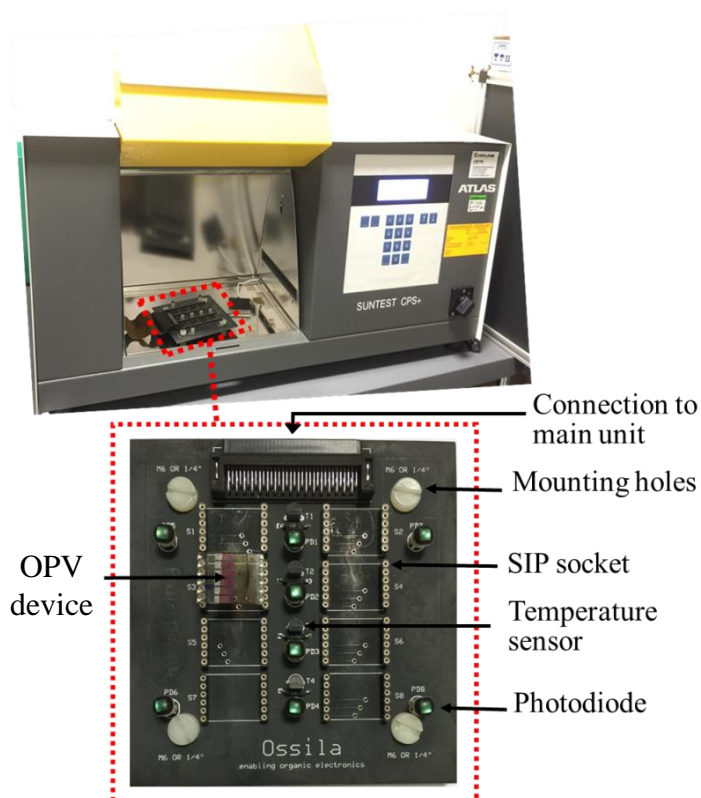


**Figure 3.9** (a) Image of an ATLAS suntest CPS+ model. (b) The circuit board containing temperature and photodiodes sensors that was used for measuring up to 8 devices.

A custom-made test board with temperature and photodiodes sensors was built by Ossila Ltd for testing up to eight OPV devices as shown in **Figure 3.9(b)**. Metal legs were used to connect the devices to SIP (Single Inline Package) sockets in the test board which is connected to the multiplexing unit for measuring 48 pixels independently. IV characterisation and temperature readings were achieved by using a Keithley 2400 source-measure unit. All the components and *JV* measurements are controlled by a MATLAB program. Calibration of the whole lifetime setup and writing the MATLAB program were carried out by Dr. Edward Bovill.

### 3.2.9 Thermal Evaporator

Thermal evaporation technique offers an excellent method for building multistacked layers, atom by atom, on a solid surface. Despite its disadvantages, such as time and energy consumption, a vacuum based thermal evaporator offers excellent control of the deposition process. Vacuum deposition technique allows atoms to evaporate at a relatively lower temperature and move in a straight path to the target. The evaporator used in this work was just employed for metals and metal oxides deposition to avoid any contamination resulting from other materials such as small molecules polymers. The thermal evaporator was attached to a nitrogen filled glovebox to keep deposited films from exposure to atmospheric gases. In addition, the chamber used had 3 sources allowing the build up of multilayer films without the need to vent the chamber. To deposit the required material on a specific area of pixel, substrates are placed on a stainless steel evaporation mask that was designed to fit the pixelated substrates as displayed in **Figure 3.10**. Subsequently, crucibles with required material are heated gradually by a tungsten coil in high vacuum of  $10^{-7}$  mbar to  $10^{-6}$  mbar. When the material evaporating starts, the shutter is kept closed until a required deposition rate is obtained

and also to allow evaporation of any contaminants that may be present in the crucible. A calibrated quartz crystal microbalance is used for monitoring deposition rate and deposited layer thickness. The deposition rate ranges between  $0.3 \text{ \AA s}^{-1}$  and  $1.2 \text{ \AA s}^{-1}$  depending on the evaporated material. After deposition, the chamber is left to cool before venting.

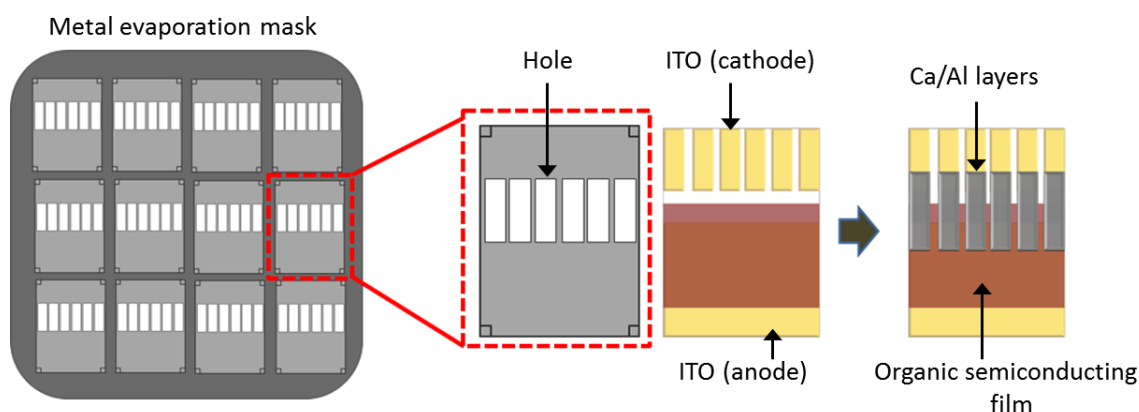


**Figure 3.10** Cathode evaporation mask for deposition of desired material over a determined area of the substrate.

### 3.2.10 Solution Deposition Technique

Fabricating thin films by solution-processed methods offers a low-energy-consuming and low-cost technique. Furthermore, a wide variety of substrates can be used in a controlled way with this technique which can be scaled up to roll-to-roll or sheet-to-sheet based deposition techniques. The spin-coating deposition method is the simplest process that has been used widely for laboratory purposes. It produces flat surfaces with good uniformity allowing an effective repeatable method. Film thickness can be finely controlled by the spin speed. In this technique a substrate is held in the chuck of the spin coater and then accelerated rotation starts. At the desired speed a small amount of solution (i.e. in the range  $20\mu\text{l}$ - $40\mu\text{l}$ ) of selected material is dispensed onto the surface

by a micropipette. This kind of spin coating was used in this work for most of the materials and is called dynamic dispense spin coating technique. Otherwise, dispensing a solution (e.g. PEDOT:PSS) was achieved before starting the spin rotation and this is called static dispense spin coating technique. In both methods the material spreads over the entire surface by centrifugal force and solvent evaporation rate depends on the rotational velocity and the boiling point of the solvent. In addition, dispensing the solution should be done on the centre of the substrate and close to the surface to avoid creating an uncoated spot in the middle.

The film thickness depends on the spin speed, the concentration of the solution, the viscosity of the solvent and their effect can be described in the following equation [26, 27]:

$$t \propto \frac{cv(c)}{\sqrt{\omega}} \quad (3.10)$$

where  $t$  is the film thickness,  $c$  is the solution concentration,  $v(c)$  is the solution viscosity and  $\omega$  is the spin speed. For example, in this work different concentrations of vanadium (V) Isopropoxide solution were prepared by diluting with IPA. **Figure 3.11** shows how the concentration of solution and spin speed determine the thickness of the film. However, spin coating technique suffers from some disadvantages such as fabrication of one thin film at a time, and the impossibility of coating large surfaces (i.e. limited scalability). In addition, it is an extremely wasteful process as a large amount of deposited solution is expelled from the substrate.

An alternative deposition method is a spray coating technique which can be used for coating large surfaces and producing a uniform thin film. **Figure 3.12** shows the typical schematic of the ultrasonic spray coater.

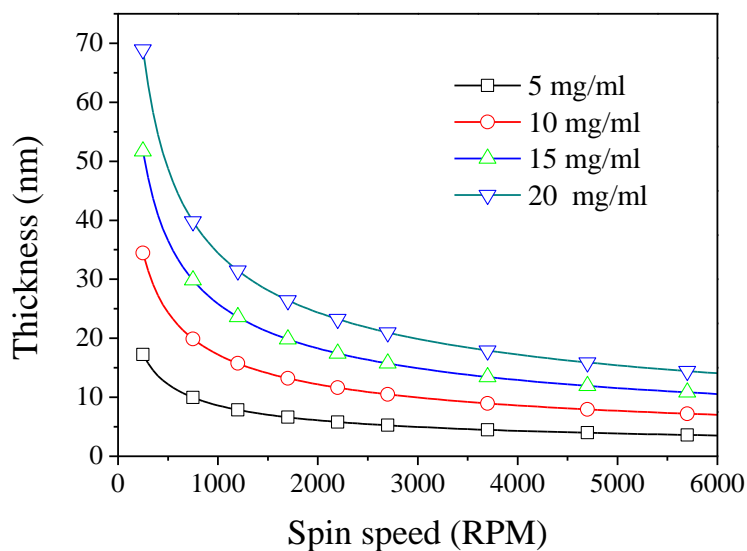


**Figure 3.11** Thicknesses of vanadium (V) oxide vs. spin speeds for different concentrations of solution.

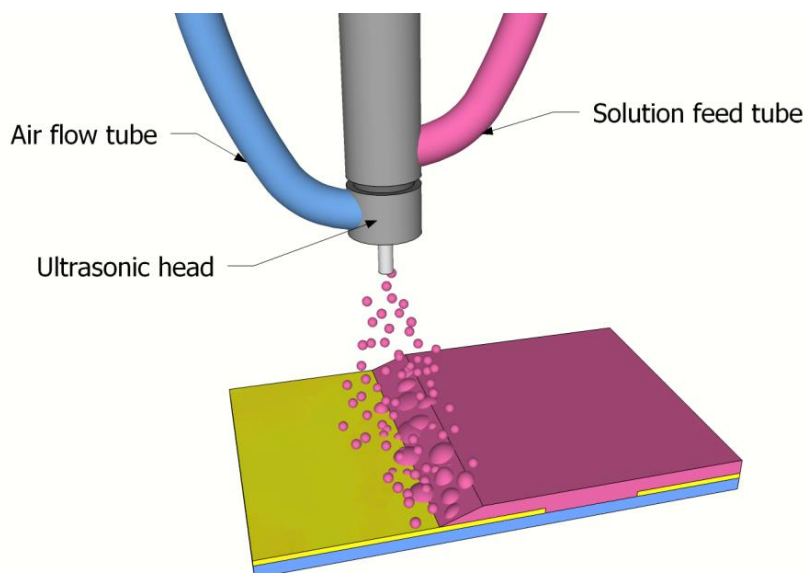


**Figure 3.12** Schematics of the ultrasonic spray coating setup, a hot plate is used during deposition process in order to control solvent evaporation rate.

For this research, a prism ultra-sonic spray coater was purchased from Ultrasonic Systems Inc (USI). It consists of the nozzle head for dispensing solution which vibrates at a high frequency to generate a thin jet of solution (i.e. small droplets in the micrometer range). Using a spray-forming tip with low pressure air provides a more precise and controlled coating process.

To fabricate a thin film the spray tip moves over the substrate and the film thickness depends significantly on the concentration of the solution and the height and the speed of the nozzle head. Ideally the solution spreads across the substrate rather than forming individual droplets. Therefore, the film dries evenly across the whole surface forming a thin film of material. The uniformity of the generated film is highly dependent on the match in polarity between the used solution and surface of the substrate. For this reason, formation of uncoated areas on the substrate can be avoided by using a good wettability solvent to form low contact angle on the surface. The surface wetting (i.e. the surface energy) can be modified by either cleaning with different solvents or via treatment of the substrate surface by oxygen plasma. In addition, there are various parameters can influence on homogeneous film formation such as the temperature of the substrate, the flow rate of the solution, the distance between the spray nozzle and the surface, the concentration of the solution, the air pressure which generate the sprayed droplets [28].

In this work, a substrate was placed on a hot surface at 40°C. The V<sub>2</sub>O<sub>x</sub> solution with a concentration of 2mg/ml is fed through a tube at pressure of 200 mbar onto a tip which vibrates at an ultrasonic frequency. The nozzle height was adjusted at 13 cm with lateral spray speed of 50 mm/s to obtain a thin layer with thickness of 5 nm.

### 3.3 OPV Device Fabrication

#### 3.3.1 Materials and Solution Preparation

All of the materials in this work were used as received from the supplier. Organic polymers and metal oxide materials that were used in this work and their specifications are as follow:

- I. PCDTBT were provided by Ossila Ltd with a purity of 95%, molecular weight ( $M_w$ ) of 42.2 g/mol, molecular weight number ( $M_n$ ) of 19.6 g/mol and polydispersity index (PDI) of 2.15
- II. PFDT2BT-8 was synthesised by the Department of Chemistry at the University of Sheffield and had  $M_w$ ,  $M_n$  and PDI of 91.6 g/mol, 62.4 g/mol and 1.47, respectively.
- III. PC<sub>70</sub>BM were supplied by Ossila Ltd with a purity of 95% and  $M_w$  of 1031 g/mol.
- IV. PEDOT:PSS were supplied by Ossila Ltd and had a weight volume of 1.1 wt.% (in water) and Viscosity in the range 8 to 30 mPas.
- V. Vanadium (V) oxytriisopropoxide was provided by Sigma-Aldrich and had density of 1.035 g/mL.
- VI. Molybdenum(VI) oxide bis(2,4-pentanedionate) powder was supplied by Alfa Aesar and had  $M_w$  of 326.16 g/mol.
- VII. Ammonium molybdate tetrahydrate powder  $[(NH_4)_6Mo_7O_{24} \cdot 4H_2O]$  was supplied by SIGMA-Aldrich and had  $M_w$  of 1,235.86 g/mol.

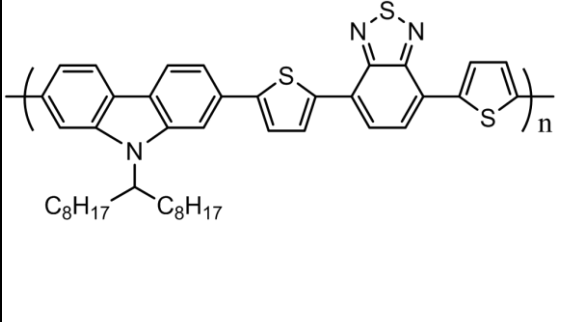
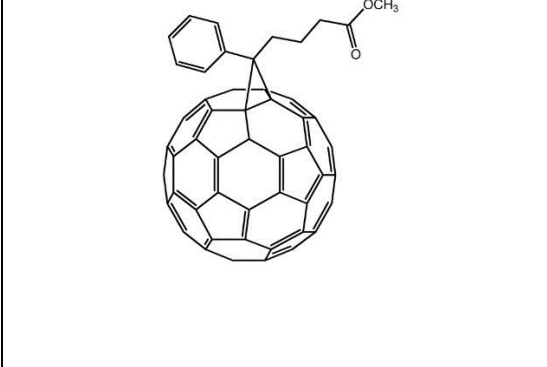
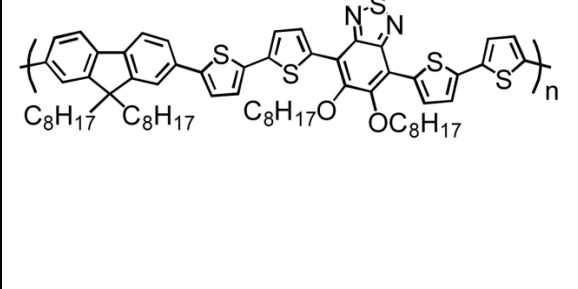
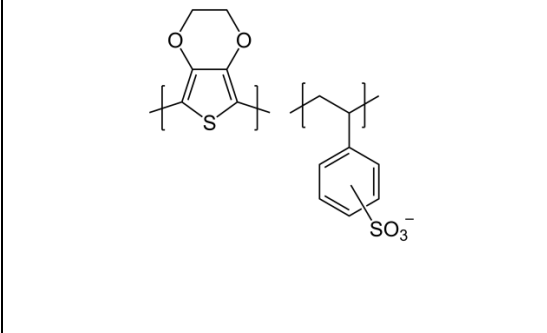
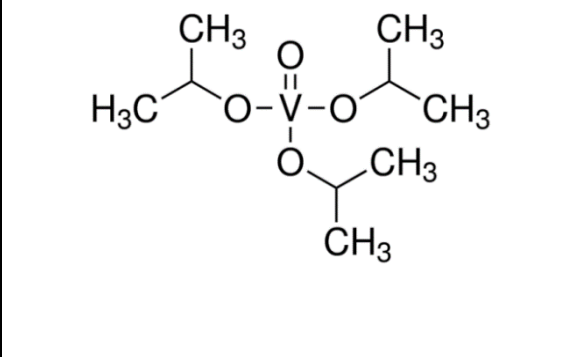
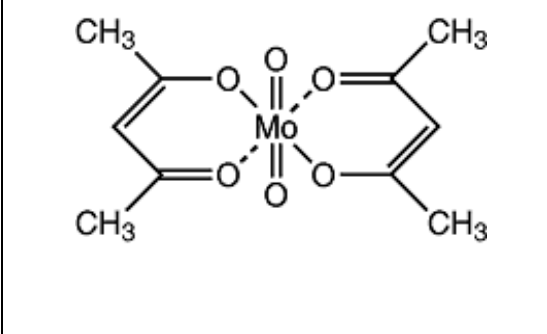
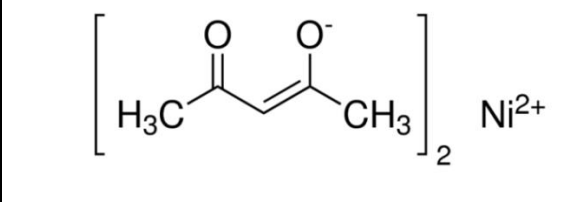
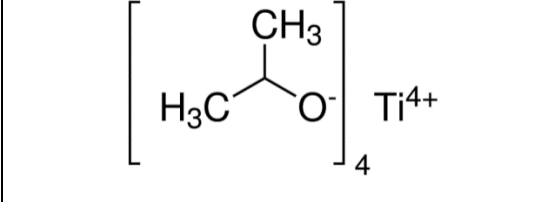
- VIII. Nickel(II) acetylacetonate (99.99%) was purchased from Sigma Aldrich and had  $M_w$  of 256.91 g/mol.
- IX. Titanium(IV) isopropoxide (99.99%) was provided by Sigma-Aldrich and had a density of 0.96 g/mL and  $M_w$  of 284.22 g/mol.

The chemical structures of most materials that were used throughout this thesis are shown in **Table 3.1**

To prepare polymer solutions, amber glass vials were washed by Acetone and IPA solvents and then dried by a nitrogen gun. PCDTBT or PFDT2BT-8 polymer donor was mixed with PC<sub>70</sub>BM material with ratio 1:4 and total weight of 20 mg. The materials were weighed out with a calibrated microbalance in ambient conditions before the solvent was added to them. The preparation of the polymer solutions was conducted in a glove box with a dry nitrogen atmosphere. The PCDTBT and the PFDT2BT-8 samples were dissolved in 1ml of chlorobenzene and chloroform respectively, to obtain a blended solution at a concentration of 20 mg/ml. Subsequently, the solutions were placed onto a hotplate at 70 °C for 24 hours. Using rotating stir bars or shaking vials occasionally was necessary to ensure all the materials had completely dissolved. The blends were then cooled for 20 minutes and filtered through a 0.45µm Polytetrafluoroethylene (PTFE) filter into cleaned amber vials. Metal oxide solutions were prepared using a similar method and the preparation details are summarised in **Table 3.2**



**Table 3.1** The chemical structures of organic and metal oxide materials that were used for fabricating OPV devices.

<p style="text-align: center;"><b>PCDTBT</b></p> <p>Poly[N-9'-heptadecanyl-2,7-carbazole-alt-5,5-(4',7'-di-2-thienyl-2',1',3'-benzothiadiazole)]</p>  <p>The structure shows a polymer chain with a central carbazole ring substituted with two octyl groups (C<sub>8</sub>H<sub>17</sub>). It is linked to two thienyl rings, which are further connected to a benzothiadiazole ring, forming an alternating copolymer structure.</p>	<p style="text-align: center;"><b>PC<sub>70</sub>BM</b></p> <p>[6,6]-Phenyl-C71-butyric acid methyl ester</p>  <p>The structure shows a C<sub>70</sub> fullerene cage with a phenyl ring and a butyric acid methyl ester group attached to one of the [6,6] bonds.</p>
<p style="text-align: center;"><b>PFDT2BT-8</b></p> <p>poly[9,9-dioctylfluorene-4,7-alt-(5,6-bis(octyloxy)-4,7-di(2,2'-bithiophen-5-yl)benzo[c][1,2,5]thiadiazole)-5,5-diyl]</p>  <p>The structure shows a polymer chain with a fluorene core substituted with two octyl groups (C<sub>8</sub>H<sub>17</sub>). It is linked to two bithiophene rings, which are further connected to a benzothiadiazole ring, forming an alternating copolymer structure.</p>	<p style="text-align: center;"><b>PEDOT:PSS</b></p> <p>Poly(3,4-ethylenedioxythiophene) poly(styrenesulfonate)</p>  <p>The structure shows two polymer chains: PEDOT (poly(3,4-ethylenedioxythiophene)) and PSS (poly(styrenesulfonate)).</p>
<p style="text-align: center;">Vanadium (V) oxytriisopropoxide</p>  <p>The structure shows a central Vanadium (V) atom coordinated to three isopropoxy groups and one oxygen atom.</p>	<p style="text-align: center;">Molybdenum(VI) oxide bis(2,4-pentanedionate)</p>  <p>The structure shows a central Molybdenum (VI) atom coordinated to two 2,4-pentanedionate ligands and two oxygen atoms.</p>
<p style="text-align: center;">Nickel(II) acetylacetonate</p>  <p>The structure shows a Nickel(II) ion coordinated to two acetylacetonate ligands.</p>	<p style="text-align: center;">Titanium(IV) isopropoxide</p>  <p>The structure shows a Titanium(IV) ion coordinated to four isopropoxy groups.</p>

**Table 3.2** Precursor name and the optimized fabrication parameters.

Precursor	Quantity (mg)	Solvent	Preparation environment	Heating °C	Filtration
Vanadium (V) oxytriisopropoxide	5, 10, 15	IPA	In air	X	X
Molybdenum(VI) oxide bis(2,4-pentanedionate)	5	Anhydrous methanol	In glovebox	60	PTFE
Ammonium molybdate tetrahydrate	6	Water + Acetonitrile	In air	70	PTFE
Nickel(II) acetylacetonate	15	toluene	In air	70	PTFE
Titanium(IV) isopropoxide	15	IPA	In glovebox	X	X

### 3.3.2 Thin Films Preparation

Solution-processed thin films were deposited in different conditions depending on the material and solvent properties. Polymer solutions were spin coated under glove box conditions, with the dry nitrogen atmosphere. PCDTBT or PFDT2BT-8 thin films were fabricated at spin speeds of 700 and 3000 RPM respectively, and had a thickness of 70 nm. A PEDOT:PSS layer with a thickness of  $30 \text{ nm} \pm 3 \text{ nm}$  was fabricated by depositing a small amount (40  $\mu\text{l}$ ) of PEDOT:PSS solution into a substrate and then spin coating in ambient conditions at a speed of 3000 RPM. Subsequently, the PEDOT:PSS-coated substrates were baked at 130 °C for 20 minutes in air and then were transferred into a dry glove box environment. There, they were baked for another 10 minutes to remove any residual water content.

Metal oxide thin films were prepared by a similar process.  $\text{V}_2\text{O}_x$  thin films were prepared from an isopropanol solution of vanadium (V) oxytriisopropoxide that was spin

cast in air without any post-annealing or plasma treatment. Spin coating speed was fixed at 3000 RPM for concentrations of 5, 10, 15, 20 mg/ml to obtain a thin layer with thicknesses of 5, 10, 15, 20 nm respectively. A  $V_2O_x$  thin layer was then formed due to the hydrolysis process of the vanadium oxytriisopropoxide precursor [29].

$MoO_3$  thin films were spin cast from two different precursors as mentioned in the previous section. Ammonium molybdate tetrahydrate (s1- $MoO_3$ ) and molybdenum(VI) oxide bis(2,4-pentanedionate) solutions (s2- $MoO_3$ ) were cast onto a substrate in ambient conditions and glove box environment at spin speeds of 3000 and 2600 RPM respectively, to obtain thin film with a thickness ( $6 \text{ nm} \pm 1.7 \text{ nm}$ ). S1- $MoO_3$  samples were annealed for 20 minutes at  $350 \text{ }^\circ\text{C}$  in air while s2- $MoO_3$  substrates were exposed to UV ozone at a pressure of 1 Torr for 1 minute.

NiO films were cast from a nickel acetylacetonate solution onto substrates in ambient conditions. Subsequently, the NiO substrate was annealed at 5 different temperatures, 100, 200, 300, 400,  $500 \text{ }^\circ\text{C}$ , for 30 minutes followed by ozone treatment for 1, 2, and 3 minutes at varying pressures and powers.  $TiO_x$  thin film with a thickness of 20 nm was prepared by spin-coating titanium(IV) isopropoxide solution (15 mg/ml) in the nitrogen glove box at a rotation speed of 2500 RPM. After that, the substrates were exposed to air for 10 minutes for the hydrolysis process to form amorphous  $TiO_x$  film [30].

### 3.3.3 Device Fabrication

All devices were fabricated onto  $15 \times 20 \text{ mm}^2$  of pixellated cathode design glass substrates that were supplied by Ossila as shown in **Figure 3.13**. These substrates are sold pre-patterned with a 100 nm layer of Indium Tin Oxide (ITO).

Prior to use, the substrates were sonicated in a warm cleaning solution of Hellmanex (3 wt%) for 5 minutes and then they were dump-rinsed in deionised (DI) water before sonicating in NaOH solution (10 wt% in water) for 5 minutes. After a further dump-rinse in DI water, the substrates were sonicated in warm IPA for 5 minutes. Finally, the substrates were dried with a compressed nitrogen flow. In some experiments the ITO surface needed a further treatment by exposing it to oxygen plasma to improve the wettability of the solution onto the substrate. After that, a hole transport layer, either a PEDOT:PSS layer or a metal oxide, was deposited on top of the ITO surface. Metal oxides in this work are deposited either by solution processing methods or by vacuum evaporation.

Discussion of metal oxide materials and their preparation from solution was given in section **4.3.1 Materials and solution preparation**. Semiconducting polymer thin films were prepared by spin casting the solution onto a substrate in a nitrogen filled glovebox. For efficient electrical contact between the cathode and the ITO or between the anode and the test board, the ITO surface had to be cleaned after each spin-coating step either with water for solution-processed metal oxides or with solvents for polymer solutions. Next, the substrates were transferred within the glove box to a high-vacuum system ( $10^{-7}$  mbar) to thermally evaporate the cathodes. The bi-layer cathodes of Ca and Al were evaporated at a rate of  $3 \text{ \AA s}^{-1}$  and  $15 \text{ \AA s}^{-1}$  respectively. Then, the Ca cathodes underwent 5 nm of deposition and the Al 100 nm of deposition. The preparation technique for cathode deposition was discussed in section **4.3.1 Materials and solution preparation**

To create the inverted structure, a  $\text{TiO}_x$  thin film with a thickness of 20 nm was fabricated by a spin-coating process as mentioned in **4.3.1 Materials and solution**

**preparation.** Next, the active layer was applied via spin-coating as described above. Finally, a hole extraction layer and Ag thin layers of 10 nm and 100 nm thickness respectively, were thermally evaporated at a pressure of  $10^{-7}$  mbar via the same technique described above for Ca and Al.

The final step in device fabrication was encapsulation of the central area of each substrate by using a glass slide and light-curable epoxy to stop any further ingress of water and oxygen into the deposited layers and then extend the lifetime for measurement and storage. After encapsulation the devices were placed under a UV light for 30 minutes prior to extraction from the glovebox to ensure a fully cured epoxy coating. The final OPV structure for normal architecture is shown in **Figure 3.13**

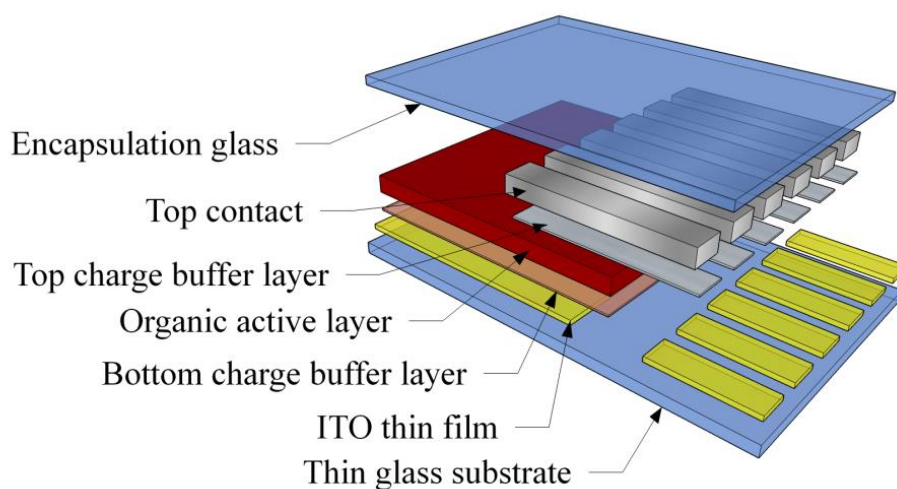


**Figure 3.13** ITO coated substrate as six pixel design. (b) shows the OPV device structure for normal architecture.

### 3.4 References

1. S. Hüfner, *Photoelectron spectroscopy: Principles and applications*, Springer Verlag 2003.
2. P. K. Ghosh, *Introduction to photoelectron spectroscopy*, John Wiley & Sons, New York, 1983.
3. D. Cahen and A. Kahn, *Electron energetics at surfaces and interfaces: Concepts and experiments*, *Advanced materials* **15** (2003), no. 4, 271-277.
4. H. Ishii, K. Sugiyama, E. Ito and K. Seki, *Energy level alignment and interfacial electronic structures at organic metal and organic organic interfaces*, *Advanced Materials* **11** (1999), no. 8, 605-+.
5. A. M. Ellis, M. Feher and T. G. Wright, *Electronic and photoelectron spectroscopy*, Cambridge University Press, New York, 2005.
6. K. Siegbahn, *Electron-spectroscopy for atoms, molecules, and condensed matter*, *Reviews of Modern Physics* **54** (1982), no. 3, 709-728.
7. S. Hüfner, *Very high resolution photoelectron spectroscopy*, vol. 715, Springer, New York, 2007.
8. J. C. Vickerman and I. S. Gilmore, *Surface analysis- the principal techniques*, John Wiley & Sons, Chichester, 2009.
9. D. R. Lide, *Handbook of chemistry and physics*, Boca Raton: CRC Press 1998.

10. Y. Leng, *Materials characterisation, introduction to microscopic and spectroscopic methods*, Wiley-VCH, Germany, 2013.
11. A. Proctor and D. M. Hercules, *Inelastic background and peak area determination in X-ray photoelectron-spectroscopy (esca)*, *Applied Spectroscopy* **38** (1984), no. 4, 505-518.
12. S. Tougaard and P. Sigmund, *Influence of elastic and inelastic-scattering on energy-spectra of electrons emitted from solids*, *Physical Review B* **25** (1982), no. 7, 4452-4466.
13. H. Tokutaka, N. Ishihara, K. Nishimori, S. Kishida and K. Isomoto, *Background removal in X-ray photoelectron-spectroscopy*, *Surface and Interface Analysis* **18** (1992), no. 10, 697-704.
14. G. A. Sawatzky and D. Post, *X-ray photoelectron and auger-spectroscopy study of some vanadium-oxides*, *Physical Review B* **20** (1979), no. 4, 1546-1555.
15. E. Meyer, *Atomic force microscopy*, *Progress in Surface Science* **41** (1992), no. 1, 3-49.
16. S. N. Magonov, V. Elings and M. H. Whangbo, *Phase imaging and stiffness in tapping-mode atomic force microscopy*, *Surface Science* **375** (1997), no. 2-3, L385-L391.

17. S. Morita, "Noncontact atomic force microscopy volume 2 introduction," *Noncontact atomic force microscopy, vol 2*, S. Morita, F. J. Giessibl and R. Wiesendanger (Editors), vol. 2, Springer-Verlag Berlin, Berlin, 2009, pp. 1-13.
18. A. Rothen, *The ellipsometer, an apparatus to measure thicknesses of thin surface films*, Review of Scientific Instruments **16** (1945), no. 2, 26-30.
19. H. G. Thomas and E. A. Irene, *Handbook of ellipsometry*, Springer, Norwich, 2005.
20. H. G. Tompkins, *A user's guide to ellipsometry*, Academic Press Limited, London, 1992.
21. G. E. Jellison, *Spectroscopic ellipsometry data analysis: Measured versus calculated quantities*, Thin Solid Films **313** (1998), 33-39.
22. R. J. Archer, *Determination of properties of films on silicon by method of ellipsometry*, Journal of the Optical Society of America **52** (1962), no. 9, 970-&.
23. T. Yamaguchi, Y. Kaneko, A. H. Jayatissa, M. Aoyama, A. V. Zotov and V. G. Lifshits, *Empirical dielectric function of amorphous materials for spectroscopic ellipsometry*, Journal of Applied Physics **77** (1995), no. 9, 4673-4676.
24. D. J. Santjojo, T. Aizawa and S. Muraishi, *Ellipsometric characterization on multi-layered thin film systems during hydrogenation*, Materials Transactions **48** (2007), no. 6, 1380-1386.



25. M. Rinio, H. J. Moller and M. Werner, *LBIC investigations of the lifetime degradation by extended defects in multicrystalline solar silicon*, *Solid State Phenomena* **63-4** (1998), 115-122.
26. C. J. Lawrence, *The mechanics of spin coating of polymer-films*, *Physics of Fluids* **31** (1988), no. 10, 2786-2795.
27. D. B. Hall, P. Underhill and J. M. Torkelson, *Spin coating of thin and ultrathin polymer films*, *Polymer Engineering and Science* **38** (1998), no. 12, 2039-2045.
28. S. Bose, S. S. Keller, T. S. Alstrom, A. Boisen and K. Almdal, *Process optimization of ultrasonic spray coating of polymer films*, *Langmuir* **29** (2013), no. 23, 6911-6919.
29. J. Livage, *Vanadium pentoxide gels*, *Chemistry of Materials* **3** (1991), no. 4, 578-593.
30. S. Mahshid, M. Askari and M. S. Ghamsari, *Synthesis of TiO<sub>2</sub> nanoparticles by hydrolysis and peptization of titanium isopropoxide solution*, *Journal of Materials Processing Technology* **189** (2007), no. 1-3, 296-300.

# Chapter 4

## Optical and Electronic Structure Characterisation of Materials

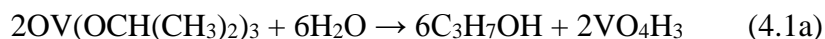
### 4.1 Introduction

In this chapter, the most commonly used materials within the experimental chapters were characterised by different techniques. These materials involve solution processed and vacuum deposited vanadium oxide  $V_2O_x$ , vacuum evaporated molybdenum oxide  $MoO_x$ , Poly[N-9'-heptadecanyl-2,7-carbazole-alt-5,5-(4',7'-di-2-thienyl-2',1',3'-benzothiadiazole)] PCDTBT and poly[9,9-dioctylfluorene-4,7-alt-(5,6-bis(octyloxy)-4,7-di(2,2'-bithiophen-5-yl)benzo[c][1,2,5]thiadiazole)-5,5-diyl] PFDT2BT-8. The work function and valence band edge of relevant materials used throughout this work were investigated ex-situ by X-ray photoelectron spectroscopy (XPS) and ultraviolet photoelectron spectroscopy (UPS). In addition, the optical properties of those materials (i.e. absorption region for organic polymers, transmission edge for metal oxides and optical band gap) were determined by absorption spectroscopy. The spectroscopic results are combined to explain the J–V characteristics of OPV devices in the following experimental chapters.

## 4.2 Metal Oxides

### 4.2.1 Vanadium Oxide

Vanadium oxide ( $V_2O_x$ ) thin films have been employed as hole extraction layers in polymer bulk heterojunction solar cells.  $V_2O_x$  films in this work were fabricated by either thermal evaporation or by spin-coating vanadium (V) oxytriisopropoxide ( $s-V_2O_x$ ) in air at room temperature without the need for further treatment such as thermal annealing or oxygen plasma treatment. The deposited vanadium (V) oxytriisopropoxide film undergoes hydrolysis in air (i.e. between the vanadium precursor and water molecules) converting to  $V_2O_x$ . This process can be described by the following chemical equations [1, 2]:



Here the hydrolysis process occurs due to the presence of water molecules in the air in which the alkyl chain ( $CH(CH_3)_2$ ) is cleaved by  $H^+$  that then binds with the singly bound oxygen on the vanadium oxide generating  $VO_4H_3$ . The positively charged alkyl chain then binds with the  $OH^-$  anion forming isopropanol molecules which evaporate over time. The water molecules in  $2VO_4H_3$  then evaporate leaving  $V_2O_x$  molecules. The deposited  $V_2O_x$  thin film was assumed to be amorphous as reported in the literature [3, 4].

The transmittance of different thicknesses of films prepared by the spin coating method was investigated with Fluoromax 4 as described in **4.2.2 Spectrofluorometer**.

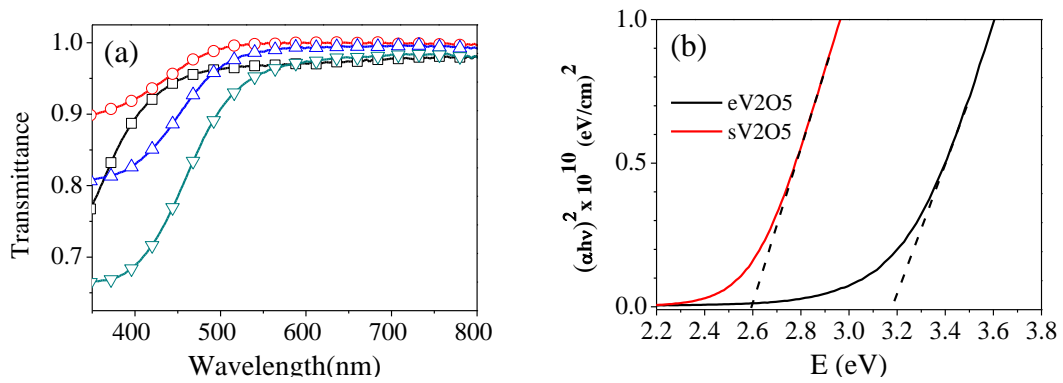


**Figure 4.1** (a) Optical transmission spectra of the  $V_2O_x$  films with different thicknesses; ( $\circ$ ) 5 nm, ( $\Delta$ ) 10 nm, ( $\nabla$ ) 20 nm, for solution-processed vanadium oxide and ( $\square$ ) 10 nm for vacuum evaporated film. The absorption coefficient  $(\alpha h\nu)^2$  as a function of the photon energy for 20 nm of  $V_2O_x$  films.

As shown in **Figure 4.1(a)**, the  $V_2O_x$  films show high transmission for wavelengths above 540 nm, so these films cover the majority of the solar spectrum. As the thickness increases, the films begin to absorb wavelengths below 540 nm (i.e. an absorption edge of s- $V_2O_x$  is 540 nm), indicating that the  $V_2O_x$  has a band gap in the range of 2.5-2.7 eV. The thin film (5 nm thickness) displayed high transmission over the whole spectrum. Therefore, thin  $V_2O_x$  films ( $< 10$  nm) are predicted to enhance the current density  $J_{sc}$  of OPVs by increasing light intensity in the active layer. Furthermore, the optical properties of solution processed vanadium (V) oxide films were compared to films fabricated by the vacuum evaporation technique. It can be seen that the vacuum deposited film with a thickness of 10 nm shows greater than 95% transmittance for wavelengths above 460 nm. As a result, vacuum deposited films are predicted to have a larger band gap than those which are solution processed.

Using Tauc's law, the bandgap of  $V_2O_x$  film was approximately determined. The relation between the band gap energy ( $E_g$ ) and the absorption coefficient ( $\alpha$ ) can be represented as [5, 6]

$$\alpha(h\nu) \propto [h\nu - E_g]^{1/N}, \quad (4.2)$$

where  $h\nu$  represents the photon energy and  $N$  is equal to 2. As can be seen in **Figure 4.1(b)**, the optical absorption coefficient  $(\alpha h\nu)^2$  is plotted as a function of the incident photon energy. By extrapolating from the straight-line portion of the plots to the energy-axis, the  $E_g$  of both  $V_2O_x$  films (i.e. solution processed and vacuum deposited) was determined at 2.6 and 3.2 eV. As shown previously in **2.6.2 Optical Effects**, the estimated  $E_g$  is in good agreement with some commonly reported values.

Several studies have reported various values of  $V_2O_x$  band gap due to the different processing conditions or the measurement method. For instance, electron spectroscopy measurements of  $V_2O_x$  layer spin-coated in air from isopropanol solution of vanadium(V) oxitriisopropoxide showed a band gap of 3.6 eV [7]. In contrast, the optical absorption experiments of the same precursor revealed a lower band gap of 2.3 eV [8]. In addition, impact of the processing conditions on the  $V_2O_x$  band gap has been reported by other authors [7, 9-12]. For example,  $V_2O_x$  samples spin-coated and annealed under  $N_2$  atmosphere had a band gap of 3.2 eV while fabrication of the films in air showed lower band gaps of 2.5 eV [11].

Characterisations of the XPS and UPS were used to investigate the oxidation state and the electronic structure of the  $V_2O_x$  thin films that were grown on an ITO substrate. In the XPS spectrum lines, the C1s of the carbon line were assigned a value of 284.5 eV

for data calibration. Therefore, a small shift of about 0.4 eV into the lower binding energies was observed due to static charging effects [13].

**Figure 4.2** shows the XPS spectrum of spin-coated vanadium oxide film prepared in ambient condition. The binding energy of O1s, V2p<sub>1/2</sub>, and V2p<sub>3/2</sub> lines correspond to 517.1 eV, 524.6 eV and 530.0 eV respectively, which is consistent with previous studies [14, 15]. Decomposition analysis reveals that V2p<sub>3/2</sub> peak consists of two different species (i.e. V<sup>5+</sup> and V<sup>4+</sup> oxidation state) with a ratio of 5.7:1. The peak position of V<sup>4+</sup> and V<sup>5+</sup> in V2p<sub>3/2</sub> spectrum was identified by using (Lorentzian-Gaussian) fitting to be 515.8 eV and 517.1 eV respectively in which V<sup>4+</sup> oxidation state arises as a low-energy shoulder in the core level of V2p<sub>3/2</sub>.

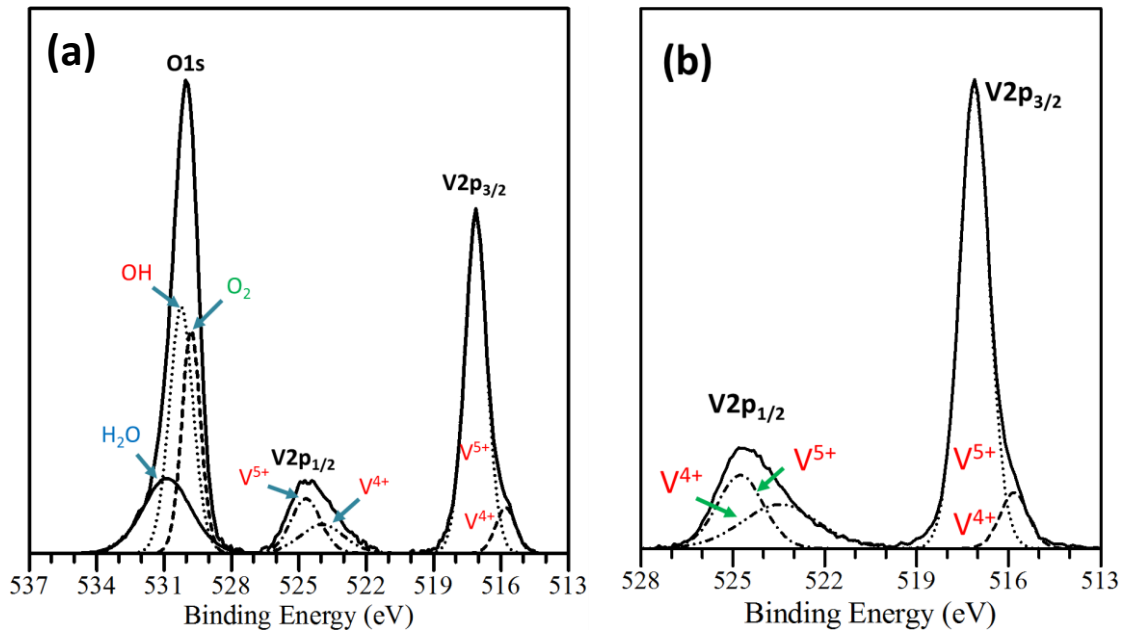


**Figure 4.2** XPS spectra of V<sub>2</sub>O<sub>x</sub> thin films deposited by (a) spin-coating method and (b) vacuum thermal evaporation. The energy difference between the O1s and V2p<sub>3/2</sub> peaks was used for measuring the oxidation state of vanadium oxide.

Fabrication conditions such as atmospheric gases and thermal annealing can increase concentration of  $V^{4+}$  species leading to the reduction of the  $V^{5+}$  to  $V^{4+}$ . For instance,  $H_2O$  molecules in air facilitate the oxygen removal such that oxygen-hydrogen interaction weakens the binding energy of the oxygen atom with the neighbouring vanadium atoms [16, 17]. Moreover, a previous study demonstrated that  $V_2O_x$  can be reduced during XPS measuring in which X-rays create vanadyl ( $V = O$ ) oxygen atoms vacancies[18].

As suggested by Coulston et al., the effective oxidation (or average oxidation) state of vanadium oxide was estimated by measuring the energy difference between the O1s (= 530.0 eV) and  $V2p_{3/2}$  lines [13, 19]. From the following linear relationship

$$V_{ox} = 13.82 - 0.68 [E_b(O1s) - E_b(V2P_{3/2})] \quad (4.3)$$

it was found that oxidation states are 4.92 and 4.96 for solution processed and vacuum deposited films respectively. This indicates that a small amount of oxygen vacancy exists in both samples due to exposure of the films to atmospheric gases. The impact of oxygen vacancies in the oxidation state of vanadium will be discussed in more detail in chapter 5.

A UPS spectrum was used to investigate the energy level structure formed at interfaces between  $V_2O_x$  and ITO layers. As shown in **Figure 4.3(a)**, the position of the secondary electron cut-off of solution processed and vacuum evaporated films was determined to be at the binding energies of 15.95 eV and 16.13 eV, exhibiting a work function of 5.25 eV and 5.07 eV. Compared to previous studies, the work function of our  $V_2O_x$  films are similar to those prepared by different processes [7, 9, 20]. The onset of the valence band for both samples was determined to be 2.35 eV below the Fermi level.

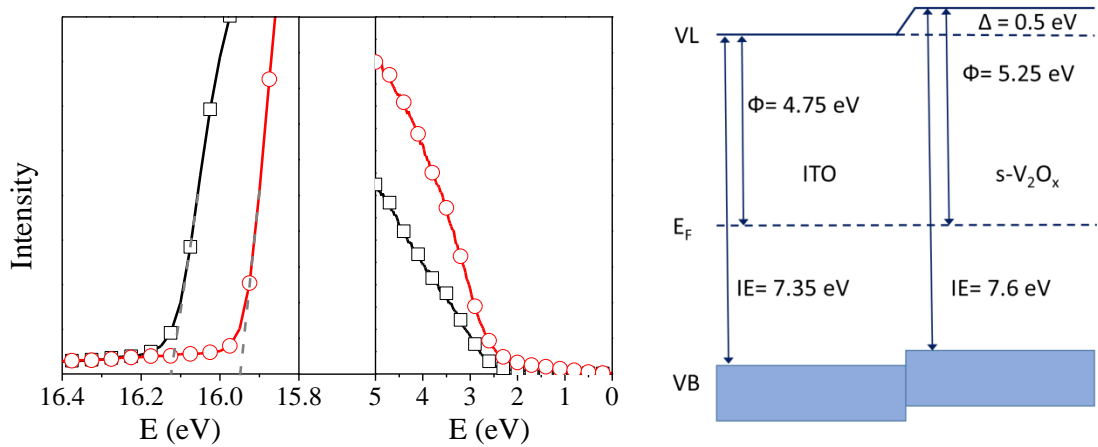


**Figure 4.3** (a) UPS measurements showing the secondary electron cut-off region and the expanded region near the Fermi level for  $V_2O_x$  films fabricated by solution ( $\circ$ ) and vacuum evaporated process ( $\square$ ) and (b) energy level alignment scheme at the ITO/ $V_2O_x$  interface showing dipole interface ( $\Delta$ ) of 0.5 eV and the work function ( $\Phi$ ) of  $s-V_2O_x$ . VL,  $E_F$  and VB are vacuum level, Fermi level and valence band, respectively.

Therefore, the ionization energy (IE) is about 7.6 eV which is in good agreement with the commonly reported values [21]. Given that the band gap had been estimated at 2.6 eV, this onset confirms that  $s-V_2O_x$  is a highly n-type semiconductor. The resulting schematic energy level diagram of the interfaces between ITO and  $V_2O_x$ , neglecting an eventual band bending, is displayed in **Figure 4.3(b)**. Note that with alignment of Fermi levels of the two layers, a dipole interface of about 0.5 eV exists at the interface. The small barrier at the ITO/ $V_2O_x$  interface facilitates hole extraction process and prevents current leakage. **Table 4.1** shows the comparison between the results obtained from photoelectron and absorption spectroscopies and those reported in literature with similar deposition process.



**Table 4.1** Comparison between the measured energy levels of V<sub>2</sub>O<sub>x</sub> thin films and those reported in literature

Material	WF (eV)		Valence band (eV)		Optical band gap (eV)	
	This work	Values in literature	This work	Values in literature	This work	Values in literature
s-V <sub>2</sub> O <sub>x</sub>	5.25 ±0.04	5.3 [7], 5.6 [11], 5.6 [21], 5.15(fresh) [22], 5.5(aged) [22], 5.4 [23], 4.85 [24]	2.35 ±0.05	2.6 [7], 2.5[11], 2.5(fresh) [22], 2.5(aged) [22]	2.6 ±0.08	Presented in Table 2.1
e-V <sub>2</sub> O <sub>x</sub>	5.07 ±0.05	7 [7], 5.3 (contaminated) [7], 6.85 [25], 4.9 [26], 7 [9]	2.35 ±0.05	2.5 [7], 2.6 (contaminated) [7], 2.4 [25], 2.4 [9]	3.2 ±0.11	

#### 4.2.2 Molybdenum Oxide

A considerable amount of literature has been published on the use of molybdenum oxide (MoO<sub>x</sub>) in organic photovoltaic devices as a hole extraction material [21, 27]. **Figure 4.4(a)** shows the transmittance data for 20 nm film of vacuum evaporated molybdenum (VI) oxide. It can be seen that more than 90% transmittance is observed for wavelengths above 460 nm suggesting a relatively large bandgap. In a similar approach to V<sub>2</sub>O<sub>x</sub>, the bandgap of MoO<sub>x</sub> was determined by using Tauc's law to be 3.31 eV as shown in **Figure 4.4(b)**. **Figure 4.5** shows the XPS spectrum of vacuum evaporated molybdenum oxide film. The de-convolution analysis of the O1s spectrum in **Figure 4.5(a)** shows the presence of three different species.

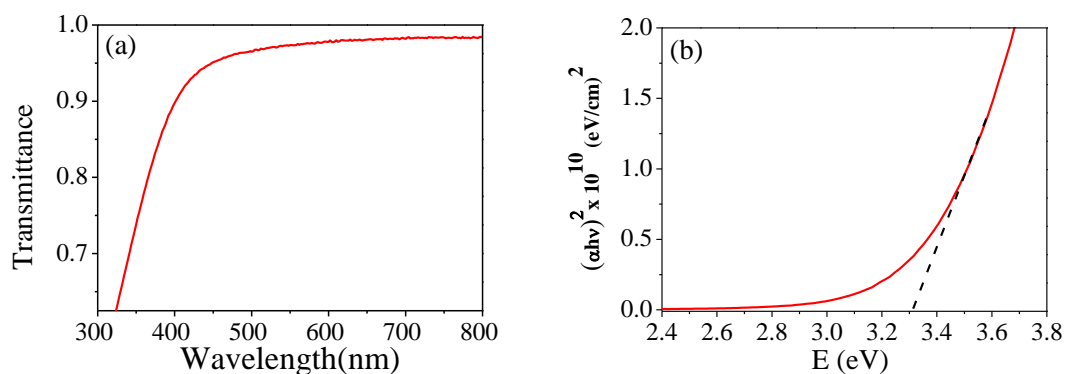


**Figure 4.4** (a) Optical transmission spectra of vacuum deposited MoO<sub>3</sub> thin film, (b) The absorption coefficient  $(\alpha h\nu)^2$  as a function of the photon energy for 20 nm of MoO<sub>3</sub> films.

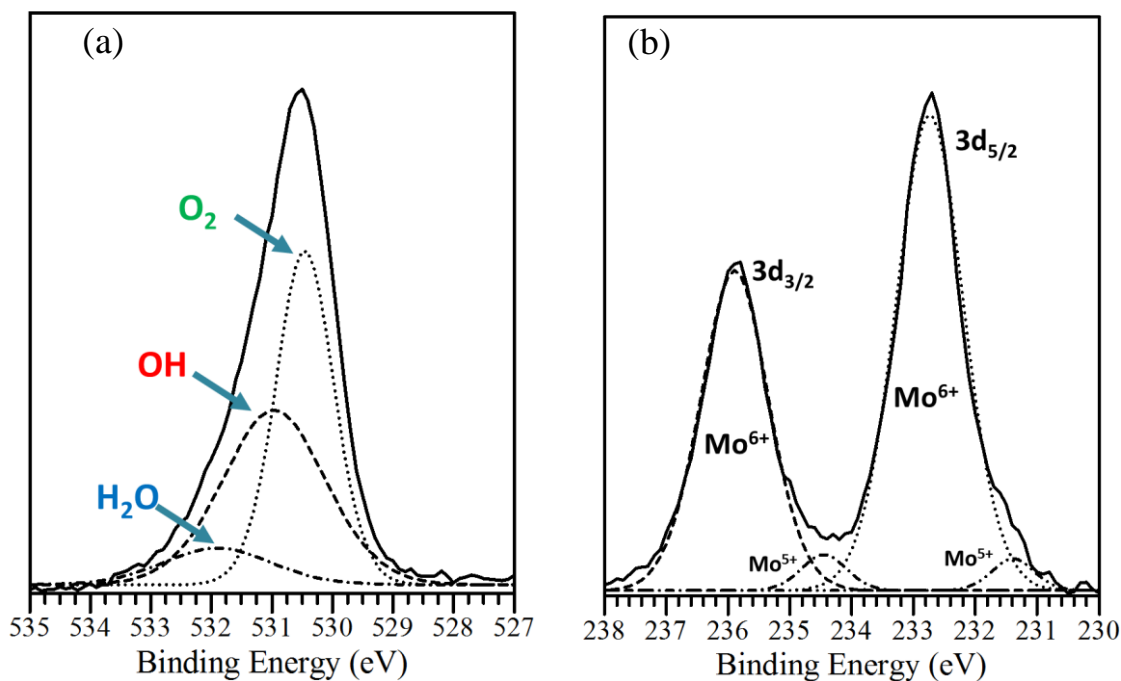


**Figure 4.5** XPS spectra of vacuum evaporated MoO<sub>3</sub> thin film, (a) the O1s peak with three different species are observed, (b) the Mo3d peaks involve two different Molybdenum species. Mo<sup>5+</sup> oxidation state arises as a low-energy shoulder in the core levels of 3d<sub>5/2</sub> and 3d<sub>3/2</sub> to deposition condition.

These oxygen species correspond to binding energies of 530.4 eV, 531 eV, and 532 eV which are ascribed to Molybdenum-Oxygen bonds, hydroxide species absorbed onto the surface and H<sub>2</sub>O molecules absorbed into the film respectively [28]. **Figure 4.5(b)** shows the Mo3d spectrum which consists of two different Molybdenum species (3d<sub>5/2</sub> and 3d<sub>3/2</sub>) with binding energies of 232.7 eV and 235.9 eV corresponding to an oxidation state of + 6 (Mo<sup>6+</sup>). In addition, the reduced oxide state Mo<sup>5+</sup> was observed at 231.4eV and 234.4eV with a percentage concentration of 8.5%. This reduction in oxidation state can be attributed to the deposition condition. The valence band and the work function of the MoO<sub>3</sub> film were determined from the UPS measurements of its near-Fermi level region and the UPS measurements of its secondary electron cut-off region respectively, as shown in **Figure 4.6**. The position of the secondary electron cut-off was determined to be at the binding energy of 16.05 eV resulting in a work function of 5.15 eV. The edge of the valence band, which is derived from oxygen 2p orbitals, was observed at 2.7 eV below the Fermi level. Therefore, the ionisation energy of MoO<sub>3</sub> was calculated to be 7.85 eV.

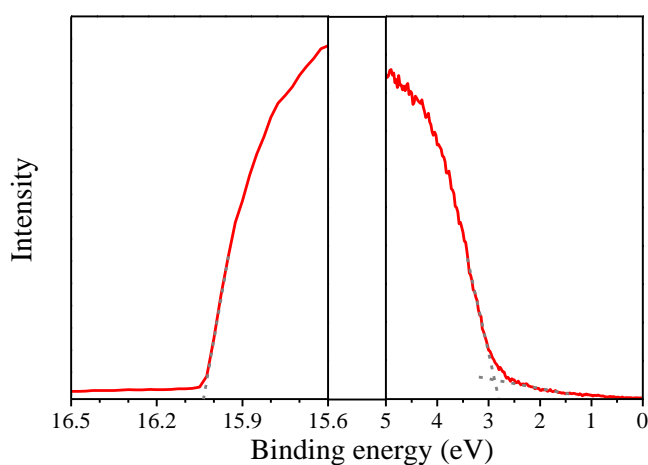


**Figure 4.6** UPS spectrum of vacuum deposited MoO<sub>3</sub> thin film showing the secondary electron cut off and the valence band region.

However, the present work function became similar to those reported in literature when the researchers exposed the samples to air, which means that the contamination of the surface of MoO<sub>3</sub> with atmospheric gases must be the main reason for the low work function. Indeed, the reduced oxide states Mo<sup>5+</sup> that appeared in Mo3d peaks is clear evidence for the low work function. Previous studies have reported several factors that might influence the value of MoO<sub>x</sub> work function, such as annealing temperature, film thickness and deposition rate [29-31]. **Table 4.2** shows the comparison between the obtained data for MoO<sub>x</sub> and those reported in previous studies.

**Table 4.2** Comparison between the measured energy levels of MoO<sub>x</sub> thin films and those reported in literature

Material	WF (eV)		Valence band (eV)		Optical band gap (eV)	
	This work	Values in literature	This work	Values in literature	This work	Values in literature
MoO <sub>x</sub>	5.15 ±0.03	6.35 [32], 6.7 [33], 5.5 [34], 6.7 [35], 5.5 (contaminated) [35], 6.9 [36], 5.7 (contaminated) [36], 6.8 [37], 6.2 [38], 6.7 [39]	2.7 ±0.04	2.6 [32], 2.8 [33], 3 [34], 3 [35], 3 (contaminated) [35], 2.8 [36], 2.8 (contaminated) [36], 2.8 [37], 2.6 [38], 2.7 [39]	3.31 ±0.1	Presented in Table 2.1

## 4.3 Organic Semiconductors

### 4.3.1 PCDTBT

The low bandgap polymer PCDTBT has been widely used as donor material in bulk heterojunction organic photovoltaic devices. Interestingly, the deep LUMO and HOMO

levels of PCDTBT significantly enhanced the environmental and chemical stability of OPV devices [40]. The chemical structure of this donor polymer has been shown previously in **Figure 3.13**. The absorption spectrum of PCDTBT thin film spun from chlorobenzene is shown in **Figure 4.7(a)**. It can be seen that PCDTBT film has two absorption peaks at 575 nm and 396 nm which are attributed to  $\pi$ - $\pi^*$  absorption band of the first and second excited states respectively [41]. The absorption onset is situated near the red region at 675 nm which corresponds to an optical bandgap of 1.83 eV. The Fermi level and the HOMO level of this polymer were determined from a UPS spectrum. As can be seen in **Figure 4.7(b)**, the Fermi level lies at 3.43 eV and the HOMO onset was measured to be 1.95 eV below the Fermi level. Therefore, the ionisation energy is estimated to be 5.38 eV. This result is very close to the HOMO level determined from CV at 5.35 eV.

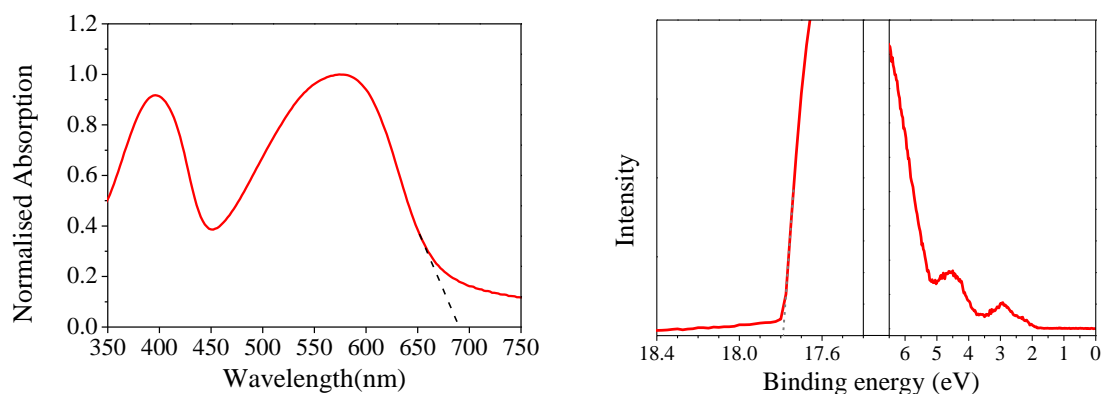


**Figure 4.7** (a) Normalised absorption spectra, and (b) UPS spectra for PCDTBT thin film spun from chlorobenzene on ITO substrate.

### 4.3.2 PFDT2BT\_8

PFDT2BT-8 was synthesised in the Department of Chemistry at the University of Sheffield, via a previously reported method [42]. The chemical structure of this donor polymer has been shown previously in **Figure 3.13**. This fluorene-based polymer showed increased solubility due to the side group unit (BT-8). **Figure 4.8** exhibits the normalised absorption spectra of PFDT2BT-8 as a thin film spun from  $\text{CHCl}_3$ .

In similar behaviour to PCDTBT, it shows two broad absorption bands with peaks at 540 nm and 416 nm. The absorption onset lies at 660 nm, resulting in an optical bandgap of 1.88 eV. However, a blue-shift in peak absorption wavelength and a larger optical energy gap are observed compared to PCDTBT. The HOMO and LUMO energy levels were determined from CV measurements at 5.33 eV and 3.34 eV.

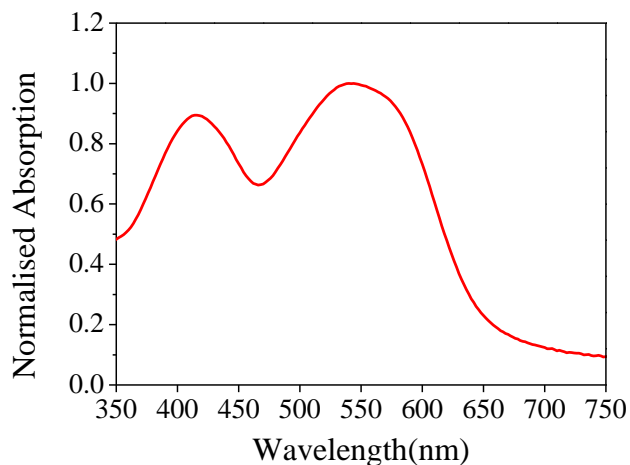


**Figure 4.8** UV-Vis absorbance spectrum of PFDT2BT-8 thin film spun from  $\text{CHCl}_3$ .

### 4.4 Conclusion

In summary, although metal oxides show high transmission across the entire visible spectrum, solution processed vanadium oxide ( $s\text{-V}_2\text{O}_x$ ) exhibits a higher absorption edge than vacuum evaporated metal oxides. Therefore, absorption in the blue region of the spectra is higher for  $s\text{-V}_2\text{O}_x$  which could result in a reduction in the amount of light that reaches the active layer in an OPV device. Indeed, the absorption of thick film of  $s\text{-V}_2\text{O}_x$  at short wavelengths corresponds to the absorption band of the semiconducting donor materials PCDTBT and PFDT2BT-8. To overcome this issue for solution processed vanadium oxide, the thickness of  $s\text{-V}_2\text{O}_x$  thin film should be optimised to be as thin as possible in polymer bulk heterojunction solar cells. Photoelectron spectroscopy studies of both molybdenum oxide and vanadium oxide exhibit relatively high work function.  $s\text{-V}_2\text{O}_x$  films offer large work function compared to vacuum deposited  $\text{MoO}_3$  and  $\text{V}_2\text{O}_x$  suggesting the Fermi level should be pinned close to the conduction band. **Figure 4.9** shows the electronic energy levels of relevant materials used throughout this work against each other as determined via spectroscopic studies of the materials or literature values [21, 40, 42]

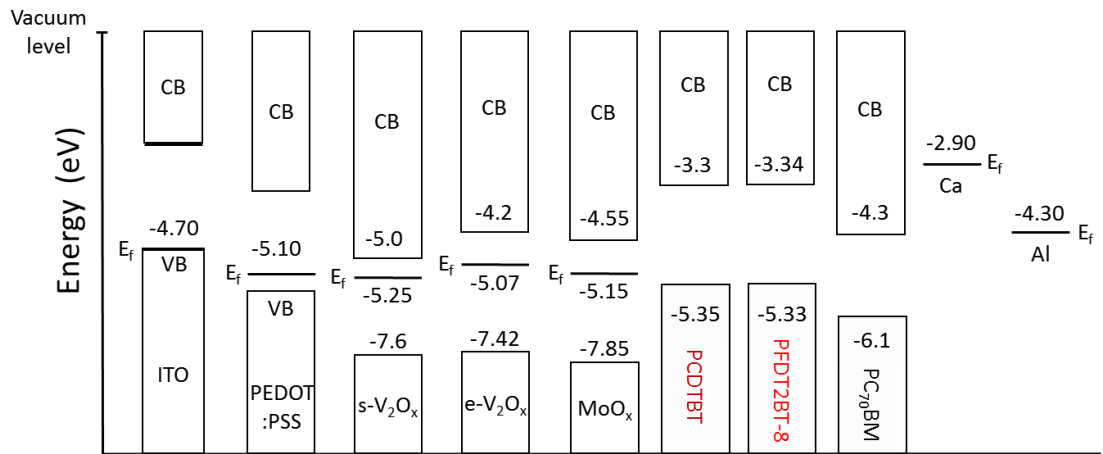


**Figure 4.9** Schematic energy level diagrams of the electrodes, HELs, and semiconducting polymers used throughout the following experimental chapters either determined through spectroscopy of materials or from literature. The energy unit is eV. ( $E_f$ : Fermi energy level, CB: conduction band, VB: valence band)



## 4.5 References

1. J. Livage, *Vanadium pentoxide gels*, Chemistry of Materials **3** (1991), no. 4, 578-593.
2. J. C. Badot, A. Mantoux, N. Baffier, O. Dubrunfaut and D. Lincot, *Electrical properties of  $V_2O_5$  thin films obtained by atomic layer deposition (ALD)*, Journal of Materials Chemistry **14** (2004), no. 23, 3411-3415.
3. J. C. Badot, S. Ribes, E. B. Yousfi, V. Vivier, J. P. Pereira-Ramos, N. Baffier and D. Lincot, *Atomic layer epitaxy of vanadium oxide thin films and electrochemical behavior in presence of lithium ions*, Electrochemical and Solid State Letters **3** (2000), no. 10, 485-488.
4. N. Ozer and C. M. Lampert, *Electrochromic performance of sol-gel deposited  $WO_3-V_2O_5$  films*, Thin Solid Films **349** (1999), no. 1-2, 205-211.
5. G. H. Guai, Q. L. Song, Z. S. Lu and C.-M. Li, *Effects of multiple heat treatment cycles on structure, optical and electrical properties of indium-tin-oxide thin films*, Surface and Coatings Technology **205** (2011), no. 8-9, 2852-2856.
6. Y. Ohhata, F. Shinoki and S. Yoshida, *Optical properties of r.F. Reactive sputtered tin-doped  $In_2O_3$  films*, Thin Solid Films **59** (1979), no. 2, 255-261.
7. K. Zilberberg, S. Trost, J. Meyer, A. Kahn, A. Behrendt, D. Luetzenkirchen-Hecht, R. Frahm and T. Riedl, *Inverted organic solar cells with sol-gel processed high*

- work-function vanadium oxide hole-extraction layers*, *Advanced Functional Materials* **21** (2011), no. 24, 4776-4783.
8. K. Zilberberg, S. Trost, H. Schmidt and T. Riedl, *Solution processed vanadium pentoxide as charge extraction layer for organic solar cells*, *Advanced Energy Materials* **1** (2011), no. 3, 377-381.
  9. J. Meyer, K. Zilberberg, T. Riedl and A. Kahn, *Electronic structure of vanadium pentoxide: An efficient hole injector for organic electronic materials*, *Journal of Applied Physics* **110** (2011), no. 3, 033710-033715.
  10. F. X. Xie, W. C. H. Choy, C. D. Wang, X. C. Li, S. Q. Zhang and J. H. Hou, *Low-temperature solution-processed hydrogen molybdenum and vanadium bronzes for an efficient hole-transport layer in organic electronics*, *Advanced Materials* **25** (2013), no. 14, 2051-2055.
  11. I. Hancox, L. A. Rochford, D. Clare, M. Walker, J. J. Mudd, P. Sullivan, S. Schumann, C. F. McConville and T. S. Jones, *Optimization of a high work function solution processed vanadium oxide hole-extracting layer for small molecule and polymer organic photovoltaic cells*, *Journal of Physical Chemistry C* **117** (2013), no. 1, 49-57.
  12. A. S. Negreira, S. Aboud and J. Wilcox, *Surface reactivity of  $V_2O_5(001)$ : Effects of vacancies, protonation, hydroxylation, and chlorination*, *Physical Review B* **83** (2011), no. 4.

13. Y. Suchorski, L. Rihko-Struckmann, F. Klose, Y. Ye, M. Alandjiyska, K. Sundmacher and H. Weiss, *Evolution of oxidation states in vanadium-based catalysts under conventional XPS conditions*, Applied Surface Science **249** (2005), no. 1–4, 231-237.
14. G. A. Sawatzky and D. Post, *X-ray photoelectron and auger-spectroscopy study of some vanadium-oxides*, Physical Review B **20** (1979), no. 4, 1546-1555.
15. M. Demeter, M. Neumann and W. Reichelt, *Mixed-valence vanadium oxides studied by XPS*, Surface Science **454–456** (2000), no. 0, 41-44.
16. K. Hermann, M. Witko, R. Druzinic and R. Tokarz, *Hydrogen assisted oxygen desorption from the  $V_2O_5(010)$  surface*, Topics in Catalysis **11** (2000), no. 1-4, 67-75.
17. D. S. Toledano, V. E. Henrich and P. Metcalf, *Surface reduction of  $Cr-V_2O_3$  by  $CO$* , Journal of Vacuum Science & Technology a-Vacuum Surfaces and Films **18** (2000), no. 4, 1906-1914.
18. M. V. Ganduglia-Pirovano and J. Sauer, *Stability of reduced  $V_2O_5(001)$  surfaces*, Physical Review B **70** (2004), no. 4.
19. G. W. Coulston, E. A. Thompson and N. Herron, *Characterization of VPO catalysts by X-ray photoelectron spectroscopy*, Journal of Catalysis **163** (1996), no. 1, 122-129.

20. Z. A. Tan, W. Q. Zhang, C. H. Cui, Y. Q. Ding, D. P. Qian, Q. Xu, L. J. Li, S. S. Li and Y. F. Li, *Solution-processed vanadium oxide as a hole collection layer on an ITO electrode for high-performance polymer solar cells*, *Physical Chemistry Chemical Physics* **14** (2012), no. 42, 14589-14595.
21. K. Zilberberg, J. Meyer and T. Riedl, *Solution processed metal-oxides for organic electronic devices*, *Journal of Materials Chemistry C* **1** (2013), no. 32, 4796-4815.
22. G. Teran-Escobar, J. Pampel, J. M. Caicedo and M. Lira-Cantu, *Low-temperature, solution-processed, layered V<sub>2</sub>O<sub>5</sub> hydrate as the hole-transport layer for stable organic solar cells*, *Energy & Environmental Science* **6** (2013), no. 10, 3088-3098.
23. X. C. Li, F. X. Xie, S. Q. Zhang, J. H. Hou and W. C. H. Choy, *MoO<sub>x</sub> and V<sub>2</sub>O<sub>x</sub> as hole and electron transport layers through functionalized intercalation in normal and inverted organic optoelectronic devices*, *Light-Science & Applications* **4** (2015), 7.
24. D. X. Long, Y. Xu, S. J. Kang, W. T. Park, E. Y. Choi, Y. C. Nah, C. Liu and Y. Y. Noh, *Solution processed vanadium pentoxide as charge injection layer in polymer field-effect transistor with Mo electrodes*, *Organic Electronics* **17** (2015), 66-76.
25. M. T. Greiner, M. G. Helander, W.-M. Tang, Z.-B. Wang, J. Qiu and Z.-H. Lu, *Universal energy-level alignment of molecules on metal oxides*, *Nature Materials* **11** (2012), no. 1, 76-81.

26. K. Hong and J.-L. Lee, *Charge generation mechanism of metal oxide interconnection in tandem organic light emitting diodes*, Journal of Physical Chemistry C **116** (2012), no. 10, 6427-6433.
27. M. C. Gwinner, R. Di Pietro, Y. Vaynzof, K. J. Greenberg, P. K. H. Ho, R. H. Friend and H. Sirringhaus, *Doping of organic semiconductors using molybdenum trioxide: A quantitative time-dependent electrical and spectroscopic study*, Advanced Functional Materials **21** (2011), no. 8, 1432-1441.
28. J. G. Choi and L. T. Thompson, *XPS study of as-prepared and reduced molybdenum oxides*, Applied Surface Science **93** (1996), no. 2, 143-149.
29. J. Meyer, A. Shu, M. Kroger and A. Kahn, *Effect of contamination on the electronic structure and hole-injection properties of MoO<sub>3</sub>/organic semiconductor interfaces*, Applied Physics Letters **96** (2010), no. 13, 133308.
30. C.-T. Lin, C.-H. Yeh, M.-H. Chen, S.-H. Hsu, C.-I. Wu and T.-W. Pi, *Influences of evaporation temperature on electronic structures and electrical properties of molybdenum oxide in organic light emitting devices*, Journal of Applied Physics **107** (2010), no. 5, 053703.
31. J. Li, Q. Y. Bao, H. X. Wei, Z. Q. Xu, J. P. Yang, Y. Q. Li, S. T. Lee and J. X. Tang, *Role of transition metal oxides in the charge recombination layer used in tandem organic photovoltaic cells*, J. Mater. Chem. **22** (2012), no. 13, 6285-6290.
32. H. Lee, S. W. Cho, K. Han, P. E. Jeon, C.-N. Whang, K. Jeong, K. Cho and Y. Yi, *The origin of the hole injection improvements at indium tin oxide/molybdenum*

- trioxide/n,n'-bis(1-naphthyl)-n,n'-diphenyl-1,1'-biphenyl-4,4'-diamine interfaces*, Applied Physics Letters **93** (2008), no. 4.
33. M. Kroeger, S. Hamwi, J. Meyer, T. Riedl, W. Kowalsky and A. Kahn, *Role of the deep-lying electronic states of MoO<sub>3</sub> in the enhancement of hole-injection in organic thin films*, Applied Physics Letters **95** (2009), no. 12.
34. M. Vasilopoulou, L. C. Palilis, D. G. Georgiadou, S. Kennou, I. Kostis, D. Davazoglou and P. Argitis, *Barrierless hole injection through sub-bandgap occupied states in organic light emitting diodes using substoichiometric MoO<sub>x</sub> anode interfacial layer*, Applied Physics Letters **100** (2012), no. 1, 013311-013314.
35. J. Meyer, A. Shu, M. Kroeger and A. Kahn, *Effect of contamination on the electronic structure and hole-injection properties of MoO<sub>3</sub>/organic semiconductor interfaces*, Applied Physics Letters **96** (2010), no. 13.
36. J. Meyer and A. Kahn, *Electronic structure of molybdenum-oxide films and associated charge injection mechanisms in organic devices*, Journal of Photonics for Energy **1** (2011).
37. K. Kanai, K. Koizumi, S. Ouchi, Y. Tsukamoto, K. Sakanoue, Y. Ouchi and K. Seki, *Electronic structure of anode interface with molybdenum oxide buffer layer*, Organic Electronics **11** (2010), no. 2, 188-194.
38. P.-S. Wang, I. W. Wu, W.-H. Tseng, M.-H. Chen and C.-I. Wu, *Enhancement of current injection in organic light emitting diodes with sputter treated molybdenum oxides as hole injection layers*, Applied Physics Letters **98** (2011), no. 17.

39. H. Wang, Z. Liu, M. F. Lo, T. W. Ng, C.-S. Lee, D. Yan and S.-T. Lee, *Organic-inorganic heterojunction field-effect transistors*, *Journal of Applied Physics* **107** (2010), no. 2.
40. N. Blouin, A. Michaud and M. Leclerc, *A low-bandgap poly(2,7-carbazole) derivative for use in high-performance solar cells*, *Advanced Materials* **19** (2007), no. 17, 2295-+.
41. F. Etzold, I. A. Howard, R. Mauer, M. Meister, T.-D. Kim, K.-S. Lee, N. S. Baek and F. Laquai, *Ultrafast exciton dissociation followed by nongeminate charge recombination in PCDTBT:PCBM photovoltaic blends*, *Journal of the American Chemical Society* **133** (2011), no. 24, 9469-9479.
42. D. C. Watters, H. Yi, A. J. Pearson, J. Kingsley, A. Iraqi and D. Lidzey, *Fluorene-based co-polymer with high hole mobility and device performance in bulk heterojunction organic solar cells*, *Macromolecular rapid communications* **34** (2013), no. 14, 1157-1162.

# Chapter 5

## Vanadium Oxide OPV Devices

### 5.1 Introduction

Currently the lifetime of devices incorporating the highest performing materials is below the 10 year mark required [1, 2]. One approach to improve the lifetime of devices is to investigate replacements for the commonly used hole extraction interfacial layer, polyethylene dioxythiophene:polystyrenesulfonate (PEDOT:PSS) [3-5]. This is because, despite the positive aspects of aqueous PEDOT:PSS, the residual moisture and the acidic nature of PEDOT:PSS can cause degradation of the electrode and organic films and therefore reduce the device's operational lifetime [6-9]. In addition PEDOT:PSS is highly hygroscopic allowing for the wicking of moisture into devices; this results in several different degradation mechanisms that can occur, including delamination of weakly adhered layers within the device, and chemical reactions, both within the bulk and at interfaces within devices, that can lead to the introduction of trap states [7].

To overcome some of these issues thin metal oxides such as  $\text{MoO}_3$ ,  $\text{WO}_3$ ,  $\text{NiO}$  and  $\text{V}_2\text{O}_5$  have been used. These materials have been shown to exhibit performances that are similar to or better than OPVs with an interfacial PEDOT:PSS layer [10-13]. However, as with PEDOT:PSS, the presence of water can lead to changes at the interface between metal oxides and organic semiconductors due to the intercalation of water within metal



oxide clusters, leading to changes within the energy level structure [14]. This makes the improvement of processing conditions and the reduction in the cost and complexity of depositing these interfacial layers highly desirable.

Solution-processing of the metal oxide interfacial layers is therefore an important target to achieve in order to reduce the cost of the deposition of these layers. However, most solution-processed metal oxides require post-deposition treatment such as thermal annealing and oxygen plasma treatment, see **2.7 Utilising Metal Oxides at the Anode Buffer Layer**. These two techniques, although not difficult to implement, are often time-consuming and energy-intensive. For technologies such as organic photovoltaics the incorporation of these post-deposition processing techniques in roll-to-roll setups is extremely impractical. On the other hand, some optoelectronic devices which are fabricated at high temperatures require developed metal oxides which must be able to retain their properties under high temperature fabrication processes.

This chapter shows that it is possible to deposit  $V_2O_x$  from a vanadium(V) oxytriisopropoxide precursor requiring no post-deposition annealing or oxygen plasma treatment. When deposited in air, the films of the precursor material undergo hydrolysis converting into  $V_2O_x$ , (further details were provided in **4.2.1 Vanadium Oxide**). Films of solution-processed  $V_2O_x$  were incorporated into OPV devices achieving a power conversion efficiency of 6.5%, comparable to PEDOT:PSS (6.5%) and vacuum-deposited  $MoO_3$  (6.3%). Furthermore, OPV devices were fabricated with annealed s- $V_2O_x$  layers at high temperatures in air before spin coating the active layer to study their thermal stability. Annealed s- $V_2O_x$  films were characterised via absorption spectroscopy, x-ray photoelectron spectroscopy (XPS), and ultraviolet photoelectron

spectroscopy (UPS) to show the variation in the optical and electronic properties of s- $V_2O_x$ .

## 5.2 Influence of ITO Surface Cleaning Method on OPV Performance

Indium–tin–oxide (ITO) has been used widely in organic solar cells as an anode owing to high conductivity and transmittance to visible light. Several studies have revealed that the method used to clean ITO surface is significantly sensitive to the work function and the surface properties [15-17]. Accordingly, it is important to explore the relationship between the cleaning method of ITO and OPV performance. In this work, ITO substrates were cleaned using three different methods:

- a) Hellmanex solution and IPA
- b) Hellmanex solution, IPA, and NaOH solution
- c) Hellmanex solution, IPA, NaOH solution, and O<sub>2</sub> plasma treatment

The procedure of ITO washing was described in detail in **4.3.3 Device Fabrication**. Here, the impact of ITO cleaning with NaOH solution (10 wt% in water) is compared with other methods. As shown in **Table 5.1**, the performance of PCDTBT:PC<sub>70</sub>BM devices improved as they underwent more cleaning processes. The efficiency of the devices increased by 10% when they were cleaned with NaOH solution and O<sub>2</sub> plasma. This optimisation in PCE is attributed to the increase of V<sub>oc</sub> and FF. The PCE of PCDTBT: PC<sub>70</sub>BM devices improved from 4.7% to 4.9% when the substrates were cleaned by a NaOH solution. Furthermore, the devices that were exposed to O<sub>2</sub> plasma showed better performance than those without the plasma treatment. Consequently,

cleaning substrates with a NaOH solution and giving them an O<sub>2</sub> plasma treatment can enhance the performance of OPV devices.

This improvement can be attributed to the removal of carbon contaminants on the ITO surface after cleaning with NaOH and O<sub>2</sub> plasma treatment which results in an increase in the work function and thus reduces the energy barrier at the interface [18, 17].

**Table 5.1** Characteristic data of PCDTBT:PC<sub>70</sub>BM devices with different cleaning methods.

The errors quoted are defined by the standard deviation about the mean.

Cleaning method	Average PCE [%]	V <sub>oc</sub> [V]	J <sub>sc</sub> [mA.cm <sup>-2</sup> ]	FF [%]
Hell. + IPA	4.8 ± 0.25	0.83	10.4 ± 0.1	57.6 ± 1.5
Hell. + NaOH + IPA	5.0 ± 0.24	0.84	10.4 ± 0.15	59.8 ± 0.9
Hell. + IPA + O <sub>2</sub> plasma	5.1 ± 0.26	0.84	10.5 ± 0.27	60.5 ± 1.2
Hell. + NaOH + IPA + O <sub>2</sub> plasma	5.2 ± 0.29	0.85	10.5 ± 0.45	60.1 ± 1.1

### 5.3 Optimisation of the Thickness of the s-V<sub>2</sub>O<sub>x</sub> Anode Buffer Layer for Organic Photovoltaic Devices

A considerable number of studies have reported that the OPV performance depends critically on the buffer layer thickness (i.e. the effect on the optical losses and serial resistance R<sub>s</sub>). To investigate the influence of solution-processed vanadium oxide s-V<sub>2</sub>O<sub>x</sub> on the efficiency of OPVs, various PCDTBT:PC<sub>70</sub>BM devices were fabricated with various s-V<sub>2</sub>O<sub>x</sub> thicknesses. All the devices shared a structure of ITO(100 nm)/s-V<sub>2</sub>O<sub>x</sub>/PCDTBT:PC<sub>70</sub>BM(70 nm)/Ca(5 nm)/Al(100 nm) but had varying V<sub>2</sub>O<sub>x</sub> thicknesses (5-25 nm). **Figure 5.1** shows the output J–V characteristics of OPV devices

upon illumination with an AM1.5G simulated solar spectrum (1 sun). The extracted solar cell parameters (i.e power conversion efficiency (PCE), open-circuit voltage ( $V_{oc}$ ), short-circuit current ( $J_{sc}$ ) and fill factor (FF)) are summarised in **Table 5.2**.

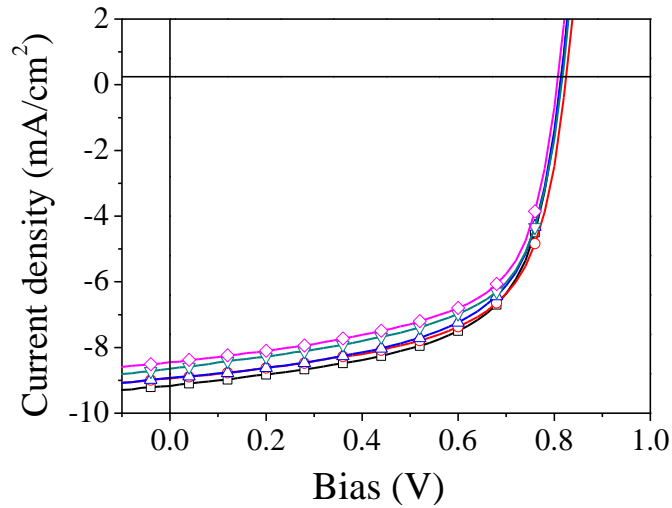


**Figure 5.1** Current density-voltage (J-V) characteristics for PCDTBT:PC<sub>70</sub>BM devices with various thicknesses of s-V<sub>2</sub>O<sub>x</sub> films; (□) 5 nm, (○) 10 nm, (△) 15 nm, (▽) 20 nm and (◇) 25 nm.

**Table 5.2** Photovoltaic parameters under the AM1.5G solar spectrum for PCDTBT:PCBM devices with different s-V<sub>2</sub>O<sub>x</sub> thicknesses.

Thickness (nm)	Maximum PCE [%]	Average PCE <sub>(av)</sub> [%]	V <sub>oc</sub> [V]	J <sub>sc</sub> [mA.cm <sup>-2</sup> ]	FF [%]	R <sub>s</sub> [Ω.cm <sup>2</sup> ]	R <sub>sh</sub> [Ω.cm <sup>2</sup> ]
5	4.63	4.5 ±0.12	0.81	9.2 ±0.22	61.1 ±1.2	10.6 ±0.9	843 ±91
10	4.67	4.5 ±0.14	0.82	9.0 ±0.13	61.3 ±1.7	11.9 ±1.0	837 ±115
15	4.53	4.4 ±0.26	0.81	8.9 ±0.14	61.0 ±2.6	11.3 ±0.7	812 ±146
20	4.35	4.3 ±0.08	0.82	8.6 ±0.41	60.8 ±2.7	13.6 ±1.7	765 ±138
25	4.27	4.2 ±0.11	0.81	8.4 ±0.12	60.6 ±0.9	17.6 ±0.4	707 ±84

As can be seen, all devices showed good performance with PCE and FF higher than 4.2% and 60%, respectively. The thickest s-V<sub>2</sub>O<sub>x</sub> device exhibited a lower PCE than the other devices due to the slightly lower J<sub>sc</sub>, as shown in **Table 5.2**. The decreased J<sub>sc</sub> can be attributed to the limit in the optical transmissivity of thick s-V<sub>2</sub>O<sub>x</sub> films at shorter wavelengths as discussed previously in **4.2.1 Vanadium Oxide**. Furthermore, an increase in the series resistance and a decrease in the shunt resistance can be observed with increase in thickness indicating increased charge carrier recombination at the interface between the anode and the active layer. Consequently, it can be concluded that devices with low s-V<sub>2</sub>O<sub>x</sub> thicknesses can work effectively and are therefore applicable to transparent organic devices.

### 5.4 Hydrolysis

As mentioned previously in **4.2.1 Vanadium Oxide**, s-V<sub>2</sub>O<sub>x</sub> thin film is formed due to different chemical reactions (i.e. hydrolysis process) and condensation of molecular precursors at lower temperature. Several studies have reported that a hydrolysis reaction in ambient atmosphere occurs quickly for sol-gel metal oxide based on a precursor solution [19-21]. To explore how long s-V<sub>2</sub>O<sub>x</sub> thin films need to be exposed to air for hydrolysis reaction, fabricated s-V<sub>2</sub>O<sub>x</sub> layers were stored in ambient air for different lengths of time before spin coating the PFDT2BT-8:PC<sub>70</sub>BM blend. The average device results obtained are illustrated in **Figure 5.2**. It can be seen that PCE and J<sub>sc</sub> are almost identical for all devices; this indicates that hydrolysis reaction occurs very fast. Furthermore, looking at the V<sub>oc</sub> values, a gradual decrease can be observed over time. To confirm this result, the same experiment was carried out with PCDTBT:PC<sub>70</sub>BM blend and similar result was obtained. Consequently, no major improvement can be seen in the performance after storing s-V<sub>2</sub>O<sub>x</sub> thin films in ambient atmosphere for long

time. This finding is in contrast with some previous reports which suggest that vanadium oxide deposited from solution should be stored in air for an hour [20, 22-25]. This difference can be ascribed to the nature of precursor they used, such as vanadium (III) acetyl acetate and  $V_2O_5$  powder, or to the different environmental conditions where the thin film is fabricated, such as nitrogen glovebox or a low humidity environment [26].

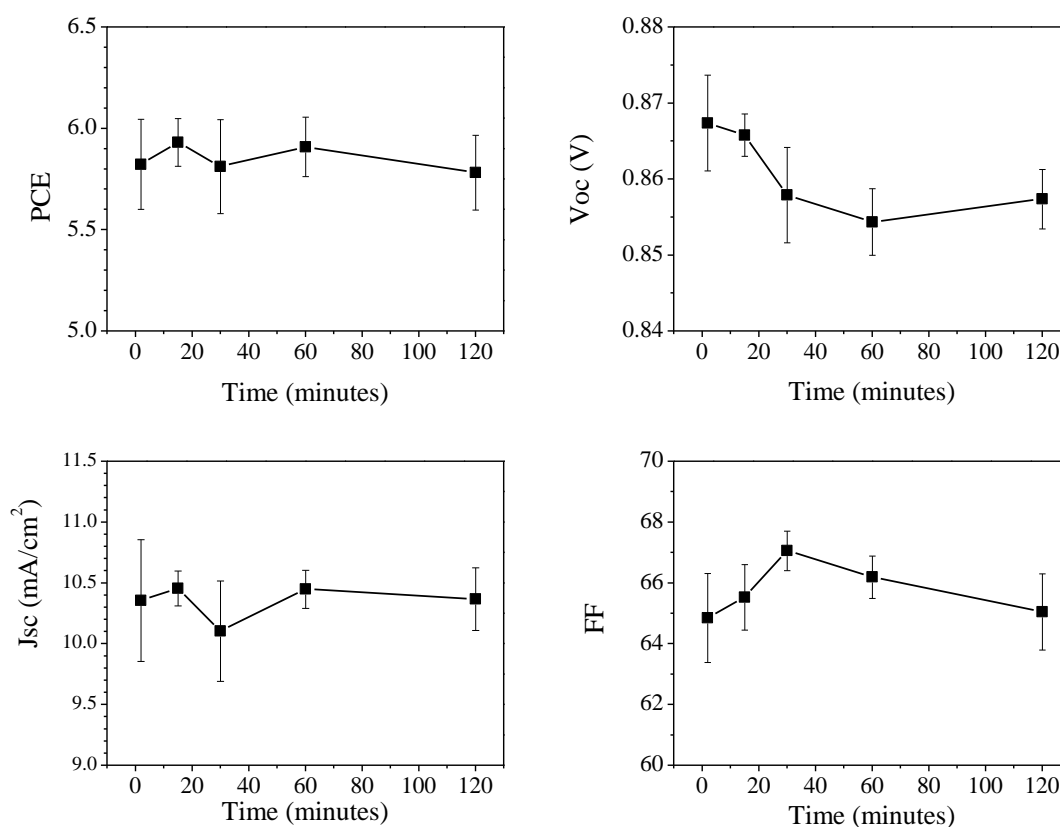


**Figure 5.2** Comparison of PFDT2BT-8:PC<sub>70</sub>BM device performance with vanadium oxide spin coated from solution and stored in ambient conditions for different periods of time.

## 5.5 Influence of Surface Roughness on OPV Device Performance

To determine the impact of the surface topography of s-V<sub>2</sub>O<sub>x</sub> thin layer on the performance of an OPV device, different concentrations of the V<sub>2</sub>O<sub>x</sub> solution (10, 5, 3, and 1 mg/ml) were spin coated in ambient conditions on clean silicon surfaces with different speeds. The topography of the surfaces was characterised by tapping-mode AFM as mentioned in **4.2.3 Atomic Force Microscopy**. **Figure 5.3** shows the AFM height images of bare Si and s-V<sub>2</sub>O<sub>x</sub> films cast from 10 mg/ml solution at speeds of 500, 1000 and 2000 RPM. As can be observed, the high-concentration solution with low speed shows a film with a root mean square (rms) roughness of 17 nm. This high roughness can be attributed to the formation of large islands due to the long evaporation time of the solvent, as shown in the phase image of **Figure 5.3** (f). In addition to causing low conductivity, which results from thick films, rough surfaces lead to poor contact at the interface with active layers [27]. When the spin-coating speed is increased to 1000 RPM, smaller islands are observed, and the surface roughness rms falls to 4.8 nm. **Figure 5.3** (d) illustrates a uniform and smooth V<sub>2</sub>O<sub>x</sub> surface with a rms roughness of 1 nm that was obtained with a spin speed of 2000 RPM. This surface is quite similar to the Si surface (rms = 0.9 nm). Consequently, the AFM images clearly indicate that s-V<sub>2</sub>O<sub>x</sub> films made from high-concentration solutions should be spun coated at speeds  $\geq$  2000 rpm to produce smooth and flat surfaces.

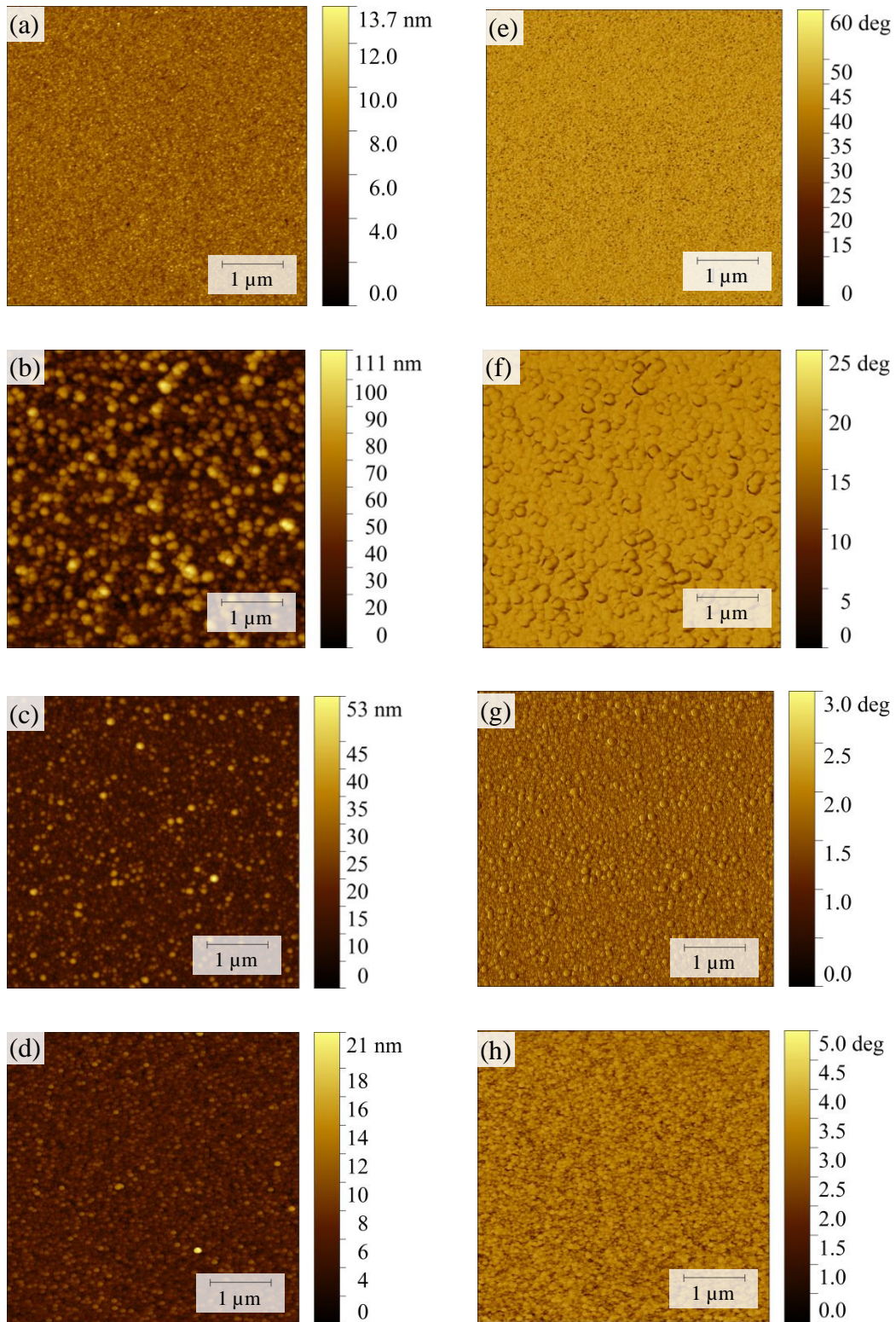


**Figure 5.3** AFM height images with a size of  $5\mu\text{m} \times 5\mu\text{m}$  for (a) the bare Si surface and (b-d)  $s\text{-V}_2\text{O}_x$  thin films spin coated on a Si surface showing rms of 17, 4.8, 1.2 nm respectively. e-h are the phase images for the same samples.



**Figure 5.4** summarises the roughness of various s-V<sub>2</sub>O<sub>x</sub> films spin coated from different concentrations and at varied spin speeds. It can be seen that low concentrations can exhibit smooth surfaces at low speeds. Nevertheless, all the s-V<sub>2</sub>O<sub>x</sub> films that were fabricated in this work were spin cast at high speeds (> 2000 RPM) to ensure smooth and flat surfaces. To confirm this result two s-V<sub>2</sub>O<sub>x</sub> films were fabricated on ITO substrate (rms roughness = 1.83 nm) instead of Si surface. s-V<sub>2</sub>O<sub>x</sub> layer cast from 5 mg/ml at low speed (1000 RPM) showed rms roughness of 3 nm while the films cast at 3000 RPM displayed a rms of 1.9 nm.

To investigate the effect of roughness on the performance of the devices, 3 PCDTBT:PC<sub>70</sub>BM devices were fabricated with 8 nm thin film of s-V<sub>2</sub>O<sub>x</sub> and different values of rms. As shown in **Table 5.3**, all devices exhibited almost similar results, even though the variation in roughness exceeded 50%. This confirms that a slightly rough surface (< 3 nm) should not influence the performance of an OPV device.

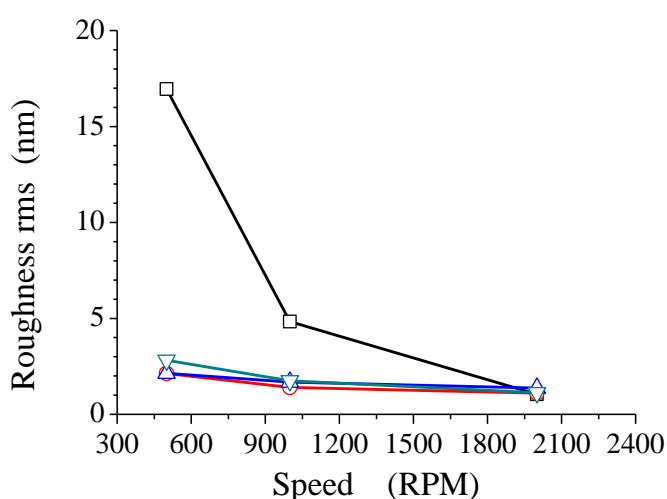


**Figure 5.4** The roughness (rms) of s-V<sub>2</sub>O<sub>x</sub> spin cast from concentrations (▽) 1 mg/ml, (△) 3 mg/ml, (○) 5 mg/ml and (□) 10 mg/ml at different spin speeds.

**Table 5.3** Photovoltaic parameters of PCDTBT:PC<sub>70</sub>BM devices with s-V<sub>2</sub>O<sub>x</sub> layers of varying surface roughness.

<b>rms (nm)</b>	<b>Average PCE [%]</b>	<b>V<sub>oc</sub> [V]</b>	<b>J<sub>sc</sub> [mA.cm<sup>-2</sup>]</b>	<b>FF [%]</b>
2.6	4.3 ± 0.15	0.78	9.1 ± 0.1	60.6 ± 1.2
1.5	4.3 ± 0.2	0.78	9.1 ± 0.4	61.3 ± 1.1
1.1	4.2 ± 0.11	0.76	8.7 ± 0.1	62.1 ± 1.2

## 5.6 Impact of Atmosphere Gases in s-V<sub>2</sub>O<sub>x</sub> Morphology

It was also assessed whether the environment in which the s-V<sub>2</sub>O<sub>x</sub> was deposited would affect the performance of OPV devices. PCDTBT:PC<sub>70</sub>BM devices were fabricated with a s-V<sub>2</sub>O<sub>x</sub> buffer layer spin coated inside a nitrogen glove box. The PCE of these devices dropped to 1.2%, which is considerably lower compared to the efficiency of 4.3% for the s-V<sub>2</sub>O<sub>x</sub> films deposited in air. The J-V characteristics showed J<sub>sc</sub> and V<sub>oc</sub> of 8 mA.cm<sup>-2</sup> and 0.35 V respectively. The low V<sub>oc</sub> indicates poor contact and charge carrier recombination at the interface between the anode and the active layer. **Figure 5.5** displays AFM images of a s-V<sub>2</sub>O<sub>x</sub> film deposited inside the nitrogen glove box. As can be seen, the film contains nano-scope voids that probably formed as a result of the changes in the solvent evaporation speed and thus change solution viscosity during film formation [25, 28]. Moreover, the solution cannot undergo a hydrolysis reaction in a nitrogen filled glovebox as the presence of water is limited to below 0.5ppm [26]. Therefore, without a hydrolysis reaction the formed film shows a metallic structure with the Fermi level pinned above the V3d orbital resulting in low work function and thus forming a high energy barrier at the interface [29].

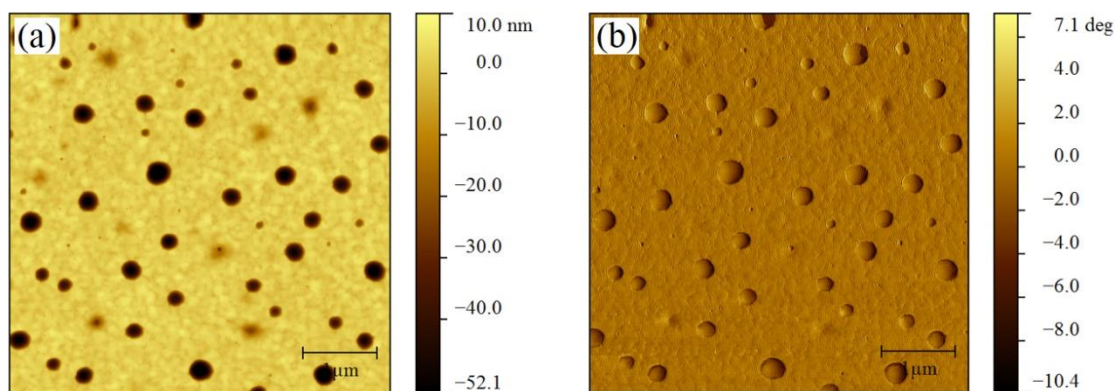


**Figure 5.5** AFM topography image of the  $s\text{-V}_2\text{O}_x$  layer deposited in the nitrogen glove box; (a) height image and (b) phase image. Small voids with diameter  $< 300$  nm was formed in the vanadium oxide film.

## 5.7 Spray Coating vs Spin Coating

In previous sections, organic photovoltaic device results are shown for vanadium oxide deposited from solution via the spin coating method. In order to eventually use vanadium oxide for commercial production, uniform  $s\text{-V}_2\text{O}_x$  films should be produced by using some commercial deposition techniques such as spray coating. Here, the comparison between OPV devices using spin coated and spray coated  $s\text{-V}_2\text{O}_x$  films is discussed. AFM topography scans for  $s\text{-V}_2\text{O}_x$  layers with a thickness of 8 nm deposited on ITO substrate are shown in **Figure 5.6**. It can be observed that the surface of spin coated vanadium oxide is smoother than spray coated film (rms roughness of 2 and 3.2 nm respectively). Nevertheless, both samples provide a uniform and flat surface which can achieve good contact with the subsequent layer. As discussed in **5.5 Influence of surface roughness on OPV device performance**, the roughness of about 3 nm does not affect the efficiency of OPV devices.

In order to determine how effective spray coated vanadium oxide is within organic photovoltaic devices it was compared against devices with spin coated s-V<sub>2</sub>O<sub>x</sub>.

**Table 5.4** presents the device metrics for both OPV devices with a PCDTBT:PC<sub>70</sub>BM active layer. It can be observed that both devices demonstrate comparable performances. The slightly lower performance of spray coated devices can be attributed to thickness variations that occur across the length of the substrate and some contamination from the used syringe in the ultrasonic spray-coating.

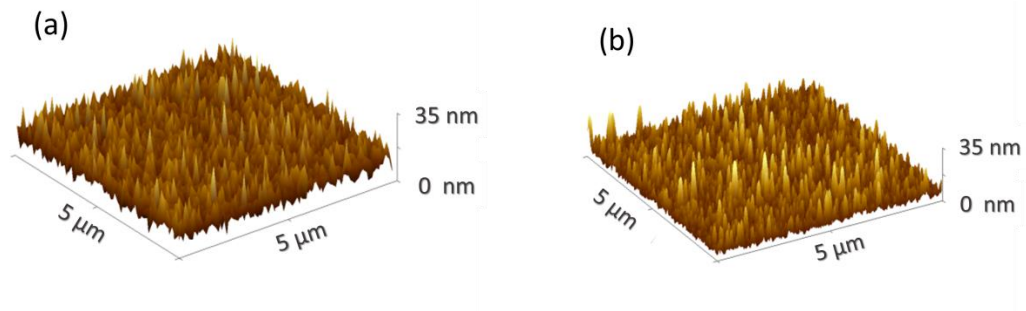


**Figure 5.6** shows surface morphology of the solution-processed V<sub>2</sub>O<sub>x</sub> film deposited by (a) spin coating and (b) spray coating techniques.

**Table 5.4** OPV operating parameters with a PCDTBT:PC<sub>70</sub>BM active layer and s-V<sub>2</sub>O<sub>x</sub> thin film deposited by either the spin coating or spray coating method.

Deposition method	Average PCE [%]	V <sub>oc</sub> [V]	J <sub>sc</sub> [mA.cm <sup>-2</sup> ]	FF [%]
Spin	4.6 ± 0.12	0.81	9.3 ± 0.2	61.4 ± 0.9
Spray	4.5 ± 0.17	0.80	8.7 ± 0.1	60.1 ± 1.1

## 5.8 Comparison of s-V<sub>2</sub>O<sub>x</sub> Films with Commonly Utilised Hole- extracting Materials

To assess the performance of OPV devices with the s-V<sub>2</sub>O<sub>x</sub> interlayer, sets of devices were fabricated with the most widely used HELs: PEDOT:PSS, solution processed MoO<sub>3</sub> and vacuum deposited MoO<sub>3</sub> and V<sub>2</sub>O<sub>x</sub>. In addition, devices were fabricated with two different donor polymers to confirm the obtained results. The first group of devices was fabricated with a poly[9,9-dioctylfluorene-4,7-alt-(5,6-bis(octyloxy)-4,7-di(2,2'-bithiophen-5-yl) benzo[c][1,2,5]thiadiazole)-5,5-diy] PFDT2BT-8:PC<sub>70</sub>BM active layer that had been spun coated on top of various HEL materials within the nitrogen filled glovebox. The fabrication method of these HEL thin films was detailed in **4.3 OPV Device Fabrication**. All devices were fabricated in parallel to reduce the variation in results that can occur due to different experimental conditions. **Figure 5.7** shows the variations in device performance parameters for OPV devices with different HEL layers which represent the average of at least 12 pixels from 18 pixels defined on three separate substrates. It can be seen that using PEDOT:PSS and s-V<sub>2</sub>O<sub>x</sub> layers as HEL showed a similar photovoltaic response which is slightly better than devices fabricated with a MoO<sub>3</sub> interlayer. Interestingly, although the low V<sub>oc</sub> of s-V<sub>2</sub>O<sub>x</sub> devices, which can be attributed to the fabrication process in ambient air, it is clear that s-V<sub>2</sub>O<sub>x</sub> film significantly enhances the fill factor (FF<sub>max</sub> = 70%). Although the resistance of most solution processed metal oxide films is typically higher than those fabricated by vacuum evaporation [30], the low series resistance R<sub>s</sub> of s-V<sub>2</sub>O<sub>x</sub> can be attributed to the limited thickness of the film (typically 4-5 nm).

Another group of devices was fabricated with a PCDTBT:PC<sub>70</sub>BM active layer and various anode buffer layers. As shown in **Figure 5.8**, vacuum evaporated HELs offer better performance than those deposited from solution. This can be ascribed to the high shunt resistance  $R_{sh}$  and low  $R_s$  of evaporated metal oxides. Despite the high performance of MoO<sub>3</sub> devices, they offer low  $V_{oc}$  which can be attributed to some experimental defects. In comparison to PFDT2BT-8:PC<sub>70</sub>BM devices it can be observed that devices with solution processed vanadium oxide show a lower performance than others. Nevertheless, the results of both groups show that the performance is the same within experimental error for the Power Conversion Efficiency (PCE), Short circuit current ( $J_{sc}$ ), and open circuit Voltage ( $V_{oc}$ ). Consequently, in comparison to other HELs materials that require post deposition treatment, either thermal annealing or O<sub>2</sub> plasma treatment, the obtained results indicate that a high performance can be achieved for OPV devices by using untreated s-V<sub>2</sub>O<sub>x</sub> films. This offers the possibility of using solution processed V<sub>2</sub>O<sub>x</sub> with large scale printing via roll-to-roll processing.

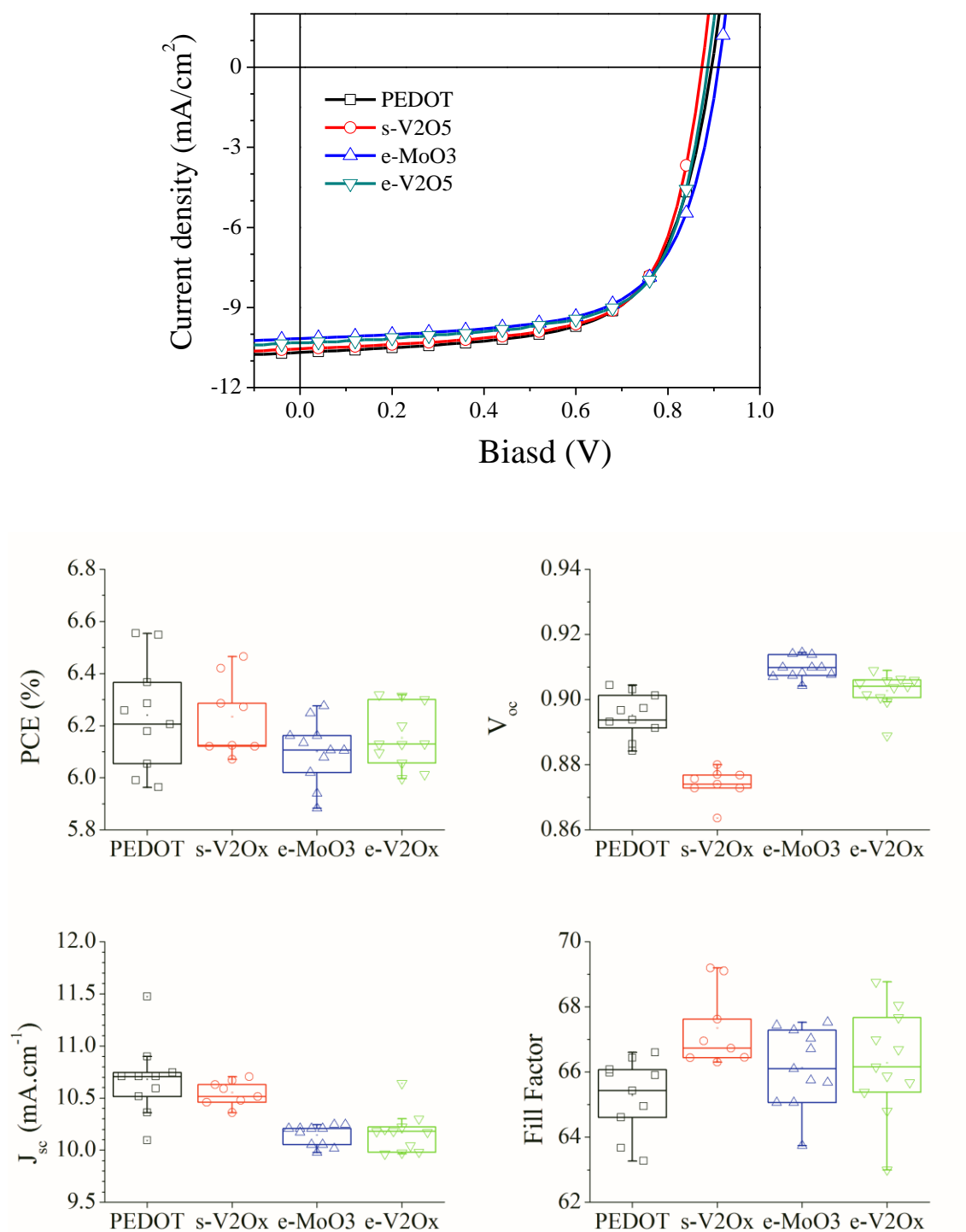


**Figure 5.7** (a) J-V characteristics of optimised devices with a PFDT2BT-8:PC<sub>70</sub>BM active layer for various hole extraction materials; PEDOT:PSS, solution processed vanadium oxide and vacuum deposited V<sub>2</sub>O<sub>x</sub> and MoO<sub>3</sub>. (b) Comparison of performance parameters of devices.

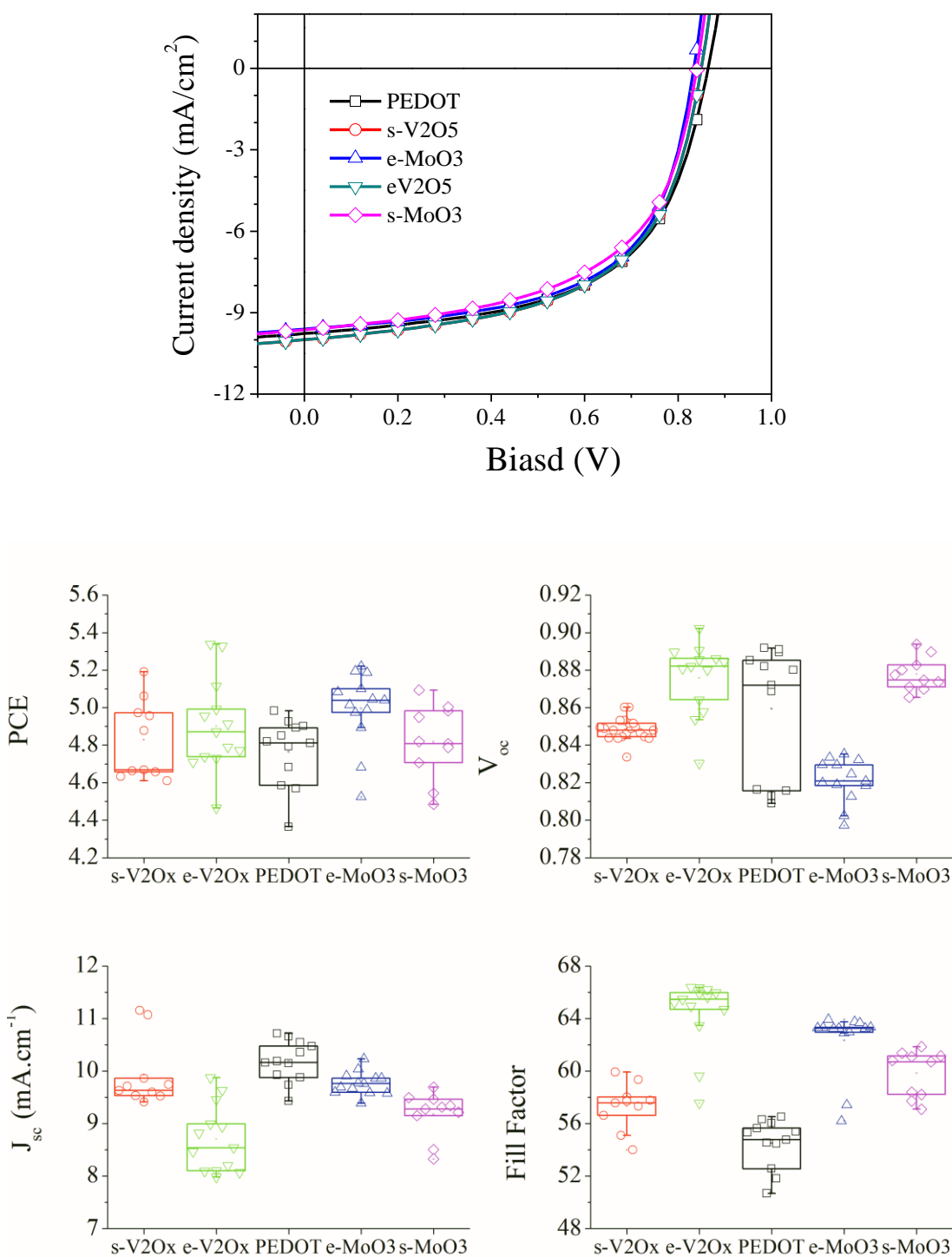


**Figure 5.8** (a) J-V characteristics of optimised devices with a PCDTBT:PC<sub>70</sub>BM active layer for various HEL materials; PEDOT:PSS, solution processed V<sub>2</sub>O<sub>x</sub> and MoO<sub>3</sub>, and vacuum deposited V<sub>2</sub>O<sub>x</sub> and MoO<sub>3</sub>. (b) Comparison of performance parameters of OPV devices.



**Table 5.5** the average values for the Power Conversion Efficiency (PCE), Short circuit current ( $J_{sc}$ ), and open circuit Voltage ( $V_{oc}$ ), Fill Factor (FF) for OPV device fabricated with either PFDT2BT-8:PC<sub>70</sub>BM and PCDTBT:PC<sub>70</sub>BM active layer and different hole extracting layers. The individual results are the average from at least 18 different pixels with error bars representing the standard deviation about the mean for the top 12 performing pixels.

HEL	Donor polymer	Maximum PCE [%]	Average PCE <sub>(av)</sub> [%]	V <sub>oc</sub> [V]	J <sub>sc</sub> [mA.cm <sup>-2</sup> ]	FF [%]	R <sub>s</sub> [Ω.cm <sup>2</sup> ]	R <sub>sh</sub> [Ω.cm <sup>2</sup> ]
s-V <sub>2</sub> O <sub>x</sub>	PFDT2BT-8	6.46	6.2 ± 0.15	0.88	10.6 ± 0.1	67.4 ± 1.2	10.6 ± 0.9	1230 ± 121
PEDOT:PSS		6.55	6.2 ± 0.2	0.9	10.7 ± 0.4	65.3 ± 1.1	11.5 ± 0.8	1130 ± 115
e-V <sub>2</sub> O <sub>x</sub>		6.31	6.2 ± 0.17	0.91	10.2 ± 0.2	66.3 ± 1.6	11.3 ± 0.7	1202 ± 146
e-MoO <sub>3</sub>		6.27	6.1 ± 0.12	0.91	10.1 ± 0.1	66.1 ± 1.2	12 ± 0.5	1270 ± 176
s-V <sub>2</sub> O <sub>x</sub>	PCDTBT	5.19	4.8 ± 0.2	0.85	9.9 ± 0.6	58 ± 1.8	16 ± 0.9	545 ± 86
PEDOT:PSS		5.00	4.7 ± 0.18	0.87	10.2 ± 0.4	55 ± 1.8	16 ± 1.3	527 ± 97
e-V <sub>2</sub> O <sub>x</sub>		5.33	4.9 ± 0.24	0.86	9.7 ± 0.6	64 ± 2.7	13.3 ± 1.7	735 ± 118
e-MoO <sub>3</sub>		5.22	5 ± 0.2	0.82	9.7 ± 0.2	62 ± 2.5	14.1 ± 0.8	707 ± 84
s-MoO <sub>3</sub>		5.1	4.8 ± 0.2	0.85	9.2 ± 0.4	60 ± 1.7	15.4 ± 1.1	495 ± 109

## 5.9 Inverted OPVs with a s-V<sub>2</sub>O<sub>x</sub> Thin Layer

### 5.9.1 Optimising TiO<sub>x</sub> as an Electron Extracting Layer with e-MoO<sub>3</sub>

In this experiment, solution-processed TiO<sub>x</sub> thin film was used in an inverted OPV structure as an electron extraction layer. Before using the solution-processed V<sub>2</sub>O<sub>x</sub> layer in an inverted structure, the solution-processed TiO<sub>x</sub> thin film had to be optimised using an e-MoO<sub>3</sub> thin film deposited on the top of the active layer. The obtained result was used as a reference for the inverted s-V<sub>2</sub>O<sub>x</sub> devices. The fabrication process of TiO<sub>x</sub> films was described in detail in **4.3 OPV Device Fabrication**. Recent studies have demonstrated a positive light-soaking effect on the performance of TiO<sub>x</sub> based OPV. For this reason, this treatment had to be investigated for an inverted device placed under the AM1.5G solar spectrum for different lengths of time as shown in **Figure 5.9**.

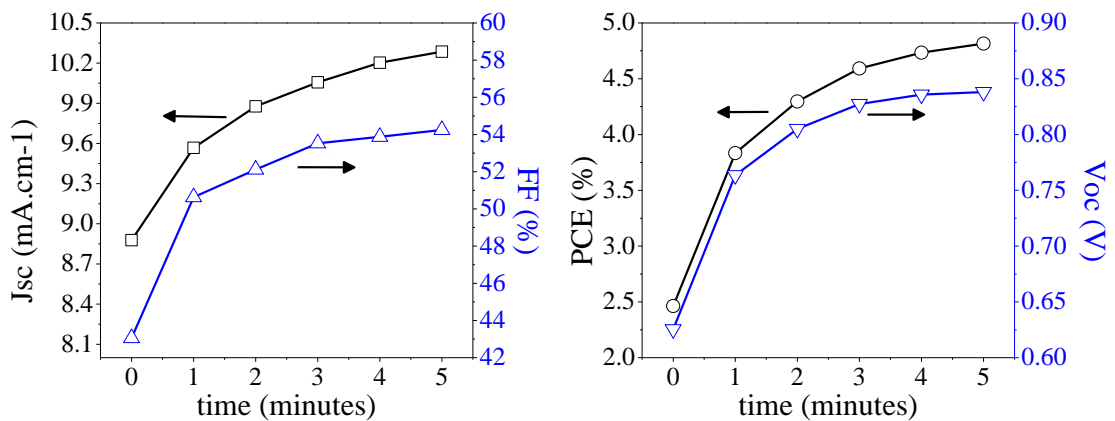


**Figure 5.9** Dependence of inverted OPV parameters upon light soaking with TiO<sub>x</sub> buffer layer as an electron extraction layer. The devices were fabricated with a PCDTBT:PC<sub>70</sub>BM active layer and vacuum deposited MoO<sub>3</sub> on the top.

It can be observed that light soaking for 5 minutes significantly enhanced the  $\text{TiO}_x$  based inverted device. Although the reason for this remains under debate, several studies have suggested that the light soaking can affect trap density in the  $\text{TiO}_x$  and thus increase the conductivity [27, 31, 32]. Other studies have reported that a few minutes of illumination can improve electron extraction at the  $\text{TiO}_x$ /active-layer interface and at the interface between ITO and  $\text{TiO}_x$  [33, 34]. Table 5.6 shows the extracted inverted PCDTBT:PC<sub>70</sub>BM device data with different  $\text{TiO}_x$  film thicknesses after 5 minutes light soaking. The highest efficiency was achieved with a thickness of 20 nm with a  $J_{sc}$  of 10.4 mA.cm<sup>-2</sup> and a PCE of 5.1 %. However, as the thickness of the  $\text{TiO}_x$  increased, the  $V_{oc}$  decreased due to decreasing the shunt resistance  $R_{sh}$ . This resulted from the increase in the charge recombination at the interface with thick  $\text{TiO}_x$ . Consequently, an active layer of 20 nm thickness was selected for fabricating devices with s- $\text{V}_2\text{O}_x$  as an anode buffer layer.

**Table 5.6** Photovoltaic parameters under the AM1.5G solar spectrum for inverted PCDTBT:PCBM devices with different  $\text{TiO}_x$  thicknesses.

Thickness (nm)	Maximum PCE [%]	Average PCE <sub>(av)</sub> [%]	V <sub>oc</sub> [V]	J <sub>sc</sub> [mA.cm <sup>-2</sup> ]	FF [%]	R <sub>s</sub> [Ω.cm <sup>2</sup> ]	R <sub>sh</sub> [Ω.cm <sup>2</sup> ]
5	4.6	4.5 ± 0.13	0.82	10.2 ± 0.14	52.6 ± 0.9	17.6 ± 1.1	693 ± 91
10	4.8	4.7 ± 0.14	0.84	10.3 ± 0.13	54.9 ± 1.0	13.3 ± 1.2	747 ± 125
20	5.1	4.9 ± 0.16	0.85	10.4 ± 0.16	55.3 ± 0.8	12.5 ± 0.7	822 ± 134
30	5.1	4.9 ± 0.09	0.85	10.4 ± 0.22	55.6 ± 1.2	12.9 ± 1.3	805 ± 115
40	4.7	4.6 ± 0.15	0.84	10.3 ± 0.17	53.6 ± 0.5	14.6 ± 0.8	759 ± 105

Moreover, it can be seen that the efficiency of the inverted devices is apparently limited by the FF, which was less than 55% for all devices. Further experiments were carried out to investigate the impact of thermal annealing, either inside or outside the nitrogen glove box, on  $\text{TiO}_x$  films. None of the results obtained showed any obvious development.

### 5.9.2 Inverted OPV Device with a s- $\text{V}_2\text{O}_x$ Layer on the Top

**Table 5.7** presents the results from the optimisation of PCDTBT:PC<sub>70</sub>BM devices based on different thicknesses of solution-processed  $\text{V}_2\text{O}_x$  films. The results were compared with OPV devices fabricated with vacuum-evaporated vanadium oxide. It can be seen that for inverted devices based on vanadium oxide the performance is lower than those fabricated with vacuum-evaporated molybdenum oxide. Looking at the individual values for the FF it can be observed that they are similar for devices based on vacuum-deposition metal oxides. However, in comparison to solution-processed  $\text{V}_2\text{O}_x$  devices the performance is significantly lower than those fabricated with vacuum- evaporated  $\text{V}_2\text{O}_x$  or  $\text{MoO}_x$ . The likely reason for this reduction is contamination of the active layer surface with atmospheric gases as deposition of vanadium oxide from solution should be carried out in ambient conditions to allow for the hydrolysis of the deposit film. The highest PCE for s- $\text{V}_2\text{O}_x$  devices can be observed for those fabricated with a thickness of 5 nm. Increasing the s- $\text{V}_2\text{O}_x$  thickness resulted in a significant reduction of  $V_{oc}$  and thus a decrease in Fill Factor. In addition, this low performance can be attributed to the reduction of the shunt resistance  $R_{sh}$  due to the increased charge carrier recombination. Moreover, as the s- $\text{V}_2\text{O}_x$  is deposited on the top of the active layer, it works as an optical spacer. As a result, increased s- $\text{V}_2\text{O}_x$  thickness leads to a deviation from the

optimal interference space. This can explain why the efficiency decreased with an increase in the thickness and then increased again for 20 nm thickness.

**Table 5.7** OPV operating parameters for inverted PCDTBT:PC<sub>70</sub>BM devices with various thickness of solution-processed V<sub>2</sub>O<sub>x</sub> and 10 nm of vacuum- evaporated V<sub>2</sub>O<sub>x</sub>.

Deposition method	Thickness (nm)	PCE [%]	V <sub>oc</sub> [V]	J <sub>sc</sub> [mA.cm <sup>-2</sup> ]	FF [%]	R <sub>s</sub> [Ω.cm <sup>2</sup> ]	R <sub>sh</sub> [Ω.cm <sup>2</sup> ]
From solution	5	3.5 ±0.15	0.81	9.4 ±0.19	45 ±1.8	34.5 ±1.3	331 ±27
	10	3.1 ±0.12	0.76	9.3 ±0.14	43 ±1.7	33.9 ±1.7	282 ±23
	15	2.6 ±0.18	0.72	8.8 ±0.12	39 ±2.6	40.3 ±0.9	227 ±26
	20	2.8 ±0.08	0.74	9.3 ±0.41	43 ±2.7	37.6 ±1.3	255 ±18
evaporating	10	4.2 ±0.19	0.82	9.7 ±0.16	53 ±1.9	23.2 ±0.4	406 ±32

## 5.10 Thermally Stable s-V<sub>2</sub>O<sub>x</sub> as a Hole Extraction Layer in OPV

To explore the effect of thermal annealing on the photovoltaic response of s-V<sub>2</sub>O<sub>x</sub>-based devices, the s-V<sub>2</sub>O<sub>x</sub> films were annealed at a low temperature for different lengths of time. Before spin coating the PFDT2BT-8:PC<sub>70</sub>BM blend, 5-nm thick s-V<sub>2</sub>O<sub>x</sub> films were spin coated onto clean ITO substrates and then annealed at 75°C in ambient conditions for durations ranging from 10 to 120 minutes. It can be seen in **Figure 5.10(a)** that thermal annealing at a low temperature does not result in significant changes in the devices behaviour. In addition, after annealing for 60 minutes the series resistance R<sub>s</sub> shows a slight decrease with an increase in the shunt resistance R<sub>sh</sub>.

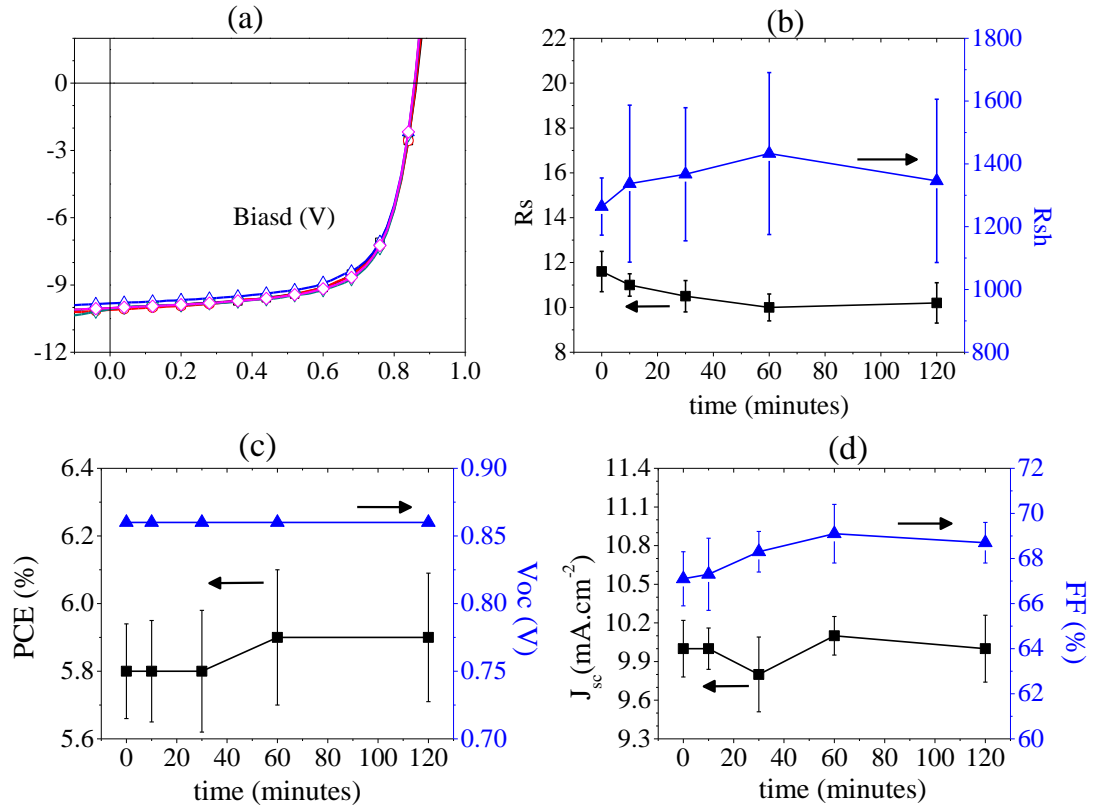


**Figure 5.10** (a) the current density-voltage characteristics of PFDT2BT-8:PC<sub>70</sub>BM devices with (□) unannealed  $s\text{-V}_2\text{O}_x$  interlayer and annealed at 75°C for (○) 10 minutes, (△) 30 minutes, (▽) 60 minutes and (◇) 120 minutes. (b) The series resistance  $R_s$  and shunt resistance  $R_{sh}$  as a function of time. (c) and (d) Comparison of performance parameters of OPV devices.

The photovoltaic parameters summarised in **Figure 5.10(b-d)** indicate a slight optimisation for devices annealed for a longer period of time due to the increase of FF. However, all the results obtained are within the error bars indicating that annealing  $s\text{-V}_2\text{O}_x$  films at low temperature does not enhance the OPV performance.

The influence of high thermal annealing ( $\geq 100^\circ\text{C}$ ) was also studied.  $s\text{-V}_2\text{O}_x$  films were annealed in air at temperatures of 100, 200, 300 and 400°C for 30 minutes. As can be seen in **Figure 5.11(a)**, the performance of devices annealed at temperatures of 100 or 200°C is quite similar to those prepared without heat treatment.

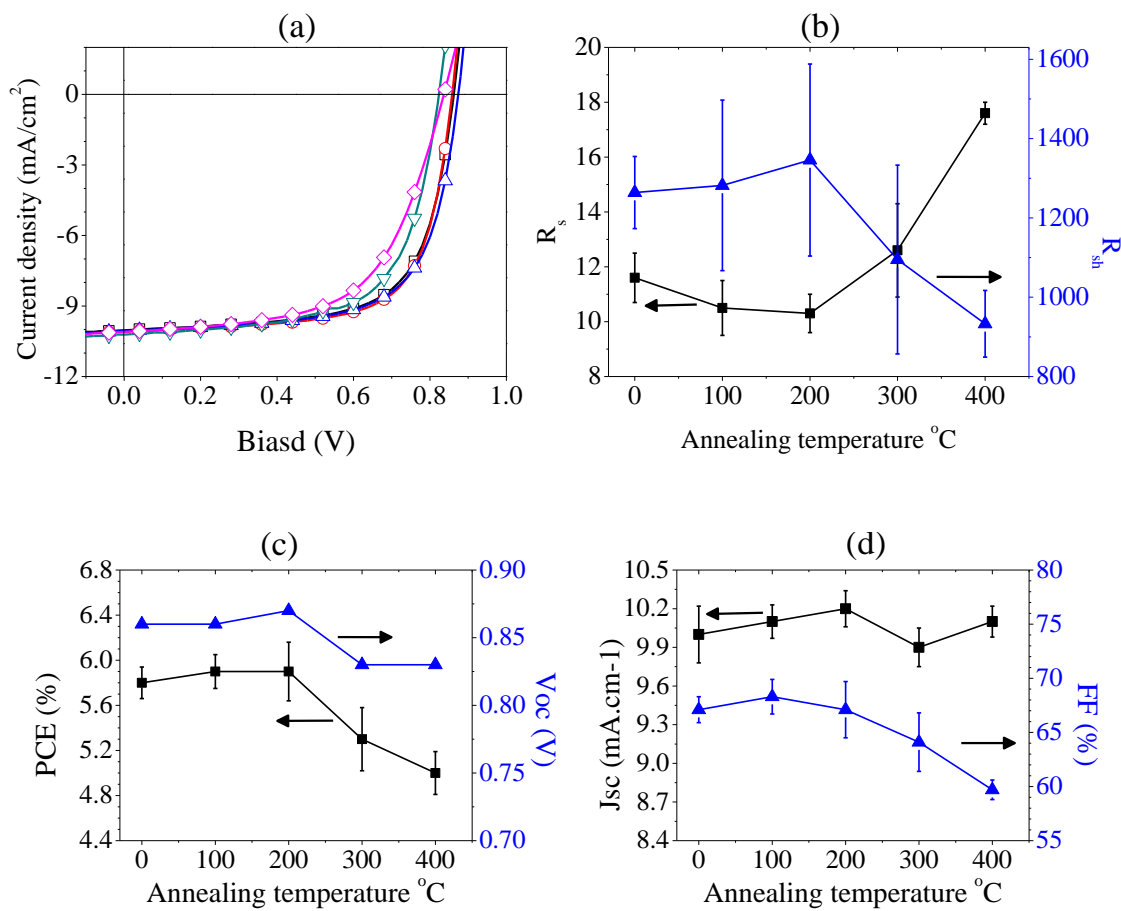


**Figure 5.11** (a) The current density-voltage characteristics of PFDT2BT-8:PC<sub>70</sub>BM based solar cell with (□) unannealed s-V<sub>2</sub>O<sub>x</sub> thin film and annealed for 30 minutes at (○) 100°C, (△) 200°C, (▽) 300°C and (◇) 400°C. (b) The series resistance  $R_s$  and shunt resistance  $R_{sh}$  as a function of annealing temperature. (c) and (d) Comparison of performance parameters of OPV devices as a function of annealing temperature.

From the average device metrics summarised in **Figure 5.11**(b-d) a slight increase can be observed in the PCE of devices annealed up to 200°C which can be ascribed to the relative increase of the shunt resistance  $R_{sh}$  and the decrease of the series resistance  $R_s$ . In contrast, as the film annealing temperature is raised to 400°C, OPV devices show a PCE of only 5% with a decrement approximately 15% lower than that of those with

unannealed films. The relative weak photovoltaic response can be attributed to the decrease in open-circuit voltage due to the change in chemical structure as can be predicted. Furthermore, the shunt resistance falls considerably on annealing above 300°C reaching a minimum  $R_{sh}$  of 933  $\Omega.cm^2$  on annealing at 400°C due to the recombination process at the anode interface. This caused a decrease in holes density at the anode interface leading to a decrease in the internal electric field [35, 36].

In order to explain the decrease in photocurrent for s- $V_2O_x$  films annealed at 400°C, a laser beam-induced current mapping technique was used to take an image of the photocurrent map within the active area of the device. This method has been described in detail in **4.2.7 Laser Beam Induced Current Mapping (LBIC)**. **Figure 5.12** shows the photocurrent map for unannealed s- $V_2O_x$  devices and those annealed at 200°C and 400°C. The pixels which are located in the centre of the device were selected for measurement in order to reduce the degradation mechanism which results from atmospheric gases. As can be seen, the photocurrent scale of images is different due to the unequal illumination intensity as the samples were measured individually. For this reason, the initial analysis of photocurrent images focused on observing any possible defects can appear as a result of thermal annealing and on comparing the uniformity of current density between samples. As can be observed, the unannealed sample shows a uniform photocurrent map, free of pinhole defects. Upon annealing at 200°C and 400°C, LBIC images display small variations in the local photocurrent distributions across the active area. The small pinhole defects observed in the image (b) can be ascribed to experimental faults. Consequently, LBIC measurements show that annealing s- $V_2O_x$  thin films does not cause any observable defects or significant non-uniform photocurrent distributions.



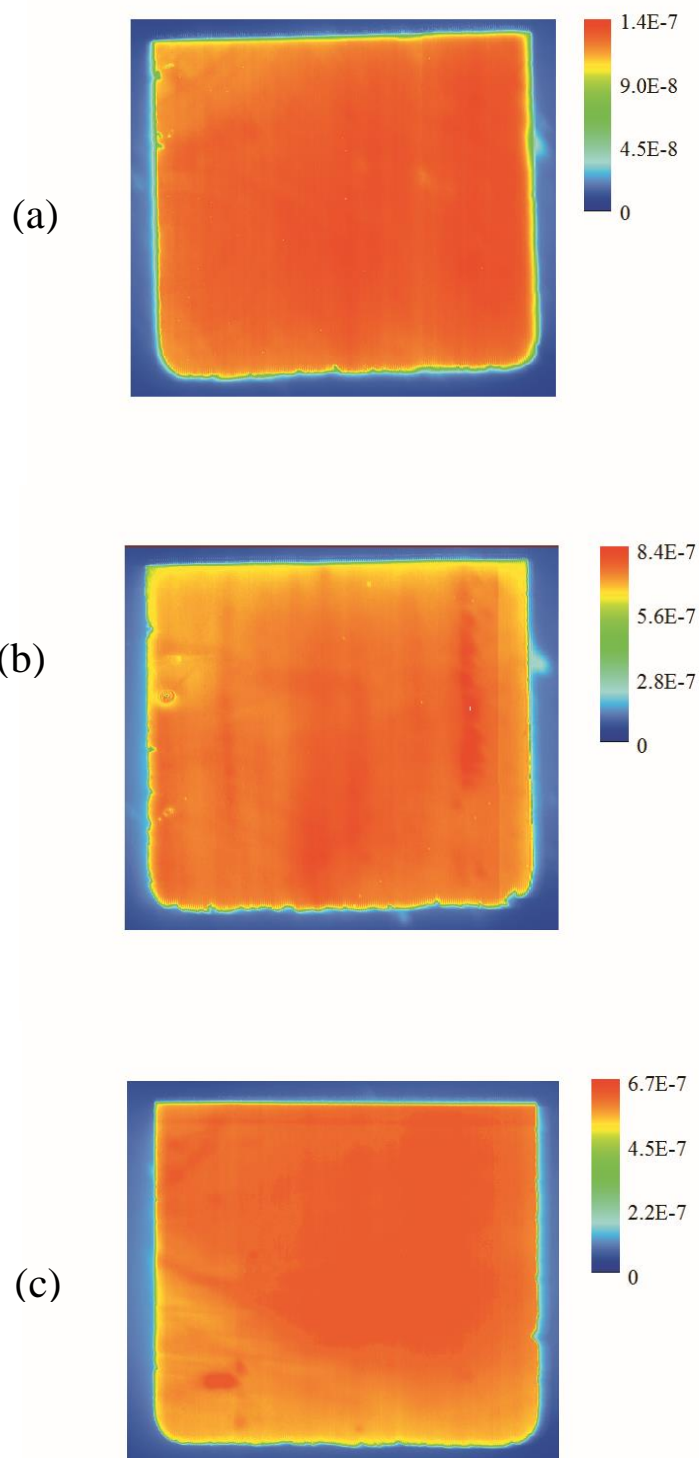


**Figure 5.12** LBIC images show photocurrent map within the active area for PFDT2BT-8:PC<sub>70</sub>BM devices with (a) unannealed  $s\text{-V}_2\text{O}_x$ , (b) annealed at  $200^\circ\text{C}$  and (c) annealed at  $400^\circ\text{C}$ . The colour scale for the LBIC images was adjusted with high generated current indicated by red, and low current indicated by dark blue.

**Figure 5.13** presents the optical transmittance of the films as a function of the wavelength for the as-deposited and annealed films. All s-V<sub>2</sub>O<sub>x</sub> films show high transmission for wavelengths above 500 nm covering the majority of the solar spectrum. The transmittance in the visible wavelength range, from 400 to 500 nm, increases slightly by annealing up to 300°C which is attributed to a change in the film refractive index related to chemical structure changes. On annealing to 400°C, the films exhibit an absorption peak at 415 nm which could be ascribed to small polaron absorption [37, 38]. This effect results from disordering defects in s-V<sub>2</sub>O<sub>x</sub> structure leading to transferring charges between neighbouring sites with a significant spread in energy. Using Tauc's law, the band gap ( $E_g$ ) of s-V<sub>2</sub>O<sub>x</sub> films was determined as explained in **4.2.1 Vanadium Oxide**. As can be seen in **Figure 5.13**, the optical absorption coefficient  $(\alpha h\nu)^2$  is plotted as a function of the incident photon energy.

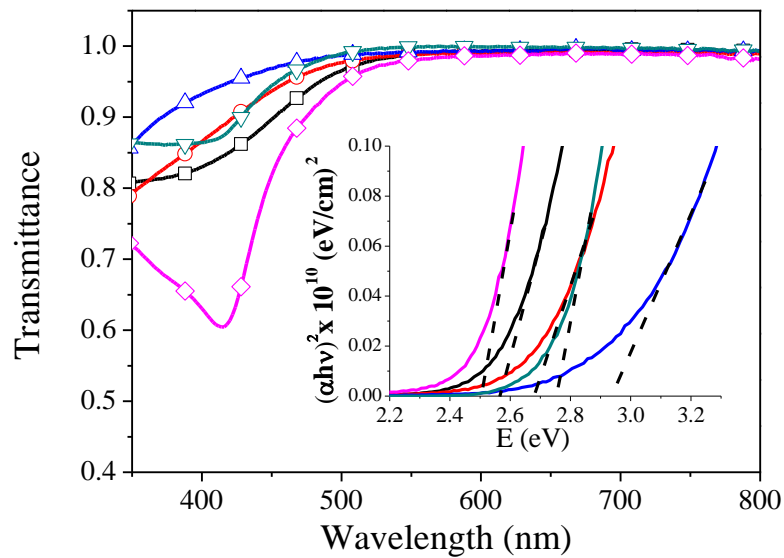


**Figure 5.13** Optical transmission spectra of the s-V<sub>2</sub>O<sub>x</sub> films with different annealing temperature; (□) unannealed, (○) 100°C, (△) 200°C, (▽) 300°C and 400°C (◇). The insert shows the absorption coefficient  $(\alpha h\nu)^2$  as a function of the photon energy.

By extrapolating from the straight-line portion of the plots to the energy-axis,  $E_g$  of the unannealed film lies at 2.57 eV. On annealing to 200°C, the band gap energy rises to 2.93 eV. On further annealing, the band gap reduces again to 2.5 eV at an annealing temperature of 400°C.

AFM scanning was performed to investigate the impact of thermal annealing on the surface topography of s-V<sub>2</sub>O<sub>x</sub>. **Figure 5.14** shows 2 μm x 2 μm AFM scans for an unannealed film (a), and films thermally annealed at 200°C and 400°C for 30 minutes ((b) and (c) respectively). RMS roughness of films decreased slightly upon annealing, from 2.5 nm for an as-cast precursor film to 1.9 nm for films annealed at 400°C, with no local crystallisation structure observed. The low rms of s-V<sub>2</sub>O<sub>x</sub> annealed samples avoided short circuit faults when they were incorporated into OPV devices as shown in **Figure 5.11(a)**.

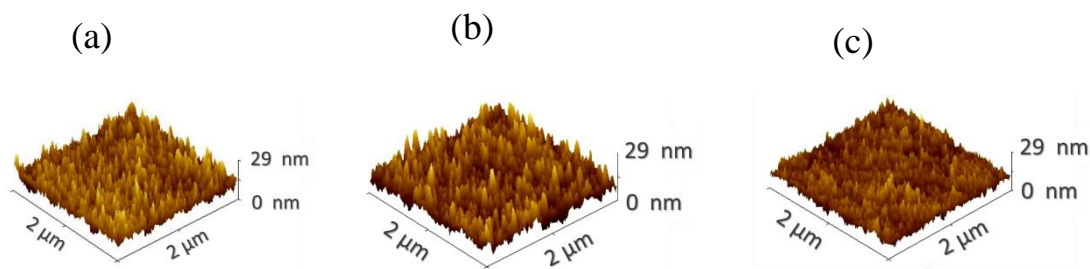


**Figure 5.14** AFM topography (2 μm x 2 μm) of a 10 nm thick s-V<sub>2</sub>O<sub>x</sub> layer deposited on top of Si with native oxide; (a) as deposited, (b) Annealed at 200°C, (C) Annealed at 400°C. The average grain size 163 was 21.3 nm, 16.8 nm and 19.6 nm, respectively.

**Figure 5.15(a)** exhibits a comparison between the XPS spectra of (i) unannealed s-V<sub>2</sub>O<sub>x</sub> films and those annealed in air at 3 different temperatures (ii) 200°C, (iii) 300°C and (iv) 400°C. The chemical and electronic structure of the s-V<sub>2</sub>O<sub>x</sub> thin film were discussed in detail in **4.2.1 Vanadium Oxide**. As observed, the binding energies of the V2p<sub>3/2</sub> and O1s core levels did not change appreciably with increasing temperature. Furthermore, as the annealing temperature increased, the V2p<sub>3/2</sub> spectrum became broader at low binding energies due to the increase of V<sup>4+</sup> species. **Table 5.8** summarises the change of the oxidation state of vanadium with annealing temperature which is consistent with previous studies [39, 40]. By deconvolution of V2p<sub>3/2</sub> lines, we did not observe any shifts in the binding energy of V<sup>4+</sup> and V<sup>5+</sup> peaks. In addition, it is evident that V<sup>4+</sup> oxidation state rises steadily with increasing annealing temperatures. Therefore, s-V<sub>2</sub>O<sub>x</sub> thin films are gradually reduced owing to the generation of more oxygen vacancies related to the hydrolysis process. This partial reduction leads to an increase in the V 3d electron density [41]. Furthermore, oxygen vacancies in V<sub>2</sub>O<sub>x</sub> can cause localisation excess electrons in unfilled 3d orbitals which can explain the absorption peak near to the ultraviolet band observed in **Figure 5.13** [37]. Moreover, reduction of vanadium oxide by thermal annealing can be explained as a result of the re-ordering of oxygen vacancy defects and thus a change of the surface morphology [42]. From **Table 5.8** it can be concluded that vanadium oxide can be partially reduced by a thermal annealing process in air for 30 minutes from V<sub>2</sub>O<sub>4.93</sub> to V<sub>6</sub>O<sub>14</sub>. Increasing the annealing temperature can result in further reduction as reported previously [39]. In the literature, there have been detailed investigations into the physical properties and gradual reduction of vanadium oxide by heating at high temperatures. For example, it has been reported that V<sub>2</sub>O<sub>x</sub> can be reduced to polycrystalline VO<sub>2</sub> with a resistivity change of about 3 orders by thermal annealing at 480°C in air [39, 43].

**Figure 5.15(b)** and (c) plots UPS spectra of  $V_2O_x$  films that have been annealed at different temperatures. The work function and valence band edge determined by the UPS are also summarised in **Table 5.8**. As shown in **Figure 5.15(b)**, the position of the secondary electron cut-off for unannealed film was determined to be at the binding energy of 15.94 eV below the Fermi level, corresponding to a work function of 5.26 eV. Compared to previous studies, the work function of our s- $V_2O_x$  films is similar to those prepared by different processes [27]. On annealing, the secondary electron cut-off shows a slight shift up to 0.07 eV toward the higher binding energy, showing a slight decrease in the work function. This small change in the work function cannot be assigned directly to the processing of the s- $V_2O_x$  due to the possible influence of adsorbates.

**Figure 5.15(c)** displays the onset of the s- $V_2O_x$  valence band to be 2.5 eV below the Fermi level which is identical with all samples. No considerable shift can be observed for the valence band maximum with increase annealing temperature. Careful observation of the valence band region of films annealed at 300°C and 400°C reveals formation of more gap states at 1 eV below the Fermi level as shown in the inset of **Figure 5.15(c)**. This suggests that oxygen vacancies shift up the Fermi level toward the conduction band leaving some occupied states within the band gap. Therefore, introducing oxygen vacancies can act as n-type dopants resulting in a decrease in the work function of vanadium oxide [44].

Photoelectron spectroscopy analysis concludes that the high temperature annealing of s- $V_2O_x$  film produces a change in the chemical structure of the vanadium oxide layer and thus slightly increases the hole-electron recombination at the interface. Nevertheless,

these results demonstrate that a s-V<sub>2</sub>O<sub>x</sub> film can be used to replace evaporated metal oxides in optoelectronic devices which are fabricated at high temperatures.

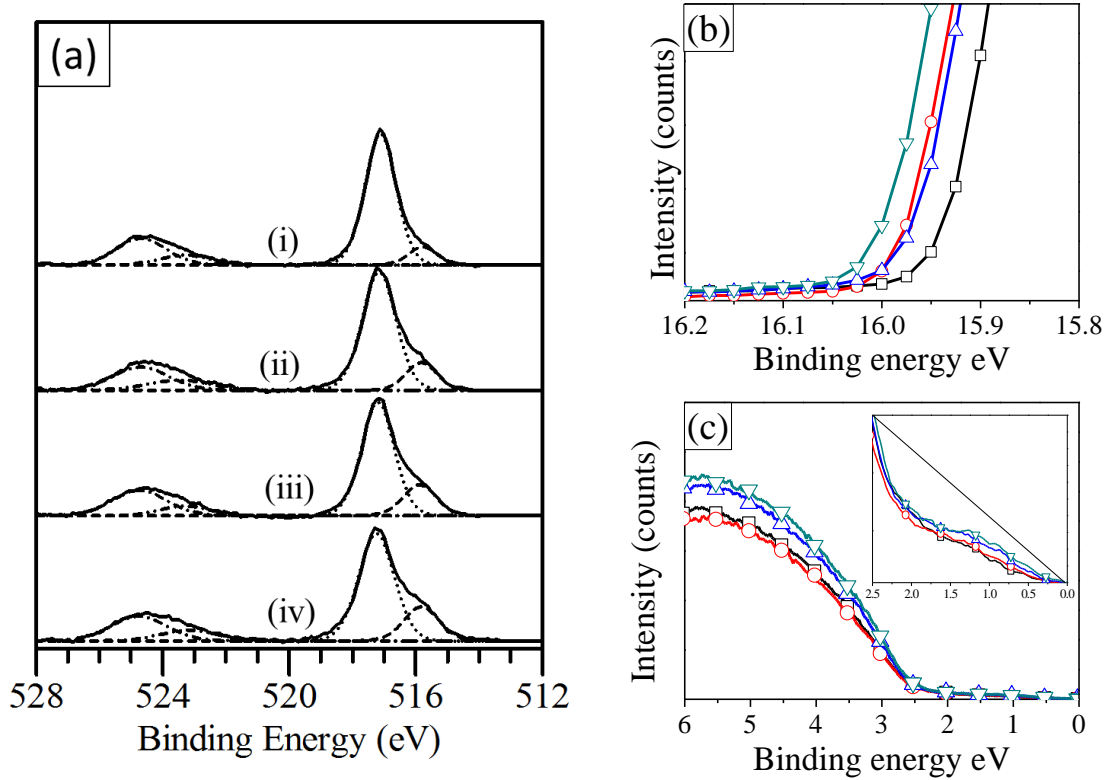


**Figure 5.15** Photoelectron spectroscopy scans of s-V<sub>2</sub>O<sub>x</sub> thin film deposited on ITO in air. (a) XPS data for (i) unannealed film and those annealed at (ii) 200°C, (iii) 300°C and (iv) 400°C. (b) UPS scans for films with (□) no annealing, (○) 200°C, (△) 300°C and (▽) 400°C.

**Table 5.8** Summary of V<sup>5+</sup> and V<sup>4+</sup> oxidation states in the V2p3/2 region for s-V<sub>2</sub>O<sub>x</sub> annealed at different temperatures.

Annealing Temperature	V <sup>4+</sup> oxidation state	V <sup>5+</sup> oxidation state	Work function (eV)	Valence band (eV)	E <sub>g</sub> (eV)
Unannealed	15%	85%	5.26	2.53	2.57
200°C	22.5%	77.5%	5.22	2.53	2.93
300°C	27%	73%	5.23	2.50	2.75
400°C	33%	67%	5.19	2.50	2.52

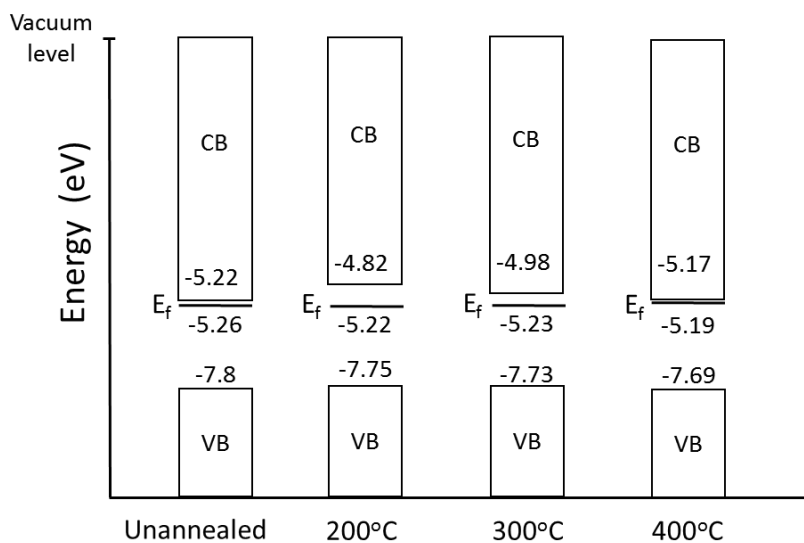


**Figure 5.16** Schematic energy level diagrams of the s- $V_2O_x$  thin film deposited on ITO in air without annealing and those annealed at 200°C, 300°C and 400°C.

## 5.11 Conclusion

It has been shown that it is possible to fabricate OPV devices with the use of a solution-processable form of Vanadium (V) Oxide called Vanadium (V) Isopropoxide. A high efficiency OPV of 6.5% with a s- $V_2O_x$  interlayer fabricated in air without any post-deposition treatment such as thermal annealing or oxygen plasma treatment has also been demonstrated. In contrast to previous studies,, thermal annealing of solution-processed vanadium oxide films does not significantly enhance the performance of OPV devices. However, the efficiency of OPV devices is reduced by 15% after annealing s- $V_2O_x$  layers at high temperatures (i.e. 400°C) due to the decrease of  $V_{oc}$  and shunt resistance. Absorption spectroscopy studies reveal that OPV performance is independent of the variable optical band gap of s- $V_2O_x$ . XPS analysis shows that annealing of vanadium oxide films for 30 minutes in air resulted in a reduction of  $V_2O_{4.93}$  to  $V_6O_{14}$  as a result of the generation of more oxygen vacancies. This reduction

causes a decrease of  $V_{oc}$  and thus the PCE of OPV device. Consequently, Nevertheless, OPV results confirm that s- $V_2O_x$  thin film is suitable for optoelectronic devices which are fabricated at 400°C, and is promising for efficient OPV with a low cost and fast manufacturing process.



## 5.12 References

1. K. Zweibel, *Should solar photovoltaics be deployed sooner because of long operating life at low, predictable cost?*, Energy Policy **38** (2010), no. 11, 7519-7530.
2. M. A. Green, *Third generation photovoltaics: Ultra-high conversion efficiency at low cost*, Progress in Photovoltaics **9** (2001), no. 2, 123-135.
3. R. Steim, F. R. Kogler and C. J. Brabec, *Interface materials for organic solar cells*, Journal of Materials Chemistry **20** (2010), no. 13, 2499-2512.
4. A. C. Arias, M. Granstrom, D. S. Thomas, K. Petritsch and R. H. Friend, *Doped conducting-polymer-semiconducting-polymer interfaces: Their use in organic photovoltaic devices*, Physical Review B **60** (1999), no. 3, 1854-1860.
5. C.-J. Ko, Y.-K. Lin, F.-C. Chen and C.-W. Chu, *Modified buffer layers for polymer photovoltaic devices*, Applied Physics Letters **90** (2007), no. 6.
6. K. Lee, J. Y. Kim, S. H. Park, S. H. Kim, S. Cho and A. J. Heeger, *Air-stable polymer electronic devices*, Advanced Materials **19** (2007), no. 18, 2445-+.
7. K. Norrman, M. V. Madsen, S. A. Gevorgyan and F. C. Krebs, *Degradation patterns in water and oxygen of an inverted polymer solar cell*, Journal of the American Chemical Society **132** (2010), no. 47, 16883-16892.

8. E. L. Ratcliff, B. Zacher and N. R. Armstrong, *Selective inter layers and contacts in organic photovoltaic cells*, Journal of Physical Chemistry Letters **2** (2011), no. 11, 1337-1350.
9. M. P. de Jong, L. J. van Ijzendoorn and M. J. A. de Voigt, *Stability of the interface between indium-tin-oxide and poly(3,4-ethylenedioxythiophene)/poly(styrenesulfonate) in polymer light-emitting diodes*, Applied Physics Letters **77** (2000), no. 14, 2255-2257.
10. V. Shrotriya, G. Li, Y. Yao, C. W. Chu and Y. Yang, *Transition metal oxides as the buffer layer for polymer photovoltaic cells*, Applied Physics Letters **88** (2006), no. 7.
11. J. H. Park, T. W. Lee, B. D. Chin, D. H. Wang and O. O. Park, *Roles of interlayers in efficient organic photovoltaic devices*, Macromolecular Rapid Communications **31** (2010), no. 24, 2095-2108.
12. R. Jose, V. Thavasi and S. Ramakrishna, *Metal oxides for dye-sensitized solar cells*, Journal of the American Ceramic Society **92** (2009), no. 2, 289-301.
13. S. Chen, J. R. Manders, S.-W. Tsang and F. So, *Metal oxides for interface engineering in polymer solar cells*, Journal of Materials Chemistry **22** (2012), no. 46, 24202-24212.
14. M. C. Gwinner, R. Di Pietro, Y. Vaynzof, K. J. Greenberg, P. K. H. Ho, R. H. Friend and H. Sirringhaus, *Doping of organic semiconductors using molybdenum*

- trioxide: A quantitative time-dependent electrical and spectroscopic study*, *Advanced Functional Materials* **21** (2011), no. 8, 1432-1441.
15. Y. Park, V. Choong, Y. Gao, B. R. Hsieh and C. W. Tang, *Work function of indium tin oxide transparent conductor measured by photoelectron spectroscopy*, *Applied Physics Letters* **68** (1996), no. 19, 2699-2701.
16. T. Kugler, A. Johansson, I. Dalsegg, U. Gelius and W. R. Salaneck, *Electronic and chemical structure of conjugated polymer surfaces and interfaces: Applications in polymer-based light-emitting devices*, *Synthetic Metals* **91** (1997), no. 1-3, 143-146.
17. K. Sugiyama, H. Ishii, Y. Ouchi and K. Seki, *Dependence of indium-tin-oxide work function on surface cleaning method as studied by ultraviolet and x-ray photoemission spectroscopies*, *Journal of Applied Physics* **87** (2000), no. 1, 295-298.
18. C. C. Wu, C. I. Wu, J. C. Sturm and A. Kahn, *Surface modification of indium tin oxide by plasma treatment: An effective method to improve the efficiency, brightness, and reliability of organic light emitting devices*, *Applied Physics Letters* **70** (1997), no. 11, 1348-1350.
19. K. Zilberberg, H. Gharbi, A. Behrendt, S. Trost and T. Riedl, *Low-temperature, solution-processed MoO<sub>x</sub> for efficient and stable organic solar cells*, *Acs Applied Materials & Interfaces* **4** (2012), no. 3, 1164-1168.

20. K. Zilberberg, S. Trost, J. Meyer, A. Kahn, A. Behrendt, D. Luetzenkirchen-Hecht, R. Frahm and T. Riedl, *Inverted organic solar cells with sol-gel processed high work-function vanadium oxide hole-extraction layers*, *Advanced Functional Materials* **21** (2011), no. 24, 4776-4783.
21. J. Livage, *Vanadium pentoxide gels*, *Chemistry of Materials* **3** (1991), no. 4, 578-593.
22. I. Litzov and C. J. Brabec, *Development of efficient and stable inverted bulk heterojunction (BHJ) solar cells using different metal oxide interfaces*, *Materials* **6** (2013), no. 12, 5796-5820.
23. S. Jin, B. J. Jung, C. K. Song and J. Kwak, *Room-temperature and solution-processed vanadium oxide buffer layer for efficient charge injection in bottom-contact organic field-effect transistors*, *Current Applied Physics* **14** (2014), no. 12, 1809-1812.
24. L. Lu, T. Xu, I. H. Jung and L. Yu, *Match the interfacial energy levels between hole transport layer and donor polymer to achieve high solar cell performance*, *Journal of Physical Chemistry C* **118** (2014), no. 40, 22834-22839.
25. K. Zilberberg, S. Trost, H. Schmidt and T. Riedl, *Solution processed vanadium pentoxide as charge extraction layer for organic solar cells*, *Advanced Energy Materials* **1** (2011), no. 3, 377-381.
26. I. Hancox, L. A. Rochford, D. Clare, M. Walker, J. J. Mudd, P. Sullivan, S. Schumann, C. F. McConville and T. S. Jones, *Optimization of a high work function*

- solution processed vanadium oxide hole-extracting layer for small molecule and polymer organic photovoltaic cells*, Journal of Physical Chemistry C **117** (2013), no. 1, 49-57.
27. K. Zilberberg, J. Meyer and T. Riedl, *Solution processed metal-oxides for organic electronic devices*, Journal of Materials Chemistry C **1** (2013), no. 32, 4796-4815.
28. X. Orignac, H. C. Vasconcelos, X. M. Du and R. M. Almeida, *Influence of solvent concentration on the microstructure of SiO<sub>2</sub>-TiO<sub>2</sub> sol-gel films*, Journal of Sol-Gel Science and Technology **8** (1997), no. 1-3, 243-248.
29. I. Novak and B. Kovac, *Polyoxometalates and vanadium alkoxides: Electronic structure and properties*, Chemical Physics Letters **474** (2009), no. 1-3, 33-35.
30. W. Cao, J. Li, H. Chen and J. Xue, *Transparent electrodes for organic optoelectronic devices: A review*, Journal of Photonics for Energy **4** (2014).
31. C. S. Kim, S. S. Lee, E. D. Gomez, J. B. Kim and Y.-L. Loo, *Transient photovoltaic behavior of air-stable, inverted organic solar cells with solution-processed electron transport layer*, Applied Physics Letters **94** (2009), no. 11.
32. C.-Y. Li, T.-C. Wen, T.-H. Lee, T.-F. Guo, J.-C.-A. Huang, Y.-C. Lin and Y.-J. Hsu, *An inverted polymer photovoltaic cell with increased air stability obtained by employing novel hole/electron collecting layers*, Journal of Materials Chemistry **19** (2009), no. 11, 1643-1647.

33. J. Kim, G. Kim, Y. Choi, J. Lee, S. H. Park and K. Lee, *Light-soaking issue in polymer solar cells: Photoinduced energy level alignment at the sol-gel processed metal oxide and indium tin oxide interface*, Journal of Applied Physics **111** (2012), no. 11.
34. H. Schmidt, K. Zilberberg, S. Schmale, H. Fluegge, T. Riedl and W. Kowalsky, *Transient characteristics of inverted polymer solar cells using titaniumoxide interlayers*, Applied Physics Letters **96** (2010), no. 24.
35. A. Wagenpfahl, D. Rauh, M. Binder, C. Deibel and V. Dyakonov, *S-shaped current-voltage characteristics of organic solar devices*, Physical Review B **82** (2010), no. 11, 115306.
36. J. Kim, H. Kim, G. Kim, H. Back and K. Lee, *Soluble transition metal oxide/polymeric acid composites for efficient hole-transport layers in polymer solar cells*, Acs Applied Materials & Interfaces **6** (2014), no. 2, 951-957.
37. A. Talledo and C. G. Granqvist, *Electrochromic vanadium-pentoxide-based films - structural, electrochemical, and optical-properties*, Journal of Applied Physics **77** (1995), no. 9, 4655-4666.
38. J. Bullo, P. Cordier, O. Gallais, M. Gauthier and F. Babonneau, *Thin-layers deposited from V<sub>2</sub>O<sub>5</sub> gels .II. An optical-absorption study*, Journal of Non-Crystalline Solids **68** (1984), no. 1, 135-146.
39. N. Y. Yuan, J. H. Li and C. L. Lin, *Valence reduction process from sol-gel V<sub>2</sub>O<sub>5</sub> to VO<sub>2</sub> thin films*, Applied Surface Science **191** (2002), no. 1-4, 176-180.

40. S. Surnev, M. G. Ramsey and F. P. Netzer, *Vanadium oxide surface studies*, Progress in Surface Science **73** (2003), no. 4-8, 117-165.
41. V. M. Bermudez, R. T. Williams, J. P. Long, R. K. Reed and P. H. Klein, *Photoemission-study of hydrogen adsorption on vanadium dioxide near the semiconductor-metal phase-transition*, Physical Review B **45** (1992), no. 16, 9266-9271.
42. K. Devriendt, H. Poelman and L. Fiermans, *Thermal reduction of vanadium pentoxide: An XPD study*, Surface Science **433** (1999), 734-739.
43. R. M. Oksuzoglu, P. Bilgic, M. Yildirim and O. Deniz, *Influence of post-annealing on electrical, structural and optical properties of vanadium oxide thin films*, Optics and Laser Technology **48** (2013), 102-109.
44. M. T. Greiner, M. G. Helander, W.-M. Tang, Z.-B. Wang, J. Qiu and Z.-H. Lu, *Universal energy-level alignment of molecules on metal oxides*, Nature Materials **11** (2012), no. 1, 76-81.

# Chapter 6

## Solution-Processed Nickel Oxide Devices

### 6.1 Introduction

Nickel oxide (NiO) is a semiconductor that has been the subject of a considerable number of research studies due to its unique optical and electrical properties such as a high work function, chemical stability, optical transparency, and high ability for electron-blocking. Although most studies on nickel oxide have used high cost fabrication processes such as vacuum evaporation or reactive sputtering technique, several studies have shown that solution-processed NiO thin films can be an effective hole extraction layer within organic photovoltaic devices [1]. This chapter shows that it is possible to solution-process nickel oxide from a nickel acetylacetonate precursor and obtain a power conversion efficiency of 5.2%. This is achieved by the use of postdeposition thermal annealing and oxygen plasma treatment. In addition, it is shown that thermal annealing of NiO thin films in air leads to the decomposition of the acetylacetonate precursor, causing an increase of the work function and a reduction in the oxidation state. Post-annealing oxygen plasma treatment further reduces the work function by oxidising the surface layer of the sample that facilitates charge extraction at the organic interface [2].



## 6.2 Optimisation of NiO Devices by Thermal Annealing

**Figure 6.1(a)** shows the current density-voltage characteristics of PCDTBT:PC<sub>70</sub>BM devices that use a thermally-annealed nickel acetylacetonate (Ni(acac)) film as the hole extraction layer. Devices incorporating as cast films of Ni(acac), and Ni(acac) films that were thermally annealed at temperatures ranging between 100 °C and 500 °C, are shown. As can be seen, devices with an as cast Ni(acac) layer show the lowest performance. However, annealing at higher temperatures results in a significant increase in device performance until a maximum value of 400°C. For unannealed NiO, the highest PCE, open circuit voltage ( $V_{oc}$ ), short circuit current density ( $J_{sc}$ ), and fill factor (FF) were 0.06%, 0.06 V, 2.91 mA.cm<sup>-1</sup> and 31.5% respectively. Annealing of NiO from 100–400 °C showed an increase in device performances in line with the increase in temperature. For example, the PCE and FF were increased from 0.1%, 32.8% (at 100°C) to 3.5%, 56.2% (at 400 °C) respectively. It was found that the optimum annealing temperature for Ni(acac) films was between 350°C and 400°C as shown in **Figure 6.1**. In addition, the J-V curves show a dramatic increase in the shunt resistance of the devices as the Ni(acac) film is annealed beyond a critical point, as indicated by the reduced gradient in the reverse bias region. The origin of this dramatic shift is likely to be due to the thermal decomposition of the Ni(acac) thin film resulting in the formation of NiO.

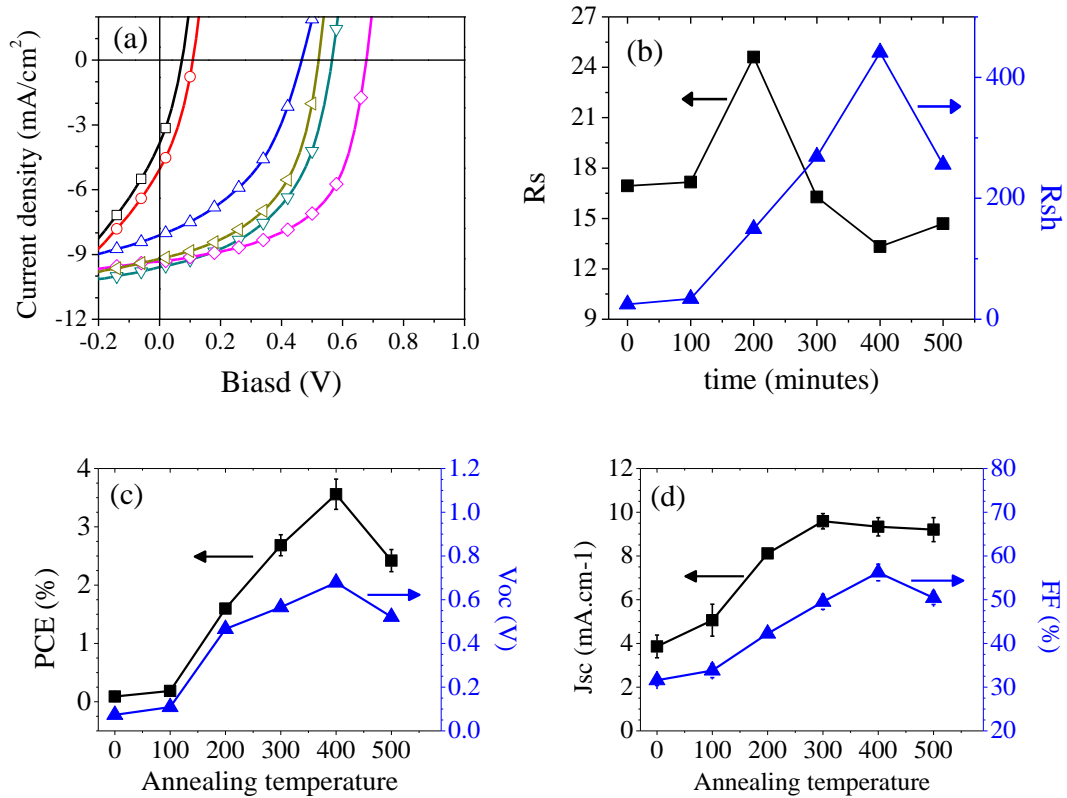


**Figure 6.1** (a) The current density-voltage characteristics of PCDTBT:PC<sub>70</sub>BM based solar cell with (□) unannealed NiO thin film and annealed for 30 minutes at (○)100°C, (△) 200°C, (▽) 300°C, (◇) 400°C and (◀) 500°C . (b) The series resistance R<sub>s</sub> and shunt resistance R<sub>sh</sub> as a function of annealing temperature. (c) and (d) Dependence of OPV parameters upon annealing temperature.

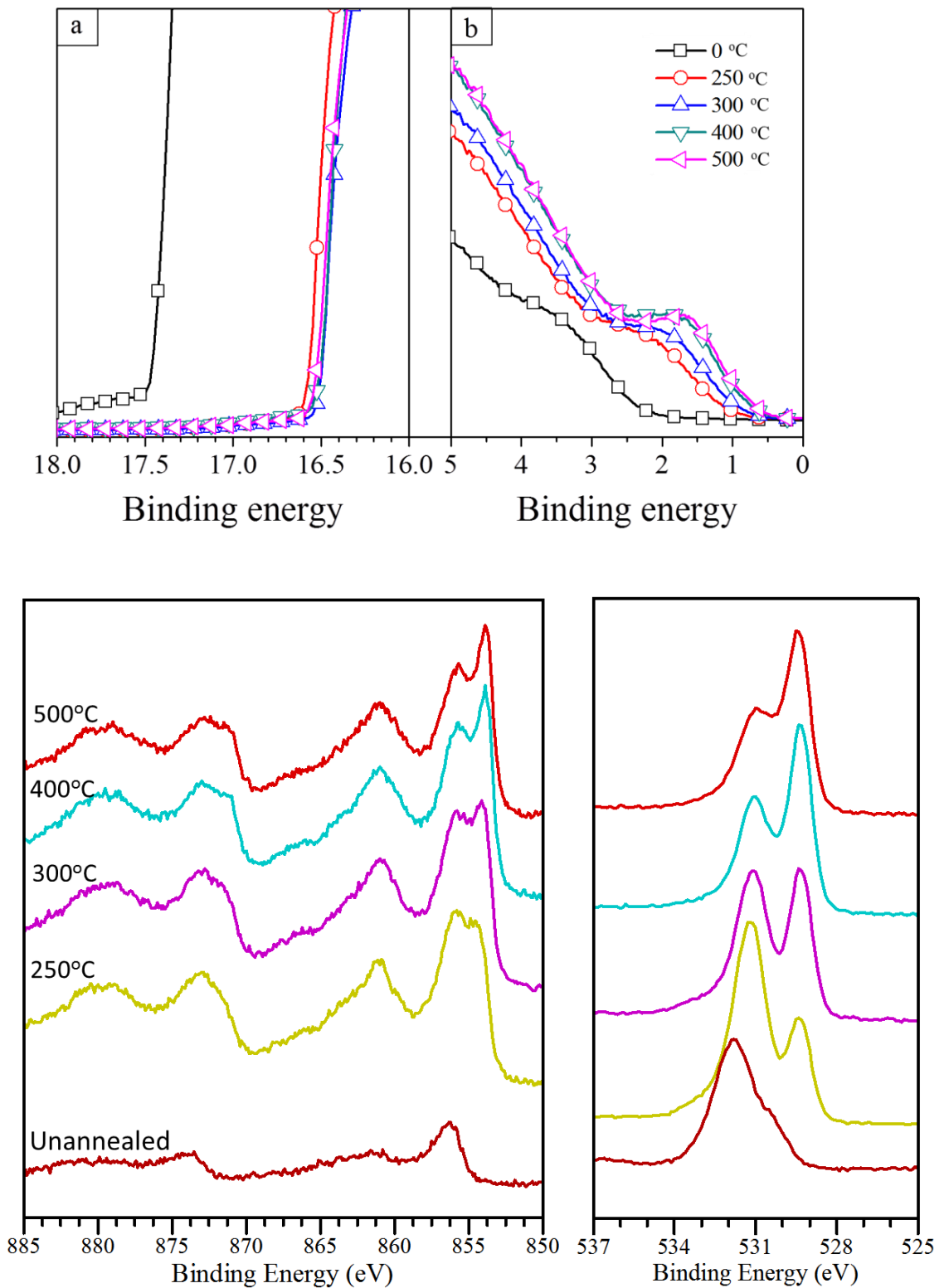
The optimum annealing time of NiO thin films was also investigated. Before spin coating the PCDTBT:PC<sub>70</sub>BM blend, 6 nm thick NiO films were spin coated onto clean ITO substrates and then annealed at 400°C in ambient conditions for durations ranging from 5 to 45 minutes. It can be observed in **Table 6.1** that OPV performance and efficiency depend strongly on the annealing time used to convert the nickel acetylacetonate to NiO. Indeed, the device in which the precursor film was annealed for 5 minutes shows the lowest performance.

Table 6.1 Photovoltaic parameters of PCDTBT:PCBM devices with solution processed NiO interlayer annealed at 400°C for different periods of time.

Ann. Time (min)	Maximum PCE [%]	Average PCE <sub>(av)</sub> [%]	Voc [V]	J <sub>sc</sub> [mA.cm <sup>-2</sup> ]	FF [%]	R <sub>s</sub> [Ω.cm <sup>2</sup> ]	R <sub>sh</sub> [Ω.cm <sup>2</sup> ]
5	2.3	2.1 ± 0.19	0.48	9.1 ± 0.34	48.7 ± 1.6	16.1 ± 1.3	197 ± 31
10	2.8	2.6 ± 0.21	0.56	9.0 ± 0.18	52.3 ± 0.9	15.5 ± 0.7	280 ± 49
20	3.0	2.6 ± 0.20	0.59	8.8 ± 0.36	50.4 ± 1.9	15.3 ± 1.6	281 ± 52
30	3.6	3.3 ± 0.14	0.66	9.2 ± 0.25	55.6 ± 0.6	14.0 ± 0.9	414 ± 66
45	3.2	3.0 ± 0.15	0.65	9.2 ± 0.31	53.6 ± 1.6	14.3 ± 1.3	385 ± 43

As the film annealing time increases, the efficiency of the OPV devices improves progressively, reaching a maximum PCE of 3.6% resulting from increasing V<sub>oc</sub> and shunt resistance R<sub>sh</sub>. Moreover, it can be observed that shunt resistance has a strong dependence upon annealing time with maximum value of 414 Ω.cm<sup>2</sup> after 30 minutes of annealing. A slight increase in the fill factor (FF) of about 15% was observed with no significant change in the J<sub>sc</sub>. Consequently, it can be concluded that nickel acetylacetonate film requires thermal annealing at 350°C for 30 minutes to convert to NiO.

**Figure 6.2** shows photoelectron spectroscopy data for nickel acetylacetonate unannealed films and films annealed at temperatures ranging from 250°C and 500°C. UPS spectra in **Figure 6.2(a)** and (b) show the impact of thermal annealing on the secondary electron cut off and the valence band region of nickel acetylacetonate films. The work function for as deposited films is determined to be 3.7 eV and after annealing this value increases to 4.7 eV. In addition, the edge of the valence band shifts to be closer to the Fermi level although the valence states do not extend to the Fermi level, indicating that the films are still semiconducting in nature.



**Figure 6.2** Photoelectron spectroscopy data of nickel acetylacetonate films deposited onto ITO for films as-deposited and with post deposition annealing between 250°C and 500°C. (a), (b) are UPS measurements (c) the Ni<sub>2p</sub> spectra, (d) O<sub>1s</sub> spectra.

This increase of the work function is more favourable for matching energy levels and forming Ohmic contact at the interface between PCDTBT and NiO. This results in considerable reduction in the contact resistance within the device leading to a large gain in  $V_{oc}$ . In addition, XPS measurements of the C1s peak suggest that the thermal decomposition of the nickel acetylacetonate occurs to completion at 300°C leading to the removal of any trap states that are present on the ligand of the precursor. Consequently, both results would explain the observed changes within the device performance.

O1s spectra and Ni2p spectra in **Figure 6.2(a)** and (b) show the evolution of oxide formation in the precursor films as a function of annealing temperature. As can be seen, for unannealed films the main peak of O1s spectrum is determined at 531.7 eV and originates from hydroxide ions that are present in the precursor. Upon annealing a secondary peak can be observed at a lower binding energy of 529.3 eV which is attributed to oxygen atoms bound to nickel within the nickel oxide film. At elevated temperatures this peak becomes a dominant feature in the O1s spectrum. A final diffuse peak manifests itself as tail states in the spectra which can be attributed to oxyhydroxide intermediates (NiOOH) resulting from oxygen atoms in adsorbed water on the surface [3].

**Figure 6.2(b)** shows the evolution of Ni2p regions which consist of several doublet peaks separated by approximately 18 eV, the ratio of the area of these doublet peaks is approximately 1:2. The spectrum consists of 3 sets of doublet peaks with the larger, low energy peaks being found at 853.9 eV for metallic nickel ( $Ni^0$ ), 854.8 eV for oxidized nickel ( $Ni^{+1}$ ), and 856.4 eV for doubly oxidized nickel peak ( $Ni^{+2}$ ). The relative peak intensities depend on both the average oxidation state of the film between the surface

and the penetration depth of the XPS instrument [4].  $\text{Ni}^{2+}$  feature often exists as  $\text{Ni}(\text{OH})_2$  which is formed due to atmospheric gases and precursor solution [5]. Therefore, the  $\text{Ni}^{+2}$  peak is dominant in the unannealed film and becomes minor after heating at high temperatures. Furthermore, it can be observed that at elevated temperatures the total amount of  $\text{Ni}^{+1}$  increases in relation to the other two peaks and corresponds with a slight shift of the Ni2p peaks to lower binding energies. This additional amount can be correlated with the evolution of the lower binding energy peak in the O1s spectrum. Consequently, this suggests that heating converts the nickel acetylacetonate films to NiO.

### 6.3 O<sub>2</sub>-plasma treatment

After thermal annealing of Nickel acetylacetonate thin films at 400°C for 30 minutes, the obtained NiO thin films were also treated using an O<sub>2</sub>-plasma with varying oxygen pressures and for different periods of time. **Figure 6.3(a)** shows the current density–voltage (J–V) curves of devices using films that were treated with an O<sub>2</sub>-plasma at the optimal pressure and time. The shunt resistance significantly increased by 62% after plasma treatment. For films treated at 1.5 Torr for 2 minutes it can be observed that there is an increase in the  $V_{oc}$  and  $J_{sc}$  of approximately 0.19 eV and 0.6 mA.cm<sup>-2</sup> respectively. **Figure 6.3(b)** and (c) summarise the OPV parameters for NiO films treated using an O<sub>2</sub>-plasma with various pressures and for different lengths of time. The enhancement in power conversion efficiency for all plasma treated devices is driven by the increase in  $V_{oc}$  of over 25% and slight increases in the  $J_{sc}$  and FF.

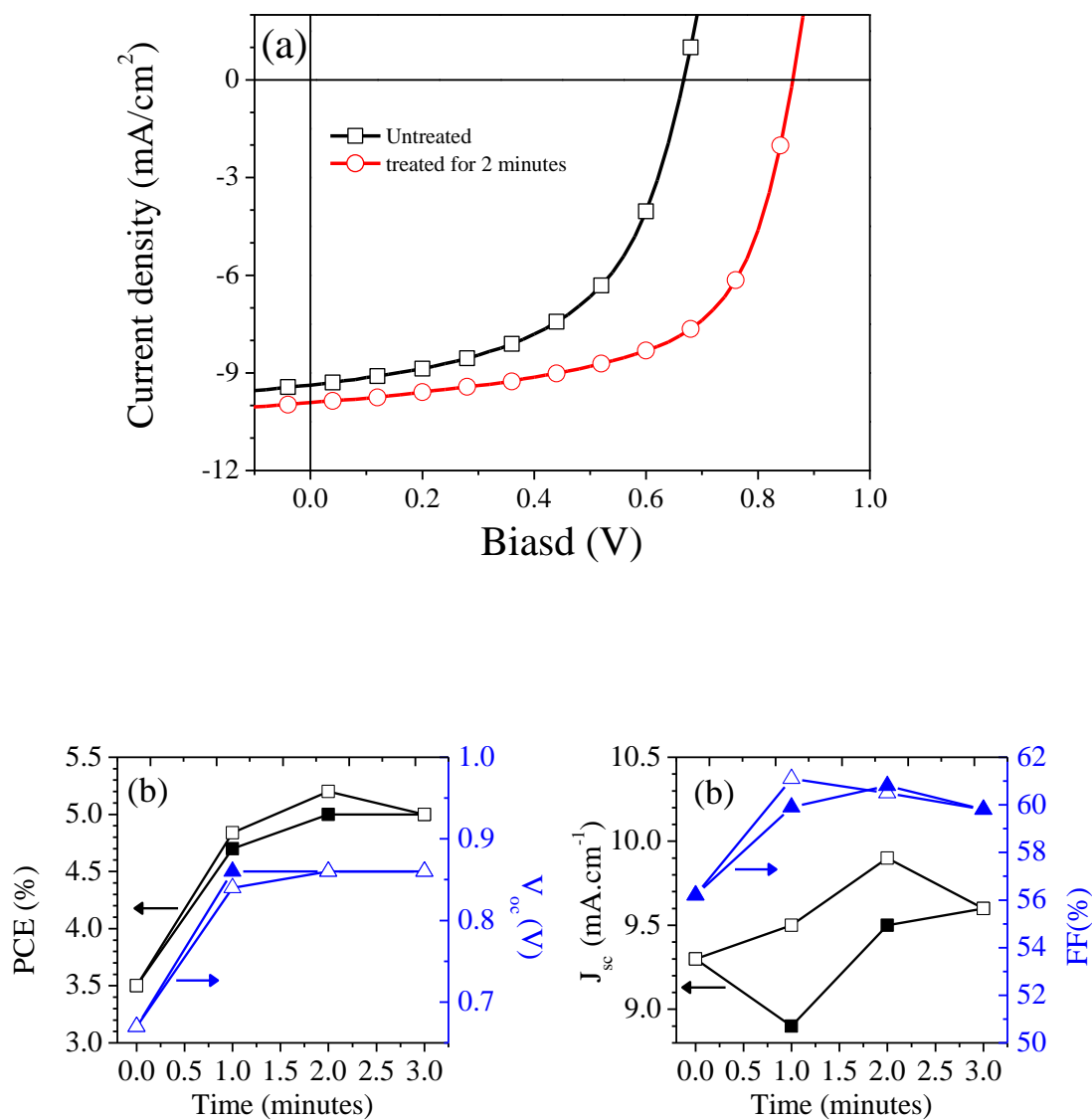


**Figure 6.3** (a) The current density-voltage characteristics of OPV devices with thermally annealed NiO films at  $400^\circ\text{C}$ ; ( $\square$ ) before  $\text{O}_2$ -plasma treatment and ( $\circ$ ) after treatment. (b) and (c) comparison of performance parameters of OPV devices for films with oxygen plasma treatment for pressure of 0.5 mbar (filled shapes) and 1.5 mbar (open shapes) after annealing at  $400^\circ\text{C}$ .

These changes are likely to have resulted from the oxidation of the surface layer of the NiO film, as the results indicate that both the  $V_{OC}$  and FF are independent of the treatment time and pressure. XPS of the C1s spectra indicate that removal of residual organic content from the surface is not the cause as the thermal annealing leads to the removal of this material. The enhancement in efficiency, however, could be due to further oxidation of the surface layer resulting in an increase of the work function as explained by UPS and XPS data below [5].

**Figure 6.4** (a) shows UPS spectra of thermally annealed NiO thin films with and without O<sub>2</sub>-plasma treatment. The work function illustrates a further increase by 0.3 eV to 0.5 eV upon treatment of the films. This increase of work function and the increase of the valence band of the material in comparison to the Fermi level is typical of highly oxidised hole-extracting metal oxides such as molybdenum oxide [6]. This indicates that the annealed precursor is a slightly reduced form of NiO and that O<sub>2</sub>-plasma treatment leads to the oxidation of the surface layer.

The O1s spectra in **Figure 6.4**(b) shows that for the treated films both the relative intensity of the hydroxide and the water peak increase in relation to the oxygen present within the NiO lattice. This indicates that an increased amount of water is present at the film surface. Previous studies on metal oxides have demonstrated the presence of an obvious relationship between film density and water adsorption [7]. Since the density of the fully oxidised NiO film is less than that of metallic Nickel it is likely that highly oxidized surface layers would lead to increased water adsorption [8].

The Ni2p peaks in **Figure 6.4**(c) show that treating the films with an O<sub>2</sub>-plasma leads to a decrease in the total amount of Ni<sup>0</sup> in relation to the other two peaks. This decrease is accompanied by an increase in the Ni<sup>+1</sup> oxidation state suggesting that the plasma



treatment converts the metallic  $\text{Ni}^0$  states to  $\text{Ni}^{+1}$  states at the surface. As a result, treatment with an  $\text{O}_2$ -plasma leads to oxidisation of further metallic surface states. The large work function of this oxidized surface allows for the efficient extraction of holes due to a reduced energy barrier at the interface in comparison to that of the  $\text{NiO}_{1-x}$  film. For metal oxide precursors that require high temperature annealing, the use of an  $\text{O}_2$ -plasma post-treatment could be an effective way of increasing device performance by reducing any potential interfacial barriers that may occur due to the presence of metallic states. It is possible that the change in surface electronic structure on annealing and/or plasma treatment has a knock-on effect on the morphology of the bulk heterojunction. Such an effect could be correlated with changes due to the energetic alignment at the anode interface. However it is fairly certain that this morphology effect is negligible compared with the impact anode energy alignment in the case of plasma treated versus untreated, since the short circuit currents of the devices without plasma treatment ( $-9.3 \text{ mA}\cdot\text{cm}^{-2}$ ) are within the experimental range of the plasma treated devices ( $-8.9$  to  $-9.9 \text{ mA}\cdot\text{cm}^{-2}$ ) indicating there has been no significant change in the mobility of the bulk polymer layer between these devices. For unannealed devices it is not so certain that morphology changes are not present. However, given the severity of the open circuit voltage reduction for unannealed films ( $<0.1\text{V}$  versus  $>0.8\text{V}$  for annealed devices) they are definitely minor compared to the changes in performance caused by the influence of the interface electronic structure.

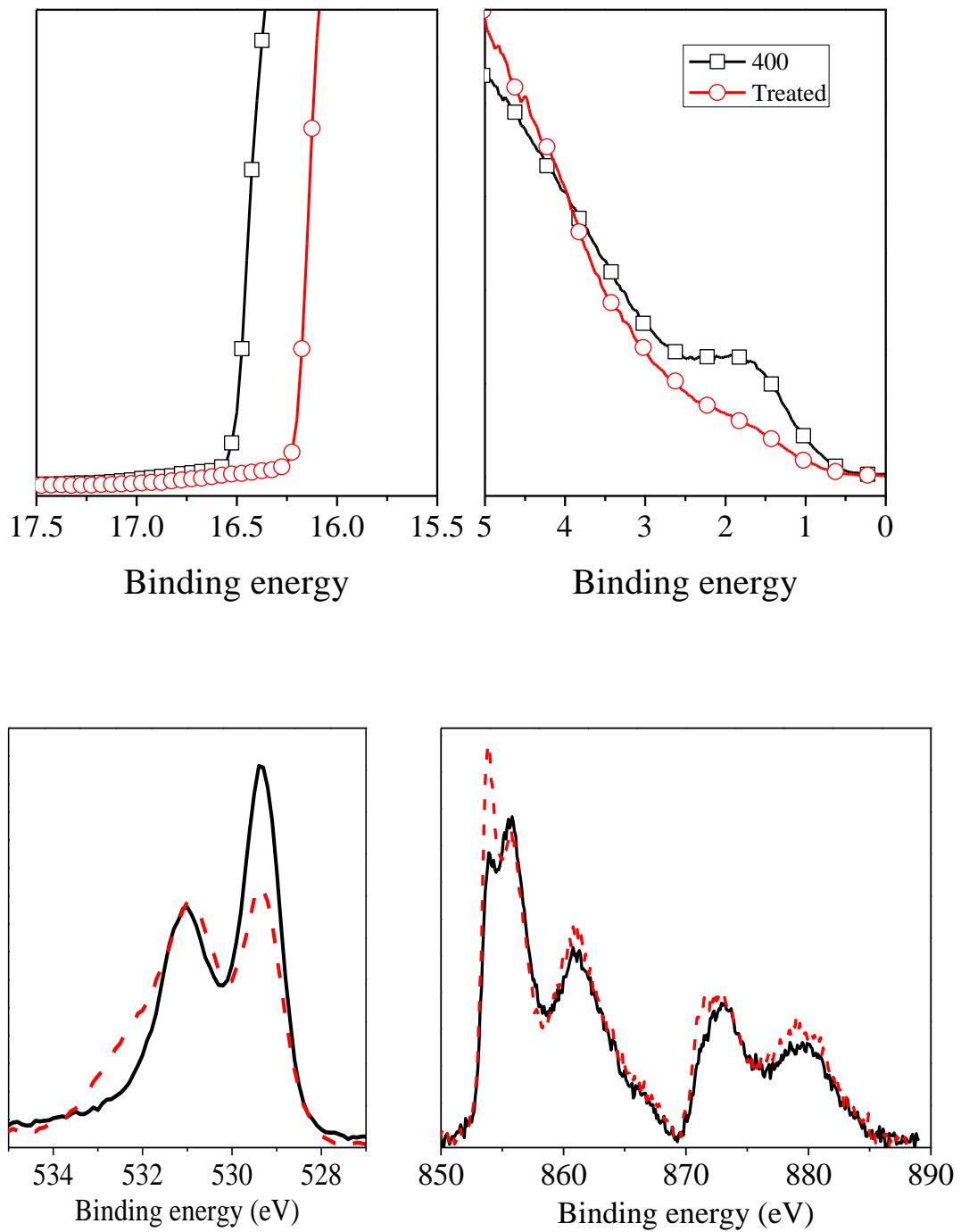


**Figure 6.4** Photoelectron spectroscopy data of nickel acetylacetonate films after pos- deposition annealing at 400°C with and without oxygen plasma treatment. (a), (b) are UPS measurements (c) O1s spectra, and (d) the Ni2p spectra.

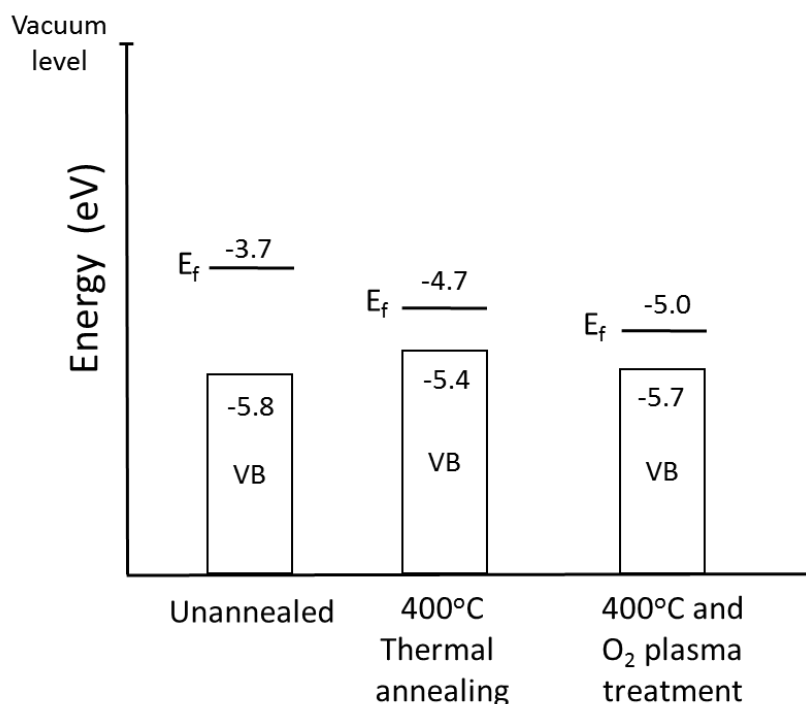


**Figure 6.5** Schematic energy level diagrams of nickel acetylacetonate films deposited onto ITO for films as-deposited, with post deposition annealing at 400°C and oxygen plasma treatment after annealing.

## 6.4 Conclusion

The solution processing of thin films of nickel oxides from a nickel acetylacetonate precursor for use in organic photovoltaics were studied. This chapter has shown that the performance of OPVs containing NiO films deposited from these precursors depend strongly upon post deposition treatment. Thermal annealing at temperatures of 300°C and above is needed to drive the conversion of the precursor into the metal oxide leading to an increase in PCEs from 0.06% to 3.5%; this has been attributed to the

larger work function of nickel oxide, 4.7 eV compared to 3.7 eV for the precursor, and reduced recombination at the organic interface. Results of photoelectron spectroscopy suggest that the high temperatures required to conversion the nickel acetylacetonate precursor to NiO result in the reduction in oxidation state of the NiO to a sub oxide  $\text{NiO}_{1-x}$ .

Treatment of annealed films with an oxygen plasma leads to further increases in efficiency with a reported peak PCE of 5.2%. This is attributed to the oxidation of reduced states at the films surface that appear due to the high temperature thermal annealing needed to convert the precursor. This oxidation leads to a further increase of the work function to 5.0 eV leading to a reduced extraction barrier at the organic interface.

## 6.5 References

1. K. Zilberberg, J. Meyer and T. Riedl, *Solution processed metal-oxides for organic electronic devices*, Journal of Materials Chemistry C **1** (2013), no. 32, 4796-4815.
2. B. Mustafa, J. Griffin, A. S. Alsulami, D. G. Lidzey and A. R. Buckley, *Solution processed nickel oxide anodes for organic photovoltaic devices*, Applied Physics Letters **104** (2014), no. 6.
3. M. C. Biesinger, B. P. Payne, L. W. M. Lau, A. Gerson and R. S. C. Smart, *X-ray photoelectron spectroscopic chemical state quantification of mixed nickel metal, oxide and hydroxide systems*, Surface and Interface Analysis **41** (2009), no. 4, 324-332.
4. M. C. Biesinger, B. P. Payne, A. P. Grosvenor, L. W. M. Lau, A. R. Gerson and R. S. C. Smart, *Resolving surface chemical states in XPS analysis of first row transition metals, oxides and hydroxides: Cr, Mn, Fe, Co and Ni*, Applied Surface Science **257** (2011), no. 7, 2717-2730.
5. E. L. Ratcliff, J. Meyer, K. X. Steirer, A. Garcia, J. J. Berry, D. S. Ginley, D. C. Olson, A. Kahn and N. R. Armstrong, *Evidence for near-surface NiOOH species in solution-processed NiO<sub>x</sub> selective interlayer materials: Impact on energetics and the performance of polymer bulk heterojunction photovoltaics*, Chemistry of Materials **23** (2011), no. 22, 4988-5000.

6. M. T. Greiner, M. G. Helander, W.-M. Tang, Z.-B. Wang, J. Qiu and Z.-H. Lu, *Universal energy-level alignment of molecules on metal oxides*, *Nature Materials* **11** (2012), no. 1, 76-81.
7. E. S. R. Bovill, J. Griffin, T. Wang, J. W. Kingsley, H. Yi, A. Iraqi, A. R. Buckley and D. G. Lidzey, *Air processed organic photovoltaic devices incorporating a  $MoO_x$  anode buffer layer*, *Applied Physics Letters* **102** (2013), no. 18.
8. K. Juodkazis, J. Juodkazyte, R. Vilkauskaite and V. Jasulaitiene, *Nickel surface anodic oxidation and electrocatalysis of oxygen evolution*, *Journal of Solid State Electrochemistry* **12** (2008), no. 11, 1469-1479.

# Chapter 7

## Lifetime Study of V<sub>2</sub>O<sub>x</sub> Devices

### 7.1 Introduction

In chapter 5, it has been shown that V<sub>2</sub>O<sub>x</sub> films can be fabricated in air by spin-coating vanadium(V) oxytriisopropoxide (s-V<sub>2</sub>O<sub>x</sub>) at room temperature without the need for further treatment such as thermal annealing or UV-ozone plasma treatment. The deposited vanadium(V) oxytriisopropoxide film undergoes hydrolysis in air converting to V<sub>2</sub>O<sub>x</sub> with optical and electronic properties comparable to vacuum deposited V<sub>2</sub>O<sub>5</sub>. Organic photovoltaic (OPV) cells with a s-V<sub>2</sub>O<sub>x</sub> hole extraction layer, and active layer of PFDT2BT-8:PC<sub>70</sub>BM, have achieved power conversion efficiencies of 6.3 (± 0.15) % comparable to both PEDOT:PSS and vacuum deposited MoO<sub>3</sub>, having power conversion efficiencies of 6.2 (± 0.2) %. In addition, another critical issue that should be taken into account for the commercialisation of OPVs in the future is to develop the stability of polymer solar cells. This chapter, therefore, describes the lifetime study which was carried out in the laboratory testing system for OPV devices utilising a PFDT2BT-8:PC<sub>70</sub>BM active layer with s-V<sub>2</sub>O<sub>x</sub> interlayer. The obtained results were compared to devices fabricated with the most widely used HELs, PEDOT:PSS and MoO<sub>3</sub>. The degradation that occurred in the OPV devices was investigated by laser beam-induced current (LBIC) mapping and X-ray Photoelectron Spectroscopy (XPS). The initial results showed that s-V<sub>2</sub>O<sub>x</sub>-based devices had the lowest stability. However,

increasing the s-V<sub>2</sub>O<sub>x</sub> thickness and thermal annealing significantly improved their lifetime.

### 7.2 Degradation and Stability of OPVs

Organic photovoltaics have been through a rapid progression of improvements in the last two decades. In the first decade, the majority of studies and reports focused on achieving high power conversion efficiency (PCE). Recently, the efficiency of single junction cells has reached 10.8 % [1] and this value can exceed 15% based on theoretical studies [2]. This trend in developing the PCE of organic solar cells is of course highly significant in order to compete with the more mature inorganic photovoltaic. However, stability of OPV devices is another critical factor for the success of this technology. Silicon-based photovoltaics show high stability which may last up to 25 years. Therefore, more attention was paid to this technology in the past 10 years with a view to the possibilities of commercialisation. A considerable number of studies has investigated degradation phenomena in OPVs and the factors that have an impact on their stability [3-6].

The PCE measurements and solar simulation were standardised according to IEC and ASTM standards [7]; the early studies, however, were carried out before standard guidelines and protocols for OPV lifetime testing had been established. Although the standard procedures had been established for inorganic PV technologies many years ago, use of these procedures with OPVs was limited due to the complex device structures and complicated dynamic behaviour of organic devices. In 2011, a set of new standardised methodologies was established after the publication of a consensus paper on testing protocols and the advent of the annual International Summit on OPV Stability



(ISOS) [8, 9]. These guidelines and protocols were developed for various types of lifetime tests such as indoor laboratory testing, outdoor measurements and shelf-life testing.

Moreover, understanding degradation and stability of OPV is still complicated due to that fact that the OPV is the most diverse solar cell type. For this reason, it can be noticed that OPV stability is developing gradually but is still below the desired level. Furthermore, the large diversity of OPVs results in many degradation paths leading to a short lifetime of the devices. These degradation paths can be classified as chemical or physical mechanisms.

Chemical degradation can occur in the dark due to the diffusion of materials in the OPV device. The best example of this aspect is electrode degradation such as the chemical reaction between the aluminium cathode and vinylene bond of Poly(*p*-phenylene vinylene) (PPV) or etching the indium-tin-oxide by PEDOT:PSS interlayer [10, 11]. In addition, some other chemical reactions can take place between atmosphere gases (i.e. oxygen and water) and the components of the solar cell. Illumination is another main reason for the chemical degradation which results in photo-oxidation and photolysis reactions. The photochemical decomposition in OPVs results in disruption of the  $\pi$  conjugation, chain scission, generation of the superoxide oxygen anion or quenching many excitons due to formation carbonyl groups [5, 12]. The mechanism of this chemical degradation has been investigated in detail in literature [13-15]

Physical degradation is related to the change in the morphology of the active layer as a result of phase separation or crystal growth. This type of degradation has not been investigated in detail yet. This can be attributed to difficulties in investigating some physical degradation aspects, such as changes in the microstructure of polymers which

require internal three-dimension scanning. Several studies have investigated the size distribution of polymer crystallites as a function of temperature by using different types of microscopy [16-20].

### 7.2.1 Anode Interfacial Layer for Stable PSCs

Early versions of organic solar cells were fabricated by sandwiching the active layer between ITO anode and evaporated metal cathode. After introducing the interlayer as a hole extraction layer (HEL), the anode contact improved and thus OPV performance became better. The first anode interlayer used was PEDOT:PSS that smoothed the ITO surface and increased the work function of the anode and therefore enhanced holes transport [21, 22]. However, it was found that the operational stability of polymer solar cells fabricated with this material was poor. Several studies investigated the degradation causes of PEDOT:PSS devices. The obtained results attributed the instability of devices to the strong acidity of PEDOT:PSS (pH of 1-3) that triggers etching the ITO surface and its hygroscopic nature [11, 23, 24]. It has been found that the acidic species of PSS triggers ITO etching leading to releasing indium ions which may spread through the PEDOT:PSS interlayer and the photoactive layer. Furthermore, water molecules absorbed by PEDOT:PSS can form spatially inhomogeneously insulating patches at the interface between PEDOT:PSS and the active layer resulting in a decrease in the photocurrent and FF of the device. Another report has suggested that PEDOT:PSS can be photo-oxidised easily [25]. It is noteworthy that there have been a considerable amount of studies for replacing ITO material to develop OPV stability and overcome long-term decay in PCE [26-29].

Using metal oxides as HELs materials has shown high performance OPVs and long-term stability compared to PEDOT:PSS devices. For instance, NiO thin film deposited by pulsed laser deposition showed high stability OPV devices after continuous AM 1.5G light illumination [30]. Solution-processed nickel oxide exhibited a similar enhanced lifetime with stability 10 times longer than the PEDOT:PSS-based devices [31]. OPV with molybdenum oxide as a HEL layer showed good performance and enhanced significantly the lifetime [32, 33]. The following section describes a detailed lifetime study that was carried out for OPV devices utilising s-V<sub>2</sub>O<sub>x</sub> thin film as HEL layer. **Table 7.1** compares the lifetime study for different forms of BHJ devices (i.e. conventional, inverted or tandem configuration) that have been reported in literature. The stability experiments in these studies were carried out under continuous irradiation. Some experimental variations such as the size of active area, power of radiation and temperature are presented.

**Table 7.1** Comparison of the stability for different forms of OPV devices in the literature. The lifetime of devices reported in these studies was measured under continuous irradiation.

Config- ation	OPV structure			Initial reading				Experimental condition	T <sub>x</sub> lifetime (hours)	Comments	Ref
	Bottom electrode	Active layer	Top electrode	PCE %	J <sub>sc</sub> (mA.cm <sup>-2</sup> )	V <sub>oc</sub> (V)	FF %				
Conventional	ITO/PEDOT:PSS	P3HT:PCBM	Ca/Al	3.8	10.4	0.6	61	N <sub>2</sub> environment	T <sub>50</sub> = 140	-	[34]
	ITO/PEDOT:PSS	P3HT:PCBM	SPPO1/Al	3.8	12	0.56	56	Temperature = 60 °C	T <sub>87</sub> = 10	Active area=0.04 cm <sup>2</sup>	[35]
	ITO/PEDOT:PSS	P3HT:PCBM	TiO <sub>x</sub> /Al	4	9.5	0.6	70	-	T <sub>94</sub> = 100	-	[36]
	Ag/PEDOT:PSS	P3HT:PCBM	Ag	1.05	5.45	4.76	56	Temperature = 70 °C	T <sub>80</sub> = 1500	Roll-to-roll	[37]
	ITO/HEL	P3HT:PCBM	Ca/Al	1.09	0.073	29	51	Xe lamp	T <sub>80</sub> = 2600	Large module, 54 identical cells (2 cm <sup>2</sup> )	[38]
	ITO/PEDOT:PSS	PCDTBT:PCBM	Ca/Al	5.6	9.9	0.85	65.9	1500W Xenon lamp with a quartz filter	T <sub>80</sub> = 650	-Active area = 0.04 cm <sup>2</sup> -The aperture mask area = 0.0261 cm <sup>2</sup>	[39]
	ITO/MoO <sub>x</sub>			5.19	8.9	0.91	64.6		T <sub>80</sub> = 14500		
	ITO/V <sub>2</sub> O <sub>5</sub>			5.2	9.4	0.85	65		T <sub>80</sub> = 236		
ITO/MoO <sub>x</sub>	PCDTBT:PCBM	Ca/Al	4.55	8.6	0.89	60	Illuminated in air by 1500W Xenon lamp with a quartz filter	T <sub>80</sub> = 274	Pd concentration in PCDTBT is 0.1 ppm	[40]	
			2.42	7.7	0.71	45		T <sub>80</sub> = 250	Pd concentration in PCDTBT is 2570 ppm		

Contued

Config- ation	OPV structure			Initial reading				Experimental condition	T <sub>x</sub> lifetime (hours)	Comments	Ref
	Bottom electrode	Active layer	Top electrode	PCE %	J <sub>sc</sub> (mA.cm <sup>-2</sup> )	V <sub>oc</sub> (V)	FF %				
Convent- ional	ITO/MoO <sub>x</sub>	PCDTBT:PCBM	TiO <sub>x</sub> /Al	6.5	10.9	0.89	67	- Stored in air - No encapsulation	T <sub>50</sub> = 720	-	[41]
	ITO/PEDOT:PSS			5.6	10.1	0.88	67		T <sub>10</sub> = 16		
Inverted	Cr/Al/Cr	P3HT:PCBM	PEDOT: PSS/Au	3.1	8	0.61	64	Temperature = 50 °C	T <sub>82</sub> = 1500	sulphur plasma lamp (1000W.m <sup>-2</sup> )	[42]
	Ti/Al/Ti	P3HT:PCBM	PEDOT: PSS/Au	3.1	8.1	0.61	62	Temperature = 50 °C	T <sub>59</sub> = 1500		[42]
	ITO/PDMAEMA	P3HT:PCBM	MoO <sub>3</sub> /Ag	3.2	9.1	0.57	62	Illuminated at AM1.5 solar radiation for 8 hours/day in air	T <sub>94</sub> = 1344	-	[43]
	ITO/ZnO			3.3	9.1	0.56	65		T <sub>79</sub> = 1344		
	ITO/ZnO	PTB7:PCBM	MoO <sub>3</sub> /Ag	7.3	14.7	0.72	69	Stored in air	T <sub>96</sub> = 840	OPV parameters were measured in N <sub>2</sub>	[44]
TiO <sub>2</sub> :Cs	6.4			14.2	0.71	63	T <sub>87</sub> = 840				
Tandem	ITO/PEDOT:PSS	PCPDTBT:PCBM	TiO <sub>x</sub> /Al	5.5	7.5	1.2	63	N <sub>2</sub> environment	T <sub>70</sub> = 40	-	[45]

## 7.3 Stability Study of V<sub>2</sub>O<sub>x</sub> Devices

### 7.3.1 Lifetime Measurement

In all experiments, the lifetime measurement of OPV devices was initiated on the same day of the fabrication experiment in order to avoid other degradation factors. More details about the lifetime tester were described previously in **3.2.9 the lifetime tester**. The OPV devices were placed in the lifetime tester (ATLAS Suntest CPS+) for between 150 and 500 hours under constant illumination. JV characterisation of the devices under ATLAS Suntest CPS+ and Newport solar simulator showed slight variation due to a spectral mismatch of the light sources and variation in pixel size and temperature. Therefore, all the devices were characterised by the Newport solar simulator before and after testing for further comparison. In addition, all device metrics quoted here (PCE,  $V_{oc}$ ,  $J_{sc}$  and FF) were determined from JV characterisation measured by the Newport solar simulator. ATLAS Suntest CPS+ data were used to show the general trends of OPV performance during the lifetime test.

Before using the ATLAS Suntest CPS+, stability of temperature and light intensity inside the test chamber was measured by temperature sensors and the photodiodes fixed on the test board as shown in **Figure 7.1**. The temperature and light intensity values shown in the figure were determined from the average reading of four temperature sensors and eight silicon photodiodes respectively. It can be observed that the average temperature for 500 hours was  $36.7^{\circ}\text{C} \pm 0.7$ . On some days, it can be noticed that temperature increased by a maximum of  $4.3^{\circ}\text{C}$  inside the chamber due to the air-conditioning and building's heating. Nevertheless, the measured values remain within the accepted variance for test protocol.

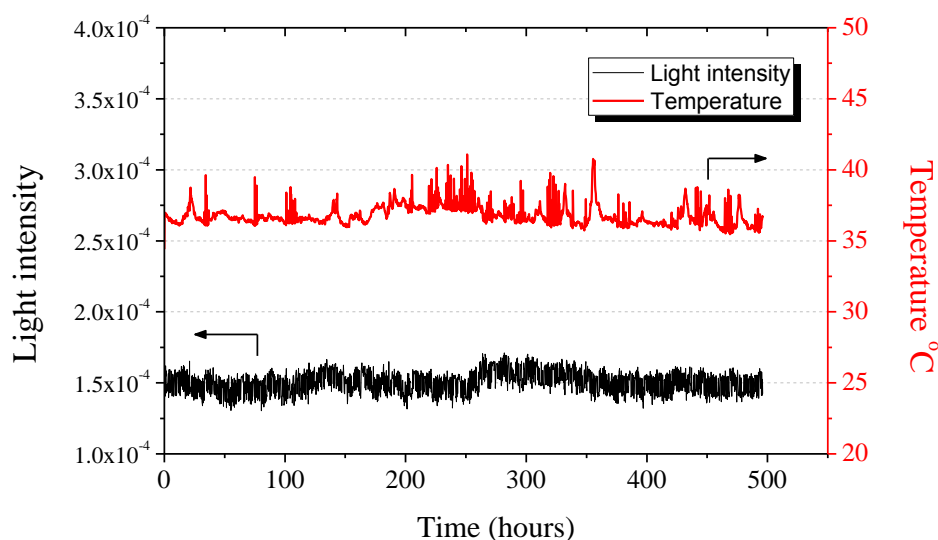


**Figure 7.1** the temperature and light intensity values measured inside the lifetime test chamber. The temperature values are the mean of four temperature sensors while the light intensity values are the mean of eight silicon photodiodes. The average temperature is  $36.7^{\circ}\text{C} \pm 0.7$ .

### 7.3.2 Stability of s-V<sub>2</sub>O<sub>x</sub> vs MoO<sub>3</sub> and PEDOT:PSS

To explore the stability of solution-processed vanadium oxide as a hole extraction layer, a comparison with the most widely used HELs, PEDOT:PSS and thermally evaporated MoO<sub>3</sub> had to be achieved. All the OPV devices were fabricated on the same day and in parallel as described in **4.3 OPV Device Fabrication**. **Figure 7.2** shows the normalised PCE,  $V_{oc}$ ,  $J_{sc}$  and FF extracted from the Suntest CPS+ data as a function of irradiation time. Each value represents the average of at least 10 pixels from 12 pixels defined on two devices. The errors quoted are defined by the standard deviation about the mean. It is worth mentioning that measuring of each pixel was repeated every 15 minutes during the lifetime test.

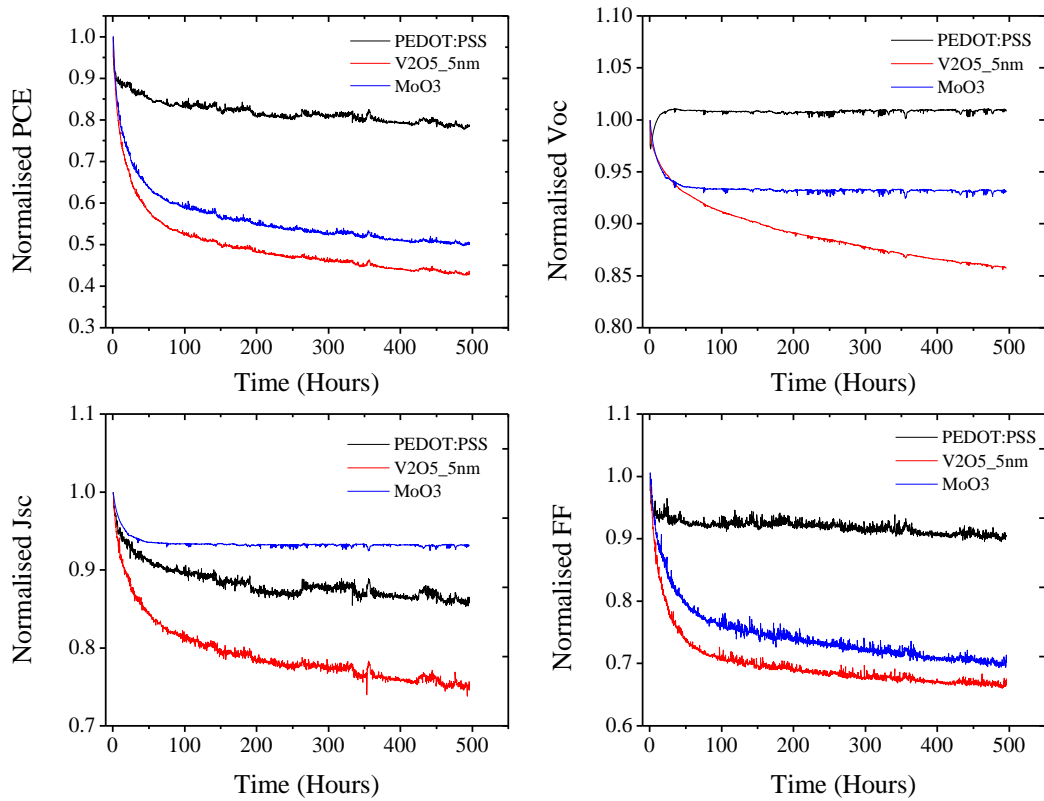


**Figure 7.2** The normalised PCE,  $V_{oc}$ ,  $J_{sc}$  and FF of PEDOT:PSS, s- $V_2O_x$  and  $MoO_3$  devices extracted from the ATLAS Suntest CPS+ data as a function of irradiation time. Each value represents the mean of at least 10 pixels from 12 pixels and each pixel was measured every 15 minutes. The linear phase of PCE curves was used for calculating  $T_{80}$  and  $T_{50}$  lifetimes.

It can be seen that the majority of photovoltaic parameters of all devices initially decreased at an exponential rate (burn-in phase) and then followed a more linear decay. The rapid decrease in burn-in phase for all devices can be attributed to photochemical reactions (e.g. photo-oxidation) in the PFDT2BT-8:PC<sub>70</sub>BM layer. These reactions increase the density of trap states which significantly decrease the carrier charge mobility [46]. After a period of time the generation of trap states tends to saturate leading to a linear trend. Therefore, the linear decay was used to describe the OPV device lifetime.



The most commonly used metric is  $T_{80}$  lifetime which means the period of time required for the efficiency to drop to 80% from the point at the beginning of the linear decay. Similarly,  $T_{50}$  is another metric, but less common, that can be used to calculate the time in which efficiency falls to 50% of the initial value of the linear decay. Here the linear-fit of the linear curves of PCE was used to determine both the  $T_{80}$  and the  $T_{50}$  lifetime of the devices, the results of which are shown in **Table 7.2**.

It can be seen in **Figure 7.2** that the PCE of s-V<sub>2</sub>O<sub>x</sub>, MoO<sub>3</sub> devices decreased rapidly in the first 50 hours. The decrease in MoO<sub>3</sub> devices was governed by a reduction in FF by 22% while  $J_{sc}$  and  $V_{oc}$  showed a relatively small reduction of about 5%. In s-V<sub>2</sub>O<sub>x</sub>-based devices, FF,  $J_{sc}$  and  $V_{oc}$  underwent a faster decrease rate than in other devices. However, PEDEOT:PSS-based devices were significantly stable in comparison with other devices. Interestingly, the  $V_{oc}$  of PEDOT:PSS devices decreased by just 3% in the first hour then increased to slightly exceed the initial value for most of the test time. This behaviour may result from modification of the work function of the PEDOT:PSS surface.

**Table 7.2** PCE decay in 100 hours and over the full 500 hours. PCE values and  $T_{80}$  and  $T_{50}$  lifetimes calculated from the ATLAS Suntest CPS+ data.

HELs material	PCE [%] (in 100 hrs)	PCE (in 500 hrs)	$T_{80}$ (hours)	$T_{50}$ (hours)
<b>PEDOT: PSS</b>	3.9 ±0.19 (- 17.1%)	3.7 ±0.14 (-21.6%)	1136 ±69.3	2840 ± 198
<b>MoO<sub>3</sub></b>	3.2 ±0.12 (- 41.1%)	2.7 ±0.08 (- 50.3%)	694 ±48.3	1735 ± 131
<b>s-V<sub>2</sub>O<sub>x</sub></b>	2.8 ±0.09 (- 46.2%)	2.3 ±0.11 (- 56.3%)	551 ±37.6	1378 ±96

Over the entire testing time it can be noticed that the PCE of devices utilising PEDOT:PSS, MoO<sub>x</sub> or V<sub>2</sub>O<sub>x</sub> as HELs reduced by 21.6%, 50.3% and 56.3% respectively. Furthermore, it was found that PEDOT:PSS devices have the best T<sub>80</sub> lifetime of 1136 hours while V<sub>2</sub>O<sub>x</sub> devices recorded the shortest lifetime, 551 hours. The largest loss in V<sub>2</sub>O<sub>x</sub> can be attributed to two different reasons. First, it was found that the acidic nature of the vanadium oxytriisopropoxide precursor leads to a disruption of conjugated polymers by an electrophilic addition to the C=C components. This resulted in an increase of densities of trap states leading to non-radiative recombination of excitons [47, 48]. Second, the used V<sub>2</sub>O<sub>x</sub> film did not undergo post-deposition treatment; thus some residues of the precursor material and atmospheric gases on the surface would have an impact on the active layer, such as generation of some structural defects, causing the fast degradation rate. T<sub>80</sub> lifetimes, as calculated from all OPV devices, are in general very low compared to other results reported in literature. This can probably be ascribed to the degradation process of the PFDT2BT-8:PC<sub>70</sub>BM layer and the decay process in the interface between the active layer and electrode cathode. This type of degradations was not investigated in this work.

For further comparison, all OPV devices were characterised by the Newport solar simulator before and after the lifetime test as shown in **Table 7.3**. It can be seen that most of the photovoltaic parameters decreased with similar magnitude to ATLAS Suntest CPS+. Here, the PCE of OPV devices based on PEDOT:PSS, MoO<sub>x</sub> or V<sub>2</sub>O<sub>x</sub> HELs reduced by 37.8%, 46.5% and 61.5% respectively. The variation in values between the Newport solar simulator and the Suntest CPS+ resulted from the spectral mismatch of the light sources and the variation in pixel size and temperature. For instance, the variation in pixel size and light intensity has an impact on the measured J<sub>sc</sub>.

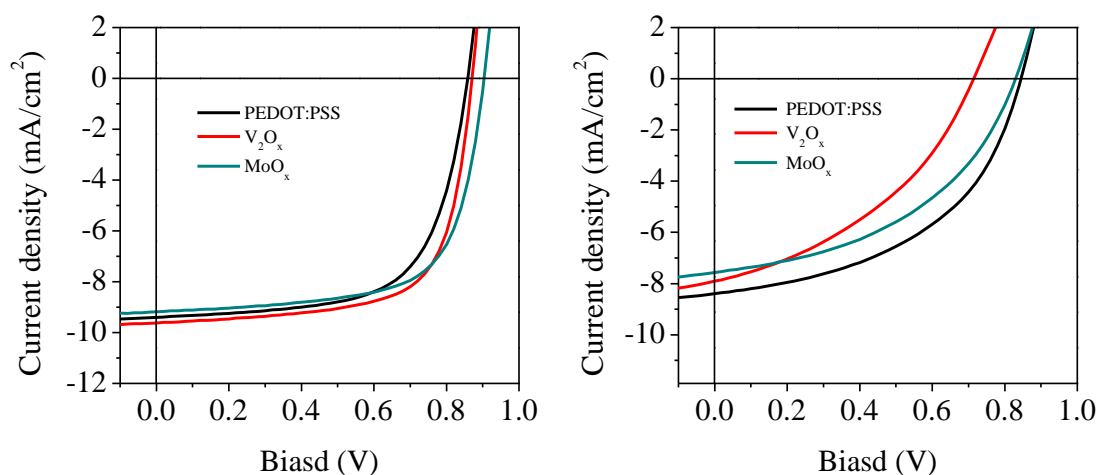


**Figure 7.3** Current density-voltage (J-V) characteristics for PEDOT:PSS,  $V_2O_x$  and  $MoO_x$  devices under the AM1.5G solar spectrum before (left) and after 500 hours of lifetime testing (right).

**Table 7.3** the average values of photovoltaic parameters under the AM1.5G solar spectrum. OPV devices with various HELs films were measured before and after 500 hours under constant illumination.

HELs material	PCE [%]	$V_{oc}$ [V]	$J_{sc}$ [ $mA \cdot cm^{-2}$ ]	FF [%]	$R_s$ [ $\Omega \cdot cm^2$ ]	$R_{sh}$ [ $\Omega \cdot cm^2$ ]	
<b>s-<math>V_2O_x</math></b>	Fresh	$5.7 \pm 0.11$	0.87	$9.6 \pm 0.14$	$69.1 \pm 0.4$	$10 \pm 0.4$	$1204 \pm 207$
	Aged	$2.2 \pm 0.16$	0.71	$7.8 \pm 0.21$	$39.9 \pm 1.2$	$37.2 \pm 3.1$	$233 \pm 24$
<b>PEDOT:PSS</b>	Fresh	$5.3 \pm 0.12$	0.86	$9.4 \pm 0.16$	$68.3 \pm 0.8$	$15.5 \pm 1.7$	$1270 \pm 137$
	Aged	$3.3 \pm 0.19$	0.85	$8.3 \pm 0.19$	$47.1 \pm 2.2$	$25.3 \pm 1.9$	$455 \pm 27$
<b><math>MoO_3</math></b>	Fresh	$5.6 \pm 0.07$	0.90	$9.2 \pm 0.06$	$67.5 \pm 0.9$	$13.1 \pm 0.8$	$1286 \pm 133$
	Aged	$3.0 \pm 0.15$	0.84	$7.7 \pm 0.15$	$46.6 \pm 1.5$	$34.2 \pm 1.7$	$423 \pm 17$

In addition, the temperature inside the test chamber was about  $36.7^{\circ}\text{C} \pm 0.7$  while OPV devices were measured by the solar simulator at  $26^{\circ}\text{C}$  which could affect the measured  $V_{oc}$ . Consequently, all these factors led to slight variations in the OPV device efficiency between the two measurements.

The high stability of PEDOT:PSS is clearly in contrast to previous reports in literature and to what has been presented previously in **7.2 Degradation and Stability of OPVs**. This can be attributed to the low degradation at the interface between the active layer and the PEDOT:PSS layer. Previous studies investigated the stability of PEDOT:PSS thin films based on P3HT polymer which is different from the donor polymer used in this work [20, 12]. It is well known that P3HT is highly sensitive to water and oxygen [33, 49] and in contrast to PEDOT:PSS which is a highly hygroscopic material [11]. Recently, several studies have reported that PEDOT:PSS-based devices show high stability comparable to other HELs materials [50, 39].

In order to explore the changes in photocurrent degradation and the density of defects in OPV devices, a LBIC mapping technique was used to take an image for the whole pixel of different devices. The experimental details of this method were given in **4.2.7 Laser Beam Induced Current Mapping (LBIC)**. **Figure 7.4** shows LBIC images of PFDT2BT-8:PC<sub>70</sub>BM devices with 5 nm thickness of s-V<sub>2</sub>O<sub>x</sub> as HELs before and after lifetime testing for 500 hours. The colour scale in the figure shows the intensity of the generated current, in which the red colour indicates high current density while the dark blue indicates low current.

It can be seen that s-V<sub>2</sub>O<sub>x</sub>-based devices showed extensive degradation that affect charge generation in the device. It is clear that the degradation process started from the edges of the pixel which means that degradation started faster in the areas not covered

with cathodes. As the V<sub>2</sub>O<sub>x</sub> film was fabricated from an oxytriisopropoxide precursor which undergoes hydrolysis process in air, some atmospheric components and the residual precursor were predicted to cause this severe degradation. Consequently, further experiments were carried out to develop stability of s-V<sub>2</sub>O<sub>x</sub>-based devices.

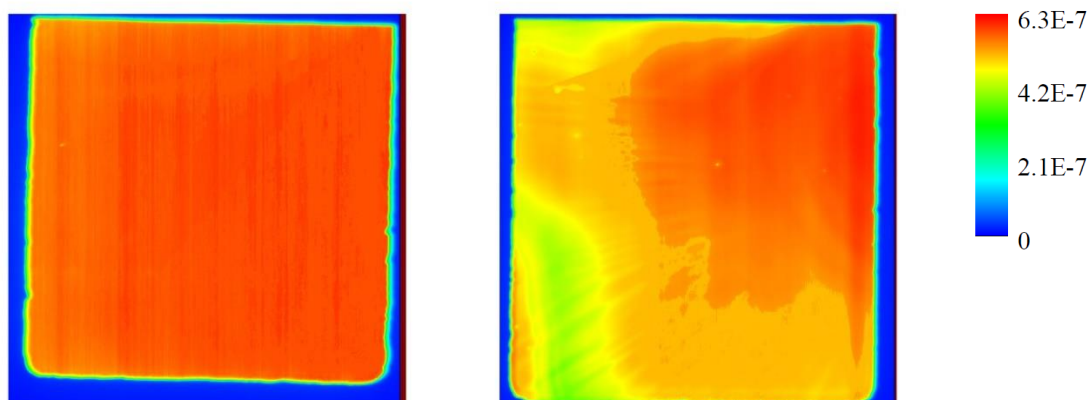


**Figure 7.4** Laser beam-induced current (LBIC) images for s-V<sub>2</sub>O<sub>x</sub>-based devices before (left) and after 500 hours of lifetime testing (right). The colour scale in the figure shows the intensity of the generated current in which the red colour indicates high current density while the dark blue indicates low current.

### 7.3.3 Thickness Impact

In order to investigate what effect, if any, that s-V<sub>2</sub>O<sub>x</sub> film thickness has on the stability of the PFDT2BT-8:PC<sub>70</sub>BM device, several devices were fabricated with various thicknesses of s-V<sub>2</sub>O<sub>x</sub>.

**Figure 7.5** shows the photovoltaic parameters extracted from the ATLAS Suntest CPS+ data for OPV devices with s-V<sub>2</sub>O<sub>x</sub> of thickness 5 nm, 10 nm, 15 nm or 20 nm. Note that the device metrics used in the figure are not normalised because all tested devices had the same materials and structure. It can be seen that after 250 hours of continued irradiation it was found that the thickest s-V<sub>2</sub>O<sub>x</sub> device had a final PCE of 2.8% which

is 33% higher than the PCE of ordinary devices (i.e. s-V<sub>2</sub>O<sub>x</sub> with 5nm of thickness). To confirm this result all devices were characterised by the Newport solar simulator before and after lifetime testing as illustrated in **Figure 7.6**. Indeed, it can be noticed that devices with 20 nm s-V<sub>2</sub>O<sub>x</sub> showed the highest PCE by a maximum of 40%.

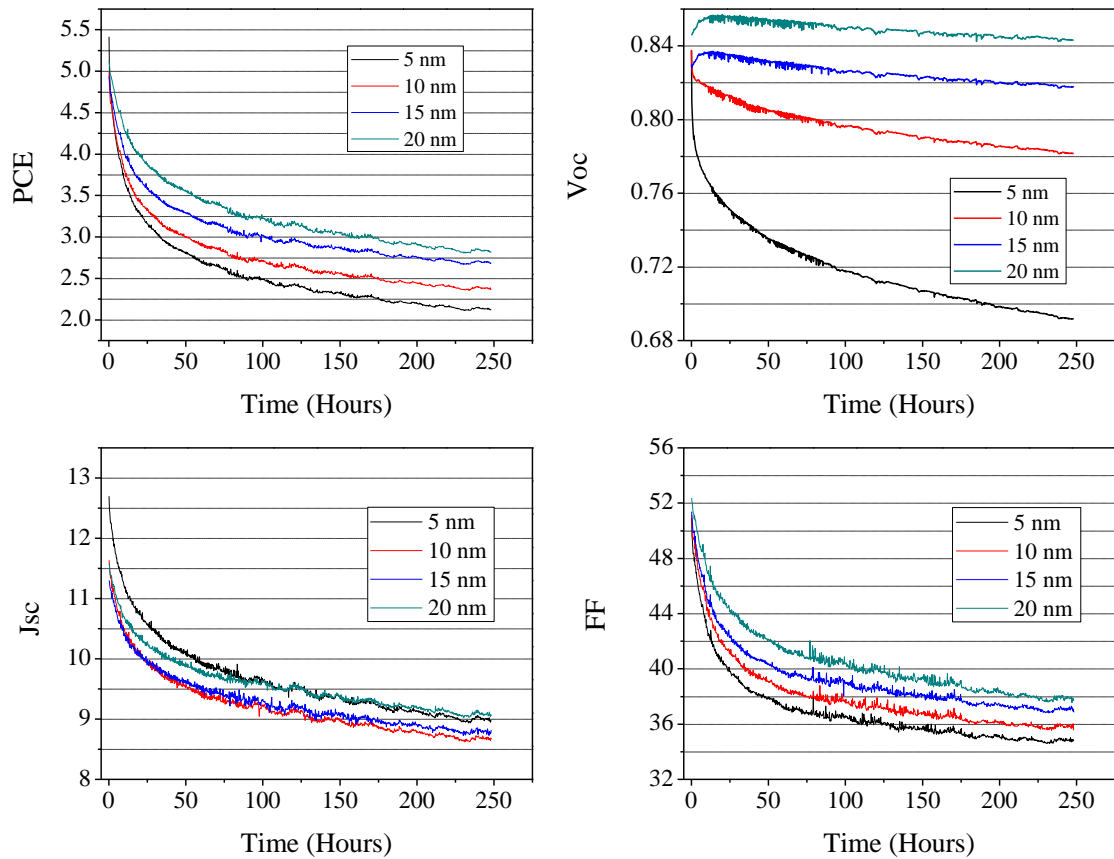


**Figure 7.5** The normalised PCE, V<sub>oc</sub>, J<sub>sc</sub> and FF of s-V<sub>2</sub>O<sub>x</sub>-based devices extracted from the ATLAS Suntest CPS+ data as a function of irradiation time. The PFDT2BT-8:PC<sub>70</sub>BM devices were fabricated with 5 nm, 10 nm, 15 nm or 20 nm thickness of s-V<sub>2</sub>O<sub>x</sub> films. Each value represents the mean of at least 10 pixels from 12 pixels and each pixel was measured every 15 minutes.

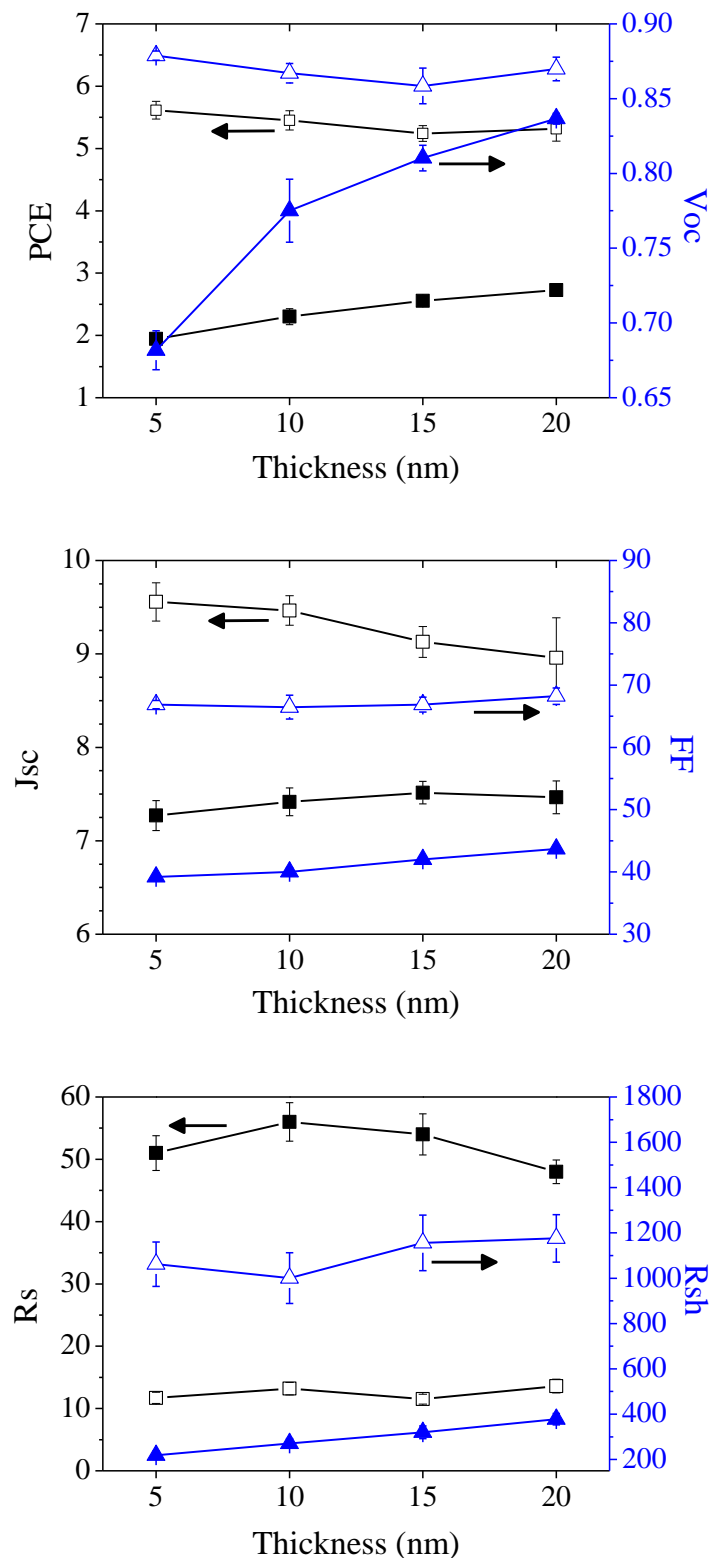


**Figure 7.6** Comparison of Photovoltaic parameters for PFDT2BT-8:PC<sub>70</sub>BM devices under the AM1.5G solar spectrum with various thicknesses of s-V<sub>2</sub>O<sub>x</sub> thin layers. The open shapes represent pre-illumination characterisation and the filled shapes represent the post-illumination measurements.

The increased thickness of the s-V<sub>2</sub>O<sub>x</sub> layer resulted in a significant reduction in the degradation of the OPV devices. It can be noticed from both data that the overall optimisation in the lifetime was dominated by the increase in the V<sub>oc</sub>. **Figure 7.6** shows that after illumination V<sub>oc</sub> decreased by 22% for the least thick s-V<sub>2</sub>O<sub>x</sub> while it decreased by only 4% for the thicker device. This result indicates the fast decay of the thin vanadium oxide film and the possibility of mixing with the active layer due to some chemical reactions induced by light.

In this experiment, it was impossible to extend the lifetime testing for longer than 250 hours due to time restrictions and the limited availability of the lifetime tester. Therefore, the T<sub>80</sub> lifetime of devices was calculated from the linear-fit to the PCE curve for the period (150 – 250 hours). It was found that T<sub>80</sub> lifetime increased from 236 hours for thin s-V<sub>2</sub>O<sub>x</sub> devices to 321 hours for 15 nm s-V<sub>2</sub>O<sub>x</sub> film. The thick device showed slightly lower stability of about 295 hours. Despite the recorded development in the devices stability, all OPV devices with varied thicknesses of s-V<sub>2</sub>O<sub>x</sub> interlayer showed less stability than PEDOT:PSS, MoO<sub>x</sub> devices. As a result, further experiments were carried out to optimise the stability of s-V<sub>2</sub>O<sub>x</sub>-based devices.

### 7.3.4 Thermal Annealing

To explore the effect of thermal annealing on the stability of s-V<sub>2</sub>O<sub>x</sub>-based devices, the s-V<sub>2</sub>O<sub>x</sub> films were thermally annealed at 150°C in ambient conditions. In this experiment two sets of OPV devices were fabricated and placed inside the lifetime chamber for 150 hours. In the first group, 5-nm thick s-V<sub>2</sub>O<sub>x</sub> films were spin-coated onto clean ITO substrates and then annealed for durations ranging from 10 to 80 minutes before spin-coating the PFDT2BT-8:PC70BM blend. **Figure 7.7** shows the



output J–V characteristics of devices upon illumination with an AM1.5G simulated solar spectrum before and after lifetime testing. The extracted solar cell parameters are illustrated in **Figure 7.8**. It can be seen that thermal annealing enhanced the PCE of devices by about 10%. This improvement was governed by an increase of both  $V_{oc}$  and  $J_{sc}$ . Furthermore, it can be noticed from **Figure 7.8** that the performance of unannealed V<sub>2</sub>O<sub>x</sub> devices was better than those annealed at different times. This result supports the previous discussion in **5.10 Thermally Stable s-V<sub>2</sub>O<sub>x</sub> as a Hole Extraction Layer in OPV** as the thermal annealing of V<sub>2</sub>O<sub>x</sub> films does not improve the performance of OPV devices.

In the previous section, **7.3.3 Thickness impact**, it has been shown that an increase in the thickness can increase the PCE of devices. As a result, various s-V<sub>2</sub>O<sub>x</sub> thicknesses were fabricated and then thermally annealed at 150°C in air for 30 minutes. In a similar procedure, all devices were characterised with Newport solar simulator (AM1.5G) before and after lifetime testing as shown in **Figure 7.9**. After irradiation for 150 hours, it can be seen that the PCE increased significantly from 2.1% to 2.9% with increased thickness of the V<sub>2</sub>O<sub>x</sub> layer as illustrated in **Figure 7.10**. The overall increase in PCE was attributed to the large increase in  $V_{oc}$ . Consequently, the combined effects of thickness and thermal annealing are significant factors for support the stability of s-V<sub>2</sub>O<sub>x</sub>-based devices.

It is well known that heating of thin films can remove residues of the precursor and atmospheric components such as water and hydrocarbon components. To explore the effect of these components, O1s and C1s spectra of XPS were investigated for unannealed s-V<sub>2</sub>O<sub>x</sub> film and annealed film at 200°C in air as shown in **Figure 7.11**. O1s spectra for both samples consist of three different species which are ascribed to

vanadium-oxygen bonds, hydroxide species absorbed onto the surface and H<sub>2</sub>O molecules absorbed into the film respectively. Concentration and position of the different chemical states present in the O1s spectra are shown in **Table 7.4**. Indeed, XPS scans showed a significant reduction in the amount and spectral intensity of both chemical states (i.e. (OH) and (H<sub>2</sub>O) states) after heating s-V<sub>2</sub>O<sub>x</sub> films at 200°C. This decrease was accompanied by the increased presence of the V-O bonds within the film. In addition, it can be noticed that concentration (C-O) species in C1s spectrum decreased after annealing due to removing some residues of the precursor.

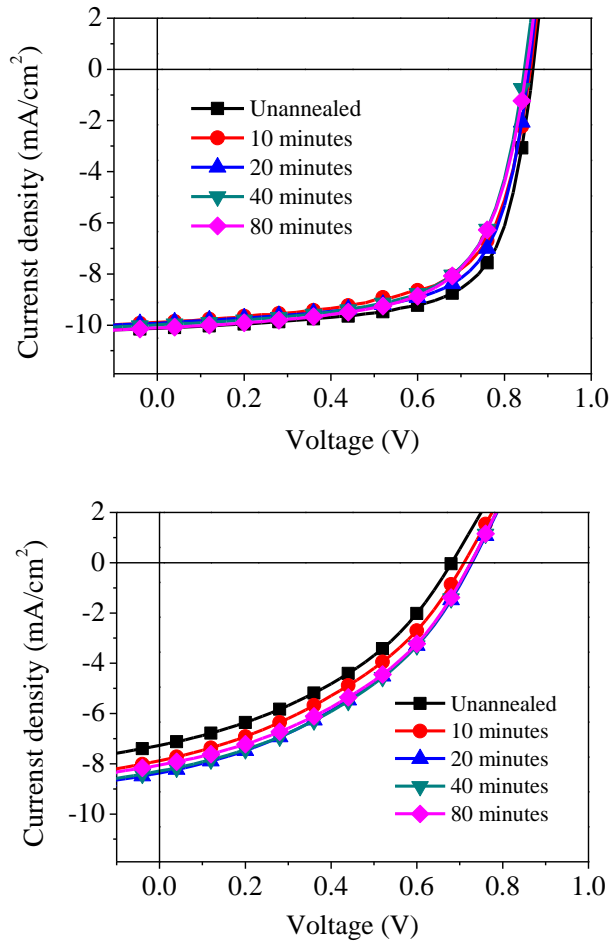


**Figure 7.7** (J-V) characteristics for s-V<sub>2</sub>O<sub>x</sub>-based devices under the AM1.5G solar spectrum before (left) and after 150 hours of illumination (right). The s-V<sub>2</sub>O<sub>x</sub> thin films with thickness of 5 nm were thermally annealed in air for durations ranging from 10 to 80 minutes before spin coating the PFDT2BT-8:PC70BM blend inside a nitrogen filled glovebox.

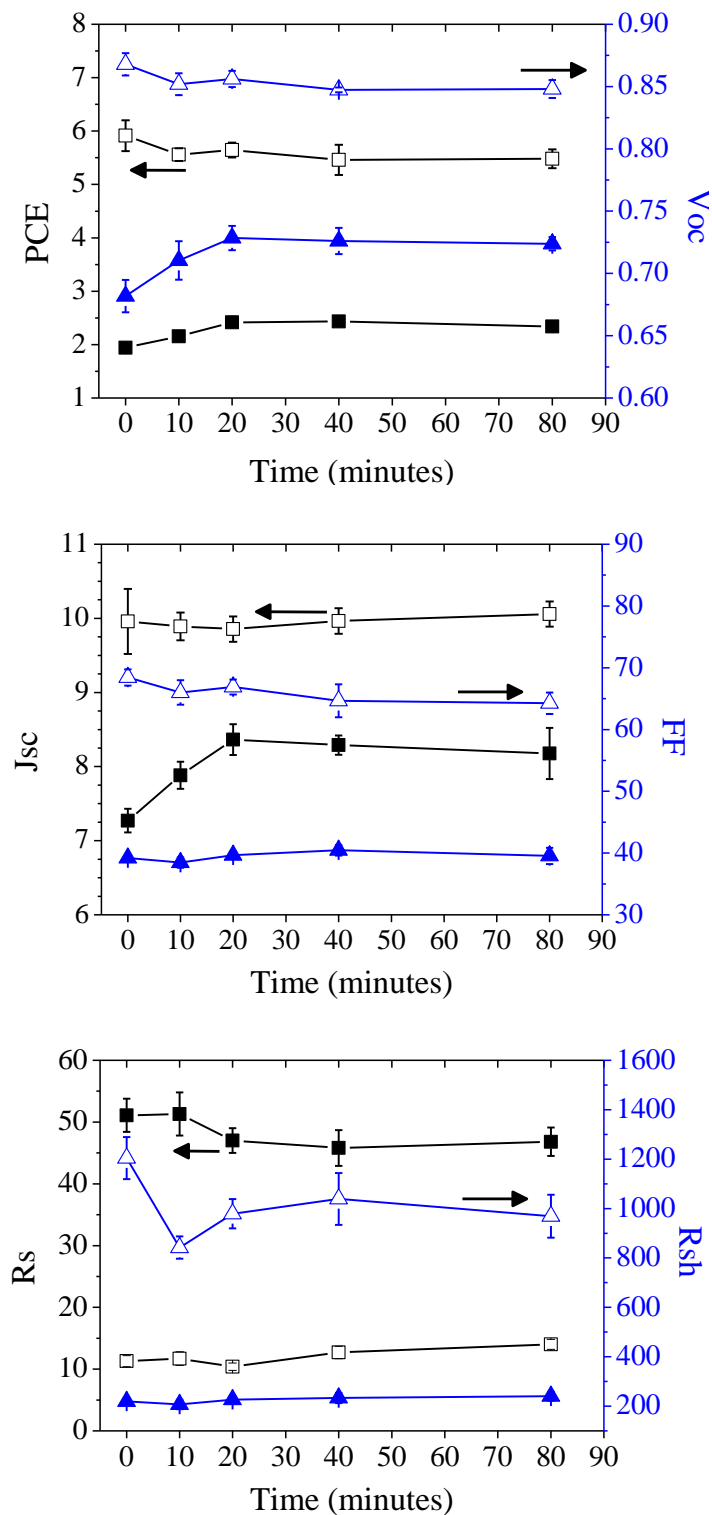


**Figure 7.8** Comparison of performance parameters for devices with 5 nm thickness of s-V<sub>2</sub>O<sub>x</sub> thin layer that were annealed between 10 to 80 minutes in air. The open shapes represent pre-illumination characterisation and the filled shapes represent the post-illumination measurements.

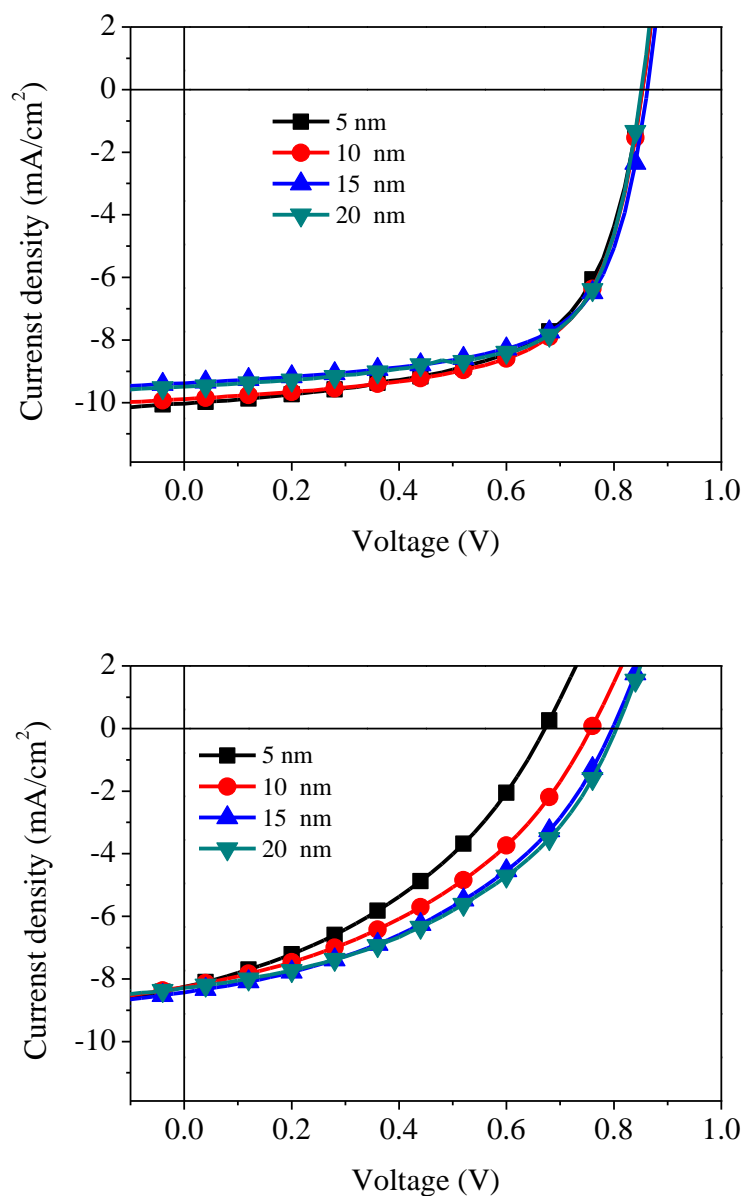


**Figure 7.9** Current density-voltage (J-V) characteristics for s-V<sub>2</sub>O<sub>x</sub>-based devices under the AM1.5G solar spectrum before (left) and after 150 hours of illumination (right). The s-V<sub>2</sub>O<sub>x</sub> thin films with thicknesses of 5, 10, 15, 20 nm were thermally annealed at 150 °C under ambient conditions for 30 minutes before spin coating the PFDT2BT-8:PC70BM blend inside a nitrogen filled glovebox.

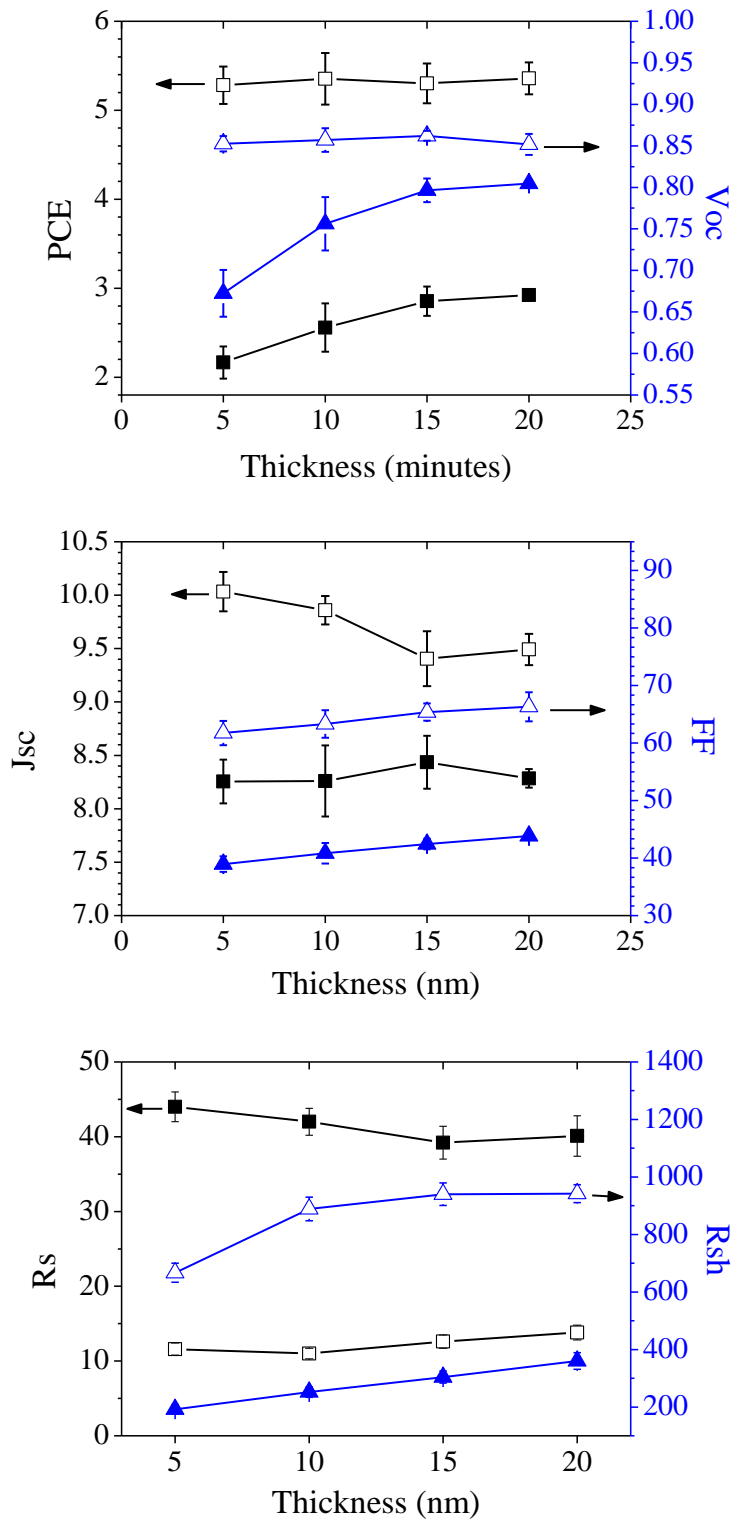


**Figure 7.10** Comparison of performance parameters for devices with various thicknesses of s-V<sub>2</sub>O<sub>x</sub> thin layers that were annealed for 30 minutes in air. The open shapes represent pre-illumination characterisation and the filled shapes represent the post-illumination measurements.

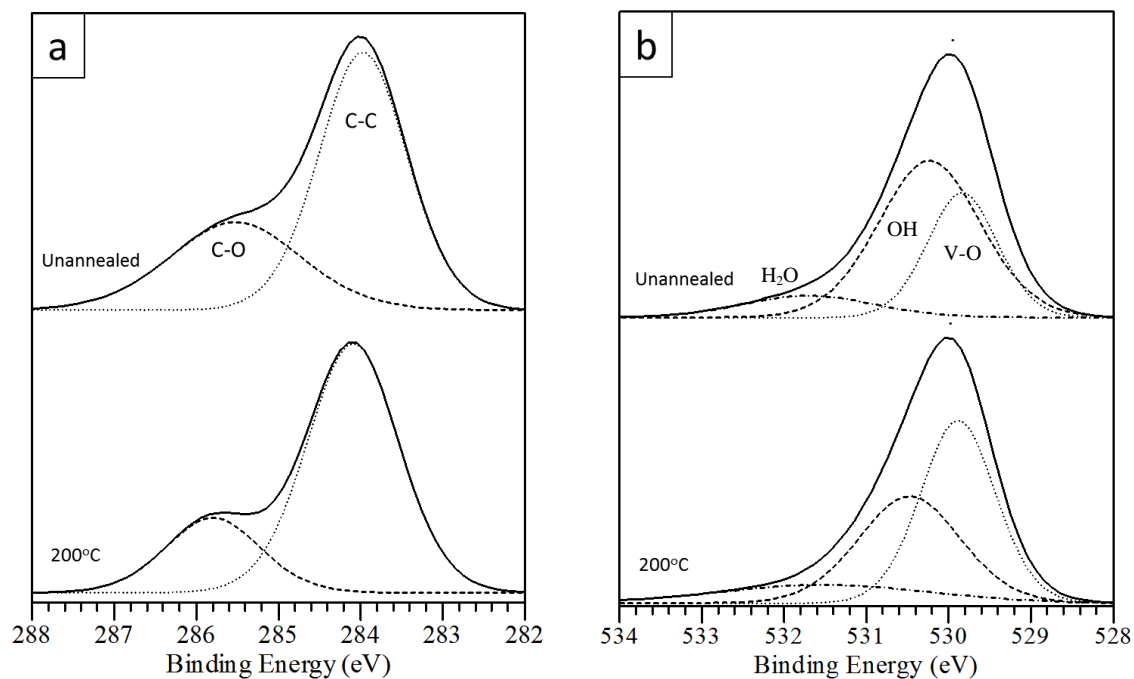


**Figure 7.11** Photoelectron Spectroscopy scans of unannealed solution processed vanadium oxide film and annealed film at 200°C in air where (a) is the C1s spectra and (b) O1s spectra.

**Table 7.4** Position and concentrations of the difference chemical peaks in the high resolution O1s and C1s spectra.

	Unannealed			200°C		
	Peak position	Concentration	Intensity	Peak position	Concentration	Intensity
<b>C-C</b>	284.0	68.2%	1467	284.1	74.6%	1447
<b>C-O</b>	285.6	31.8%	928	285.8	25.4%	880
<b>O-H</b>	530.5	35.8%	3740	530.5	33.6%	3190
<b>H<sub>2</sub>O</b>	531.5	24.4%	1130	531.6	19.3%	860

According to previous reports it is well known that semiconducting polymer films react with water and oxygen in varying degrees to cause oxidation (i.e., chemical degradation) [7, 4]. The oxidation rate of organic materials increases considerably with illumination (i.e. photo-oxidation) resulting in the formation of deep traps. In a previous study, the impact of water and oxygen on the mobility of C60 films was examined [51]. It was found that exposing the film to air led to the generation of trap-state energies below the LUMO energy of C60 and thus reduced the mobility. Heating the films in a helium atmosphere removed those trap states. Furthermore, presence of these materials at the interface with the active layer in OPVs results in the formation of interfacial voids and insulating layers leading to an increase in the recombination process. At the ITO interface, oxygen atoms from the ITO electrode can exchange with the incoming oxygen (from either molecular oxygen or water). In some cases, both water and molecular oxygen can diffuse through all the layers of the OPV device to the cathode interface causing oxidation of Ca layer. In this work, this diffusion was not determined because the heating of 5 nm thick of V<sub>2</sub>O<sub>x</sub> films did not show a significant development in the performance. Therefore, it is believed that the resulting degradation in OPV devices occurred at the interface between the ITO electrode and the active layer.

In order to compare the developed stability of s-V<sub>2</sub>O<sub>x</sub>-based devices with those fabricated with a PEDOT:PSS or MoO<sub>x</sub> interlayer, T<sub>80</sub> lifetime was determined after a period of 500 hours of illumination. **Figure 7.12** shows the normalised photovoltaic parameters for devices with various HEL layers extracted from the Suntest CPS+ data as a function of irradiation time. In s-V<sub>2</sub>O<sub>x</sub>-based devices the anode interlayer was fabricated with 15 nm thickness of s-V<sub>2</sub>O<sub>x</sub> and then annealed at 150°C in air.

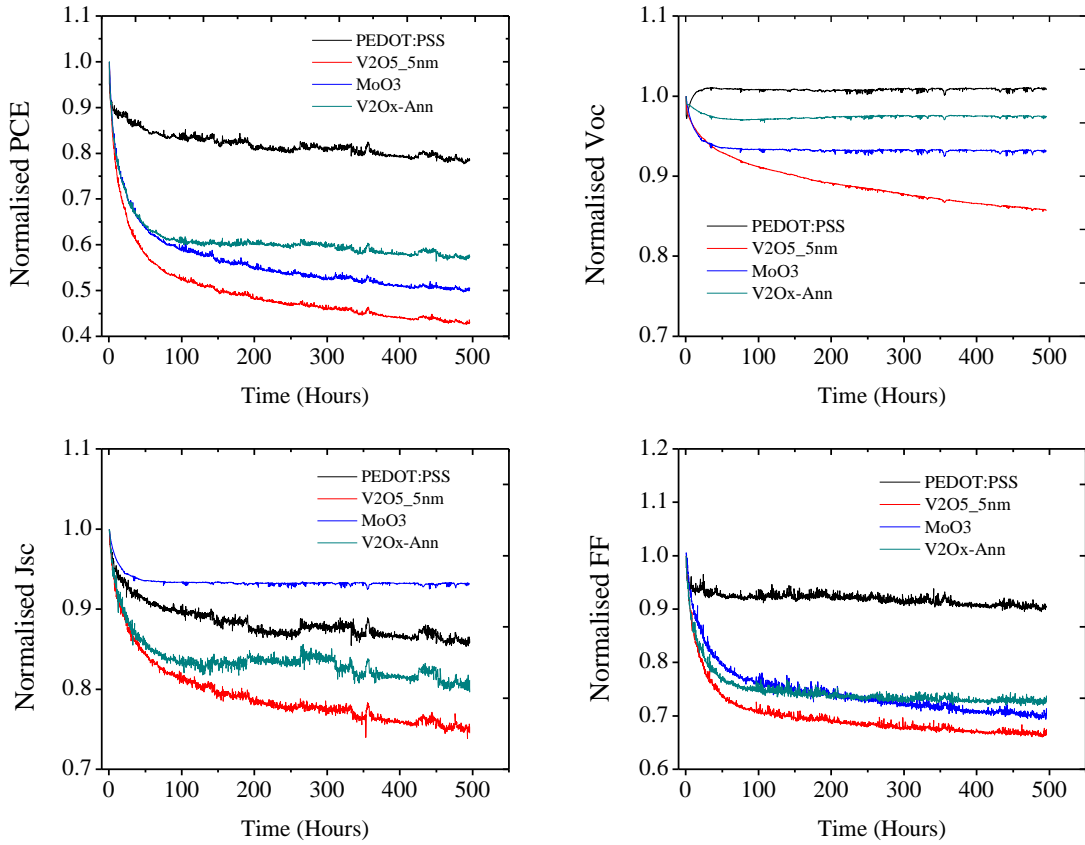


**Figure 7.12** The normalised photovoltaic parameters extracted from the ATLAS Suntest CPS+ data as a function of irradiation time for OPV devices utilising the different HEL materials. Each value represents the mean of at least 10 pixels from 12 pixels and each pixel was measured every 15 minutes. The linear phase of PCE curves was used for calculating  $T_{80}$  lifetimes.

It can be seen that the drop in the PCE during the initial burn-in period of thick vanadium devices is significantly less than those fabricated with thin  $s\text{-V}_2\text{O}_x$  or with  $\text{MoO}_x$ . This improvement in  $s\text{-V}_2\text{O}_x$  devices was dominated by the high stability of the  $V_{oc}$ . In addition, the  $T_{80}$  decay lifetime was calculated to be 1047 hours which is a comparable value with devices utilising a PEDOT:PSS interlayer ( $T_{80} = 1136$  hours). Furthermore, all devices were measured by the Newport solar simulator before and after the lifetime test as shown in **Table 7.5**. It can be seen that despite the observed improvement in the performance of  $s\text{-V}_2\text{O}_x$ -based devices, their efficiency is still lower than others.



**Table 7.5** the average values of photovoltaic parameters under the AM1.5G solar spectrum. OPV devices with various HELs films were measured before and after 500 hours under constant illumination.

<b>HELs material</b>		<b>PCE [%]</b>	<b>V<sub>oc</sub> [V]</b>	<b>J<sub>sc</sub> [mA.cm<sup>-2</sup>]</b>	<b>FF [%]</b>	<b>R<sub>s</sub> [Ω.cm<sup>2</sup>]</b>	<b>R<sub>sh</sub> [Ω.cm<sup>2</sup>]</b>
<b>s-V<sub>2</sub>O<sub>x</sub></b>	Fresh	5.7 ±0.11	0.87	9.6 ±0.14	69.1 ± 0.4	10 ±0.4	1204 ±207
	Aged	2.2 ±0.16	0.71	7.8 ±0.21	39.9 ± 1.2	37.2 ±3.1	233 ±24
<b>s-V<sub>2</sub>O<sub>x</sub> 135°C Annealing</b>	Fresh	5.1 ±0.10	0.86	9.0 ±0.11	66.1 ± 1.0	12.5 ±0.8	118 ±67
	Aged	2.6 ±0.02	0.81	7.6 ±0.09	42.1 ± 0.25	35.5 ±1.6	334 ±9
<b>PEDOT: PSS</b>	Fresh	5.3 ±0.12	0.86	9.4 ±0.16	68.3 ± 0.8	15.5 ±1.7	1270 ±137
	Aged	3.3 ±0.19	0.85	8.3 ±0.19	47.1 ± 2.2	25.3 ±1.9	455 ±27
<b>MoO<sub>3</sub></b>	Fresh	5.6 ±0.07	0.90	9.2 ±0.06	67.5 ±0.9	13.1 ±0.8	1286 ±133
	Aged	3.0 ±0.15	0.84	7.7 ±0.15	46.6 ± 1.5	34.2 ±1.7	423 ±17

The low PCE of thick s-V<sub>2</sub>O<sub>x</sub> devices can be ascribed to the increased series resistance of devices due to the relatively thick V<sub>2</sub>O<sub>x</sub> interlayer, as can be noticed in the initial measurement. Indeed, it was found that the PCE of thick V<sub>2</sub>O<sub>x</sub> devices decreased by 49%, which is very close to MoO<sub>x</sub>-based devices (46.5%). Moreover, as mentioned previously, the high reactivity of the vanadium precursor, which is known as a Lewis acid, can damage conjugated polymers causing the formation of main-chain defects and trap states and thus reducing the performance of OPV devices.

Fabrication of s-V<sub>2</sub>O<sub>x</sub> thin films using a different precursor could overcome the acidic issue at the interface. In the literature it has been reported that V<sub>2</sub>O<sub>x</sub> thin film can be deposited from different precursors such as vanadium acetylacetonate solution [52], V<sub>2</sub>O<sub>x</sub> powder [53], vanadium trichloride solution[54], sodium metavanadate [55] and vanadium (III) acetylacetonate [56]. Some of V<sub>2</sub>O<sub>x</sub>-based devices fabricated with these

components have shown a good performance with a PCE similar to those fabricated with an oxytriisopropoxide precursor.

### 7.4 Conclusion

It has been shown that HEL materials used in OPVs at the interface between the active layer and the anode electrode have a significant effect on the degradation rate of the device. These materials can lead to the generation of structural and electronic defects at the interface and thus increase the density of trap states. Despite the burn-in phase which occurs due to photochemical reactions in the active layer and affects its charge mobility, the nature of HEL materials have an impact on both burn-in and subsequent linear decay.

In contrast to findings in literature, OPV devices utilising a PEDOT:PSS interlayer have shown the best device stability in comparison to MoO<sub>x</sub> or V<sub>2</sub>O<sub>x</sub> devices. The observed high stability was attributed to the nature of PEDOT:PSS used in this work that may have a more neutral pH. However, OPV devices with thin V<sub>2</sub>O<sub>x</sub> have shown a very fast degradation rate which was dominated by a reduction in V<sub>oc</sub>. They also showed a short T<sub>80</sub> decay lifetime that was just 20% of PEDOT:PSS devices. The stability of s-V<sub>2</sub>O<sub>x</sub> devices was developed significantly by increasing the thickness of the s-V<sub>2</sub>O<sub>x</sub> film and thermally annealing at 150°C; a result that became comparable to PEDOT:PSS devices. Nevertheless, the overall PCE of s-V<sub>2</sub>O<sub>x</sub>-based devices after 500 hours of illumination was lower than other devices utilising PEDOT:PSS or MoO<sub>x</sub>. This confirmed that the acidic nature of the vanadium oxytriisopropoxide precursor did indeed affect the electronic structure and the formation of additional defects at the interface. Additional

experiments are needed to develop both stability and performance of s- V<sub>2</sub>O<sub>x</sub>-based devices after continuous illumination.

## 7.5 References

1. Y. Liu, J. Zhao, Z. Li, C. Mu, W. Ma, H. Hu, K. Jiang, H. Lin, H. Ade and H. Yan, *Aggregation and morphology control enables multiple cases of high-efficiency polymer solar cells*, Nature Communications **5** (2014).
2. K. M. Coakley and M. D. McGehee, *Conjugated polymer photovoltaic cells*, Chemistry of Materials **16** (2004), no. 23, 4533-4542.
3. F. C. Krebs, *Stability and degradation of organic and polymer solar cells*, Wiley, Chichester, 2012.
4. J. U. Lee, J. W. Jung, J. W. Jo and W. H. Jo, *Degradation and stability of polymer-based solar cells*, Journal of Materials Chemistry **22** (2012), no. 46, 24265-24283.
5. N. Grossiord, J. M. Kroon, R. Andriessen and P. W. M. Blom, *Degradation mechanisms in organic photovoltaic devices*, Organic Electronics **13** (2012), no. 3, 432-456.
6. H. Cao, W. He, Y. Mao, X. Lin, K. Ishikawa, J. H. Dickerson and W. P. Hess, *Recent progress in degradation and stabilization of organic solar cells*, Journal of Power Sources **264** (2014), 168-183.
7. M. Jorgensen, K. Norrman and F. C. Krebs, *Stability/degradation of polymer solar cells*, Solar Energy Materials and Solar Cells **92** (2008), no. 7, 686-714.
8. M. O. Reese, S. A. Gevorgyan, M. Jorgensen, E. Bundgaard, S. R. Kurtz, D. S. Ginley, D. C. Olson, M. T. Lloyd, P. Moryllo, E. A. Katz, A. Elschner, O. Haillant,

- T. R. Currier, V. Shrotriya, M. Hermenau, M. Riede, K. R. Kirov, G. Trimmel, T. Rath, O. Inganäs, F. Zhang, M. Andersson, K. Tvingstedt, M. Lira-Cantu, D. Laird, C. McGuinness, S. Gowrisanker, M. Pannone, M. Xiao, J. Hauch, R. Steim, D. M. DeLongchamp, R. Roesch, H. Hoppe, N. Espinosa, A. Urbina, G. Yaman-Uzunoglu, J.-B. Bonekamp, A. J. J. M. van Breemen, C. Girotto, E. Voroshazi and F. C. Krebs, *Consensus stability testing protocols for organic photovoltaic materials and devices*, *Solar Energy Materials and Solar Cells* **95** (2011), no. 5, 1253-1267.
9. R. Roesch, T. Faber, E. von Hauff, T. M. Brown, M. Lira-Cantu and H. Hoppe, *Procedures and practices for evaluating thin-film solar cell stability*, *Advanced Energy Materials* **5** (2015), no. 20, 24.
10. F. C. Krebs, J. E. Carle, N. Cruys-Bagger, M. Andersen, M. R. Lilliedal, M. A. Hammond and S. Hvidt, *Lifetimes of organic photovoltaics: Photochemistry, atmosphere effects and barrier layers in ITO-MEHPPV:PCBM-Aluminium devices*, *Solar Energy Materials and Solar Cells* **86** (2005), no. 4, 499-516.
11. M. P. de Jong, L. J. van Ijzendoorn and M. J. A. de Voigt, *Stability of the interface between indium-tin-oxide and poly(3,4-ethylenedioxythiophene)/poly(styrenesulfonate) in polymer light-emitting diodes*, *Applied Physics Letters* **77** (2000), no. 14, 2255-2257.
12. M. Jorgensen, K. Norrman, S. A. Gevorgyan, T. Tromholt, B. Andreasen and F. C. Krebs, *Stability of polymer solar cells*, *Advanced Materials* **24** (2012), no. 5, 580-612.

13. R. D. Scurlock, B. J. Wang, P. R. Ogilby, J. R. Sheats and R. L. Clough, *Singlet oxygen as a reactive intermediate in the photodegradation of an electroluminescent polymer*, Journal of the American Chemical Society **117** (1995), no. 41, 10194-10202.
14. B. H. Cumpston and K. F. Jensen, *Photooxidative stability of substituted poly(phenylene vinylene) (PPV) and poly(phenylene acetylene) (PPA)*, Journal of Applied Polymer Science **69** (1998), no. 12, 2451-2458.
15. H. Neugebauer, C. Brabec, J. C. Hummelen and N. S. Sariciftci, *Stability and photodegradation mechanisms of conjugated polymer/fullerene plastic solar cells*, Solar Energy Materials and Solar Cells **61** (2000), no. 1, 35-42.
16. X. N. Yang, J. K. J. van Duren, R. A. J. Janssen, M. A. J. Michels and J. Loos, *Morphology and thermal stability of the active layer in poly(p-phenylenevinylene)/methanofullerene plastic photovoltaic devices*, Macromolecules **37** (2004), no. 6, 2151-2158.
17. R. J. Kline, M. D. McGehee, E. N. Kadnikova, J. S. Liu, J. M. J. Frechet and M. F. Toney, *Dependence of regioregular poly(3-hexylthiophene) film morphology and field-effect mobility on molecular weight*, Macromolecules **38** (2005), no. 8, 3312-3319.
18. S. Berson, R. De Bettignies, S. Bailly and S. Guillerez, *Poly (3-hexylthiophene) fibers for photovoltaic applications*, Advanced Functional Materials **17** (2007), no. 8, 1377-1384.

19. X. N. Yang, J. Loos, S. C. Veenstra, W. J. H. Verhees, M. M. Wienk, J. M. Kroon, M. A. J. Michels and R. A. J. Janssen, *Nanoscale morphology of high-performance polymer solar cells*, *Nano Letters* **5** (2005), no. 4, 579-583.
20. C. J. Schaffer, C. M. Palumbiny, M. A. Niedermeier, C. Jendrzewski, G. Santoro, S. V. Roth and P. Muller-Buschbaum, *A direct evidence of morphological degradation on a nanometer scale in polymer solar cells*, *Advanced Materials* **25** (2013), no. 46, 6760-6764.
21. S. A. Carter, M. Angelopoulos, S. Karg, P. J. Brock and J. C. Scott, *Polymeric anodes for improved polymer light-emitting diode performance*, *Applied Physics Letters* **70** (1997), no. 16, 2067-2069.
22. Y. Cao, G. Yu, C. Zhang, R. Menon and A. J. Heeger, *Polymer light-emitting diodes with polyethylene dioxythiophene-polystyrene sulfonate as the transparent anode*, *Synthetic Metals* **87** (1997), no. 2, 171-174.
23. K. Kawano, R. Pacios, D. Poplavskyy, J. Nelson, D. D. C. Bradley and J. R. Durrant, *Degradation of organic solar cells due to air exposure*, *Solar Energy Materials and Solar Cells* **90** (2006), no. 20, 3520-3530.
24. A. M. Nardes, M. Kemerink, M. M. de Kok, E. Vinken, K. Maturova and R. A. J. Janssen, *Conductivity, work function, and environmental stability of PEDOT:Pss thin films treated with sorbitol*, *Organic Electronics* **9** (2008), no. 5, 727-734.
25. M. Vazquez, J. Bobacka, A. Ivaska and A. Lewenstam, *Influence of oxygen and carbon dioxide on the electrochemical stability of poly(3,4-ethylenedioxythiophene)*

- used as ion-to-electron transducer in all-solid-state ion-selective electrodes*, Sensors and Actuators B-Chemical **82** (2002), no. 1, 7-13.
26. S.-I. Na, J.-S. Lee, Y.-J. Noh, T.-W. Kim, S.-S. Kim, H.-I. Joh and S. Lee, *Efficient ITO-free polymer solar cells with pitch-converted carbon nanosheets as novel solution-processable transparent electrodes*, Solar Energy Materials and Solar Cells **115** (2013), 1-6.
27. J.-W. Lim, D.-Y. Cho, K. Jihoon, S.-I. Na and H.-K. Kim, *Simple brush-painting of flexible and transparent Ag nanowire network electrodes as an alternative ITO anode for cost-efficient flexible organic solar cells*, Solar Energy Materials and Solar Cells **107** (2012), 348-354.
28. S. Bose, S. S. Keller, T. S. Alstrom, A. Boisen and K. Almdal, *Process optimization of ultrasonic spray coating of polymer films*, Langmuir **29** (2013), no. 23, 6911-6919.
29. L. J. Andres, M. F. Menendez, D. Gomez, A. L. Martinez, N. Bristow, J. P. Kettle, A. Menendez and B. Ruiz, *Rapid synthesis of ultra-long silver nanowires for tailor-made transparent conductive electrodes: Proof of concept in organic solar cells*, Nanotechnology **26** (2015), no. 26, 9.
30. M. D. Irwin, B. Buchholz, A. W. Hains, R. P. H. Chang and T. J. Marks, *P-type semiconducting nickel oxide as an efficiency-enhancing anode interfacial layer in polymer bulk-heterojunction solar cells*, Proceedings of the National Academy of Sciences of the United States of America **105** (2008), no. 8, 2783-2787.



31. K. X. Steirer, P. F. Ndione, N. E. Widjonarko, M. T. Lloyd, J. Meyer, E. L. Ratcliff, A. Kahn, N. R. Armstrong, C. J. Curtis, D. S. Ginley, J. J. Berry and D. C. Olson, *Enhanced efficiency in plastic solar cells via energy matched solution processed NiO<sub>x</sub> interlayers*, *Advanced Energy Materials* **1** (2011), no. 5, 813-820.
32. C. Girotto, E. Voroshazi, D. Cheyns, P. Heremans and B. P. Rand, *Solution-processed MoO<sub>3</sub> thin films as a hole-injection layer for organic solar cells*, *Acs Applied Materials & Interfaces* **3** (2011), no. 9, 3244-3247.
33. E. Voroshazi, B. Verreet, A. Buri, R. Mueller, D. Di Nuzzo and P. Heremans, *Influence of cathode oxidation via the hole extraction layer in polymer:fullerene solar cells*, *Organic Electronics* **12** (2011), no. 5, 736-744.
34. M. O. Reese, A. J. Morfa, M. S. White, N. Kopidakis, S. E. Shaheen, G. Rumbles and D. S. Ginley, *Pathways for the degradation of organic photovoltaic P3HT:PCBM based devices*, *Solar Energy Materials and Solar Cells* **92** (2008), no. 7, 746-752.
35. S. O. Jeon and J. Y. Lee, *Improved lifetime in organic solar cells using a bilayer cathode of organic interlayer/Al*, *Solar Energy Materials and Solar Cells* **101** (2012), 160-165.
36. A. Hayakawa, O. Yoshikawa, T. Fujieda, K. Uehara and S. Yoshikawa, *High performance polythiophene/fullerene bulk-heterojunction solar cell with a TiO<sub>x</sub> hole blocking layer*, *Applied Physics Letters* **90** (2007), no. 16.

37. D. Angmo, S. A. Gevorgyan, T. T. Larsen-Olsen, R. R. Sondergaard, M. Hosel, M. Jorgensen, R. Gupta, G. U. Kulkarni and F. C. Krebs, *Scalability and stability of very thin, roll-to-roll processed, large area, indium-tin-oxide free polymer solar cell modules*, *Organic Electronics* **14** (2013), no. 3, 984-994.
38. R. Tipnis, J. Bernkopf, S. Jia, J. Krieg, S. Li, M. Storch and D. Laird, *Large-area organic photovoltaic module-fabrication and performance*, *Solar Energy Materials and Solar Cells* **93** (2009), no. 4, 442-446.
39. E. Bovill, N. Scarratt, J. Griffin, H. Yi, A. Iraqi, A. R. Buckley, J. W. Kingsley and D. G. Lidzey, *The role of the hole-extraction layer in determining the operational stability of a polycarbazole: Fullerene bulk-heterojunction photovoltaic device*, *Applied Physics Letters* **106** (2015), no. 7.
40. C. Bracher, H. N. Yi, N. W. Scarratt, R. Masters, A. J. Pearson, C. Rodenburg, A. Iraqi and D. G. Lidzey, *The effect of residual palladium catalyst on the performance and stability of PCDTBT:PC<sub>70</sub>BM organic solar cells*, *Organic Electronics* **27** (2015), 266-273.
41. Y. Sun, C. J. Takacs, S. R. Cowan, J. H. Seo, X. Gong, A. Roy and A. J. Heeger, *Efficient, air-stable bulk heterojunction polymer solar cells using MoO<sub>x</sub> as the anode interfacial layer*, *Advanced Materials* **23** (2011), no. 19, 2226-+.
42. B. Zimmermann, U. Wuerfel and M. Niggemann, *Longterm stability of efficient inverted P3HT:PCBM solar cells*, *Solar Energy Materials and Solar Cells* **93** (2009), no. 4, 491-496.

43. M. J. Tan, S. Zhong, R. Wang, Z. Zhang, V. Chellappan and W. Chen, *Biopolymer as an electron selective layer for inverted polymer solar cells*, Applied Physics Letters **103** (2013), no. 6.
44. J. You, C.-C. Chen, L. Dou, S. Murase, H.-S. Duan, S. A. Hawks, T. Xu, H. J. Son, L. Yu, G. Li and Y. Yang, *Metal oxide nanoparticles as an electron-transport layer in high-performance and stable inverted polymer solar cells*, Advanced Materials **24** (2012), no. 38, 5267-5272.
45. J. Y. Kim, K. Lee, N. E. Coates, D. Moses, T.-Q. Nguyen, M. Dante and A. J. Heeger, *Efficient tandem polymer solar cells fabricated by all-solution processing*, Science **317** (2007), no. 5835, 222-225.
46. C. H. Peters, I. T. Sachs-Quintana, W. R. Mateker, T. Heumueller, J. Rivnay, R. Noriega, Z. M. Beiley, E. T. Hoke, A. Salleo and M. D. McGehee, *The mechanism of burn-in loss in a high efficiency polymer solar cell*, Advanced Materials **24** (2012), no. 5, 663-+.
47. C.-Y. Chang, F.-Y. Tsai, S.-J. Jhuo and M.-J. Chen, *Enhanced OLED performance upon photolithographic patterning by using an atomic-layer-deposited buffer layer*, Organic Electronics **9** (2008), no. 5, 667-672.
48. M. Yoshizawa, A. Yasuda and T. Kobayashi, *Ultrafast optical-response in polydiacetylenes and polythiophenes*, Applied Physics B-Photophysics and Laser Chemistry **53** (1991), no. 5-6, 296-307.

49. J. Schafferhans, A. Baumann, A. Wagenpfahl, C. Deibel and V. Dyakonov, *Oxygen doping of P3HT:PCBM blends: Influence on trap states, charge carrier mobility and solar cell performance*, *Organic Electronics* **11** (2010), no. 10, 1693-1700.
50. C. H. Peters, I. T. Sachs-Quintana, J. P. Kastrop, S. Beaupre, M. Leclerc and M. D. McGehee, *High efficiency polymer solar cells with long operating lifetimes*, *Advanced Energy Materials* **1** (2011), no. 4, 491-494.
51. T. Matsushima, M. Yahiro and C. Adachi, *Estimation of electron traps in carbon-60 field-effect transistors by a thermally stimulated current technique*, *Applied Physics Letters* **91** (2007), no. 10.
52. Z. A. Tan, W. Q. Zhang, C. H. Cui, Y. Q. Ding, D. P. Qian, Q. Xu, L. J. Li, S. S. Li and Y. F. Li, *Solution-processed vanadium oxide as a hole collection layer on an ITO electrode for high-performance polymer solar cells*, *Physical Chemistry Chemical Physics* **14** (2012), no. 42, 14589-14595.
53. C. P. Chen, Y. D. Chen and S. C. Chuang, *High-performance and highly durable inverted organic photovoltaics embedding solution-processable vanadium oxides as an interfacial hole-transporting layer*, *Advanced Materials* **23** (2011), no. 33, 3859-+.
54. A. Bouzidi, N. Benramdane, A. Nakrela, C. Mathieu, B. Khelifa, R. Desfeux and A. Da Costa, *First synthesis of vanadium oxide thin films by spray pyrolysis technique*, *Materials Science and Engineering B-Solid State Materials for Advanced Technology* **95** (2002), no. 2, 141-147.

55. G. Teran-Escobar, J. Pampel, J. M. Caicedo and M. Lira-Cantu, *Low-temperature, solution-processed, layered V<sub>2</sub>O<sub>5</sub> hydrate as the hole-transport layer for stable organic solar cells*, *Energy & Environmental Science* **6** (2013), no. 10, 3088-3098.
56. H.-Q. Wang, N. Li, N. S. Guldal and C. J. Brabec, *Nanocrystal V<sub>2</sub>O<sub>5</sub> thin film as hole-extraction layer in normal architecture organic solar cells*, *Organic Electronics* **13** (2012), no. 12, 3014-3021.

# Chapter 8

## Conclusion and Further Work

### 8.1 Conclusions of Work Undertaken

Solution-processing of the metal oxide interfacial layers is an important target to achieve in order to reduce the cost of the deposition of these layers. However, most of those solution processed metal oxides require post-deposition treatment such as thermal annealing and oxygen plasma treatment [1-4]. These two techniques, although not difficult to implement, are often time-consuming and energy-intensive. For technologies such as organic photovoltaics, the incorporation of these post deposition processing techniques in roll-to-roll setups is extremely impractical.

The basic properties of materials that have been used within the experimental chapters were characterised with various techniques. The results of both absorption and photoelectron spectroscopies for solution processed metal oxides showed the high transparency across the visible region of the spectrum and high work functions which are in good agreement with the commonly reported values[5-7]. These properties allowed those metal oxides to have good potential for use as hole extraction layers and thus fabrication of high performance devices using various semiconducting donor polymers such as PCDTBT and PFDT2BT-8.

Throughout this work focus has been placed upon the impact of post-deposition treatments on the performance of solution processed metal oxides with OPV devices with the aim of trying to use effective HEL layer without the need for post-deposition treatment. It has been shown that it is possible to fabricate OPV devices with the use of solution-processed  $V_2O_x$  thin film from Vanadium (V) Isopropoxide precursor without any post-deposition treatment such as thermal annealing or oxygen plasma treatment. A high efficiency devices were achieved which are comparable to with the most widely used HELs: PEDOT:PSS and vacuum deposited  $MoO_3$  promising for efficient OPV with a low cost manufacturing process. Furthermore, OPV devices fabricated with annealed s- $V_2O_x$  layers at  $400^\circ C$  OPV showed a good performance and thus it can be suitable for optoelectronic devices which are fabricated at high temperatures.

The operational lifetime study of s- $V_2O_x$ -based devices was carried out in the indoor laboratory testing system. The results were compared with OPV devices utilising PEDOT:PSS and vacuum deposited  $MoO_3$ . PEDOT:PSS-based devices offered the highest stability, which is in contrast to the previous reports in literature. This discrepancy could be attributed to using different grades of PEDOT:PSS that may have more neutral pH. In addition, it was found that increasing the s- $V_2O_x$  thickness to 15 nm and then thermally annealing in air at  $150^\circ C$  resulted in a marked improvement in the stability of the OPV device. The significant reduction in the amount of some chemical components that may come from precursor residues and atmospheric components can be the main factor for improving the device stability. On the other hand, the low PCE of s- $V_2O_x$ -based devices after burn-in period can be ascribed to the acidic nature of the vanadium oxytriisopropoxide precursor that affects the electronic structure and forms additional defects at the interface.

Finally, the solution processing of thin films of nickel oxides from a nickel acetylacetonate precursor for use in organic photovoltaics were studied. This work has shown that the performance of OPVs containing NiO films deposited from this precursor depends strongly upon post deposition treatment. Thermal annealing was needed to drive the conversion of the precursor into the metal oxide. Moreover, treatment of annealed films with an oxygen plasma leads to further increases in efficiency with a reported peak PCE of 5.2%. This treatment resulted in a further increase of the work function leading to a reduced extraction barrier at the organic interface.

### 8.2 Suggestions for Further Work

The work presented in this thesis has provided some insight into the capability of several commonly-used metal oxides to be deposited from solution via various techniques to produce high OPV device performances. The most promising solution-processable forms of metal oxides are those fabricated without the need for post-deposition treatment or deposited with low-temperature processes. Although  $V_2O_x$  films were deposited from vanadium(V) oxytriisopropoxide at room temperature and then were thermally annealed at low temperature, the lifetime test of  $V_2O_x$ -based devices showed low performance after illumination. Using a different precursor such as vanadium acetylacetonate solution [8],  $V_2O_x$  powder [9], vanadium trichloride solution [10], sodium metavanadate [11] and vanadium (III) acetylacetonate [12] can overcome the acidic issue of vanadium(V) oxytriisopropoxide and improve the device stability. Some of the  $V_2O_x$ -based devices fabricated with these components have shown a good performance with a PCE similar to those fabricated with oxytriisopropoxide precursor. Furthermore, long term OPV cell stability measurements



are crucial and need to be designed to indicate the potential of cell commercialisation. This would require testing facilities that can measure stability over months rather than days and under various conditions, such as indoor and outdoor testing with variation of humidity and cell temperature. Moreover, The factors behind the high stability of the PEDOT:PSS-based devices are not fully understood. Therefore, further experiments could be carried out using various pH solutions and different donor polymers.

Characterisation by techniques such as secondary ion mass spectroscopy would help to determine which layers in the OPV cell are most susceptible to degradation. In addition, the dark J-V characteristic for OPV devices should be used to give important further insight into changes in device fill-factor and open-circuit voltage.

Using a solution- processable metal oxides in inverted architecture is a preferred technique in order to achieve a fully solution processed device. Therefore, a deposition solution-processed metal oxide on the top of organic layer at low temperature is a crucial step to avoid damaging the active layer. In addition to the heating issue, certain solvents used with metal oxide precursors may not be suitable for organic polymers. Some of these solvents can lead either to a non-uniform layer with the organic layer or to the dissolving the active layer itself and thus changing its morphology and causing the diffusion of some metal oxide components into the organic layer. If an inverted structure with three solution-processed layers is achieved with high performance the next step would be to study its lifetime and investigate the chemical reactions (photo-oxidation process) that are likely to occur at the interfaces. Finally, a suitable solution-processable replacement for the transparent electrode (ITO) was the envisaged design for fabrication of a fully solution- processable device. Currently, efforts are being made by many groups to find a suitable solution processable electrode [13-17].

Consequently, additional work should be carried out to develop a fully solution-processable device, investigate its stability over time and explain the possible chemical reactions at interfaces and their impact on the interface energetics. At the same time, finding strategies to prevent the solution-processed interlayers from damaging the active layer is desired to achieve optimum electronic functionality at the anode interlayer/organic interface and thus overall improved device characteristics.

### 8.3 References

1. V. Shrotriya, G. Li, Y. Yao, C. W. Chu and Y. Yang, *Transition metal oxides as the buffer layer for polymer photovoltaic cells*, Applied Physics Letters **88** (2006), no. 7.
2. R. Jose, V. Thavasi and S. Ramakrishna, *Metal oxides for dye-sensitized solar cells*, Journal of the American Ceramic Society **92** (2009), no. 2, 289-301.
3. S. Chen, J. R. Manders, S.-W. Tsang and F. So, *Metal oxides for interface engineering in polymer solar cells*, Journal of Materials Chemistry **22** (2012), no. 46, 24202-24212.
4. J. Meyer, S. Hamwi, M. Kroger, W. Kowalsky, T. Riedl and A. Kahn, *Transition metal oxides for organic electronics: Energetics, device physics and applications*, Advanced Materials **24** (2012), no. 40, 5408-5427.
5. G. Silversmit, D. Depla, H. Poelman, G. B. Marin and R. De Gryse, *Determination of the  $v2p$  xps binding energies for different vanadium oxidation states ( $v5+$  to  $v0+$ )*, Journal of Electron Spectroscopy and Related Phenomena **135** (2004), no. 2-3, 167-175.
6. G. A. Sawatzky and D. Post, *X-ray photoelectron and auger-spectroscopy study of some vanadium-oxides*, Physical Review B **20** (1979), no. 4, 1546-1555.
7. M. Demeter, M. Neumann and W. Reichelt, *Mixed-valence vanadium oxides studied by xps*, Surface Science **454–456** (2000), no. 0, 41-44.

8. Z. A. Tan, W. Q. Zhang, C. H. Cui, Y. Q. Ding, D. P. Qian, Q. Xu, L. J. Li, S. S. Li and Y. F. Li, *Solution-processed vanadium oxide as a hole collection layer on an ito electrode for high-performance polymer solar cells*, *Physical Chemistry Chemical Physics* **14** (2012), no. 42, 14589-14595.
9. C. P. Chen, Y. D. Chen and S. C. Chuang, *High-performance and highly durable inverted organic photovoltaics embedding solution-processable vanadium oxides as an interfacial hole-transporting layer*, *Advanced Materials* **23** (2011), no. 33, 3859-+.
10. A. Bouzidi, N. Benramdane, A. Nakrela, C. Mathieu, B. Khelifa, R. Desfeux and A. Da Costa, *First synthesis of vanadium oxide thin films by spray pyrolysis technique*, *Materials Science and Engineering B-Solid State Materials for Advanced Technology* **95** (2002), no. 2, 141-147.
11. G. Teran-Escobar, J. Pampel, J. M. Caicedo and M. Lira-Cantu, *Low-temperature, solution-processed, layered v<sub>2</sub>o<sub>5</sub> hydrate as the hole-transport layer for stable organic solar cells*, *Energy & Environmental Science* **6** (2013), no. 10, 3088-3098.
12. H.-Q. Wang, N. Li, N. S. Guldal and C. J. Brabec, *Nanocrystal v<sub>2</sub>o<sub>5</sub> thin film as hole-extraction layer in normal architecture organic solar cells*, *Organic Electronics* **13** (2012), no. 12, 3014-3021.
13. C. M. Muiva, T. S. Sathiaraj and K. Maabong, *Effect of doping concentration on the properties of aluminium doped zinc oxide thin films prepared by spray pyrolysis for transparent electrode applications*, *Ceramics International* **37** (2011), no. 2, 555-560.

14. K. S. Kim, Y. Zhao, H. Jang, S. Y. Lee, J. M. Kim, K. S. Kim, J.-H. Ahn, P. Kim, J.-Y. Choi and B. H. Hong, *Large-scale pattern growth of graphene films for stretchable transparent electrodes*, Nature **457** (2009), no. 7230, 706-710.
15. S. Bae, H. Kim, Y. Lee, X. Xu, J.-S. Park, Y. Zheng, J. Balakrishnan, T. Lei, H. R. Kim, Y. I. Song, Y.-J. Kim, K. S. Kim, B. Ozyilmaz, J.-H. Ahn, B. H. Hong and S. Iijima, *Roll-to-roll production of 30-inch graphene films for transparent electrodes*, Nature Nanotechnology **5** (2010), no. 8, 574-578.
16. H. Wu, D. Kong, Z. Ruan, P.-C. Hsu, S. Wang, Z. Yu, T. J. Carney, L. Hu, S. Fan and Y. Cui, *A transparent electrode based on a metal nanotrough network*, Nature Nanotechnology **8** (2013), no. 6, 421-425.
17. A. Kim, Y. Won, K. Woo, C.-H. Kim and J. Moon, *Highly transparent low resistance zno/ag nanowire/zno composite electrode for thin film solar cells*, Acs Nano **7** (2013), no. 2, 1081-1091.